CORE-SHELL COMPOUND DROPLET IMPACT ON A SOLID SURFACE

ISMAIL ALKOMY

A DISSERTATION SUBMITTED TO

THE FACULTY OF GRADUATE STUDIES

IN PARTIAL FULFILLMENT OF THE REQUIREMENTS

FOR THE DEGREE OF

DOCTOR OF PHILOSOPHY

GRADUATE PROGRAM IN MECHANICAL ENGINEERING

YORK UNIVERSITY

TORONTO, ONTARIO

February 2026

ABSTRACT

Droplet impact on solid surfaces controls critical outcomes in printing, coating, spray cooling, encapsulation and additive manufacturing, where both the impact regime and the maximum spreading factor, (i.e., $\beta_{\max}$, that is the maximum coverage diameter the drop leaves on the surface normalized by its initial diameter), set footprint, coverage and material retention. In these processes, multicomponent core-shell droplets offer internal structure as an additional degree of freedom, yet their impact behavior is far less understood than that of single-liquid droplets. This thesis investigates the normal impact of millimetric core-shell droplets on smooth solid surfaces, with the aim of predicting impact outcome and $\beta_{\max}$ using a unified framework that combines experiments, an energy-balance model and machine learning. Experiments are performed with water and water-glycerol cores encapsulated by silicone oil shells of varied viscosity, while systematically varying impact velocity and core volume fraction. High-speed imaging is used to classify impacts into jetting, partial rebound, spreading-contact and their splashing counterparts, and to measure $\beta_{\max}$. The data are expressed in a compact multicomponent non-dimensional space based on an equivalent Weber number that accounts for both external and internal interfaces, together with phase-specific Reynolds numbers for core and shell. On this foundation, a compound-droplet energy-balance model is formulated that treats $\beta_{\max}$ as the outcome of a global balance between initial kinetic and surface energies and viscous dissipation in core and shell, with separate scaling laws for each phase. The model predicts $\beta_{\max}$ accurately across the experimental parameter range and reveals how energy partitioning shifts with equivalent Weber number, core fraction and shell viscosity exploiting the comprehension of the underlying physics

behind the process. In parallel, supervised machine learning models, trained on the same non-dimensional features, deliver high-fidelity predictions of both impact outcome and $\beta_{\max}$, while interpretability analyses recover and even improve the dominant physical controls identified by experiments and the energy-balance model. Together, these three pillars demonstrate how internal structure in core-shell droplets can be exploited to manipulate impact behavior and provide predictive tools suitable for analysis and design.

ACKNOWLEDGMENTS

I would like to thank my mentor and supervisor, Prof. Alidad Amirfazli, for his steady guidance and support throughout my PhD, both academically and on a personal level. I am also grateful to Prof. Marco Marengo for his depth of expertise and detailed feedback, especially on the modelling aspects of this work, which strengthened the analysis considerably. I thank Prof. Roger Kempers for his constructive comments and helpful input during committee meetings. I am deeply grateful to my mother, father and brother for their continuous support, patience, and encouragement. Finally, I thank my beautiful supportive sisters, my lab mates and friends: Milad, Beenu, Roshi and Pierre for their friendship and day-to-day experiences, Ahmed Azzam for valuable technical advice, and Yating Hu for being a constant support over nearly five years, including the simple but important encouragement of working side by side. I am grateful to all opportunities and incredible support I have received throughout my journey since I first came to Canada and even before, Jill, Mira, Yvonne, Nancy, Almey, Dimitri, Garrett, Arlethita, Khaled Youssef, and many others.

TABLE OF CONTENTS

ABSTRACT ii

ACKNOWLEDGMENTS iv

TABLE OF CONTENTS v

LIST OF TABLES ix

LIST OF FIGURES x

NOMENCLATURE xvii

Chapter 1 Introduction and motivation 1

1.1 Motivation and significance 1

1.2 Scope: Multi-component droplets 6

1.3 Theoretical background 12

1.4 Approaches to study and predict droplet impact outcome 16

1.5 Problem statement and knowledge gaps 20

1.6 Thesis objectives and structure 23

1.7 References 26

Chapter 2 Experimental approach [1] 35

2.1 Introduction 35
2.1.1 Impact outcome 38
2.1.2 Maximum spreading 41
2.2 Materials and Method 43
2.2.1 Experiment parameters range 44
2.2.2 Experimental apparatus 49
2.3 Results and Discussion 51
2.3.1 Impact outcome 51
2.3.2 Maximum spreading 60
2.4 Conclusions – Key highlights 65
2.5 References 66
Chapter 3 Mathematical modelling approach[2] 73
3.1 Introduction 73
3.2 Modelling method and validation domain 83
3.3 Experimental methods and materials 87
3.4 Energy balance 89
3.4.1 Initial energy before impact (E1) 89
3.4.2 Energy at the maximum spreading (E2) 90
3.4.3 Empirical model coefficients 95

3.5 Results and Discussion 97
3.5.1 Model validation 97
3.5.2 Spreading dependency on impact parameters 101
3.5.3 Energy analysis for spreading factor 105
3.6 Conclusion – Key highlights 110
3.7 References 111
Chapter 4 Machine learning approach[3] 117
4.1 Introduction 117
4.1.1 Machine learning for impact regime classification (single-liquid droplets) ... 123
4.1.2 Machine learning for maximum spreading regression (single-liquid droplets) 126
4.2 Machine learning method 130
4.2.1 Data source, features, and preparation 131
4.2.2 Train-test splitting and cross-validation 133
4.2.3 Model families and capacity-controlled hyperparametric presets 142
4.2.4 Model selection criteria 147
4.3 Results and Discussion 148
4.3.1 Classification results 148
4.3.2 Regression results 157

4.4 Conclusions – Key highlights 165

4.5 References 166

Chapter 5 Conclusions and future work 174

5.1 Integrated summary and contributions 174

5.2 Limitations and scope of validity 180

5.3 Future directions 184

APPENDICES 188

Appendix A: Chapter 2 supplementary information 188

Appendix B: Chapter 3 supplementary information 192

- Model Calibration and Optimization Workflow 192
- Accuracy Metrics for Model Validation 195
- Residual Histogram 196

Appendix C: Chapter 4 supplementary information 197

- Accuracy metrics 197
- Stratified splitting 198
- Model families and presets accuracy 204
- Neural-network-predicted regime map in the We–α plane 208

LIST OF TABLES

Table 2-1 Liquids properties for the core and shell materials used. All measurements are at 20°C 45

Table 2-2 Liquid combinations used in the experiments with the abbreviations used to describe the liquid-set. All experiments are done at 20°C 49

Table 3-1 Physical properties of the core and shell liquids used in the experiments. All values were measured at 20°C. 88

Table 4-1 Sensitivity of compound-drop impact outcomes to We, α, Rei, and Reo. Entries encode the direction and strength of the tendency in outcome likelihood as each predictor varies. 121

Table 4-2 Sensitivity of the maximum spreading factor βmax for encapsulated-spreading impacts (i.e., cases where cores remain encapsulated up to βmax, such as jetting and partial rebound) to We, α, Rei, and Reo..... 122

Table 4-3 Model families and capacity-controlled presets with defining hyperparameters and brief rationale..... 145

LIST OF FIGURES

Figure 1-1. Schematic illustration of canonical single liquid droplet impact outcomes on a smooth solid surface, together with the definition of the maximum spreading factor $\beta max = D/d$. Top row: deposition, prompt splash, and corona splash. Bottom row: partial rebound, full rebound, and rebound with splash. 4

Figure 1-2 Overview of droplet-impact research organized by drop composition, highlighting the subset of single-interface compound drops (core–shell) within the broader class of complex drops. Adapted from "Impact of compound drops: a perspective" [20]. 7

Figure 2-1 Thermodynamic stability of core shell configuration. Numbers (1, 2 and 3) refer to phase 1, phase 2 and surrounding phase 3. Phase 2 in 3 has lower interfacial tension than phase 1 in 3 ($\sigma 13 > \sigma 23$). Core-shell configuration is thermodynamically stable when ($S2 > 0$) and ($S3, S1 < 0$) 37

Figure 2-2 Experiment apparatus. Two high speed cameras, Coaxial needles adjustable setup, lighting, target solid surface and syringe pumps with feeding lines and fittings. The computer was used to control and collect recorded data 50

Figure 2-3 Impact of drops (silicon oil "a" and water "b") and a compound water-in-oil "c" of core size (α=0.5) on glass surfaces. The initial Weber number for all cases is We≈65 51

Figure 2-4 a) Equivalent Weber number variation with increasing the core size for different impact velocities. b) Modified versus unmodified Weber number values across a range of impact velocities. Both graphs show data for water in silicon oil (5 cSt). 53

Figure 2-5 From jetting to partial rebound: Impact of a compound droplet of water inside silicone oil (5cSt) with a core size of α=0.7 on glass surface. Equivalent Weber numbers for a-d are 19.5, 37.7, 65.5 and 96, respectively. 54

Figure 2-6 Spreading of core and shell phases without jetting. Water core inside silicon oil (5cSt) shell (α=0.9). The equivalent Weber number is (110). 55

Figure 2-7 The regime map of water core inside silicon oil (5cSt) for a full range of core sizes including single-component drops. Inset for prompt splash is the bottom view 56

Figure 2-8 Transition to splashing by varying core size of (W/S5) compound drops. The equivalent Weber number is 88. Core sizes are 0.0 'pure S5 oil', 0.2, 0.4 and 0.7 from top to bottom. 57

Figure 2-9 The regime maps for different liquid combinations in parameter space of Equivalent Weber number and core size. The direction a-b-c indicates increasing the shell viscosity from 5-10-20 cSt while the core is water (1 cSt). The direction of a-d-e indicates increasing the core viscosity from 1-16-22.5 mPa.s and the shell is fixed 5 cSt oil. 59

Figure 2-10 The Energy at the incoming droplet just before impact is (1), the energy stored and dissipated up to maximum spreading (2). 60

Figure 2-11 The maximum spreading factor (βmax) as a function of average Weber number. Data shown are for Water in silicon oil (5 cSt) with three core sizes (0.3, 0.5 and 0.7). 61

Figure 2-12 The maximum spreading factor as function of the core size is illustrated for different liquid combinations. Different equivalent Weber numbers are shown here. 63

Figure 2-13 Maximum spreading factor as a function of equivalent Weber number for an increasing shell viscosity. Various core sizes are shown. 64

Figure 3-1 Schematic representation of a concentric core-shell compound droplet. The inner core diameter and the overall droplet diameter are denoted by di and do, respectively. Properties associated with the inner core are indicated by the subscript i, and those related to the outer shell by the subscript o. 80

Figure 3-2 Schematic illustration of a compound droplet impact, showing the droplet immediately before impact (state 1) and at its maximum spreading extent (state 2). 85

Figure 3-3 Comparison between experimentally measured and model-predicted maximum spreading factors for compound droplets on the unseen test set (We=10-260, Rei=38-3637, Reo =16-720; across all core sizes α). The solid line marks the ideal 1:1 agreement, and the dotted lines indicate the maximum error band (±13%). 98

Figure 3-4 Model prediction error across droplet impact outcomes and initial parameters; (a) is a boxplot of residuals grouped by impact outcome, and (b) is a heatmap of relative error over equivalent Weber number and core size, with the yellow contour marking the observed jetting-rebound transition region across liquid combinations. 99

Figure 3-5 Time sequence of a W/S20 compound droplet with core size ratio α≈0.1 impacting at $We \approx 17$, showing minimal core deformation throughout the spreading process. 100

Figure 3-6 Model predictions (Equation 3-16) of maximum spreading, βmax, versus core volume ratio, α, for five shell viscosities (S5-S100, corresponding to a-b panels). Markers color and size reflect the Weber number We. 102

Figure 3-7 Normalized spreading βmax (θ)/βmax (5°) versus contact angle θ for viscosity sets S5–S100; lines with circular markers denote medians, and box-and-whisker symbols show

distributions at each θ; legend colors identify S5–S100. A higher normalized value indicates weaker sensitivity of βmax to wettability (smaller reduction relative to the 5 ∘ baseline), not larger absolute spreading. 104

Figure 3-8 Energy budget distribution for compound droplet impacts across varying Weber numbers. Each column shows the percentage of initial kinetic and interfacial energy ($K.E.1$ and $S.E.1$) and its redistribution into final interfacial energy ($S.E.2$) and viscous dissipation within the core (Wi) and shell (Wo). Panels (a) and (b): water–glycerol core (70% glycerol, percentage in volume) in 5 cSt. Panels (c) and (d): water core in 5 cSt oil shell. Panels (e) and (f): water core in 20 cSt oil shell. All cases span increasing Weber numbers along the horizontal axis. Small cores are (α = 0.2), while large cores are (α = 0.8) for all cases. 107

Figure 3-9 Regime classification map showing surface-dominated (yellow), viscous-dominated (green), and transitional (red x) impact cases based on the relative contribution of final interfacial energy and total viscous dissipation. Points are model-predicted and plotted as a function of core size α and equivalent Weber number We. Classification is based on a 5% threshold in the relative difference between $S.E.2$ and Wv. 109

Figure 4-1 Class imbalance in the classification corpus ($Nclass = 550$). Bars show outcome prevalence as percentages with counts in parentheses; hatched bars denote splash counterparts. 132

Figure 4-2 Schematic of the train–test and cross-validation settings used for the classification and regression datasets, with three global splits (70/30, 75/25, 80/20) and 5-, 7-, and 10-fold cross-validation on the training subsets. 134

Figure 4-3 Pairwise scatter–histogram matrix of the nondimensional predictors We, α, Rei, and Reo for the classification corpus; marker shape and fill denote non-splashing outcomes (J, PR, SC), and red-outlined markers indicate their splashing counterparts (J+S, PR+S, SC+S). 136
Figure 4-4 Class-wise train and test proportions under the three global splits. 138
Figure 4-5 Outcome composition by liquid combination (stacked by outcome class), with overlaid curves indicating the achieved training fraction for each global split (70/30, 75/25, 80/20). 139
Figure 4-6 Train versus test distributions of standardized predictors for all splitting settings, violins and boxplots indicate matched location, spread, and tails. 140
Figure 4-7 Stratified train–test allocation for the regression subset across liquid combinations under the three global settings; stacked bars encode training and test fractions per combination. 141
Figure 4-8 Global-standardized distributions of predictors for the regression train and test partitions; violins with embedded boxplots, pooled across all split ratios. 142
Figure 4-9 Family-level heat map of test Micro-F1 scores (%) across the nine split–fold settings. Rows are model families and columns are split–fold combinations..... 149
Figure 4-10 Preset-level performance dispersion aggregated over all nine split–fold settings. Points show the mean test Micro-F1 score per preset and vertical bars indicate the range across settings. 151
Figure 4-11 Confusion matrices for the Medium Neural Network at the best-performing setting (i.e., 80/20 with 5-folds): (a) cross-validated folds and (b) held-out test set. Rows are true classes

and columns are predicted classes. Side panels report class-wise true positive rates and false negative rates. 153

Figure 4-12. Mean absolute Shapley values for the top performing preset (i.e., Medium Neural Network) by class and predictor. Solid fill denotes non-splashing classes (J, PR, SC) and hatched bars denote splashing counterparts (J+S, PR+S, SC+S). Larger bars indicate stronger influence. 154

Figure 4-13 Class-score dependency profiles for the top preset (i.e., Medium Neural Network) versus (a)We, (b) α, (c) Rei, and (d) Reo. Curves show predicted class scores with the other predictors fixed at their medians. Solid lines denote non-splashing classes and dashed lines denote splashing counterparts. 156

Figure 4-14 Family-level heat map of test RMSE across the nine split–fold settings. Rows are model families and columns are split–fold combinations. Lower values indicate better accuracy. 158

Figure 4-15 Preset-level performance aggregated over all nine split–fold settings. Points show the mean test RMSE per preset and vertical bars indicate the range across settings. 159

Figure 4-16 Parity plots for the top preset (Matérn $5/2$GPR): left, training folds; right, held-out test set. Each marker is one impact and the solid line is the identity. 160

Figure 4-17 Shapley beeswarm for the top preset. Each point is a prediction; horizontal position is the Shapley value for the labeled predictor; color encodes the predictor's value from low to high. Positive values increase predicted βmax. 161

Figure 4-18 One-predictor dependency profiles for the top preset showing βmax versus We, α, Rei, and Reo with the remaining predictors fixed at their medians. 163

NOMENCLATURE

Symbol	Description	Units
d	Initial droplet diameter (before impact)	[m]
D	Maximum footprint diameter at largest spread	[m]
Ω	Volume of a drop, or a segment of the drop (core or shell)	[m³]
$\beta_{\max} = D/d$	Maximum spreading factor	[non-dimensional]
t	Time from initial contact between drop and solid surface	[s]
t_{m}	Time to maximum spreading	[s]
U	Impact velocity of the droplet just before impact	[m s^{-1}]
g	Acceleration due to gravity	[m s^{-2}]
θ	Static (equilibrium) contact angle of the liquid on the solid	[°]
α	Core volume fraction	[non-dimensional]
ρ	Liquid density (single-phase)	[kg m^{-3}]
ρ_{i}	Density of the inner/core liquid phase	[kg m^{-3}]
ρ_o	Density of the outer/shell liquid phase	[kg m^{-3}]
ρ_g	Density of the ambient gas	[kg m^{-3}]
μ	Dynamic viscosity (single-phase)	[Pa s]
μ_{i}	Dynamic viscosity of the core liquid	[Pa s]
μ_{o}	Dynamic viscosity of the shell liquid	[Pa s]
σ	Liquid–gas surface tension (single-phase)	[N m^{-1}]
σ_{o}	Shell–gas surface tension	[N m^{-1}]
σ_{i}	Core–gas surface tension (when present)	[N m^{-1}]
σ_{io}	Core–shell interfacial tension	[N m^{-1}]
S_{i}	Spreading factor of a phase i	[N m^{-1}]

$\gamma = \sigma_{io}/\sigma_o$	Ratio of internal to outer/shell surface tension	[non-dimensional]
m	Mass of the drop, or a segment of it	[kg]
$We = \rho U^2 d/\sigma$	Weber number (inertia to capillarity ratio)	[non-dimensional]
$\overline{We}$	Equivalent Weber number for a core–shell droplet	[non-dimensional]
$Re = \rho U d/\mu$	Reynolds number (inertia to viscosity ratio)	[non-dimensional]
$P = We \cdot Re^{-4/5}$	Impact parameter distinguishing capillary- vs viscous-dominated regimes	[non-dimensional]
Re_i	Reynolds number of the core phase (based on ρ_i, μ_i)	[non-dimensional]
Re_o	Reynolds number of the shell phase (based on ρ_o, μ_o)	[non-dimensional]
$Oh = \mu/\sqrt{\rho\sigma d}$	Ohnesorge number (viscous to inertial–capillary ratio)	[non-dimensional]
$Bo = \rho g d^2/\sigma$	Bond number (gravity to capillarity ratio)	[non-dimensional]
KE_1	Initial kinetic energy of the droplet before impact	[J]
SE_1	Initial surface energy (external + internal interfaces)	[J]
SE_2	Surface energy at maximum spreading	[J]
W_v	Total viscous work (total viscous dissipation up to β_{max})	[J]
W_i	Viscous dissipation in the core phase	[J]
W_o	Viscous dissipation in the shell phase	[J]
E_1	Total initial energy (kinetic + surface)	[J]
E_2	Total energy at maximum spreading	[J]
ε	Relative energy-balance error	[non-dimensional]
D_i, D_o	Maximum lateral extents of core and shell at β_{max}	[m]
L_i, L_o	Effective lamella thickness scales for core and shell at β_{max}	[m]
X_n, n	Empirical coefficients in the core flattening–Reynolds scaling law	[non-dimensional]
X_m, m	Empirical coefficients in the shell flattening–Reynolds scaling law	[non-dimensional]

C_{h}	Empirical coefficient representing the relative thickness of shell and core lamellae	[non-dimensional]
y_{j}	Measured value of $\beta_{\max}$ for case j	[non-dimensional]
$\hat{\mathrm{y}}_{\mathrm{j}}$	Model-predicted value of $\beta_{\max}$ for case j	[non-dimensional]
SST	Total sum of squares (variance of experimental data about the mean)	[non-dimensional]
SSE	Sum of squared errors (model residual sum of squares)	[non-dimensional]
R^2	Coefficient of determination (fraction of variance explained)	[non-dimensional]
$RMSE$	Root-mean-square error of predictions	[non-dimensional]
MAE	Mean absolute error of predictions	[non-dimensional]
K	Number of folds in cross-validation	[non-dimensional]
Z	Standardized value of a variable	[non-dimensional]
J	Jetting outcome class (encapsulated rebound with central jet)	[non-dimensional]
PR	Partial-rebound outcome class	[non-dimensional]
SC	Spreading-contact outcome class	[non-dimensional]
$+S$	Jetting-, partial-rebound-, and spreading-contact-with-splash outcome classes	[non-dimensional]
i	Inner or core liquid phase	[$subscript$]
o	Outer or shell liquid phase	[$subscript$]
c	Compound drop as total	[$subscript$]
g	Gas phase	[$subscript$]
∞	Surrounding medium	[$subscript$]
max	Value at maximum spreading	[$subscript$]
$class$	Classification	[$subscript$]
reg	Regression	[$subscript$]

Chapter 1 Introduction and motivation

1.1 Motivation and significance

Droplet impact on solid surfaces underpins a wide range of processes in engineering, science, and everyday life. Examples include inkjet printing [1], [2] and additive manufacturing [3], where individual droplets build up lines and layers, spray coating [4] and cleaning [5], where controlled coverage and film formation are required, spray cooling and quenching in thermal management [6], [7], [8], fuel injection in combustion systems [9], pesticide deposition on leaves [10], and biomedical dispensing in diagnostics and bio printing [11]. In all of these systems, droplets arrive with some velocity, collide with a target, and pass through a sequence of deformation, spreading, and possible fragmentation before reaching a final state. The morphology of the final deposit and the details of the transient evolution control quantities such as footprint area, film thickness, surface coverage, and atomization losses, which in turn feed directly into performance metrics like line edge fidelity in printing, cooling efficiency in spray systems, or dosage and localization in pharmaceutical and bio printing applications.

Although droplet impact has been studied extensively for compositionally uniform liquids, many emerging technologies increasingly rely on multicomponent droplets that contain two or more immiscible phases arranged in a controlled internal structure. Among these, core-shell droplets introduce an internal interface and distinct core and shell properties, creating phase-specific pathways for inertia, viscous dissipation, and interfacial-energy storage that are not captured by classical single-liquid regime maps and spreading correlations. The central problem addressed in this thesis is to develop a unified and physics-consistent description that predicts

both impact outcome and the maximum spreading factor, $\beta_{\max}$, for core-shell droplets within a compact multicomponent non-dimensional space. Addressing this problem requires complementary evidence and tools: experiments to establish a consistent outcome and $\beta_{\max}$ dataset, an energy-balance model to expose dominant mechanisms and scaling trends, and complementary predictive machine-learning models to capture coupled nonlinear interactions and regime-boundary behavior within the same non-dimensional framework.

The impact outcome is the first high-level descriptor that links controlling physics to function. In inkjet and 3D printing, a desirable outcome is usually clean spreading and deposition without rebound or splash. Rebound leads to missing dots and poor adhesion, while splashing generates satellite droplets that blur edges and reduce resolution. In spray coating, the same splashing process can eject material away from the intended region, creating overspray and thick non-uniformity, whereas insufficient spreading leaves gaps and pinholes. In spray cooling and quenching, deposition with large, stable spreading enhances wetted area and heat transfer, while strong rebound or partial rebound reduces contact time and can lower cooling rates; excessive splashing can produce fine droplets that evaporate prematurely and never contribute to cooling the target.

For agricultural sprays, impact outcome controls how much pesticide actually adheres to a leaf surface versus how much bounces or drips away. Deposition and modest spreading maximize effective dose, whereas rebound and splashing generate drift, environmental contamination, and wasted chemical. In biomedical and pharmaceutical dispensing, such as microdose delivery to tissues or diagnostic chips, a controlled spreading contact outcome is needed to ensure that active

components remain localized where they are released. Strong splashing generates aerosols and cross contamination risks, while rebound can remove material from the intended region entirely.

These main possibilities are summarized schematically in Figure 1-1. The first row illustrates deposition, prompt splash, and corona splash. In deposition, the droplet spreads into a cap/disk like shape and remains attached to the surface, producing a compact footprint. In prompt splash, small secondary droplets are ejected almost immediately from the advancing contact line (where the advancing liquid lamella meets the solid surface surrounded by the medium air) while the lamella is still growing. In corona splash, the advancing lamella lifts from the surface into a crown-shaped sheet with a thick rim that later breaks into droplets away from the wall. The second row shows partial rebound, full rebound, and a combined rebound and splash case. In partial rebound, a central portion of the drop lifts off while a residual film remains on the substrate. In full rebound, the drop regains a nearly spherical shape and detaches completely. In rebound with splash, a rising drop coexists with satellite droplets emitted from the rim. These idealized sketches provide a generic taxonomy for single liquid impacts and form the reference against which the richer multi-component drops outcomes later will be interpreted.

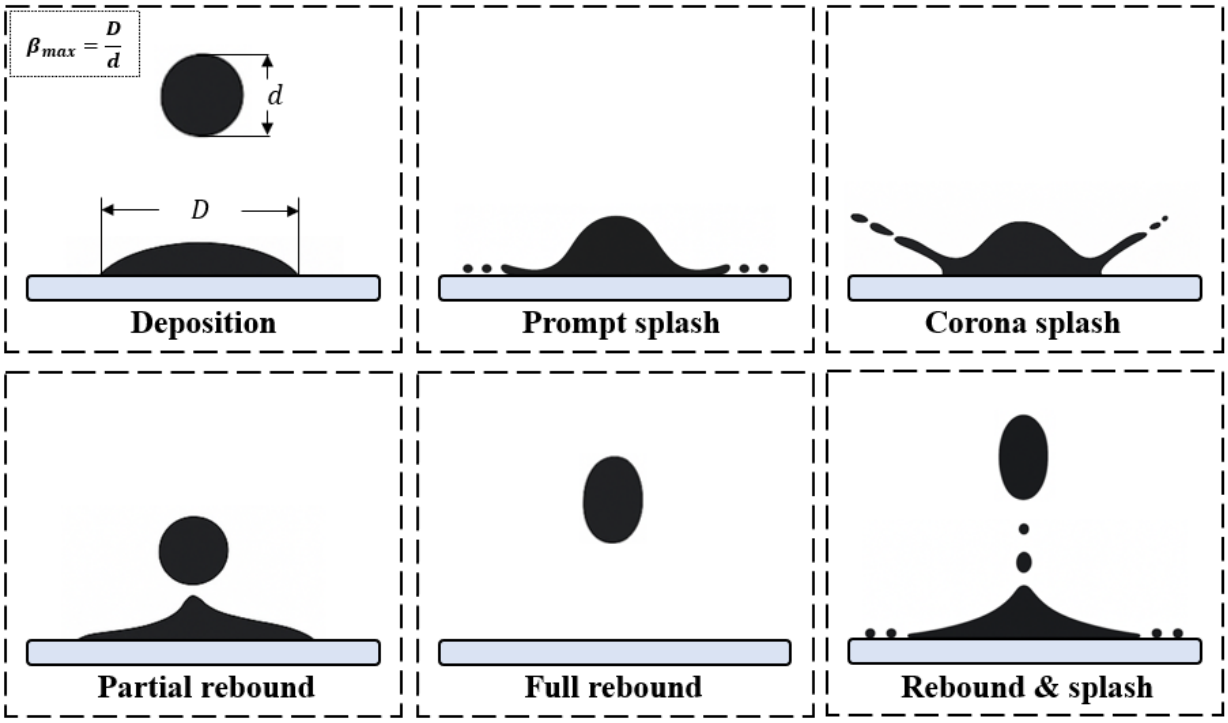

Figure 1-1. Schematic illustration of canonical single liquid droplet impact outcomes on a smooth solid surface, together with the definition of the maximum spreading factor $\beta_{max} = D/d$. Top row: deposition, prompt splash, and corona splash. Bottom row: partial rebound, full rebound, and rebound with splash.

The maximum spreading factor $\beta_{\max}$ is the second key link to applications, because it sets the maximum area that a single droplet can cover at a given volume. In Figure 1-1, the inset defines $\beta_{\max}$ as the ratio between the maximum footprint diameter D at the instant of largest spread and the initial droplet diameter d. In printing and patterning, $\beta_{\max}$ determines the dot diameter and therefore line width, overlap between neighboring droplets, and final film thickness. In thermal management, $\beta_{\max}$ governs the instantaneous wetted area during impact and thus the local heat transfer area. In pesticide and coating sprays, it controls the percentage of surface covered by

each impact and the average local layer thickness after drying or curing. For microstructured or chemically patterned substrates, $\beta_{\max}$ decides whether a droplet can bridge between features or remain confined to a single element [12], [13].

From a mechanistic point of view, impact outcome and $\beta_{\max}$ are not arbitrary labels, but the macroscopic result of a specific droplet-surface-ambient system and its impact conditions. For a given event, four groups of control parameters can be identified. The first group is the droplet properties, such as density, viscosity, surface tension, initial diameter, and, in more complex formulations (like multi-component drops), internal structure. The second group is the solid surface, characterized by its roughness, chemical composition, equilibrium and dynamic contact angles, and, in some cases, its compliance or thermal state. The third group is the surrounding medium, typically a gas with given density, viscosity, and pressure. The fourth group collects the impact dynamics, such as impact velocity, trajectory, and the presence or absence of prior liquid on the surface. Any change in these properties alters the balance between inertia, surface tension, viscosity, and wettability during impact, and therefore can shift the system from deposition to rebound, from smooth spreading to splashing, or from small to large $\beta_{\max}$ [12], [13], [14], [15].

Because of these connections, predicting outcome and $\beta_{\max}$ is not an academic exercise but a central requirement for process design and optimization. Reliable predictions allow the definition of operating windows in terms of impact speed, droplet size, and liquid formulation that guarantee deposition without unwanted splash or rebound. They enable rational design of surface coatings and textures to promote or suppress rebound, depending on whether retention or self cleaning is desired. They are also essential for digital design tools and reduced order models of

sprays, in which each individual impact is not resolved in detail but must be represented by effective outcome and spreading laws that remain valid across many combinations of parameters.

Across these applications, two macroscopic descriptors are therefore especially important. The first is the impact outcome, that is, whether the droplet spreads and deposits, rebounds partially or completely, or undergoes splashing with the formation of satellites. The second is the maximum spreading factor, $\beta_{\max}$, defined as the ratio between the maximum lateral extent of the droplet footprint and its initial diameter. Together, outcome and $\beta_{\max}$ summarize how the impact event interacts with the substrate and provide compact targets for both mechanistic models and data-driven predictors.

1.2 Scope: Multi-component droplets

Classical droplet impact studies treat the droplet as a single liquid with uniform density, viscosity, and surface tension. Under this assumption, the only ways to alter impact behavior are to change the bulk liquid properties, the substrate, the ambient conditions, or the impact velocity and geometry. Over more than a century of work, this view has led to extensive experimental, theoretical, and numerical studies that have mapped out regimes of deposition, rebound, and splashing, and that have provided empirical and semi-empirical correlations for the maximum spreading factor on specific surfaces [16], [17], [18], [19].

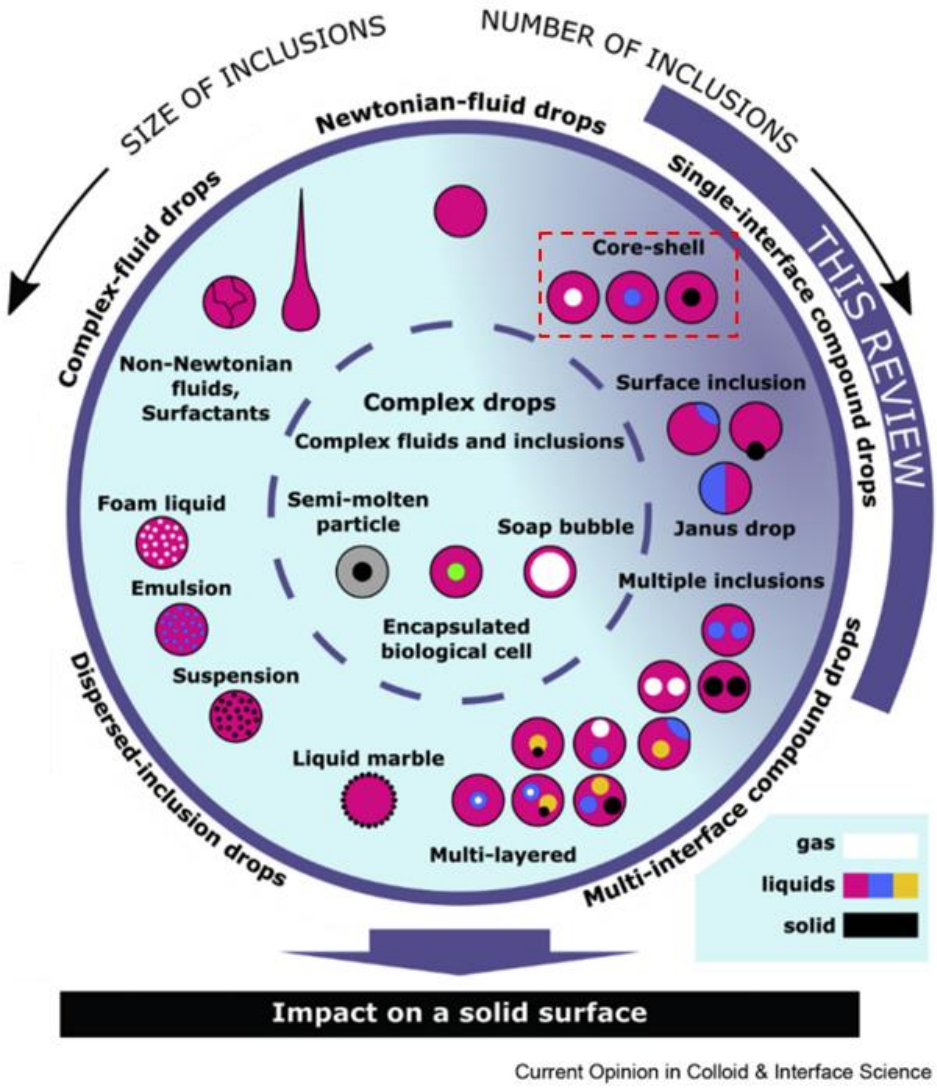

Figure 1-2 Overview of droplet-impact research organized by drop composition, highlighting the subset of single-interface compound drops (core-shell) within the broader class of complex drops. Adapted from "Impact of compound drops: a perspective" [20].

Figure 1-2 situates droplet impact within the broader class of complex drops, spanning Newtonian single-liquid drops, complex-fluid drops, and droplets containing inclusions or multiple internal interfaces. Within this landscape, single-interface compound droplets represent the minimal internal complexity that still introduces an additional interface and phase-specific

pathways for inertia, dissipation, and interfacial-energy storage. The present thesis focuses on core–shell droplets within this class, using controlled internal structure to quantify how core fraction and phase properties shift impact outcome and the maximum spreading factor relative to single-liquid reference behavior, and to enable a compact, physics-organized nondimensional description suitable for both mechanistic modeling and machine-learning prediction.

Many modern formulations, however, employ droplets that contain two or more immiscible liquids arranged in a controlled internal structure. Such droplets are referred to broadly as compound droplets or multicomponent droplets, and they include several architectures. Janus droplets contain two liquids side by side in a single droplet. Layered droplets contain concentric liquid layers with more than one internal interface. Core–shell droplets, which are the focus here, consist of an inner liquid core fully encapsulated by an outer liquid shell, surrounded by an ambient gas [20], [21].

The interest in compound droplets originates from the additional design freedoms they provide. In a single-liquid droplet, changing viscosity or surface tension inevitably changes all other properties of that liquid as well. In a compound droplet, by contrast, the core and shell can be chosen independently. This makes it possible to tune several aspects of the system that are important for impact:

- The outer shell determines the liquid that directly contacts the environment and the solid surface. Its viscosity, surface tension, and wettability control lamella formation, spreading, and the motion of the contact line.

- The inner core carries mass, inertia, and possibly active or functional components such as solutes, particles, or biological cargo. Its viscosity and density determine how easily it deforms and how strongly it participates in recoil and jet formation.
- The core–shell interface contributes an internal surface tension that stores interfacial energy whenever the core or shell is deformed relative to the other. This internal surface energy can be released during recoil and can either assist or resist the formation of jets and partial rebound.
- The core size or core volume fraction controls shell thickness and the area of the internal interface. Small cores give a thick shell that behaves almost like a single liquid with additional internal energy storage, while large cores lead to thin shells and strong coupling between core motion and shell integrity.

Beyond impact, compound and core-shell droplets are widely encountered in microfluidics and materials science. Microfluidic devices and coaxial nozzles are routinely used to generate core-shell droplets and particles with precisely controlled sizes and core fractions. These structures serve as templates for encapsulation and controlled release, as carriers in drug delivery, as reaction vessels in microreactors, and as building blocks for functional materials. Reviews of microfluidic core-shell generation techniques emphasize the ability to decouple core and shell composition, to stabilize sensitive cores inside protective shells, and to achieve narrow size distributions that are difficult to realize with conventional emulsification methods [22], [23], [24].

These same features that are attractive for encapsulation and transport also have important implications for impact. When a compound droplet strikes a surface, the outer shell behaves as the impacting liquid in the classical sense, forming the lamella and experiencing the wall shear stresses associated with spreading and receding. The core may remain insulated from the surface by the shell film or may eventually contact the surface if the shell ruptures or drains. The internal interface can stretch, tilt, or wrinkle, altering the distribution of stresses and the storage of interfacial energy during the event. Because core and shell typically have different viscosities and densities, viscous dissipation in the shell and in the core follow distinct pathways, and gravity can influence the pre-impact alignment of the core within the shell.

Recent work on compound droplet impact has begun to chart this richer behavior. Numerical simulations of viscous compound droplets impacting flat surfaces have shown how different viscosity ratios and interfacial tension values affect the shape of the lamella, the motion of the core, and the onset of breakup or film rupture [25], [26], [27]. Experiments and simulations on water-in-oil compound droplets impacting solid surfaces have demonstrated self-lubricated rebound, in which a water core encapsulated in a thin oil shell can rebound from surfaces that would normally be strongly wetting for pure water [28], [29], [30]. The shell acts as a lubricating film that maintains separation between the core and the solid, allowing the compound droplet to behave like a droplet impacting a liquid-infused surface while the lubricating layer is supplied by the droplet itself.

These studies show that core-shell droplets can realize impact outcomes that are not accessible to single liquids with the same outer phase. For example, a pure water droplet on a hydrophilic

glass surface typically spreads and deposits, with no rebound beyond very narrow parameter windows. A water core in a viscous oil shell, by contrast, can exhibit robust rebound or partial rebound on the same hydrophilic glass surface, because the oil film mediates contact with the substrate and modifies dissipation. Similarly, the onset of splashing, the character of the rim, and the maximum spreading factor can be shifted by adjusting shell viscosity and core fraction, even when the outer shell liquid that contacts the environment remains the same [21], [31].

Alongside these opportunities, compound droplets also introduce new challenges. The thermodynamic stability of the core–shell configuration depends on the hierarchy of interfacial tensions and can be compromised if the core or shell partially wets the outer fluid or the surrounding gas. Density mismatches between core and shell can cause the core to migrate within the droplet under gravity before impact, altering the local shell thickness at the point of contact. Thin shells may rupture during impact, allowing the core to contact the substrate and switching the effective impact liquid mid-event. Generating stable compound droplets with reproducible core fraction at the millimeter scale of many impact experiments requires careful design of the injection and breakup process.

Despite growing interest, the body of work on compound droplet impact is still small compared with the extensive literature on single-liquid droplets. Recent perspectives emphasize that many basic questions remain open, including how to construct regime maps that incorporate internal structure, how to generalize non-dimensional groups such as the Weber and Reynolds numbers (that are ratios of controlling forces governing the droplet impact phenomenon) to account for multiple phases and interfaces, and how to design predictive models that remain

accurate across different liquid pairs and core fractions. This contrast between a mature single-liquid field and a still-developing compound-droplet field is central to the present work.

Within the broad family of compound droplets, this thesis focuses on core-shell droplets impacting smooth hydrophilic glass. The outer shell is chosen to control lamella formation, spreading, and interaction with the solid, while the inner core provides a tunable internal energy reservoir and additional viscous and inertial pathways. By varying core volume fraction, shell viscosity, and impact conditions, it becomes possible to explore how this added internal structure modifies impact outcome and maximum spreading compared with single-liquid droplets and how these effects can be captured in a unified predictive framework.

1.3 Theoretical background

The detailed sequence of spreading, receding, rebound, and splashing for single and multicomponent droplets will be described quantitatively in later chapters. Only the main theoretical tools that will be used throughout the thesis are introduced here. These tools provide a compact way to connect the physical controls discussed in Sections 1.1 and 1.2 with the two central descriptors of interest, namely the impact outcome and the maximum spreading factor $\beta_{\max}$.

A first organizing idea is the energetic viewpoint of droplet impact. Before impact, the droplet carries kinetic energy associated with its translational motion and surface energy associated with its liquid-gas interface. During impact and spreading, part of the kinetic energy is converted into additional surface energy as the interface area grows, and part is irreversibly lost through viscous

dissipation in the thin lamella and near the solid surface. For millimetric droplets at moderate velocities, changes in gravitational potential energy during the short impact event are usually small compared with these three contributions and are often neglected in first-order models. At the instant of maximum spreading, when the footprint maximal diameter reaches D, the radial motion is arrested and the instantaneous kinetic energy has been strongly reduced compared with its initial value (however, even if the contact line is at rest, a flow inside the droplet is still present), while surface energy and viscous losses account for most of the energy budget. During recoil and possible rebound, a portion of the stored surface energy is converted back into kinetic form, while viscous dissipation continues to drain energy until a final state is reached. This energy balance perspective naturally connects impact conditions and fluid properties with $\beta_{\max}$, since the amount of spreading that can occur is limited by how much of the initial kinetic energy can be converted into surface energy rather than dissipated. Empirical and semi-empirical models for $\beta_{\max}$ can be viewed as reduced representations of this balance.

A second key element is the use of non-dimensional groups to condense the many dimensional parameters of the problem into a small set of ratios that capture the relevant force or energy balances. For a single liquid droplet with density ρ, viscosity μ, surface tension σ, diameter d, and impact velocity U, in a gravitational field with acceleration g, the Weber number, Reynolds number, Ohnesorge number, and Bond number are widely used. The Weber number compares inertial forcing to surface tension and is defined as $We = \rho U^2 d/\sigma$. The Reynolds number compares inertia to viscous resistance, $Re = \rho U d/\mu$. The Ohnesorge number combines viscosity, inertia, and surface tension into a single parameter, $Oh = \mu/\sqrt{\rho\sigma d}$, and is especially

useful for distinguishing regimes in which viscous effects are negligible, comparable, or dominant. The Bond number, $Bo = \rho g \mathrm{d}^2/\sigma$, compares gravity to surface tension and indicates whether gravity significantly distorts the droplet over its own diameter. These groups provide a compact "state vector" for the droplet, collapsing changes in fluid properties, droplet size, and impact velocity into a few dimensionless quantities that can be used to construct regime maps and correlations [32], [33].

Classical regime maps express impact outcome as regions in the (We, Re) or (We, Oh) plane, with boundaries that depend on substrate wettability and roughness. Inertia-capillary regimes at low viscosity are associated with deposition and prompt splashing as We increases, while inertia-viscous regimes at higher viscosity exhibit reduced spreading and suppressed splash. Empirical and semi-empirical correlations for the maximum spreading factor are often written as functions of We and Re, reflecting the balance between the inertial tendency to spread and the combined influence of surface tension and viscosity in limiting the extent of the lamella. In low-viscosity regimes, $\beta_{\max}$ typically increases strongly with We, while in more viscous or larger-scale regimes the dependence on We weakens and the dependence on Re becomes more important. These trends are consistent with detailed numerical and experimental energy budget analyses, which show that viscous dissipation becomes progressively more important relative to stored surface energy as viscosity and droplet size increase [16], [34], [35], [36], [37], [38].

Compound droplets, and in particular core-shell droplets, require an extension of this framework. The presence of multiple liquid phases with different densities and viscosities and

the existence of an internal core-shell interface introduce additional energetic and hydrodynamic pathways. In a core-shell droplet, the shell forms the lamella and interacts directly with the solid surface and the ambient gas, so its properties control much of the viscous dissipation and the capillary forces at the contact line. The core contributes additional inertia and viscosity and carries an internal surface that stores interfacial energy whenever the core and shell deform relative to each other. Treating the droplet as a single effective fluid with averaged properties would obscure these distinct roles. For this reason, the present work employs an equivalent Weber number that accounts for the total inertia of the compound droplet relative to both the external and internal interfacial energies, together with phase-specific Reynolds numbers that quantify inertia against viscosity separately in the core and in the shell. These generalized groups retain the organizing power of classical non-dimensional analysis while respecting the internal structure of the droplet.

Finally, from a modeling and prediction standpoint, impact outcome and maximum spreading can be viewed as outputs of mappings from this non-dimensional state space. In a mechanistic energy-balance model, these mappings are expressed in terms of algebraic relations derived from global balances of kinetic, surface, and viscous energies using the chosen non-dimensional groups as inputs. In data-driven and machine-learning approaches, the same non-dimensional groups serve as features in supervised learning tasks, with impact outcome treated as a discrete classification label and $\beta_{\max}$ as a continuous regression target. Both viewpoints rely on the same theoretical background summarized above: impact physics expressed through energy balances and non-dimensional ratios. The subsequent chapters build on this foundation to construct and

validate predictive models for core–shell droplets that couple these theoretical ideas with experimental data.

1.4 Approaches to study and predict droplet impact outcome

The literature on droplet impact has developed along several complementary methodological directions. Each provides a different balance between physical fidelity, interpretability, and computational or experimental cost. Together, they form the toolbox from which the present thesis selects its main components.

The first and most fundamental approach is experimental investigation. Single/compound droplet impacts are generated using controlled release devices with syringe pumps, and are recorded using high-speed imaging with synchronized illumination. Image processing then yields time-resolved droplet silhouettes, from which footprint diameter, β_{max}, contact time, rebound height, rim evolution, and the presence or absence of splashing can be extracted. Systematic parametric studies vary impact velocity, droplet size, liquid properties, substrate wetting and roughness, ambient pressure, and, more recently, droplet internal structure. Experiments provide direct access to real fluids and surfaces and are indispensable for constructing regime maps, calibrating models, and validating numerical simulations. Their main limitations are the time and effort required to cover high-dimensional parameter spaces, and the sensitivity of some observables to small variations in impact conditions and surface state [18], [20], [39], [40].

The second class of approaches consists of empirical and semi-empirical correlations, especially for the maximum spreading factor. In these models, β_{max} is expressed as a function

of the Weber and Reynolds numbers and, in some cases, the static contact angle or surface roughness. Coefficients and exponents are fitted to experimental data for particular liquid-surface-ambient combinations. Such correlations can be extremely convenient in practice, since they require only simple algebraic evaluations once the relevant non-dimensional numbers are known. They capture, in compact form, the inertia-capillary and inertia-viscous balances that control spreading and provide a fast way to estimate β_{max} over the range of conditions for which they were calibrated. Their main limitation is restricted generality: accuracy degrades when applied outside their calibration window or to fluids and surfaces that differ significantly from those originally studied, and extension to multi-component droplets is not straightforward [28], [29], [41].

A third family of methods comprises analytical and energy-balance models. These models start from the global energy budget introduced in Section 1.3 and derive approximate relations for β_{max} by equating the initial kinetic energy to the sum of increased surface energy and viscous dissipation at maximum spreading, often under simplified assumptions about lamella geometry, film thickness, and flow profile. Refinements account for dynamic contact angles, time-dependent lamella thickness, and more realistic dissipation pathways. Compared with purely empirical correlations, energy-balance models incorporate more physics and can provide insight into which mechanisms dominate in a given regime. They remain relatively inexpensive to evaluate, since they reduce the dynamics to a small number of algebraic expressions, and can sometimes be extended to new fluids or surfaces with modest recalibration. For compound droplets, and especially core-shell systems, energy-based models must be extended to include

separate dissipation contributions from core and shell and to include internal interfacial energy in the balance, otherwise the distinct roles of the phases are lost in effective averaged properties [34], [42], [43], [44], [45].

The trade-off is that energy-balance models are inherently global and endpoint-based: they collapse the transient, momentum-governed deformation into a relation between the pre-impact state and the configuration at maximum spreading. Consequently, they do not resolve the time-dependent evolution of the lamella or local pressure and velocity fields, nor can they directly capture contact-line dynamics and instability mechanisms such as rim corrugation, splashing, or shell rupture, which instead require differential transient formulations based on momentum balance or fully resolved simulations. Within their intended scope, however, energy-balance models provide a compact and interpretable estimate of β_{max} and clarify dominant energy pathways.

The fourth major approach is numerical simulation. Interface-resolving methods such as Volume of Fluid, Level Set, phase-field, and front tracking schemes solve the Navier-Stokes equations for the liquid and gas phases while explicitly tracking the liquid-gas interface. These simulations can capture detailed velocity and pressure fields, lamella thickness, rim instabilities, and the formation of jets and droplets, and have been used to study single-liquid splashing, impact on textured and heated surfaces, and, more recently, selected cases of compound droplet impact. Multi-component simulations introduce additional complexity by requiring the representation of multiple interfaces and discontinuities in density and viscosity. Although numerical methods provide rich information that is often inaccessible experimentally, they are computationally

intensive, particularly when high spatial and temporal resolution is needed and when multiple cases are required to cover a broad parameter space. This makes them less suitable for direct use in design optimization across broad parameter spaces [27], [46], [47]. For core-shell droplets, these challenges are amplified by the need to resolve multiple coupled interfaces and, in many cases, very thin shell films and near-wall layers, which sharply increases the required spatial and temporal resolution. As a result, numerical studies of compound and core-shell impact have typically focused on carefully selected liquid pairs and restricted ranges of core fraction and impact conditions, often aiming to elucidate specific mechanisms rather than to provide broad predictive coverage. This motivates continued integration of numerical insight with systematic experiments and reduced-order or data-driven predictors when wide parameter sweeps are required.

Finally, there is a growing body of work on data-driven and machine-learning approaches to droplet impact. In these studies, experimental or numerical datasets are assembled in which each impact is represented by a set of input features, typically non-dimensional groups that encode impact conditions, and by outputs such as outcome labels or measured values of β_{max}. Supervised learning algorithms, including decision-tree ensembles, support vector machines, neural networks, and Gaussian process regression, are then trained to approximate the mapping from inputs to outputs. Once trained, these models can provide rapid predictions of outcome or β_{max} for new combinations of parameters and can be used to explore sensitivities and optimal operating regions. In single-liquid systems, such machine-learning models have demonstrated high accuracy in predicting regime maps and spreading behavior when trained on sufficiently

rich data, and model-interpretability tools have been used to relate the learned mappings back to known physical trends. Challenges include the need for carefully curated and representative datasets, avoidance of overfitting and non-physical extrapolation, and the design of feature sets that reflect the underlying physics rather than arbitrary variables [48], [49], [50], [51], [52].

These methodological strands are complementary rather than competing. Experiments provide the data and physical intuition needed to formulate mechanistic models and train machine-learning algorithms. Analytical and energy-balance models offer interpretable relations that can be embedded in larger simulations or control schemes. Numerical simulations fill gaps where experiments are difficult and enable detailed diagnostics, while data-driven models exploit available data to deliver fast predictions and systematic sensitivity analyses. In the context of multicomponent and core-shell droplets, the relative scarcity of existing data and models motivates an approach that combines these tools: targeted experiments to populate a consistent dataset, an energy-balance model tailored to compound droplets, and a machine-learning framework that uses physically motivated non-dimensional features to predict impact outcome and maximum spreading. The remaining sections of this chapter formalize the problem statement, identify the main knowledge gaps that motivate this combined strategy, and summarize the objectives and structure of the thesis.

1.5 Problem statement and knowledge gaps

The previous sections have outlined why droplet impact on solid surfaces matters in technology, how impact outcome and the maximum spreading factor β_{max} control performance in a wide range of applications, how multicomponent and core-shell droplets provide additional

internal degrees of freedom, and which theoretical and methodological tools are available to analyze this class of problems. Despite this long development, several specific gaps remain at the intersection of core–shell droplet impact, energy-based modeling, and data-driven prediction.

A first gap concerns systematic experimental data for core-shell droplet impact on simple, well-defined solid substrates. For single-liquid droplets, the literature includes extensive regime maps and quantitative datasets that span large ranges of Weber and Reynolds numbers, surface textures, and thermal conditions. In contrast, existing work on compound droplets is more fragmented. Many studies focus on a limited selection of liquid pairs, core volume fractions, and impact velocities, or are confined to microfluidic scales and specialized geometries. Often, outcome classification is qualitative, and measurements of β_{max} are sparse or not reported consistently. As a result, there is a lack of single-laboratory (i.e., internally consistent) datasets that follow a unified protocol, systematically vary core fraction and impact conditions, and report both impact outcome and β_{max} for core-shell droplets impacting a nominally smooth, rigid solid surface. This limits the ability to construct robust regime maps for compound droplets, to compare different predictive approaches on a common footing, and to quantify how internal droplet structure modifies impact behavior relative to single-liquid references [21], [25], [31].

A second gap involves physics-based predictive models for the maximum spreading factor of compound droplets. Classical empirical and semi-empirical relations for β_{max} have been derived for single liquids and are written in terms of the Weber and Reynolds numbers, possibly augmented by contact angle or roughness parameters. Energy-balance models based on global balances of kinetic, surface, and viscous energies have improved the physical transparency of

these relations and clarified the relative importance of inertia, capillarity, and viscosity in different regimes [33], [45], [53]. However, these formulations invariably assume a homogeneous liquid with a single viscosity and a single surface tension with respect to the surrounding gas. Direct extension to compound droplets by inserting effective averaged properties hides the distinct roles of shell and core in lamella formation, dissipation, and interfacial energy storage, and does not represent the explicit contribution of the internal core-shell interface. There is therefore a need for an energy-balance model that respects the internal structure of core-shell droplets by separating viscous dissipation in shell and core, incorporating internal interfacial energy, and expressing β_{max} in terms of non-dimensional groups that are tailored to multicomponent systems rather than constructed from simple averages.

A third gap lies in data-driven and machine-learning prediction for multicomponent droplet impact. Supervised learning has recently been applied to single-liquid droplet impact, where models trained on experimental or numerical datasets have reproduced regime maps and β_{max} trends on surfaces with varied wettability, texture, and temperature. These studies have shown that, when non-dimensional groups are used as input features, machine-learning models can achieve high predictive accuracy and that interpretability tools can recover known physical trends and identify dominant controls [49], [50], [52], [54], [55]. Almost all such work, however, is restricted to compositionally uniform droplets. For compound and core-shell droplets, feature design must capture not only inertia-capillary-viscous balances but also phase-specific properties and the presence of an internal interface. At present, there is no physics-organized machine-learning framework that uses a compact set of multicomponent non-dimensional predictors, such

as an equivalent Weber number combined with core and shell Reynolds numbers and core volume fraction, and that is benchmarked against both mechanistic models and a carefully curated experimental dataset under consistent conditions.

These observations motivate the following problem statement. There is a need for a unified, physics-consistent framework that combines: (i) a systematic experimental characterization of impact outcomes and maximum spreading for core-shell droplets over broad ranges of equivalent Weber number, core volume fraction, and phase-specific Reynolds numbers, (ii) an energy-balance model for β_{max} that explicitly represents the internal core-shell interface and phase-separated dissipation in terms of multicomponent non-dimensional groups, and (iii) machine-learning models for impact outcome and β_{max} that operate on the same non-dimensional feature space and are trained and interpreted using the experimental dataset. Addressing this problem would couple detailed experimental phenomenology, mechanistic understanding, and data-driven prediction in a single framework for core-shell droplet impact and provide a template that can be adapted to other multicomponent droplets, substrates, and impact conditions.

1.6 Thesis objectives and structure

The overall objective of this thesis is to establish a coherent framework that combines experiments, a compound-droplet energy-balance model, and machine-learning predictors in order to describe and predict both impact outcome and the maximum spreading factor β_{max} for core-shell droplets impacting smooth solid surfaces.

This objective is pursued through three specific objectives:

- **Experimental characterization of core-shell droplet impact.**

  Design and conduct a systematic experimental program in which core-shell droplets with selected liquid pairs and core volume fractions impact a smooth, rigid solid surface over a broad range of impact velocities. For each impact, record high-speed visualizations, classify the impact outcome related to the core-shell compound drops using a consistent taxonomy that distinguishes jetting, partial rebound, spreading-contact, and their splashing counterparts, and measure β_{max}. Assemble these measurements into a single-laboratory dataset in which all events are represented in a multi-component non-dimensional feature space defined by an equivalent Weber number, core volume fraction, and phase-specific Reynolds numbers for core and shell.

- **Development of a compound-droplet energy-balance model.**

  Formulate an energy-balance model for β_{max} of core-shell droplets in which the initial kinetic energy is balanced against changes in external and internal interfacial energy and viscous dissipation in core and shell. Use an equivalent Weber number and phase-specific Reynolds numbers as inputs, and represent core and shell dissipation by separate scaling laws with fitted coefficients. Calibrate the model on a subset of the experimental data, test it on an independent subset to assess accuracy and robustness across liquid pairs and core fractions, and use the calibrated model to examine energy partitioning and dominant mechanisms controlling β_{max} in different regions of the multi-component non-dimensional space.

- **Construction of machine-learning models for impact outcome and β_{max}.**

  Build supervised learning models for impact outcome (classification) and β_{max} (regression) using the experimental dataset and the same multi-component non-dimensional predictors employed in the energy-balance model. Benchmark multiple model families, including decision-tree ensembles, support vector machines, neural networks, and Gaussian process regression, under stratified train/test splits and k-fold cross-validation schemes that preserve the physical structure of the data. Evaluate performance using descriptive accuracy metrics for classification and regression. Apply interpretability tools to quantify the influence of each predictor on outcome probabilities and on β_{max}, and compare these dependencies with trends inferred from the energy-balance model and direct experimental analysis.

Within this framework, the thesis makes three main contributions. It provides a curated experimental dataset of core-shell droplet impacts expressed in a compact multicomponent non-dimensional space. It introduces and validates an energy-balance model that extends classical single-liquid formulations by incorporating internal interfaces and phase-specific dissipation in a transparent way. It develops a machine-learning framework that operates on the same non-dimensional predictors and delivers both accurate predictions and interpretable relationships between inputs and outputs, demonstrating how internal structure in core-shell droplets can be used to manipulate impact behavior and how that behavior can be captured in predictive tools suitable for analysis and design.

The remainder of the thesis is organized as follows. Chapter 2 presents the experimental methodology, including core-shell droplet generation, impact configuration, imaging, and data reduction, and reports the resulting regime maps and β_{max} trends in the chosen non-dimensional space. Chapter 3 develops the compound-droplet energy-balance model, describes its calibration strategy, and evaluates its predictive performance and energy partitioning against the experimental data. Chapter 4 introduces the machine-learning framework for impact outcome classification and β_{max} regression, compares the performance and stability of different model families, and uses interpretability analyses to relate the learned mappings to the underlying physics. Chapter 5 synthesizes the findings from these three pillars, discusses limitations and possible extensions, and outlines directions for future work on multi-component droplet impact and its applications.

1.7 References

[1] H. Wijshoff, "Drop dynamics in the inkjet printing process," *Curr Opin Colloid Interface Sci*, vol. 36, pp. 20–27, 2018.

[2] M. J. Docherty, P. Naderi, G. Grau, K. Sefiane, and A. Amirfazli, "Inkjet printing on hydrophobic surface: Practical implementation of stacked coin strategy," *Adv Eng Mater*, vol. 26, no. 11, p. 2400237, 2024.

[3] S. Fathi, P. Dickens, and F. Fouchal, "Regimes of droplet train impact on a moving surface in an additive manufacturing process," *J Mater Process Technol*, vol. 210, no. 3, pp. 550–559, 2010.

[4] R. Andrade, O. Skurtys, and F. Osorio, “Drop impact behavior on food using spray coating: Fundamentals and applications,” *Food research international*, vol. 54, no. 1, pp. 397–405, 2013.

[5] K. Xu *et al.*, “Removal of nano-particles by aerosol spray: effect of droplet size and velocity on cleaning performance,” *Solid State Phenomena*, vol. 145, pp. 31–34, 2009.

[6] W.-L. Cheng, W.-W. Zhang, H. Chen, and L. Hu, “Spray cooling and flash evaporation cooling: The current development and application,” *Renewable and Sustainable Energy Reviews*, vol. 55, pp. 614–628, 2016.

[7] W. M. Grissom and F. A. Wierum, “Liquid spray cooling of a heated surface,” *Int J Heat Mass Transf*, vol. 24, no. 2, pp. 261–271, 1981.

[8] G. Liang and I. Mudawar, “Review of spray cooling–Part 1: Single-phase and nucleate boiling regimes, and critical heat flux,” *Int J Heat Mass Transf*, vol. 115, pp. 1174–1205, 2017.

[9] A. L. N. Moreira, A. S. Moita, and M. R. Panao, “Advances and challenges in explaining fuel spray impingement: How much of single droplet impact research is useful?,” *Prog Energy Combust Sci*, vol. 36, no. 5, pp. 554–580, 2010.

[10] B. Wang *et al.*, “Sustained agricultural spraying: from leaf wettability to dynamic droplet impact behavior,” *Global Challenges*, vol. 7, no. 9, p. 2300007, 2023.

[11] S. V Murphy and A. Atala, "3D bioprinting of tissues and organs," *Nat Biotechnol*, vol. 32, no. 8, pp. 773–785, 2014, doi: 10.1038/nbt.2958.

[12] B.-J. Wei *et al.*, "Droplet impact outcomes: Effect of wettability and Weber number," *Physics of Fluids*, vol. 36, no. 7, 2024.

[13] A. Amirfazli, M. D. Bustamante, Y. Hu, and L. Ó Náraigh, "Bounds on the spreading radius in droplet impact: the inviscid case," *Proceedings of the Royal Society A*, vol. 480, no. 2294, p. 20230760, 2024.

[14] R. Choudhury *et al.*, "Uncovering the effect of physical conditions and surface roughness on the maximum spreading factor of impinging droplets using a supervised artificial neural network model," *Ind Eng Chem Res*, vol. 62, no. 49, pp. 21208–21221, 2023.

[15] W. Yu *et al.*, "A comparison of models for predicting the maximum spreading factor in droplet impingement," *Physics of Fluids*, vol. 36, no. 7, 2024.

[16] C. Josserand and S. T. Thoroddsen, "Drop impact on a solid surface," *Annu Rev Fluid Mech*, vol. 48, pp. 365–391, 2016, doi: 10.1146/annurev-fluid-122414-034401.

[17] G. Riboux and J. M. Gordillo, "Experiments of drops impacting a smooth solid surface: a model of the critical impact speed for drop splashing," *Phys Rev Lett*, vol. 113, no. 2, p. 024507, 2014, doi: 10.1103/PhysRevLett.113.024507.

[18] A. L. Yarin, "Drop impact dynamics: splashing, spreading, receding, bouncing…," *Annu. Rev. Fluid Mech.*, vol. 38, no. 1, pp. 159–192, 2006.

[19] R. Rioboo, C. Tropea, and M. Marengo, “Outcomes from a drop impact on solid surfaces,” *At. Sprays*, vol. 11, no. 2, 2001.

[20] I. Alkomy, M. Marengo, and A. Amirfazli, “Impact of a core–shell compound droplet on a solid surface,” *Exp Fluids*, vol. 66, no. 5, p. 97, 2025.

[21] N. Blanken, M. S. Saleem, M.-J. Thoraval, and C. Antonini, “Impact of compound drops: a perspective,” *Curr Opin Colloid Interface Sci*, vol. 51, 2020, doi: 10.1016/j.cocis.2020.09.002.

[22] Y. Du, L. Dai, L. Qian, F. Zhou, and Y. Ma, “Impact of a compound droplet on a solid surface: The effect of the shell on the core,” *Exp Therm Fluid Sci*, vol. 160, p. 111330, 2025.

[23] J. Tian, H. Wang, S. Mehendale, Z. Zhang, and M. Wu, “Analysis of the impact dynamics of water-in-oil composite droplets on metal plates,” *J Mol Liq*, vol. 406, p. 125057, 2024.

[24] J. Zheng *et al.*, “Controlling the impact dynamic behavior of a water-in-oil compound drop using the dielectrowetting effect,” *Chem Eng Sci*, vol. 273, p. 118637, 2023.

[25] Z. Zhang, C.-Y. Zhang, H.-R. Liu, and H. Ding, “Impact dynamics of compound drops of fluids with density contrast,” *J Fluid Mech*, vol. 964, p. A34, 2023.

[26] I. P. Gulyaev and O. P. Solonenko, “Hollow droplets impacting onto a solid surface,” *Exp Fluids* , vol. 54, pp. 1–12, 2013, doi: 10.1007/s00348-012-1432-z.

[27] S. Tasoglu, G. Kaynak, A. Szeri, … U. D.-P. of, and undefined 2010, "Impact of a compound droplet on a flat surface: A model for single cell epitaxy," *pubs.aip.org*, Accessed: Oct. 30, 2023. [Online]. Available: https://pubs.aip.org/aip/pof/article/22/8/082103/256539

[28] D. Liu and T. Tran, "The ejecting lamella of impacting compound droplets," *Appl Phys Lett*, vol. 115, no. 7, p. 073702, 2019, doi: 10.1063/1.5097370.

[29] D. Liu and T. Tran, "Emergence of two lamellas during impact of compound droplets," *Appl Phys Lett*, vol. 112, no. 20, p. 203702, 2018, doi: /10.1063/1.5026821.

[30] N. Blanken, M. S. Saleem, C. Antonini, and M.-J. Thoraval, "Rebound of self-lubricating compound drops," *Sci Adv*, vol. 6, no. 11, p. eaay3499, 2020, doi: 10.1126/sciadv.aay3499.

[31] R. H. Chen, M. J. Kuo, S. L. Chiu, J. Y. Pu, and T. H. Lin, "Impact of a compound drop on a dry surface," *J Mech Sci Technol*, vol. 21, pp. 1886–1891, 2007, doi: 10.1007/BF03177445.

[32] J. Du, X. Wang, Y. Li, Q. Min, and X. Wu, "Analytical consideration for the maximum spreading factor of liquid droplet impact on a smooth solid surface," *Langmuir*, vol. 37, no. 24, pp. 7582–7590, 2021.

[33] P. Attané, F. Girard, and V. Morin, "An energy balance approach of the dynamics of drop impact on a solid surface," *Phys. Fluids*, vol. 19, no. 1, 2007.

[34] S. Chandra and C. T. Avedisian, “On the collision of a droplet with a solid surface,” *Proc R Soc Lond A Math Phys Sci*, vol. 432, no. 1884, pp. 13–41, 1991.

[35] J. B. Lee, D. Derome, R. Guyer, and J. Carmeliet, “Modeling the maximum spreading of liquid droplets impacting wetting and nonwetting surfaces,” *Langmuir*, vol. 32, no. 5, pp. 1299–1308, 2016, doi: 10.1021/acs.langmuir.5b04557.

[36] I. V Roisman, “Inertia dominated drop collisions. II. An analytical solution of the Navier–Stokes equations for a spreading viscous film,” *Phys. Fluids*, vol. 21, no. 5, 2009.

[37] S. Moghtadernejad, C. Lee, and M. Jadidi, “An introduction of droplet impact dynamics to engineering students,” *Fluids*, vol. 5, no. 3, p. 107, 2020.

[38] B.-J. Wei *et al.*, “Droplet impact outcomes: Effect of wettability and Weber number,” *Physics of Fluids*, vol. 36, no. 7, 2024.

[39] A. Amirfazli, M. D. Bustamante, Y. Hu, and L. Ó Náraigh, “Bounds on the spreading radius in droplet impact: the inviscid case,” *Proceedings of the Royal Society A*, vol. 480, no. 2294, p. 20230760, 2024.

[40] L. Xu, L. Barcos, and S. R. Nagel, “Splashing of liquids: Interplay of surface roughness with surrounding gas,” *Physical Review E—Statistical, Nonlinear, and Soft Matter Physics*, vol. 76, no. 6, p. 066311, 2007.

[41] A. Mohammad Karim, “Physics of droplet impact on various substrates and its current advancements in interfacial science: A review,” *J Appl Phys*, vol. 133, no. 3, 2023.

[42] C. Clanet, C. Béguin, D. Richard, and D. Quéré, “Maximal deformation of an impacting drop,” *J Fluid Mech*, vol. 517, pp. 199–208, 2004.

[43] E. W. Collings, A. J. Markworth, J. K. McCoy, and J. H. Saunders, “Splat-quench solidification of freely falling liquid-metal drops by impact on a planar substrate,” *J Mater Sci*, vol. 25, no. 8, pp. 3677–3682, 1990.

[44] J. Madejski, “Solidification of droplets on a cold surface,” *Int J Heat Mass Transf*, vol. 19, no. 9, pp. 1009–1013, 1976.

[45] C. Ukiwe and D. Y. Kwok, “On the maximum spreading diameter of impacting droplets on well-prepared solid surfaces,” *Langmuir*, vol. 21, no. 2, pp. 666–673, 2005.

[46] S. Tasoglu, G. Kaynak, A. J. Szeri, U. Demirci, and M. Muradoglu, “Impact of a compound droplet on a flat surface: A model for single cell epitaxy,” *Phys. Fluids*, vol. 22, no. 8, 2010.

[47] T. V. Vu and P. H. Pham, “Numerical study of a compound droplet moving toward a rigid wall in an axisymmetric channel,” *Int J Heat Fluid Flow*, vol. 82, p. 108542, Apr. 2020, doi: 10.1016/J.IJHEATFLUIDFLOW.2020.108542.

[48] M. Pierzyna, D. A. Burzynski, S. E. Bansmer, and R. Semaan, “Data-driven splashing threshold model for drop impact on dry smooth surfaces,” *Physics of Fluids*, vol. 33, no. 12, 2021.

[49] E. Heidari, A. Daeichian, M. A. Sobati, and S. Movahedirad, “Prediction of the droplet spreading dynamics on a solid substrate at irregular sampling intervals: Nonlinear Auto-Regressive eXogenous Artificial Neural Network approach (NARX-ANN),” *Chemical Engineering Research and Design*, vol. 156, pp. 263–272, 2020.

[50] I. Yoon, J. Chergui, D. Juric, and S. Shin, “Maximum spreading of droplet-particle collision covering a low Weber number regime and data-driven prediction model,” *Physics of Fluids*, vol. 34, no. 10, 2022.

[51] D. A. de Aguiar, H. L. França, and C. M. Oishi, “Predicting energy budgets in droplet dynamics: A recurrent neural network approach,” *Int J Numer Methods Fluids*, 2024.

[52] L. Au-Yeung and P. A. Tsai, “Predicting impact outcomes and maximum spreading of drop impact on heated nanostructures using machine learning,” *Langmuir*, vol. 39, no. 50, pp. 18327–18341, 2023.

[53] M. Pasandideh-Fard, Y. M. Qiao, S. Chandra, and J. Mostaghimi, “Capillary effects during droplet impact on a solid surface,” *Phys. Fluids*, vol. 8, no. 3, pp. 650–659, 1996.

[54] R. Choudhury *et al.*, “Uncovering the effect of physical conditions and surface roughness on the maximum spreading factor of impinging droplets using a supervised artificial neural network model,” *Ind Eng Chem Res*, vol. 62, no. 49, pp. 21208–21221, 2023.

[55] M. Tembely, D. C. Vadillo, A. Dolatabadi, and A. Soucemarianadin, “A machine learning approach for predicting the maximum spreading factor of droplets upon impact on surfaces with various wettabilities,” *Processes*, vol. 10, no. 6, p. 1141, 2022.

Chapter 2 Experimental approach [1]

2.1 Introduction

Droplet impact on solid surfaces is of critical importance in both natural and industrial contexts. The collision of raindrops on the leaves and soil influences the distribution of water, a key factor influencing plant growth and health [1]. Similarly, in advanced technological applications, e.g., in inkjet printing, the accuracy of each microscopic ink droplet is crucial for achieving sharp, high-quality images; in fuel injection systems, the efficiency of combustion engines hinges on the precise behavior of fuel droplets as they collide and spread [2], [3]. Drop impact outcomes like deposition or bouncing off the surface, splashing or non-splashing, maximum spreading after impact, are all crucial parameters for these processes.

When a droplet impacts a solid surface, its behavior can be broadly classified into several phases: spreading (the droplet flattens out upon impact till it reaches the maximum expansion), relaxation (where the droplet attempts to minimize surface energy before possible retraction), and in some cases recoil phase occurs (the droplet contracts back towards its center) [4]. The exact outcome of these phases is influenced by a multitude of controlling factors, including the surface properties, the surrounding medium, and the droplet's velocity, density, viscosity, and surface tension [4], [5].

Droplet composition is not only one of the controlling parameters of the impact event, but also has many practical applications where the impacting drops are not just a homogenous material.

---

[1] *This chapter has been published as a peer-reviewed journal article under the title "Impact of a core-shell compound droplet on a solid surface" in Experiments in Fluids Journal.*

Examples are targeted drug delivery and controlled release of the active agents [6], production of cosmetics and personal care items [7], atomization enhancement of blended fuel for better combustion efficiency, encapsulation of flavors and nutrients in food industry [10]. Additionally, these multi-component drops are utilized in the development of pesticides for effective crop protection [11] and the fabrication of porous foams for insulation and cushioning materials [12], [13].. The manipulation of droplet composition and behavior is also crucial in advanced manufacturing processes such as bioprinting and microfluidic device design [14], [15].

The term "compound droplet" encompasses various configurations of multi-component or complex drops, including emulsions, liquid marbles, and non-Newtonian drops [16]. In this study, we focus on the simplest form: a single inclusion in a core-shell configuration, where one liquid phase is encapsulated within another immiscible liquid. A common example is a water-in-oil droplet, which is particularly stable under gravity due to the comparable densities of water and oil (see Figure 2-1). This density similarity allows to ignore the movement of the core within the shell layer during the brief period before impact. This simplification is not valid for longer in-flight time (e.g., higher impact heights) [17]. The viscosity of the shell layer contributes to the stability of the compound drops with large cores, as it damps the thinning of the oil layer [18].

Stability in core-shell droplets also arises from thermodynamic factors. For the core to remain fully encapsulated by the shell, the system must minimize its energy [19]. This condition is met when the spreading coefficient $S_i = \sigma_{jk} - (\sigma_{ij} + \sigma_{ik})$ where $(i \neq j \neq k = 1,2,3)$ of the outer phase (shell) is positive, while those of the core and the surrounding medium are negative; i, j, k are referring to the three fluids: two liquid phases (i, j) and the gas phase, k. Figure 2-1 illustrates

this concept, showing the condition under which one phase engulfs another based on their respective spreading coefficient.

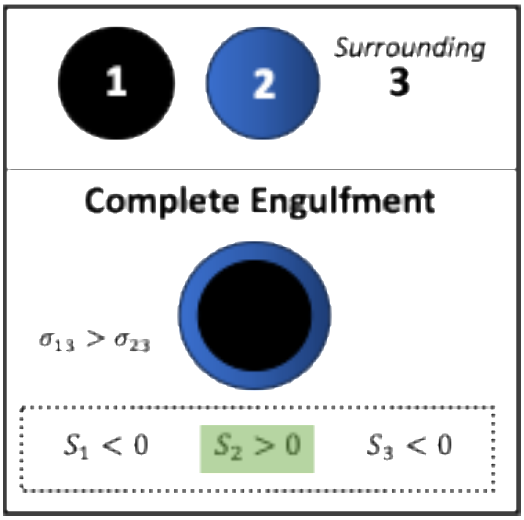

Figure 2-1 Thermodynamic stability of core shell configuration. Numbers (1, 2 and 3) refer to phase 1, phase 2 and surrounding phase 3. Phase 2 in 3 has lower interfacial tension than phase 1 in 3 ($\sigma_{13} > \sigma_{23}$). Core-shell configuration is thermodynamically stable when ($S_2 > 0$) and ($S_3, S_1 < 0$)

Moving from single-component droplets to core-shell compound droplets introduces several additional impact-controlling parameters. These include the volume ratio (α) of the core to the total compound drop ($\alpha = \Omega_{core}/\Omega_{tot}$), where Ω_{core} is core volume and Ω_{tot} is the total drop volume, the density and viscosity of the core and shell layers (ρ_i, ρ_o, μ_i, μ_o), the surface tension of each liquid (σ_i, σ_o), compound droplet diameter (d_o), and the interfacial energy at the core-shell interface (σ_{io}). Here, the subscripts (i, o) denote the inner (core) and outer (shell) phases, respectively.

Below we first examine studies on the impact outcomes of core-shell compound droplets, followed by a discussion of those focused on the spreading phase.

2.1.1 Impact outcome

The impact outcome of a compound droplet of core-shell configuration has been studied within different ranges of controlling parameters. Two pioneering studies looked at the impact of compound droplets on inclined heated surfaces [9], [20]. Motivation was to compare the impact of pure (e.g., one component) drops with multicomponent drops with potential use in blended fuels. A stream of small core compound drops (core-to-shell mass ratio: 0 - 0.306) of water inside diesel oil shells was created to impact an inclined stainless steel heated plate (well above Leidenfrost temperature 'non-wetting impact'). For pure diesel drops, reflection of the drops after hitting the heated inclined surface (with or without disintegration of secondary drops) was the main outcome. Adding small cores was of slightly heavier core (i.e., water) found to break the symmetrical shapes of the reflecting column seen for single-component drops. Heavier or larger cores could even escape the rebounding column. The residence time for the compound drops was found to be less than that of pure diesel drops. The impact velocity had no effect on residence time; however, the size of the total drop was proportional to the residence time. Larger cores introduced an extra area at the water-diesel interface, thereby increasing the interfacial force, which lowered the residence time due to a stronger and faster receding phase. However, these studies only explored the impact of a narrow range of small cores, with the viscosity ratio between core and shell material fixed at ~1/3. Additionally, the outcomes map primarily focused on disintegration versus non-disintegration after impacting the inclined heated surface, leaving other potential controlling factors unaddressed.

One of earliest experimental investigations of compound drops colliding horizontal unheated quartz surfaces was done by Chen et. al. [21], resulted in some similar impact outcomes seen in pure drops impact events; namely deposition, partial rebound, and splashing. However, rebound on high energy surfaces (e.g., glass) was an unexpected outcome for the compound drop impact. This rebound was further understood by the experiments done by Blanken et al. [17]. They proposed that the rebound of the core is due to a mechanism referred to as self-lubricating, since the lubricant is part of the incoming drop (i.e. the oil shell layer). They defined lower and upper limits for the rebound regime. The lower limit occurs at low Weber numbers due to insufficient energy to cause a partial rebound. The upper limit is due to the breakage of the oil lubricating layer and the suppression for the core liquid caused by the wettability of the glass surface, which hinders the rebound. If the spreading shell does not rupture, the core spreads, recedes, and rebounds on top of the shell layer material that has spread on the high energy surface, with the surface's wettability having no influence on the core receding dynamics or the rebounded volume [17]. The studies primarily focused on the effect of core size on the rebounded volume across a wide range of Weber numbers, highlighting that the rebound process is controlled by the core size and its interfacial tension with the shell material. However, the viscosity of both the core and shell significantly influences the amount of energy dissipated during the receding phase and the damping of the rebounded column breakup, an aspect that warrants further exploration, which was not considered.

Gulyaev and Solonenko [22] observed the formation of a counter-jet during the spreading of hollow drops, a type of core-shell compound drop with the core being air. This counter-jet, which

moves inward and upward, contrasts the typical outward and downward direction of impact. Unlike the rebound jet seen in liquid-liquid compound drops, which is primarily driven by the release of stored interfacial energy, the counter-jet in hollow drops is formed due to the liquid supply from the shell. This liquid simultaneously feeds the outward spreading lamella and the inward central flow that generates the counter-jet.

Splashing behavior for compound drop impact has been studied as well. Splashing of water-in-diesel compound drops impacting quartz surfaces was noticed at the same threshold Weber number as pure diesel drops (i.e. shell material) regardless of the existence of a core. The core-to-total mass ratios ranged between (0.07-0.7) [21]. In contradiction to this fixed splash threshold, another experiment for rather very thin shell oil layers (core-to-total volume ratios between 0.8-0.96) [23], splashing was influenced by the size of the core. Larger cores damped splashing. This contradiction may be due to the effect of larger cores on the dynamics of two spreading lamellae (i.e., core and shell). At the moment when the two lamellae emerge during spreading, the dynamics of the outer rim undergo a perturbation. The time of this perturbation, observed as a dip in the spreading factor graphs by [23], is referred to as the 'shoulder time (t_b)'. Their study found that this shoulder time is largely influenced by the size of the core, with larger cores leading to earlier emergence and subsequent reduction of the contact line velocity.

A further element to take into consideration for compound droplets is the position of the core within a compound droplet, both vertically and horizontally, the core position is influenced by various factors such as the drop generation method, the density difference between the core and shell, and the free-fall time before impact on the surface [16]. For example, coaxial needles

generate droplets with the core initially positioned at the top, while side injection of a core into a preformed shell drop allows the slightly heavier core to settle at the bottom of the compound droplet [17]. This latter technique results in a thinner oil layer beneath the core before impact, leading to the rupture of the lubricating shell layer at lower Weber numbers and smaller core sizes compared to coaxially generated drops. The core's contact with the surface significantly affects the impact outcome. For hollow compound drop impact, the core's horizontal shift in position causes the counter-jet to bend and appear as an arc [22], [24]. For water-in-oil drop impact, the core's horizontal position can break the symmetry of the rebounded bowling-pin-shaped jet in on inclined heated plates. In some cases, the core escapes the rebounded jet due to horizontal asymmetry.

Despite the efforts in the literature to identify the key parameters controlling the impact outcome of compound drops, there remains a significant gap in understanding how core and shell viscosities influence these outcomes, particularly across the entire range of core sizes. This gap is critical, as the morphology of the spreading and the resulting impact outcomes, such as changes in splashing thresholds linked to core size, are essential areas that require further investigation.

2.1.2 Maximum spreading

The maximum spreading β_{max} is defined as the maximum diameter of the spreading drop normalized by its original outer diameter before impact. Predicting the maximum spreading is beneficial for applications requiring precise drop deposition.

The numerical investigation done by Liu et al. [25] assumed similar density and viscosity values for both core and shell impacting onto a hydrophobic surface. Hence, it only looked at

introducing a core-shell interface inside a pure drop. The larger the core, the larger the interface that leads to less spreading on the surface. This is because surface tension is resisting the flattening of the droplet on the surface. This result holds true when the core and shell layers of the compound drop have similar properties, as differing properties leads to varying levels of energy dissipation during spreading. Numerically, they covered a wide range of Weber numbers ($10 < We < 1000$) and surface tension ratios ($\gamma = \frac{\sigma_{io}}{\sigma_o}$, ranged $0 \leq \gamma \leq 10$). However, from a practical perspective, at such high Weber numbers, the spreading compound drop will experience splashing as seen in [17], [21]. Surprisingly, splashing was not reported in their numerical simulations. Also, the very low values of surface tension ratio ($\gamma < 1$) indicates that the inner interface has a much lower interfacial tension, which could introduce thermodynamic instability especially for medium to large core sizes [19], [26] as previously indicated, see Figure 2-1. They defined two flow regimes, namely, joint rim when the core is large enough to enter the rim, and jammed regime where the core deformation or size does not allow core liquid to enter the rim. The effect of the core size on the maximum spreading was found to be less significant for joint rim regime than jammed regime. This result contradicts the experimental observations of very large cores (e.g., joint rim flow regime: $\alpha = 0.72 - 0.96$) [23]. The maximum spreading was found to depend on the core size for a given impact velocity. The explanation is while the core size increases, the core-shell interfacial energy increases, but also the overall viscosity of the compound drop changes significantly; an effect that was not considered for the numerical simulations by Liu and Tran [23].

Core viscosity had no influence on the early spreading dynamics of very thin shell oil layers compound drops (at t < 0.1 ms), particularly the ejection velocity of the lamella [27]. An important predicting parameter found to influence the transition threshold to splashing in single-component impact studies [28], [29]. Another study [30] reported insignificant effect of core viscosity on maximum spreading for a fixed medium core size ($\alpha = 0.575$) when core viscosity is less than the shell's. However, when core size was varied using the same liquids (e.g., water in biodiesel oil), the maximum spreading factor increased [31]. They attributed this increase in spreading to the significant reduction of the total drop viscous dissipation caused by the less viscous core.

Despite recent research focusing on the impact of core-shell droplets on solid surfaces, a fundamental understanding of the underlying physics governing these complex interactions remains elusive. Even with few existing studies, inconsistencies in results and a lack of comprehensive parameter exploration persist. This study systematically investigated the influence of core size (small, medium, and large), core and shell viscosities, and introduction of a modified Weber number on impact outcomes and maximum spreading. By varying these controlling parameters across a wide range and using different liquid combinations, the study attempts to elucidate their influence on impact outcomes and maximum spreading.

2.2 Materials and Method

The experimental investigation focused on how core size α, core viscosity μ_i, shell viscosity μ_o, and equivalent Weber number $\overline{We}$ influenced the impact outcome and the maximum spreading factor β_{max} of core-shell compound droplets on a hydrophilic surface. The range for

each variable was systematically explored and illustrated first, followed by the experimental apparatus used for testing.

2.2.1 Experiment parameters range

The range of the parameters for the experimental investigations varied as follows: The co-axial generation method produces core-shell droplets with adjustable core sizes. By independently controlling the flow rates of the core and shell fluids, the core-to-total volume ratio ($\alpha = \Omega_{core}/\Omega_{tot}$) was varied from 0.15 to 0.9 for compound droplets with an outer diameter ranging from 2.4 to 2.5 mm.

The weight method was selected over optical measurement to validate the core size, as the oil layer's magnifying effect distorted the core's apparent size. Therefore, 30 drops of each volume ratio were collected, and the liquid phases were separated using a centrifugal separator. By weighing each component and knowing the densities of the liquids, the volume ratios were confirmed with an error margin of less than 4% for largest and smallest core ratios (e.g., α = 0.15, 0.8, 0.9). To prevent water from climbing up the inner needles, due to surface tension, and disrupting the flow, the needles were hydrophobized. Cleaning needles involved using acetone and ethanol in an ultrasonic device for 20 minutes. Hydrophobization was performed via dip-coating in a mixture of 0.017g trichloro octadecylsilane polymer and 25ml toluene, followed by placing the coated needles in a vacuum oven at 60°C for 2 hours (similar method used in [32], [33]). Silicone oils with varying viscosities were sourced from Sigma Aldrich®, and aqueous water-glycerol solutions were prepared to achieve different core viscosities. Viscosity measurements were conducted using a parallel plates TA rheometer, were values found to be

comparable to literature data [34], [35] (see Table 2-1 below). Water-based food coloring enhanced the visual contrast between the core and shell phases (less than 2 wt.%). Interfacial tension values were measured using the pendant drop method with a KRÜSS drop shape analyzer, with the core-shell interface exhibiting a tension of 40 mN/m.

Table 2-1 Liquids properties for the core and shell materials used. All measurements are at 20°C

	Liquids tested	**Abbreviation**	**Density** (g/ml)	**Viscosity** (mPa·s)	**Interfacial tension with air** (mN/m)
Core	Water	W	1.00	1.01	72.00
Core	60%GLY/water	WG60	1.15	16.00	68.44
Core	70%GLY/water	WG70	1.18	22.50	67.80
Shell	Silicone oil (5 cSt)	S5	0.91	4.57	19.70
Shell	Silicone oil (10 cSt)	S10	0.95	9.35	20.10
Shell	Silicone oil (20 cSt)	S20	0.95	19.00	20.60

The Weber number must be redefined from the form commonly used in most of the discussed literature for compound drops ($We = \frac{[\rho_i\alpha+(1-\alpha)\rho_o]U^2 d_o}{\sigma_o}$) to involve the core-shell interfacial energy. This energy, which is twice the magnitude of the shell's surface energy with air, cannot be neglected considering the Weber number as ratio between the kinetic energy and the surface energy. Incorporating this interfacial energy into a modified Weber number Equation 2-1 provides a more appropriate means to understand the impact dynamics, reflecting the complex exchanges of different energy forms.

$$\overline{We} = \frac{[\rho_i\alpha + (1-\alpha)\rho_o]U^2 d_o}{\sigma_o + \sigma_{io}\alpha^{2/3}}, \qquad For\ 0 \le \alpha < 1 \qquad \textit{Equation 2-1}$$

Here, $\alpha^{2/3}$ accounts for interfacial-area scaling: the core-shell interfacial area scales with the core surface area $\sim d_i^2$, and since $d_i \sim \alpha^{1/3} d_o$, the interfacial-area contribution scales as $\left(d_i/d_o\right)^2 = \alpha^{2/3}$

The droplet's velocity just before impact, denoted by U, was estimated using energy conservation in free fall, $U = \sqrt{2gH}$, that showed strong agreement with measured values, especially for impact heights H < 20 cm (as also described by Yee et al. [36]). This calculation neglects air drag, internal core buoyancy-driven motion within the compound drop, and any initial velocity imparted during pinch-off. The effect of air drag is negligible within the range of parameters tested, as prior research (e.g., Kurniawan et al. [37]) has established that its influence on free-fall motion is insignificant when the ratio of impact height to droplet outer diameter satisfies $\frac{H}{d_o} \leq 89$. In our experiments, this ratio remained well below this threshold (with a maximum value of 50), confirming that air resistance does not significantly alter the droplet's trajectory. The contribution of core buoyancy-driven motion is also negligible, as experimental observations indicate that the core consistently remained at the top of the compound droplet throughout free fall till impacting the surface. This implies that the time scale of internal core motion is significantly shorter than the free-fall duration, preventing substantial displacement of the core during descent. The assumption of negligible initial velocity is further supported by the experimental conditions, where droplets were generated using a total infusion flow rate of 10 µl/min and a small-diameter needle. Under these conditions, detachment was governed primarily by surface tension rather than inertia, leading to a nearly static release. The supplementary (i.e.,

Appendix A) Fig. SI 2-1 further illustrates this assumption, as the experimentally observed drop trajectory closely matches the theoretical free-fall prediction assuming zero initial velocity. In contrast, incorporating an estimated initial velocity using the suggested empirical formula by Kurniawan et al. [37] (i.e., $U_0 = 2{d_o}^{2.836}$ results in an overprediction of the droplet's position, indicating that any initial velocity at pinch-off is either negligible or rapidly dissipated before significantly influencing the descent.

The modified Weber number was varied (between 15 and 199) by adjusting the height of the coaxial needle (from 2 to 12 cm) using an adjustable mount. Maximum spreading values were determined by analyzing the spreading lamella through image processing, for equivalent Weber numbers up to the splashing threshold for each combination of liquid sets and core sizes tested (see Table 2-2). The uncertainty in the modified Weber number was estimated to be less than 5% using standard error propagation, incorporating measurement uncertainties in the droplet diameter, volume fraction, and impact velocity.

Droplet oscillation after pinch-off from the needle is known to influence droplet shape before impact, particularly at low impact velocities and for large droplet sizes [37], [38], [39]. However, in this study, oscillation is not a concern within the impact height range tested, as viscous and capillary forces rapidly dampen oscillations. Our observations showed that all droplets maintained a spherical shape before impact for $120 \geq H \geq 30$ mm. Droplets containing small cores ($\alpha \leq 0.5$) stabilizing stabilized the fastest. As a result, oscillations did not affect our observations, data interpretation, or conclusions regarding impact outcomes and maximum spreading behavior. At low impact heights ($H < 20\ mm$), where oscillations were present,

droplets exhibited periodic deformations between elongated (prolate) and compressed (oblate) shapes due to the balance between surface tension and inertia. The dominant oscillation mode was quadrupole ($n = 2$) for both single and compound droplets, consistent with the core's top-positioned mass shift along the vertical axis. Higher-order modes ($n > 2$) would typically result from horizontal core displacement, which was not observed in this study. Only 8% of the tested range of data falls within the oscillation range, and the outcome of the impact has not changed measurably.

Clean hydrophilic glass substrates (Thermo-Fisher Scientific™) were used as the target plate for all tests. Contact angle measurements were conducted using the sessile drop method with a KRÜSS drop shape analyzer. The static contact angle for water/water-glycerol mixtures is 6° ± 1°, and less than 5° for silicone oils. Additionally, advancing and receding contact angles were measured, showing receding dynamic angles below 5° and advancing contact angles of 10° ± 0.5° for water/water-glycerol mixtures and 8° ± 1° for silicone oils. All experiments were conducted at a room temperature of approximately 20°C, with the impact surfaces maintained at the same temperature. Small variations in surface temperature would not significantly affect the impact outcomes, as the shell layer, composed of thermally stable silicone oil, exhibits a gradual and linear decrease in surface tension with temperature, at a rate of approximately 0.15 mN/m per °C [40]. These variations are minor relative to the overall liquid properties and remain negligible within the studied range of impact conditions. Furthermore, the impact process occurs within just a few milliseconds, far shorter than the timescale required for a small temperature

variation to meaningfully alter liquid properties, ensuring that such fluctuations have no measurable effect on the observed outcomes.

Table 2-2 Liquid combinations used in the experiments with the abbreviations used to describe the liquid-set. All experiments are done at 20°C

	Abbreviation	Core	Shell
Viscous Shells	W/S20	Water	Silicone oil (20 cSt)
	W/S10	Water	Silicone oil (10 cSt)
Reference Combination	W/S5	Water	Silicone oil (5 cSt)
Viscous Cores	WG60/S5	Aqueous glycerol solution (60 wt.%)	Silicone oil (5 cSt)
	WG70/S5	Aqueous glycerol solution (70 wt.%)	Silicone oil (5 cSt)

The liquid combination with the lowest total viscosity (W/S5) was selected as the reference data point. More viscous cores and shells were then introduced for comparison. For each liquid set, the core-to-total volume ratio was adjusted, and each core size was tested across a range of initial droplet energies, up to the splashing threshold. All recorded videos were analyzed to extract qualitative and quantitative data on outcomes and spreading parameters, which will be discussed in the results section. All experiments were repeated at least three times, and the resulting variation in the maximum spreading factor remained below 3.5%. Since this uncertainty was small relative to the reported trends, error bars were omitted from the plots for visual clarity.

2.2.2 Experimental apparatus

The experimental apparatus, depicted in Figure 2-2, consists of three main parts: the compound drop generation system, the high-speed imaging system, and the target solid substrate. The compound drop generation system employs a co-axial needle setup with an inner gauge of

28 and an outer gauge of 22, purchased from Ramé-Hart Instrument. Two KdScientific syringe pumps were used to deliver the core and shell fluids, with flow rates adjusted to achieve various core-to-total volume ratios. Rigid, narrow feeding lines were used to ensure precise control of the core and shell fluid flows, preventing any elastic deformation of the feeding line walls during operation. The high-speed imaging system included two synchronized cameras: the Phantom Miro M310 mounted horizontally and the Phantom V1611 mounted vertically below the surface. The horizontal camera records droplet size and pre-impact velocity as well as reporting the outcome of the impact, while the vertical camera captures the evolution of lamella spreading and maximum diameters during impact. The cameras operate at frame rates of 10,000 fps for the side view and 20,000 fps for the bottom view. Calibration of the cameras is performed using a 5 cm × 5 cm × 0.01 mm grid, with lens calculations achieving a pixel resolution of 40 px/mm for the side view and 30 px/mm for the bottom view.

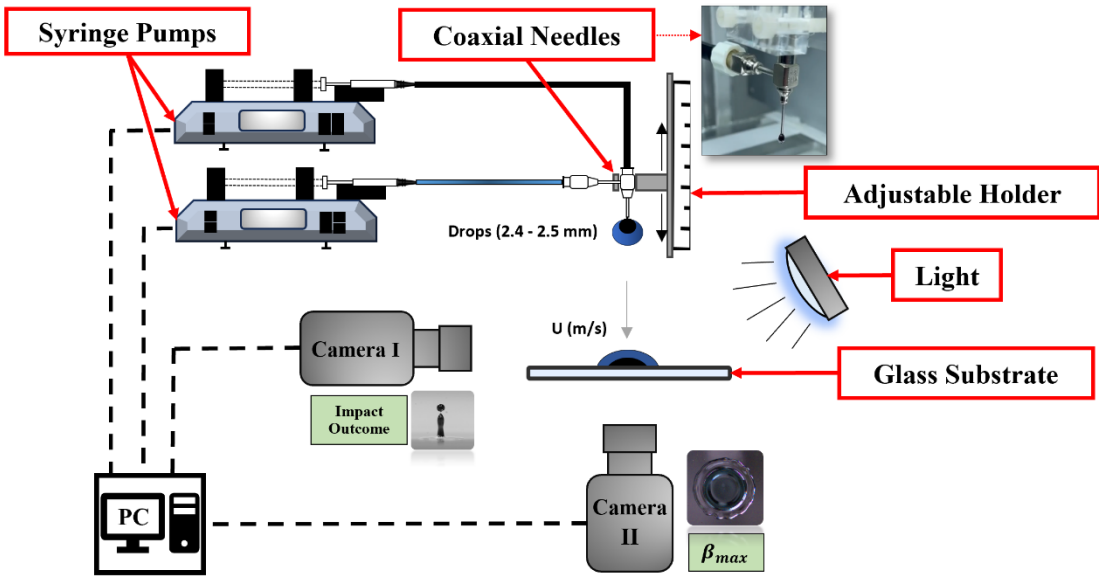

Figure 2-2 Experiment apparatus. Two high speed cameras, Coaxial needles adjustable setup, lighting, target solid surface and syringe pumps with feeding lines and fittings. The computer was used to control and collect recorded data

2.3 Results and Discussion

Results are split into two sections namely impact outcome and maximum spreading. The influence of the modified Weber number, core size, and the droplet core and shell viscosities are explained in their corresponding subsections.

2.3.1 Impact outcome

The spreading-only impact outcome is commonly observed for many single-component drops, such as pure water or pure oil, when they spread on hydrophilic surfaces at low impact velocities. When a water drop falls on a dry hydrophilic glass substrate, it rapidly spreads to reach maximum expansion. From the bottom view, the contact line appears stationary because the small receding contact angle of water on glass prevents it from moving. Silicon oil drops exhibit similar behavior under the same impact conditions (Figure 2-3a, b). However, the viscosity of silicon oil (S5) is five times higher than that of pure water, resulting in greater resistance to spreading. Generally, higher viscosity oil drops spread less compared to water on glass.

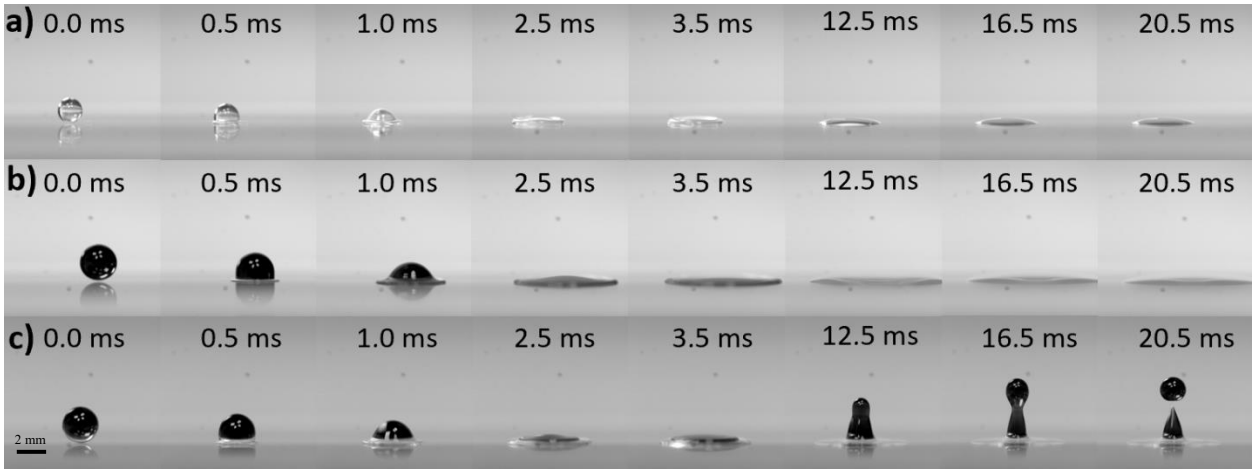

Figure 2-3 Impact of drops (silicon oil "a" and water "b") and a compound water-in-oil "c" of core size (α=0.5) on glass surfaces. The initial Weber number for all cases is We≈65

Encapsulating a water core within an oil shell leads to distinct spreading and receding behavior (Figure 2-3c). Both the core and shell spread on the surface, partially converting the drop's kinetic energy into surface energy at the interfaces, with some energy dissipated due to core and shell viscosity. The water core, shielded from direct contact with the hydrophilic glass, retracts and rebounds atop the oil layer, provided the shell remains intact during spreading. This phenomenon, observed in experiments by Chen et al. [41], with water droplets on thin oil films, shows that the oil layer facilitates core retraction after maximum spreading. Occasionally, the receding core generates a central vertical jet, predominantly composed of core liquid.

Various drop impact outcomes were observed from the experiments of compound droplets (core-shell configuration) colliding glass surfaces. Jetting is when both the core and shell layers spread on the surface, and the core then retracts on top of the lubricating shell layer, forming a central vertical jet. Partial rebound happens when this jet breaks, leading to the formation of one or more secondary droplets (see Figure 2-3 bottom right frame). In some cases, the droplets only spread on the surface, with the receding phase lacking the strength to generate a central jet. Prompt splashing occurs when the drop has enough energy to eject secondary droplets at the contact line of the spreading lamella, sometimes in combination with partial rebound.

2.3.1.1 Effect of the equivalent weber number on impact outcome

The total mass of the compound droplet is $m_c = \frac{\pi}{6} d_o^3[(\rho_i - \rho_o)\alpha + \rho_o]$. Compound drops increase the total interfacial energy due to core-shell interface. Figure 2-4a illustrates the influence of the core size on the equivalent Weber number, considering the effect of the core on

the inertia and total interfacial energy within the drop before impact. For similar impact velocities, larger cores correspond to lower equivalent Weber number values. This reduction is substantial for higher impact velocities.

Figure 2-4b highlights the importance of accurately representing the ratio between inertial and interfacial energies compared to the unmodified Weber number of compound drops used in earlier studies (i.e., without accounting for the core-shell interface energy). Generally, the modified Weber numbers ($\overline{We}$) are lower than the unmodified ones (We): Larger cores add interfacial energy, further reducing the Weber number, which contrasts with the trend observed in the unmodified Weber numbers, which only consider the outer layer surface energy. This divergence of values is magnified for higher impact velocities and could lead to contradictions due to misrepresentation of the initial drop driving to resisting energy ratio. For single-component drops both definitions overlap, see dashed red line in Figure 2-4b.

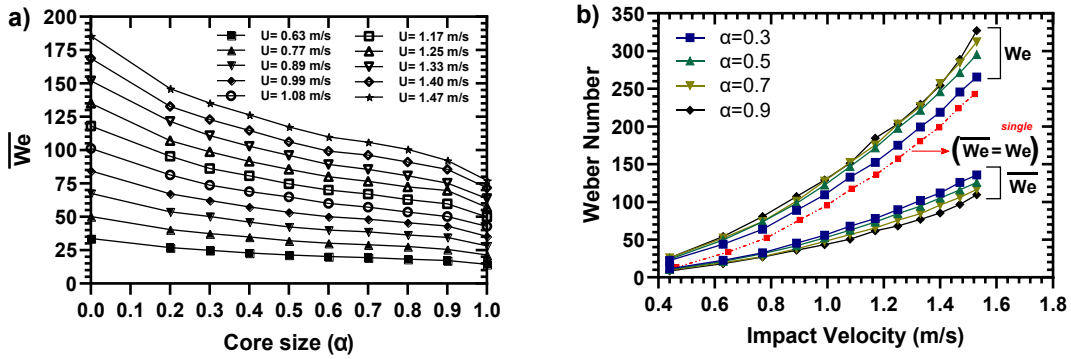

Figure 2-4 a) Equivalent Weber number variation with increasing the core size for different impact velocities. b) Modified versus unmodified Weber number values across a range of impact velocities. Both graphs show data for water in silicon oil (5 cSt).

High Weber numbers cause the core and shell to flatten more on the surface, increasing interfacial energy and intensifying the receding phase. Figure 2-5 illustrates the enhanced central vertical jet formed by incrementally increasing the Weber number (from 5a to 5d), as evidenced by the increasing height of the rebounded column. When the initial energy (i.e., Weber number) is sufficiently high, core material can partially break away from the jet, forming one or more secondary drops.

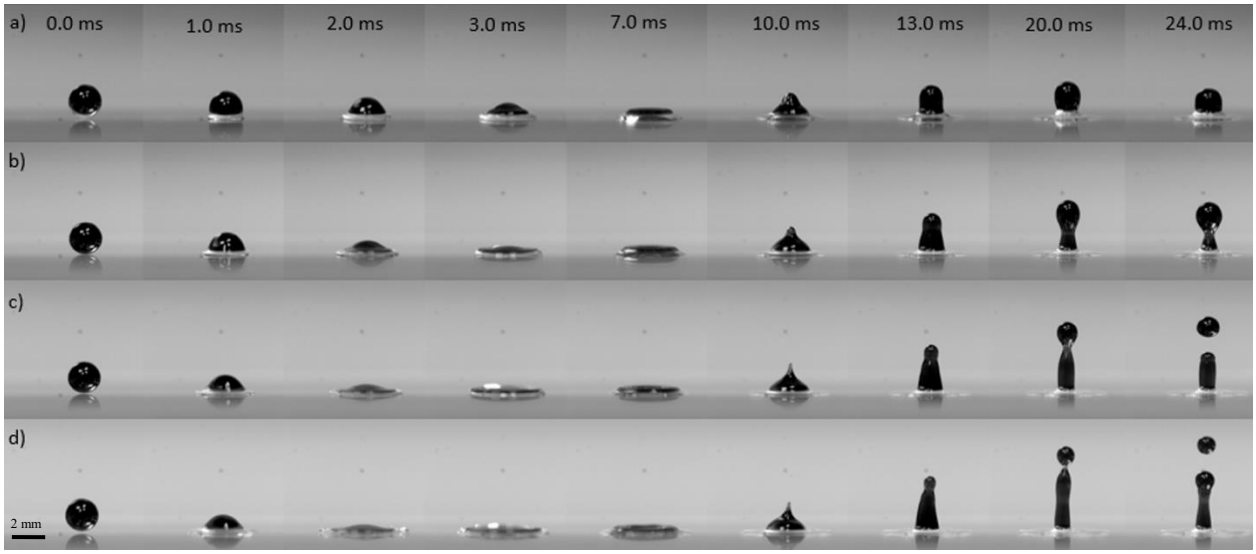

Figure 2-5 From jetting to partial rebound: Impact of a compound droplet of water inside silicone oil (5cSt) with a core size of α=0.7 on glass surface. Equivalent Weber numbers for a-d are 19.5, 37.7, 65.5 and 96, respectively.

In the experiments, the water core often retracts on top of the oil lubricating layer left by the shell. However, further increases in Weber number can result in the spreading of both core and shell liquids. The hydrophilicity of the glass surface affects the core liquid flow, preventing retraction, especially for larger cores. This occurs because the shell layer beneath the flattening drop is thinner, increasing the likelihood of its rupture causing contact between the core and the

substrate (see Figure 2-6 below). When ruptures, the water core wets the hydrophilic surface, preventing the core rebound from happening.

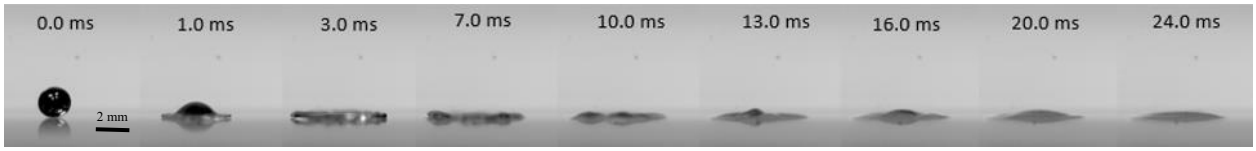

Figure 2-6 Spreading of core and shell phases without jetting. Water core inside silicon oil (5cSt) shell (α=0.9). The equivalent Weber number is (110).

Regardless of rebound, when the impact inertia of the flattening droplet becomes sufficiently large relative to surface tension (i.e., at high Weber number), the rapidly expanding shell lamella becomes unstable and develops undulations near the rim/contact-line region, which can lead to the ejection of secondary droplets; this outcome is referred to here as prompt splash (Figure 2-7). The secondary droplets primarily originate from the shell layer, even for large core sizes. The dyed high-surface-tension cores do not appear to break up during these prompt-splashing cases, but instead remain largely intact and begin to recede (see Appendix A Fig. SI 2-3).

2.3.1.2 Effect of core size on impact outcome

The larger the core, the larger the interfacial energy of the compound droplet. Consequently, when the drop is flattening after impact, the core size amplifies the amount of interfacial energy built up within the compound droplet until it reaches its maximum spreading. This energy controls the receding process. To quantify the initial impact parameters required to produce each impact outcome, Regime maps in the parameter space of equivalent Weber number and core size are developed. For instance, the water in oil (S5) regime map (Figure 2-7) illustrates that for pure oil (α=0) or pure water (α=1), the impact outcome is only spreading on glass surface. Once a water core is added to the oil drop, the core will retract on top of the oil layer and jetting at the

center of the flattened compound drop occurs. Larger cores lead to stronger central vertical jet and early transition from jetting to partial rebound. The transition threshold drops from ($\overline{We} \approx 110$) for small core size (i.e., $\alpha = 0.1$), to as low as ($\overline{We} \approx 40$) for larger cores ($\alpha \geq 0.6$). When cores are very large ($\alpha \geq 0.9$), the oil shell layer is very thin and ruptures during spreading. This leads to contact of the water core and the hydrophilic surface, which damps the receding of the core leading to only spreading of both segments of the compound droplet. The regime maps developed in this work provide a refined representation of the energies governing impact outcomes (e.g., equivalent Weber number) as a function of core size. They enhance the accuracy of regime transition boundaries compared to previous studies while extending the range of parameters analyzed, offering a more comprehensive and detailed depiction of transitions across different core sizes.

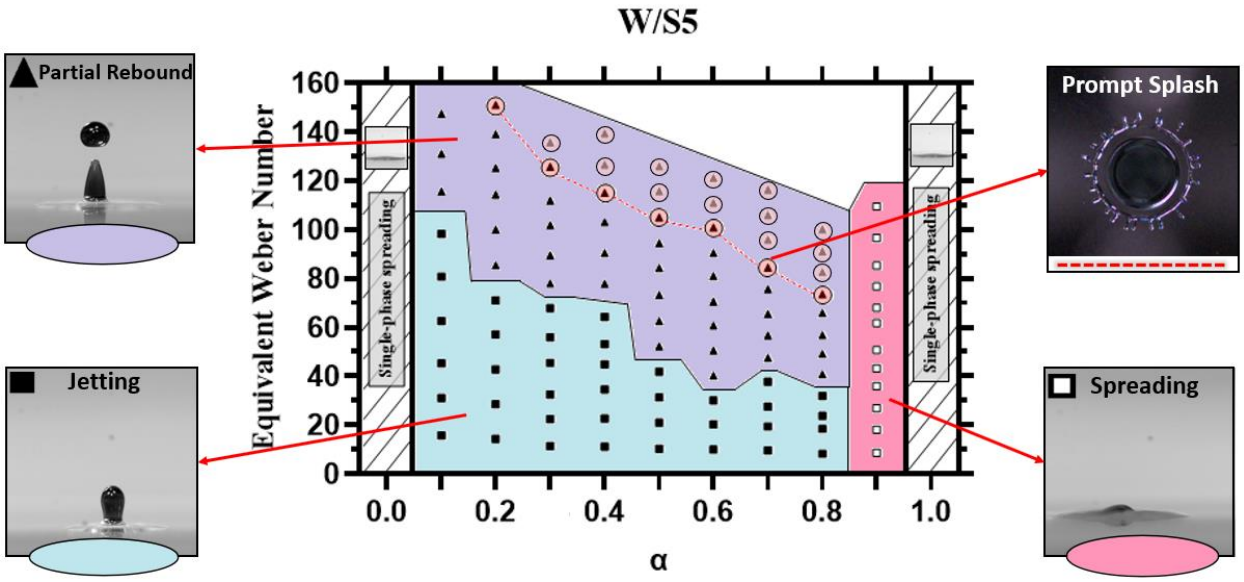

Figure 2-7 The regime map of water core inside silicon oil (5cSt) for a full range of core sizes including single-component drops. Inset for prompt splash is the bottom view.

The splashing threshold for single drop of silicon oil (of 5 cSt viscosity) happens at We ≥ 295. However, adding cores of slightly heavier liquid cause the transition to happen at lower equivalent Weber numbers. Snapshots of the impact of pure oil (S5), water-in-oil compound drops with varying core sizes are illustrated in (Figure 2-8). Larger cores lead to earlier transition to splashing regime at the same Weber number. This can be attributed to increasing the total inertia of the compound droplet compared to the single-component inertia of only the lighter shell liquid (i.e., oil). In experiments, the time of the emergence of the core and shell lamellae (i.e., joint rim), the contact line undergo extra disruption that promotes the undulations at the contact line promoting the breakup of secondary drops (Figure 2-8d at t=3.0 ms).

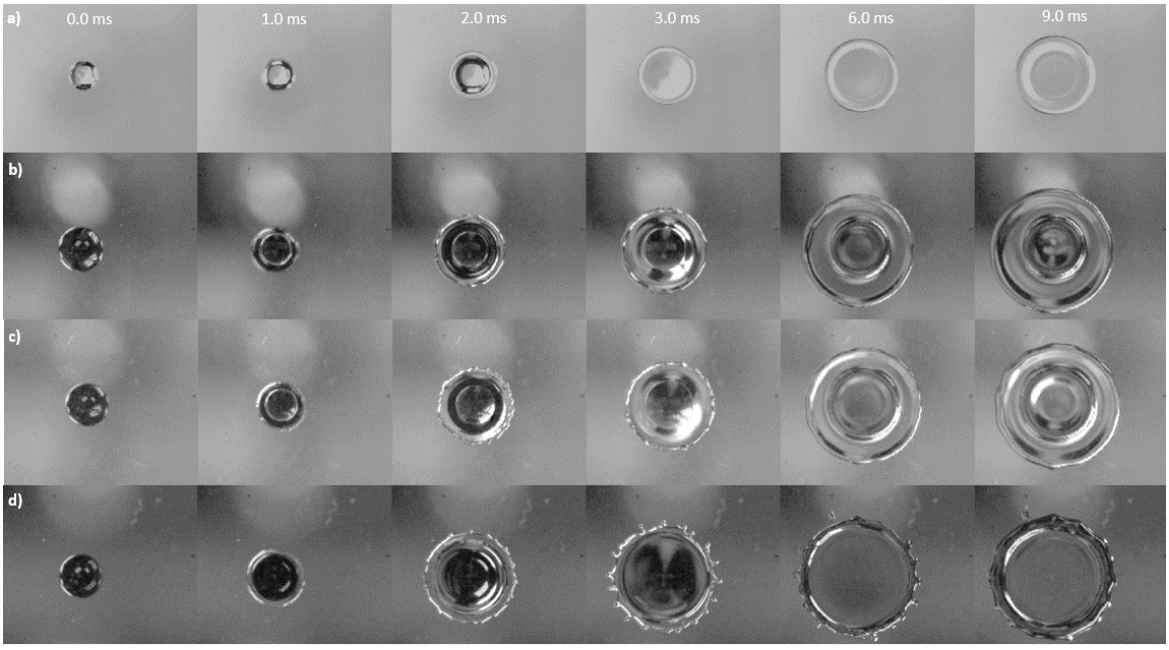

Figure 2-8 Transition to splashing by varying core size of (W/S5) compound drops. The equivalent Weber number is 88. Core sizes are 0.0 'pure S5 oil', 0.2, 0.4 and 0.7 from top to bottom.

2.3.1.3 Effect of core and shell viscosities on impact outcome

Figure 2-9 illustrates the impact outcome of compound droplets with varying liquid combinations. The viscosity of the shell layer encapsulating a water core increases from 5 to 10 to 20 cSt in Figure 2-9a, 9b, and 9c, respectively. The shell viscosity affects the partial rebound zone (illustrated through the shrinking partial rebound zone). Higher viscosity leads to greater dissipation of the initial energy during both the spreading and receding phases, particularly at the outer rim of the spreading lamella where the shell liquid is predominant. This increased viscosity restricts contact line movement, causing the core to spread less on the surface and store less energy at the interfaces, thus damping the central jet (as shown in Appendix A Fig. SI 2-4).

When the core viscosity is increased, more energy is dissipated within the bulk of the spreading compound droplet. During the receding phase, the core material forms the central jet. The increased core viscosity dampens the undulations at the perimeter of the rebounded liquid column, preventing jet breakup. Universal damping of the partial rebound zone is observed for very viscous cores (WG70/S5) in the regime maps (Figure 2-9e).

Splashing with partial rebound is seen across various liquid combinations. For highly viscous cores (Figure 2-9e), a splashing threshold can be reached at higher Weber numbers without partial rebound. Another observation is that the rupture of the shell layer at high core sizes is slightly dampened more by increasing the core viscosity than by increasing the shell layer viscosity.

The transition threshold to splashing is not affected by core viscosity (Figure 2-9d and 9e) since prompt splashing primarily occurs at the spreading contact line over the solid surface, which consists mainly of shell material. Thus, increasing shell viscosity significantly dampens prompt splashing for all core sizes compared to increasing core viscosity, as evident in the regime maps (Figure 2-9b and Figure 2-9c). This confirms that core viscosity has a negligible effect not only on the early dynamics of the ejecting lamella, as previously discussed, but also on the splashing threshold.

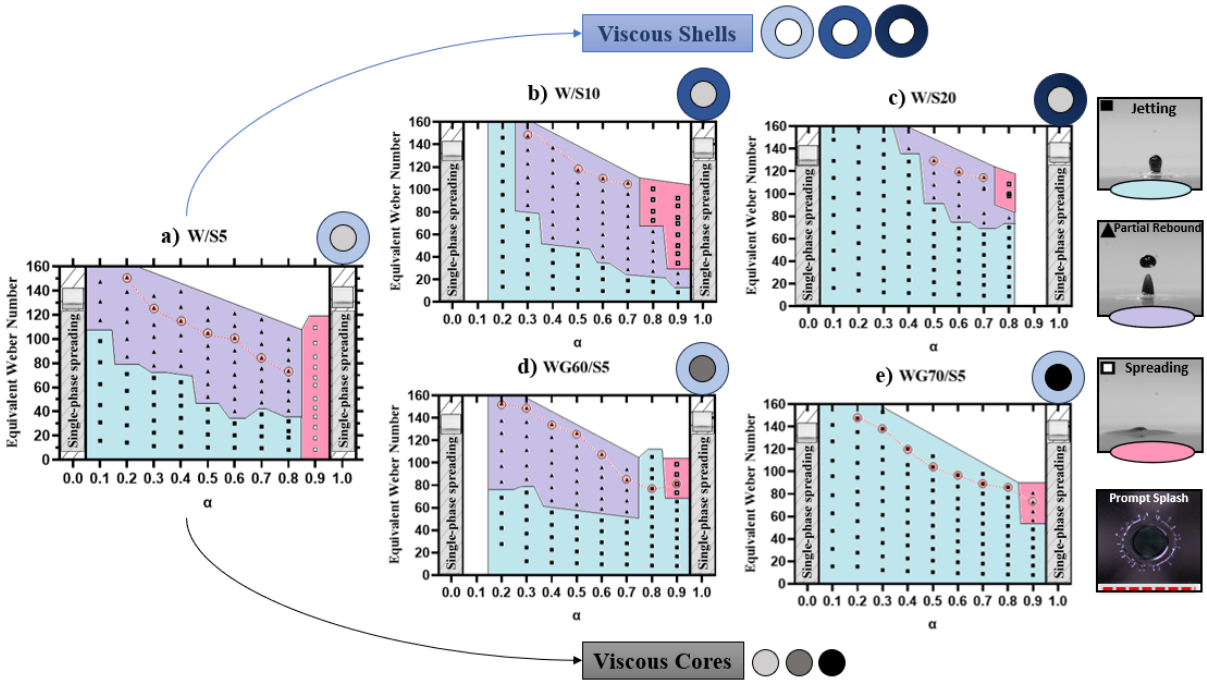

Figure 2-9 The regime maps for different liquid combinations in parameter space of Equivalent Weber number and core size. The direction a-b-c indicates increasing the shell viscosity from 5-10-20 cSt while the core is water (1 cSt). The direction of a-d-e indicates increasing the core viscosity from 1-16-22.5 mPa.s and the shell is fixed 5 cSt oil.

2.3.2 Maximum spreading

From an energy perspective, the maximum spreading factor ($\beta_{\max}$) of an impacting droplet is controlled by the kinetic energy, interfacial energy and viscous dissipation. The energy budget of the compound droplet prior impact (state 1 in Figure 2-10) consists of two components: kinetic energy ($\mathrm{K.E._1}$) and surface energy ($\mathrm{S.E._1}$). This total initial energy is converted into the expansion of the droplet's interfacial areas ($\mathrm{S.E._2}$) at the maximum spreading (state 2 in Figure 2-10). A portion of this energy dissipates primarily as a result of viscosity (W_v). The energy equilibrium from the instant of impact to the point of maximum spreading can be described as follows:

$$\mathrm{K.E._1} + \mathrm{S.E._1} \rightleftharpoons \mathrm{S.E._2} + \mathrm{W}_v \qquad \textit{Equation 2-2}$$

This energy argument is used to understand the effect of adding a core to a single component drop, since it proved its robustness in previous maximum spreading studies done in the literature [5], [42]. The effect of the core size and liquid properties influence all energies in Equation 2-2. Hence, the energy equilibrium is used as framework for driving and resisting energies controlling the spreading.

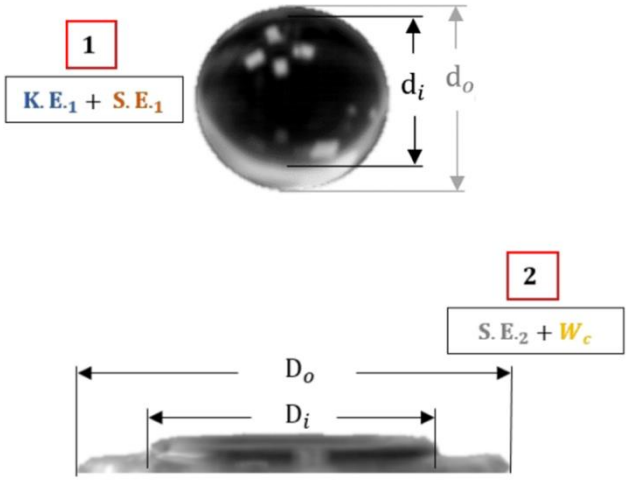

Figure 2-10 The Energy at the incoming droplet just before impact is (1), the energy stored and dissipated up to maximum spreading (2).

2.3.2.1 *Effect of the Equivalent Weber Number on Maximum Spreading*

An increase in the Weber number within the tested range (e.g., $15 \leq \overline{\mathrm{We}} \leq 175$) indicates a greater availability of kinetic energy that drives the deformation and stretching of the compound droplet interfaces. This process generates additional surface area while dissipating some of the energy through viscous losses. As a result, higher Weber numbers consistently lead to larger spreading diameters, irrespective of core size or liquid combination (Figure 2-11). The same influence of Weber number was seen for single-component drops impacting solid surfaces in our experiments and previous studies [42], [43]. Notably, the relationship between equivalent Weber number and maximum spreading diameter is not linear across the entire range. For $\overline{\mathrm{We}} \leq 50$, the maximum spreading increases rapidly with rising equivalent Weber numbers, reflecting the dominance of kinetic energy in driving deformation. However, at higher equivalent Weber numbers, increased impact velocities introduce greater viscous dissipation, which moderates the spreading. Consequently, the slope of the maximum spreading curve decreases, eventually begins plateauing at the upper end of the tested range.

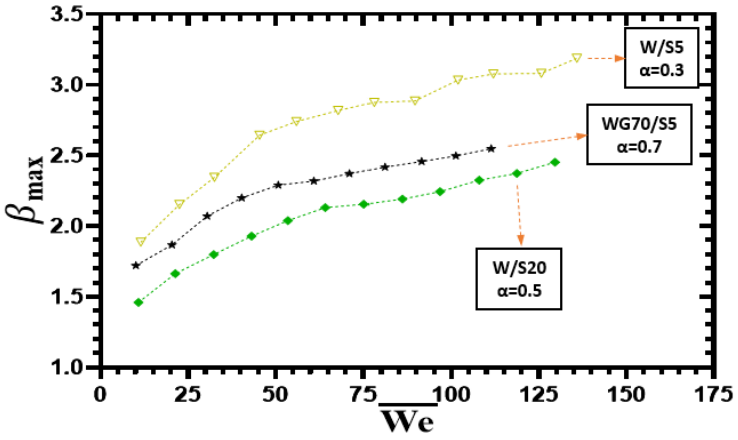

Figure 2-11 The maximum spreading factor (β_{max}) as a function of average Weber number. Data shown are for Water in silicon oil (5 cSt) with three core sizes (0.3, 0.5 and 0.7).

2.3.2.2 Effect of core size on maximum spreading

The effect of core size on the maximum spreading of a compound droplet involves a balance between interfacial energy and viscous dissipation. For small core sizes ($\alpha \leq 0.5$), the deviation in values of the maximum spreading of pure shell drops (e.g., silicone oil) is minimal. In this range, the addition of an extra interface (small core) influences the outcome (e.g., jetting and partial rebound) more than the maximum spreading factor itself. Since the central top part of the compound drop where the core is located, does not contribute to the early ejection of the lamella. Moreover, it is not part of the spreading rim. However, even a small core was found to be driving the receding phase and creating a central vertical jet. Hence, the viscosity variation between the core and shell is insignificant in this range of small cores on the maximum spreading factor.

For larger core sizes ($\alpha > 0.5$), the increased area of the core-shell interface often contributes to rim formation, a phenomenon previously termed the 'joint rim' in numerical simulations by Liu et al. [25]. As the core size increases, the resistance to stretching the interfaces becomes dominant, resulting in less spreading. The total viscous dissipation of the droplet can vary depending on the properties of the core and shell. When the core is more viscous than the shell, the core size significantly impacts the maximum spreading, with larger, more viscous cores providing greater resistance to spreading and thus reducing the maximum spreading factors (Figure 2-12d and Figure 2-12e). Viscous and interfacial terms in Equation 2-2 increase resistance to spreading effectively in this range of viscous core size.

In contrast, when the core-to-shell viscosity ratio is less than 1 (Figure 2-12b and Figure 2-12c), larger cores decrease the overall compound droplet viscosity, reducing resistance to

lamella spreading while increasing interfacial energy. This contrasting effect leads to minimal maximum spreading values at different core sizes for each liquid combination.

These experimental findings highlight the importance of considering the combined effects of density and viscosity variations between the core and shell materials across different core sizes (e.g., spreading morphologies), particularly for small cores (jammed regime) and larger cores (joint rim regime). Not accounting for the interplay between core size and its density and viscosity could lead to misleading trends in the dependency of maximum spreading factors on core size, as seen in the opposite trend in the numerical simulations by Liu et al. [25]. Future work utilizing energy or momentum balance frameworks could provide valuable insights for predicting and controlling the maximum spreading factor, emphasizing its dependence on liquid properties and core size.

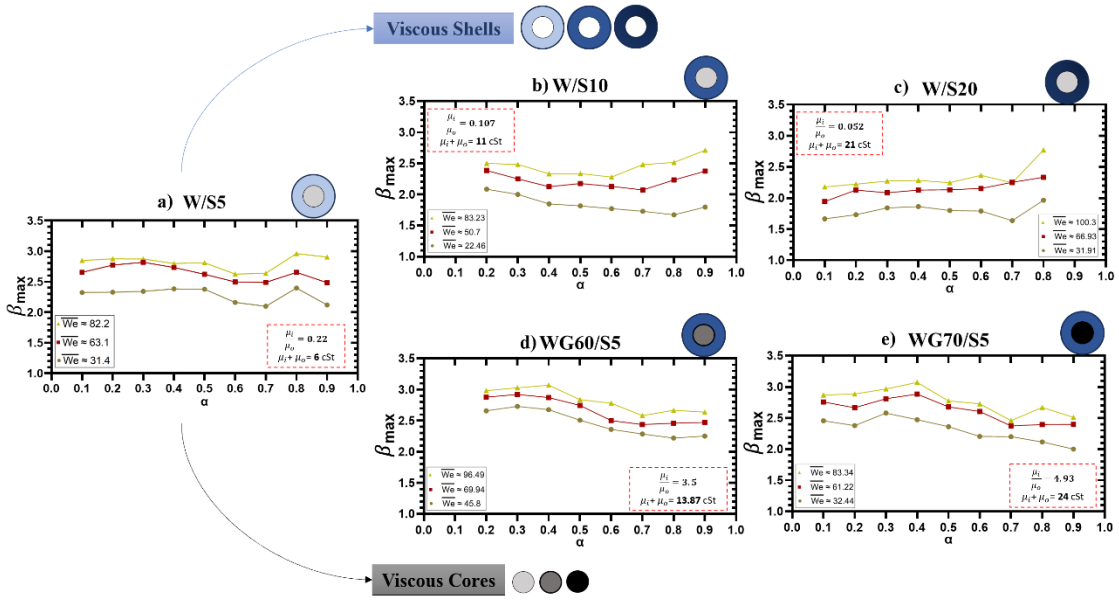

Figure 2-12 The maximum spreading factor as function of the core size is illustrated for different liquid combinations. Different equivalent Weber numbers are shown here.

2.3.2.3 *Effect of core and shell viscosities on maximum spreading*

Higher shell viscosity consistently leads to reduced spreading on the surface. When the shell layer viscosity is high, the spreading is primarily controlled by this shell's high viscosity and the influence of varying the core size on maximum spreading diminishes. Figure 2-13b demonstrates that the maximum spreading factor for highly viscous shells (S20) remains consistent across all core sizes, indicating that varying core sizes will not effectively control the maximum spreading for such droplets. Conversely, varying the core viscosity (in the range tested where $\mu_i > \mu_o$) has an insignificant effect on maximum spreading across all core sizes (see Appendix A, Fig. SI 2-5). For cases with large core sizes ($\alpha \geq 0.8$), where the oil shell ruptures upon impact (i.e., spreading regime), the droplet exhibits greater spreading due to the rapid wetting of the high-energy surface by the exposed water core, resulting in a substantially larger maximum spreading factor. The viscosity of the shell influences the rupture dynamics, with lower-viscosity shells exhibiting asymmetric rupture, including failure at the contact line (see Appendix A, Fig. SI 2-3a). In contrast, higher-viscosity shells consistently rupture at the bottom of the spreading droplet, without significant thinning of the spreading rim (see supplementary Fig. SI 2-6c).

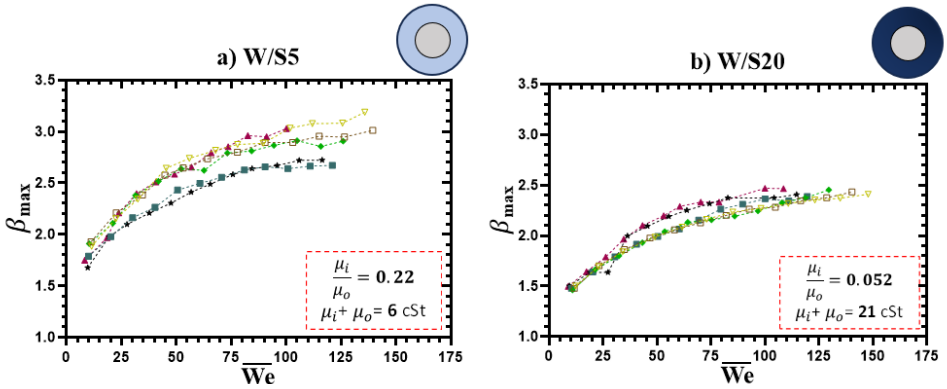

Figure 2-13 Maximum spreading factor as a function of equivalent Weber number for an increasing shell viscosity. Various core sizes are shown.

2.4 Conclusions – Key highlights

- Introduced an equivalent Weber number that incorporates core-shell interfacial energy and, together with core volume fraction and shell viscosity, was shown to govern both impact outcome and maximum spreading.
- Constructed regime maps in equivalent Weber number–core fraction space that clearly delineate jetting, partial rebound, spreading-contact, and prompt-splashing regimes for multiple core–shell viscosity combinations.
- Demonstrated that increasing equivalent Weber number or core fraction promotes stronger central jetting and the transition to partial rebound, while shell and core viscosities damp jet rebound and suppress energetic outcomes.
- Showed that maximum spreading is primarily enhanced by higher equivalent Weber number and lower shell viscosity, with core viscosity having only a minor influence; large cores ($\alpha > 0.5$) reduce spreading through increased viscous dissipation and interfacial resistance, whereas small cores ($\alpha < 0.5$) have little effect.
- Quantified how these controllable parameters shift regime boundaries and $\beta_{\max}$, providing guidance for applications such as fuel injection, inkjet printing, and agricultural spraying where precise control of droplet impact behavior is critical.

2.5 References

[1] A. R. Vaezi, M. Ahmadi, and A. Cerdà, "Contribution of raindrop impact to the change of soil physical properties and water erosion under semi-arid rainfalls," *Sci. Total Environ.*, vol. 583, pp. 382–392, 2017, doi: 10.1016/j.scitotenv.2017.01.078.

[2] A. L. N. Moreira, A. S. Moita, and M. R. Panao, "Advances and challenges in explaining fuel spray impingement: How much of single droplet impact research is useful?," *Prog Energy Combust Sci*, vol. 36, no. 5, pp. 554–580, 2010, doi: 10.1016/j.pecs.2010.01.002.

[3] B. Derby, "Inkjet printing of functional and structural materials: fluid property requirements, feature stability, and resolution," *Annu Rev Mater Res*, vol. 40, pp. 395–414, 2010, doi: 10.1146/annurev-matsci-070909-104502.

[4] C. Josserand and S. T. Thoroddsen, "Drop impact on a solid surface," *Annu Rev Fluid Mech*, vol. 48, pp. 365–391, 2016, doi: 10.1146/annurev-fluid-122414-034401.

[5] S. Chandra and C. T. Avedisian, "The Collision of a Droplet with a Solid Surface," *Phys Fluids*, vol. 2, no. 9, p. 1525, Sep. 1990, doi: 10.1063/1.4738846.

[6] M. Delcea, H. Möhwald, and A. G. Skirtach, "Stimuli-responsive LbL capsules and nanoshells for drug delivery," *Adv Drug Deliv Rev*, vol. 63, no. 9, pp. 730–747, 2011, doi: 10.1016/j.addr.2011.03.010.

[7] M.-H. Lee, S.-G. Oh, S.-K. Moon, and S.-Y. Bae, "Preparation of silica particles encapsulating retinol using O/W/O multiple emulsions," *J Colloid Interface Sci*, vol. 240, no. 1, pp. 83–89, 2001, doi: 10.1006/jcis.2001.7699.

[8] T. Y. Xiong and M. C. Yuen, "Evaporation of a liquid droplet on a hot plate," *Int J Heat Mass Transf*, vol. 34, no. 7, pp. 1881–1894, 1991, doi: 10.1016/0017-9310(91)90162-8.

[9] S.-L. Chiu and T.-H. Lin, "Experiment on the dynamics of a compound drop impinging on a hot surface," *Phys. Fluids*, vol. 17, no. 12, 2005, doi: 10.1063/1.2139101.

[10] C. W. Visser, T. Kamperman, L. P. Karbaat, D. Lohse, and M. Karperien, "In-air microfluidics enables rapid fabrication of emulsions, suspensions, and 3D modular (bio) materials," *Sci Adv*, vol. 4, no. 1, p. eaao1175, 2018, doi: 10.1126/sciadv.aao117.

[11] P. Taylor, "The wetting of leaf surfaces," *Curr Opin Colloid Interface Sci*, vol. 16, no. 4, pp. 326–334, 2011, doi: 10.1016/j.cocis.2010.12.003.

[12] C. W. Visser, D. N. Amato, J. Mueller, and J. A. Lewis, "Architected polymer foams via direct bubble writing," *Advanced materials*, vol. 31, no. 46, p. 1904668, 2019, doi: 10.1002/adma.201904668.

[13] D. N. Amato, D. V Amato, M. Sandoz, J. Weigand, D. L. Patton, and C. W. Visser, "Programmable porous polymers via direct bubble writing with surfactant-free inks," *ACS Appl Mater Interfaces*, vol. 12, no. 37, pp. 42048–42055, 2020, doi: 10.1021/acsami.0c07945.

[14] S. V Murphy and A. Atala, "3D bioprinting of tissues and organs," *Nat Biotechnol*, vol. 32, no. 8, pp. 773–785, 2014, doi: 10.1038/nbt.2958.

[15] M. T. Guo, A. Rotem, J. A. Heyman, and D. A. Weitz, “Droplet microfluidics for high-throughput biological assays,” *Lab Chip*, vol. 12, no. 12, pp. 2146–2155, 2012, doi: 10.1039/C2LC21147E.

[16] N. Blanken, M. S. Saleem, M.-J. Thoraval, and C. Antonini, “Impact of compound drops: a perspective,” *Curr Opin Colloid Interface Sci*, vol. 51, 2020, doi: 10.1016/j.cocis.2020.09.002.

[17] N. Blanken, M. S. Saleem, C. Antonini, and M.-J. Thoraval, “Rebound of self-lubricating compound drops,” *Sci Adv*, vol. 6, no. 11, p. eaay3499, 2020, doi: 10.1126/sciadv.aay3499.

[18] S. Zhu, A. Kherbeche, Y. Feng, and M.-J. Thoraval, “Impact of an air-in-liquid compound drop onto a liquid surface,” *Phys. Fluids*, vol. 32, no. 4, 2020, doi: 10.1063/5.0005702.

[19] S. Torza and S. G. Mason, “Coalescence of two immiscible liquid drops,” *Science (1979)*, vol. 163, no. 3869, pp. 813–814, 1969, doi: 10.1126/science.163.3869.813.

[20] R.-H. Chen, S.-L. Chiu, and T.-H. Lin, “Resident time of a compound drop impinging on a hot surface,” *Appl Therm Eng*, vol. 27, no. 11–12, pp. 2079–2085, 2007, doi: 10.1016/j.applthermaleng.2006.11.014.

[21] R. H. Chen, M. J. Kuo, S. L. Chiu, J. Y. Pu, and T. H. Lin, “Impact of a compound drop on a dry surface,” *J Mech Sci Technol*, vol. 21, pp. 1886–1891, 2007, doi: 10.1007/BF03177445.

[22] I. P. Gulyaev and O. P. Solonenko, “Hollow droplets impacting onto a solid surface,” *Exp Fluids* , vol. 54, pp. 1–12, 2013, doi: 10.1007/s00348-012-1432-z.

[23] D. Liu and T. Tran, “Emergence of two lamellas during impact of compound droplets,” *Appl Phys Lett*, vol. 112, no. 20, p. 203702, 2018, doi: /10.1063/1.5026821.

[24] M. Nasiri, G. Amini, C. Moreau, and A. Dolatabadi, “Flattening of a hollow droplet impacting a solid surface,” *J Fluid Mech*, vol. 962, p. A1, 2023, doi: 10.1017/jfm.2023.182.

[25] H.-R. Liu, C.-Y. Zhang, P. Gao, X.-Y. Lu, and H. Ding, “On the maximal spreading of impacting compound drops,” *J Fluid Mech*, vol. 854, p. R6, 2018.

[26] R. E. Johnson and S. S. Sadhal, “Fluid mechanics of compound multiphase drops and bubbles,” *Annu Rev Fluid Mech*, vol. 17, no. 1, pp. 289–320, 1985, doi: 10.1146/annurev.fl.17.010185.001445.

[27] D. Liu and T. Tran, “The ejecting lamella of impacting compound droplets,” *Appl Phys Lett*, vol. 115, no. 7, p. 073702, 2019, doi: 10.1063/1.5097370.

[28] G. Riboux and J. M. Gordillo, “Experiments of drops impacting a smooth solid surface: a model of the critical impact speed for drop splashing,” *Phys Rev Lett*, vol. 113, no. 2, p. 024507, 2014, doi: 10.1103/PhysRevLett.113.024507.

[29] H. Almohammadi and A. Amirfazli, “Droplet impact: Viscosity and wettability effects on splashing,” *J Colloid Interface Sci*, vol. 553, pp. 22–30, 2019, doi: 10.1016/j.jcis.2019.05.101.

[30] A. Kumar and D. K. Mandal, “Impact Dynamics of a Compound Drop on a Plane Solid: Effect of the Core Drop Viscosity,” in *Conf Fluid Mech Fluid Power*, Springer, 2021, pp. 391–396. doi: 10.1007/978-981-19-7055-9_66.

[31] A. Kumar and D. K. Mandal, “Impact of compound drops on a plane solid: Role of the core diameter,” *At. Sprays*, vol. 32, no. 2, pp. 1–18, 2022, doi: 10.1615/AtomizSpr.2021038825.

[32] F. Arianpour, M. Farzaneh, and R. Jafari, “Hydrophobic and ice-phobic properties of self-assembled monolayers (SAMs) coatings on AA6061,” *Prog Org Coat*, vol. 93, pp. 41–45, 2016, doi: 10.1016/j.porgcoat.2015.12.008.

[33] Y. Hu, J. Ou, and A. Amirfazli, “Application of Surface Wettability to Control Spreading of an Impacting Droplet,” *Langmuir*, vol. 40, no. 9, pp. 4623–4634, 2024, doi: 10.1021/acs.langmuir.3c03153.

[34] K. Takamura, H. Fischer, and N. R. Morrow, “Physical properties of aqueous glycerol solutions,” *J Pet Sci Eng*, vol. 98, pp. 50–60, 2012, doi: 10.1016/j.petrol.2012.09.003.

[35] M. L. Sheely, “Glycerol viscosity tables,” *Ind Eng Chem*, vol. 24, no. 9, pp. 1060–1064, 1932, doi: 10.1021/ie50273a022.

[36] J. Yee, A. Yamanaka, and Y. Tagawa, “Image features of a splashing drop on a solid surface extracted using a feedforward neural network,” *Physics of Fluids*, vol. 34, no. 1, 2022, doi: 10.1063/5.0077050.

[37] T. Kurniawan, P.-H. Tsai, S.-S. Chen, D. H. Frakes, C.-C. Chen, and A.-B. Wang, “Practical notes toward higher quality and more reliable experiments on drop and liquid surface interactions,” *Exp Fluids*, vol. 63, pp. 1–27, 2022, doi: 10.1007/s00348-021-03346-w.

[38] E. Becker, W. J. Hiller, and T. A. Kowalewski, “Experimental and theoretical investigation of large-amplitude oscillations of liquid droplets,” *J Fluid Mech*, vol. 231, pp. 189–210, 1991.

[39] A.-B. Wang, C.-C. Kuan, and P.-H. Tsai, “Do we understand the bubble formation by a single drop impacting upon liquid surface?,” *Physics of Fluids*, vol. 25, no. 10, 2013.

[40] E. Ricci, R. Sangiorgi, and A. Passerone, “Density and surface tension of dioctylphthalate, silicone oil and their solutions,” *Surf Coat Technol*, vol. 28, no. 2, pp. 215–223, 1986.

[41] H. Chen, N. Chen, A. Mozafari, and A. Amirfazli, “Receding phase and rebound behavior for drop impact onto an ultrathin film,” *Langmuir*, vol. 37, no. 13, pp. 3849–3857, 2021, doi: 10.1021/acs.langmuir.0c03374.

[42] P. Attané, F. Girard, and V. Morin, “An energy balance approach of the dynamics of drop impact on a solid surface,” *Phys Fluids*, vol. 19, no. 1, 2007, doi: 10.1063/1.2408495.

[43] J. B. Lee, D. Derome, R. Guyer, and J. Carmeliet, “Modeling the maximum spreading of liquid droplets impacting wetting and nonwetting surfaces,” *Langmuir*, vol. 32, no. 5, pp. 1299–1308, 2016, doi: 10.1021/acs.langmuir.5b04557.

Chapter 3 Mathematical modelling approach[2]

3.1 Introduction

The study of droplet impact traces back to the pioneering work of Worthington [1], who first explored the behavior of milk and mercury droplets on smoked glass surfaces in the late 19th century. While initially pursued out of curiosity, droplet impact research has since evolved, driven by its relevance to both natural phenomena and technological applications [2], [3], [4], [5]. When a droplet impacts a solid surface, it can deposit, splash, or bounce, depending on the impact conditions. Upon impact, the droplet undergoes distinct phases: spreading, where the drop flattens to its maximum extent; relaxation, as it attempts to minimize its surface energy; and sometimes recoil, where it contracts back toward its center. These dynamics are governed by factors such as droplet velocity, density, viscosity, surface tension, surface properties, and the surrounding medium [2], [5]. A deeper understanding of the factors influencing these outcomes is essential for optimizing applications ranging from spray cooling and printing to surface coating and microfabrication [6], [7], [8].

Among the various droplet impact outcomes, accurately predicting and controlling the maximum spreading of a droplet upon impact on a solid surface is particularly critical. In applications like spray painting and cooling, greater spreading enhances surface coverage and process efficiency [6]. Conversely, in printed electronics and high-resolution inkjet printing, minimizing the spread of droplets is essential for achieving finer detail [8], [9], [10]. The

[2] *This chapter is submitted and under review as a peer-reviewed journal article under the title "Maximum spreading of a core-shell compound droplet upon impact on a solid surface: an energy-based model" in Physics of Fluids Journal.*

maximum spreading factor, β_{max}, is defined as the droplet's maximum spreading diameter (D) to its initial diameter (d). To investigate the parameters influencing β_{max}, researchers have employed a combination of experimental, numerical, and analytical methods, primarily focusing on single-component droplets [11], [12], [13], [14], [15], [16]. Growing interest has emerged towards the study of more complex, multi-component droplets. These droplets, which feature multiple phases and interfaces, are increasingly relevant in processes such as tissue engineering, fuel combustion, atomization, surface coating, pharmaceutical microencapsulation, precise droplet deposition, and 3D and inkjet printing [7], [17], [18], [19]. This trend underscores the importance of developing a thorough understanding of their impact dynamics, particularly with regard to predicting and controlling their maximum spreading.

Before exploring multi-component droplet dynamics, it is essential to establish a clear understanding of how single-component droplet behavior has been modelled and characterized. From an energy perspective, the droplet builds up kinetic energy during freefall after detaching from its source. Upon impact on a solid surface, this initial energy drives the droplet to spread radially outward, converting the total initial energy into surface energy as the liquid interface stretches into an expanding, pancake-shaped lamella. During spreading, a portion of this initial energy is dissipated due to the liquid's internal viscosity and frictional interactions with the solid surface [5], [11], [20]. Controlling the spreading of a droplet is achieved by altering the parameters that define the competing energies driving the spreading process: kinetic energy, surface energy, and viscous dissipation. Traditionally, the spreading phase in droplet impact studies is characterized using dimensionless ratios that relate these governing energies. The

Weber number ($We = \frac{\rho U^2 d}{\sigma}$) represents the ratio of kinetic energy to surface tension forces, while the Reynolds number ($Re = \frac{\rho U d}{\mu}$) compares kinetic energy to viscous dissipation. Here, ρ, U, d, σ and μ denote the droplet's density, impact velocity, diameter, surface tension, and dynamic viscosity, respectively.

Energy-based arguments are commonly employed to model the spreading of the single-component drops on a solid surface. A primary advantage of this approach compared with direct numerical simulations of the Navier–Stokes equations is its simplicity and clarity for parametric exploration, as it captures the dominant forces without requiring full resolution of the flow field. These models offer a physically intuitive framework that highlights the interplay between inertia, capillarity, and viscosity by incorporating the dimensionless energy ratios (i.e., the Weber and Reynolds numbers), enabling generalization across a range of impact conditions. To quantify the spreading behavior, this framework relies on an energy balance between inertia, surface tension, and viscous dissipation, typically written as:

$$\mathrm{K.E._1} + \mathrm{S.E._1} \rightleftharpoons \mathrm{S.E._2} + \mathrm{W_v} \qquad \textit{Equation 3-1}$$

where $\mathrm{K.E._1}$ and $\mathrm{S.E._1}$ denote the droplet's initial kinetic and surface energies, respectively (at the moment just before impact, subscript '1'); $\mathrm{S.E._2}$ is the total interfacial energy of the drop-surface system at maximum spreading (subscript '2'), and $\mathrm{W_v}$ accounts for energy dissipated primarily through viscous frictional effects during the spreading phase.

Unlike empirical spreading correlations that compress behavior into fitted exponents, an energy-balance formulation makes the governing mechanisms explicit by separating interfacial-

energy storage from phase-specific viscous losses. In this role, modelling serves as a conceptual lens for interpreting trends in $\beta_{\max}$, not only as a predictive fit.

The evolution of the predictive energy-based framework began with a foundational, albeit oversimplified, work of Jones [21]. which introduced an analytical framework assuming that the initial kinetic energy of a droplet is entirely dissipated by viscous forces during spreading. This led to a power-law scaling of the maximum spreading factor, β_{max}, with the Reynolds number, while neglecting interfacial effects between the liquid and the solid surface. Madejski later proposed a model that coupled droplet spreading dynamics with solidification effects caused by the cold substrates, incorporating variations in surface tension before impact and at maximum spreading [22]. In the absence of freezing, this model represented an improvement over Jones' approach and demonstrated greater predictive accuracy within a high Weber number range ($\mathrm{We} = 1000 - 20{,}000$) [23]. However, the influence of wettability and liquid–solid interfacial interactions remained unaccounted. Subsequent experimental studies revealed that wettability significantly affects maximum spreading, particularly at lower Weber numbers ($\mathrm{We} < 450$), where variations in the equilibrium contact angle θ_e from 30º to 140º resulted in a reduction of β_{max} by up to 40% [5], [24]. In higher inertia impacts, the effect of wettability becomes reasonably negligible, limiting the applicability of Madejski model to the range of high Weber and Reynolds numbers. Collings et al. introduced an alternative formulation that neglected viscous dissipation entirely to estimate an upper bound for spreading [25]. This model assumed full conversion of the potential energy of a pendant droplet (prior to detachment) into interfacial energy during spreading, effectively equating interfacial energy at maximum spreading (i.e.,

$S.E._2$) with the droplet's pre-impact kinetic energy. The model ignored the initial surface energy of the incoming droplet (i.e., $S.E._1$), however, it was found that it could account for more than 25% of the total interfacial energy at the maximum spreading (i.e., $S.E._2$) [24]. Thus, the maximum spreading factor in their work was ultimately expressed as a ratio of inertial forces to the resisting interfacial forces governed by the Weber number and the equilibrium contact angle θ_e.

The maximum spreading factor can be categorized based on its scaling criteria with either the Weber number, corresponding to the capillary-dominated regime, or the Reynolds number, corresponding to the viscous-dominated regime. The transition between these regimes is determined by the relative dominance of capillary and viscous effects, quantified through an impact parameter defined as $P \sim WeRe^{-4/5}$ [16], [26]. Values of $P < 1$ indicate the capillary regime (low-viscosity limit), whereas $P > 1$ corresponds to the viscous regime. Scaling the maximum spreading with both Weber and Reynolds numbers (without neglecting the effect of wettability) was found to cover a wider range of impact conditions [5], [24]. Chandra and Avedisian incorporated both, capillary and viscous effects, into an energy-based model [5]. However, the viscous dissipation term (W_v) was underestimated in their order-of-magnitude analysis, resulting in a model that was later shown to overpredict β_{max} by 20% - 40% compared with experimental data [11], [24]. This discrepancy stemmed primarily from two key assumptions. First, the characteristic length scale used to estimate the velocity gradient for viscous dissipation was taken as the droplet height at maximum spreading (h). Since most viscous losses occur in a thinner boundary layer near the solid surface, this overestimated the effective

length scale and thus underestimated the local shear rate, leading to a lower approximation of viscous dissipation. Second, the timescale for viscous dissipation was estimated by scaling the time to reach maximum spreading (t_m) with the initial droplet diameter ($t_m \sim \frac{d}{U}$). This assumption resulted in a timescale shorter than that observed experimentally, further contributing to the underestimation of the total viscous energy dissipation during the spreading process [14], [15].

Pasandideh-Fard et al. [15] built upon Chandra's model, boosting the value of the viscous dissipation term (W_v) in the energy balance equation [i.e., Equation 3-1]. Instead of using the droplet height at maximum spreading as the characteristic length scale for local shear, the model introduced the boundary layer thickness (δ), a thinner region adjacent to the substrate where viscous dissipation is most significant. This boundary layer was expressed as a function of the Reynolds number, a scaling relationship that was later supported by independent studies [12], [16]. Additionally, the time to reach maximum spreading (t_m) was reassessed based on mass conservation, using an analogy in which the liquid from the spherical bulk of the droplet flows into a disk-like lamella of thickness (h). This approach led to a revised timescale for spreading that was more than double the value estimated in Chandra's model, resulting in a significantly stretched prediction of viscous dissipation. The performance of this improved model was tested against a wide range of Weber and Reynolds numbers (i.e., $26 < \mathrm{We} < 641$ and $213 < \mathrm{Re} < 35{,}339$), resulting in an error less than 15% mostly as an underestimation of β_{max} at low Reynolds number zone [20]. Further refinement was introduced by Ukiwe and Kwok, who incorporated the lateral surface energy of the lamella into the energy balance [13]. However, this

modification resulted in only minimal improvements in predictive accuracy while notably increasing the complexity of the final expression for the maximum spreading factor.

Energy-based models often simplify the spreading droplet as a quasi-static disk lamella, a common assumption that facilitates energy estimation at maximum spreading while yielding nearly accurate predictions of spreading factors across a wide wettability range ($\theta_e < 140$) [15], [20]. The main limitation of this approach lies in the initial phase of spreading, where the droplet shape deviates significantly from a disk, typically during the first 5% to 15% of the total spreading time [20]. However, this early stage is dominated by inertial forces rather than viscous effects, making the disk approximation sufficiently valid for capturing the overall spreading behavior.

Core-shell compound droplets (see Figure 3-1) introduce an additional degree of tunability to impact dynamics due to the presence of an internal core-shell interface and the potential disparity in the physical properties of the two fluids composing the compound drop [27]. These features significantly influence the impact outcomes, such as deposition, splashing, and rebound, and, in particular, the maximum spreading diameter [28], [29], [30]. Unlike single-component droplets, which typically deposit on hydrophilic surfaces at low impact speeds, water-in-oil compound droplets have exhibited core rebound upon impact on such substrates. This distinct outcome is attributed to a self-lubricating mechanism, in which the shell's oil layer acts as a barrier that prevents direct core-substrate contact, enabling the core to spread, retract, and rebound atop the lubricating film [31]. However, at higher impact inertia or with very large cores ($\alpha > 0.8$), this oil layer destabilizes, resulting in core–substrate contact and suppression of the rebound

behavior. Splashing was found to be promoted by increasing the core size, and significantly damped by the viscosity of the shell layers rather than the core's [27].

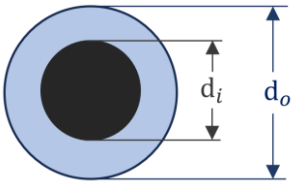

Figure 3-1 Schematic representation of a concentric core-shell compound droplet. The inner core diameter and the overall droplet diameter are denoted by d_i and d_o, respectively. Properties associated with the inner core are indicated by the subscript i, and those related to the outer shell by the subscript o.

Compound drops not only exhibit distinct impact outcomes in terms of deposition, rebound and splashing, but also, they attain altered maximum spreading values compared to single-component drops [29], [30], [32]. During the spreading phase, both the core and shell liquids deform upon impact and spread on the solid surface until their respective lamellae reach maximum expansion. For small cores ($\alpha \leq 0.4$), the time required for each layer to reach its maximum (denoted as t_{mi} for the core and t_{mo} for the shell) varies based on the initial impact conditions, such as velocity, fluid properties and most notably, the core size [33]. The latter is characterized by the core-to-total volume ratio $\alpha = \left(\frac{d_i}{d_o}\right)^3$, where the subscripts i and o refers to the inner (core) and outer (shell) layers, respectively. As the core size increases, the core deforms into a lamella that merges with the advancing rim of the shell layer, significantly altering the maximum spreading behavior [27], [29], [33], [34]. To effectively represent the dynamics of core-shell droplets, previous studies have introduced equivalent forms of the Weber and Reynolds numbers that account for the core-shell interfacial contribution (i.e., σ_{io}) and the distinct viscosities of each layer (see Equation 3-2 and Equation 3-3 below) [27], [32].

$$\overline{We} = \frac{[(\rho_i - \rho_o)\alpha + \rho_o]U^2 d_o}{\sigma_o + \sigma_{io}\alpha^{\frac{2}{3}}}, \qquad \text{For } 0 \leq \alpha < 1 \qquad \textit{Equation 3-2}$$

$$\overline{Re} = \frac{[(\rho_i - \rho_o)\alpha + \rho_o]U d_o}{\alpha\mu_i + (1-\alpha)\mu_o}, \qquad \text{For } 0 \leq \alpha \leq 1 \qquad \textit{Equation 3-3}$$

Numerical simulations of core-shell compound droplets have illuminated the significant role of core size and interfacial properties in determining the maximum spreading factor [29]. The larger the core size, the less the spreading factor β_{max}. The core and shell liquids were assumed to have similar densities and viscosities, thus, the limited spreading was primarily due to the increased internal interfacial resistance. Interestingly, another experimental study examining the ejection velocity of the lamella found that variations in core viscosity had minimal impact on maximum spreading, pointing to the dominance of other factors like shell viscosity and core size [33], [34]. This conclusion has been extended experimentally on only a single core size (0.575) demonstrated that changes in core viscosity alone do not significantly influence the maximum spreading [35]. However, once varying the core size of low viscosity cores, an increase in the maximum spreading factor was observed, which is attributed to the overall reduced viscosity of the compound droplet [36]. A recent comprehensive parametric study underscores the dominance of both core size and the overall viscosity, particularly for the range of core sizes exceeding 0.4, on the maximum spreading [27]. The viscosity of the shell has a more pronounced effect on the maximum spreading than core viscosity.

It should be noted that spreading for compound droplets has two distinct modes, i.e., (i) the droplet may spread (both core and shell) as we understand for single liquid droplets impact; in this case the core wets the substrate (unless at extremely low We); and (ii) while the shell spreads "normally" the core initially spreads over the shell, while encapsulated, and then can retract over the shell liquid and exhibit either a jetting or a partial rebound (due to lubricating effect of shell liquid as described above). In this case the core liquid does not contact and wet the substrate; this is the most observed behavior over a wide range of We were splashing is absent. Here, jetting refers to cases where the core retracts over the lubricating shell layer and forms a central upward jet. Partial rebound refers to cases where this upward jet breaks, leading to the formation of one or more secondary droplets.

Despite the various attempts to understand the underlying physics of the spreading of core-shell compound droplets, the literature still lacks a predictive scheme for the maximum spreading factor that remains valid across broad ranges of Weber and Reynolds numbers and core sizes. The present study builds on established energy-based models for single-component droplet impact and extends the same framework to core-shell systems. It is grounded in our previously reported experimental observations [27] while expanding the explored parameter space to further test and generalize the predictive capability and mechanistic interpretation of $\beta_{\max}$ under varying impact conditions. The scope of the model is restricted to the parameter range in which the spreading behavior described in mode (ii) above is observed, with cases involving splashing excluded.

3.2 Modelling method and validation domain

In the present energy-based modeling, the analysis is confined to impact scenarios in which the compound droplet remains intact throughout the spreading phase, i.e., the core remains fully encapsulated by the shell up to β_{max}. This means during spreading phase of the shell, the core can spread with the shell. However, once the shell spreading has been arrested, the core can retract and show jetting or partial rebound. Such behavior is seen for droplets with core size ratios $\alpha \leq 0.8$ [27], [31], where the core does not contact the substrate, and for equivalent Weber numbers below the prompt-splashing threshold (~100–260). The lower bound of this range is particularly relevant for droplets with larger cores and/or shells of lower viscosity, conditions under which spreading dynamics become more susceptible to destabilization. Our observations show that the $\alpha \leq 0.8$ limit can be extended to core sizes as large as 0.9, for higher-viscosity shells (e.g., 50 cSt and 100 cSt); as such, the model developed here can still be applicable.

To preserve the stability of compound droplets under gravitational field, the density ratio between the core and the shell liquids should be close to unity ($\frac{\rho_i}{\rho_o} \approx 1$). This condition justifies neglecting any buoyancy-driven motion during both, the short droplet freefall time, and the subsequent spreading phase considered in the modelling. To maintain the integrity of the core-shell configuration, a favorable thermodynamic state, characterized by minimal interfacial energy, must be met. This stability criterion is evaluated in terms of the energetic spreading factors (S), which indicate whether a particular phase tends to spread (positive value) or retract (negative value). Spreading factor is defined based on interfacial tensions among the core (inner,

subscript i), shell (outer, subscript o), and surrounding medium (subscript ∞), as given by Equation 3-4:

$$S_j = \sigma_{jk} - (\sigma_{ij} + \sigma_{ik}), \quad where\ i \neq j \neq k = i, o, \infty \qquad \textit{Equation 3-4}$$

For thermodynamic stability of the core-shell configuration, the spreading factor of the shell phase must be positive ($S_o > 0$), whereas the spreading factors of the core and surrounding medium must both be negative ($S_i, S_\infty < 0$) [19].

Once the above criteria is met, the compound droplet is modelled as an axisymmetric core-shell configuration of an inner core continuously encapsulated by an outer liquid shell. Prior to impact (i.e., state 1 in Figure 3-2), the compound droplet comprises two concentric spherical layers characterized by their respective diameters: d_i for the inner core, and d_o for the outer shell and the overall droplet. The assumption of concentricity oversimplifies real scenarios, where the core position may vary vertically depending on the droplet generation method, such as coaxial needle injection (core at the top) or side injection of the core into a pendant shell droplet (core near the bottom) [31]. Such vertical deviations can significantly influence the model's validity, as lower core positions increase the risk of early core-substrate contact at lower Weber numbers, thus restricting the applicable parameter range.

Upon impact with a flat solid substrate, the droplet spreads radially until reaching a maximum extent, adopting a quasi-static, disk-like shape, see Figure 3-2. At maximum spreading (i.e., state 2 in Figure 3-2), the droplet geometry is represented by two concentric disks defined by outer and inner diameters D_o and D_i, respectively, and the corresponding layer thicknesses: h_o for the

shell, and h_i for the core. This disk approximation was shown to reliably estimate the energy at maximum spreading for single-component droplets over a broad range of substrate wettability and impact conditions [20].

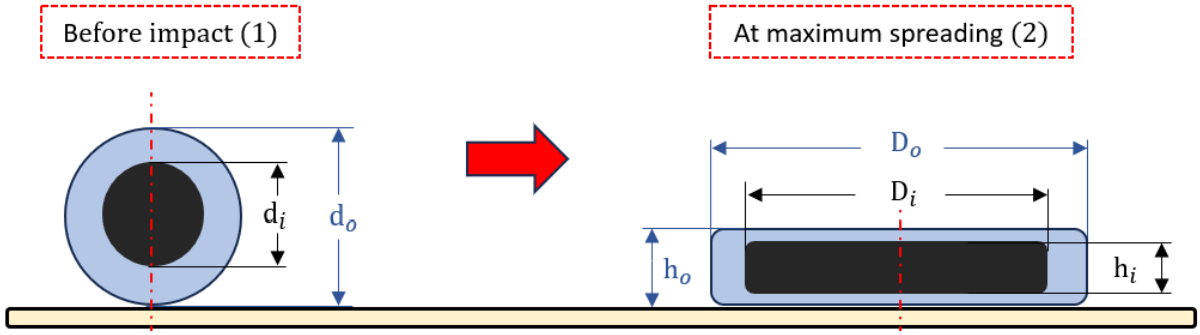

Figure 3-2 Schematic illustration of a compound droplet impact, showing the droplet immediately before impact (state 1) and at its maximum spreading extent (state 2).

Volume conservation is maintained throughout the impact and spreading process, ensuring that the total volume of the compound droplet, as well as the individual volumes of the core and shell phases, remain constant between the initial and maximum spreading states. This condition supports a consistent definition of the core volume fraction α, which links the pre-impact spherical geometry to the post-impact disk configuration.

The equilibrium relations $\alpha = \left(\frac{d_i}{d_o}\right)^3 = \frac{{D_i}^2 h_i}{{D_o}^2 h_o}$ serve as a key constraint in the model, enabling the use of equivalent geometric parameters across different stages.

Although the compound droplet is represented here as a concentric axisymmetric configuration, exact concentricity is not expected in freely falling experiments and was not treated as a standalone control parameter in the present study. In practice, slight vertical migration

of the core within the shell may occur before impact, particularly for coaxially generated droplets. For the present energy-based model, however, the key requirement is not perfect concentricity, but that the core remains fully encapsulated and that the shell continues to act as the lamella-forming phase up to maximum spreading. Under those conditions, moderate vertical offset is expected to influence the impact primarily by altering the local shell thickness beneath the core, and therefore the likelihood of premature shell rupture or early core-substrate contact, rather than the first-order shell-controlled radial spreading that determines $\beta_{\max}$. This interpretation is supported by the work of Blanken et al. [31], who altered the internal core position through the droplet-generation method and showed that, for $\alpha = 0.3$, the threshold for core-substrate contact shifted substantially while the rebounded volume remained of comparable magnitude in the rebound regime. In the present work, sensitivity to this effect was assessed in a practical sense through repeatability of nominally identical impacts under the same coaxial generation protocol, together with preliminary side-injection tests at $\alpha = 0.3$. These checks showed that the measured $\beta_{\max}$ remained within the same repeatability range reported for the study, i.e., below 3.5%, indicating no measurable first-order change in spreading under encapsulated conditions. Accordingly, vertical asymmetry is interpreted here as primarily modifying the stability of the lubricating shell layer beneath the core, whereas the dominant spreading–retraction mechanism remains governed by the shell as long as encapsulation is preserved. The concentric representation adopted here should therefore be interpreted as a reduced-order idealization valid for encapsulated, shell-dominated spreading up to $\beta_{\max}$.

Marangoni stresses can arise in immiscible systems if significant surface/interfacial-tension gradients exist (e.g., thermal gradients or trace surfactants). The present experiments were performed under nominally isothermal conditions without added surfactants; consequently, Marangoni-driven flows are expected to be secondary relative to inertial, capillary, and viscous effects for $\beta_{\max}$ in the studied range, and are not modeled explicitly.

3.3 Experimental methods and materials

To support the applicability of the modelling estimations, a validation scheme is being developed based on experimental data obtained from a wide range of compound droplet impact conditions. The core and shell liquids were selected to be immiscible, ensuring phase separation and meeting the stability condition. Core viscosity was varied using water and water-glycerol mixtures, while silicone oils of different viscosities were used to modify the shell properties. The tested fluids and their measured properties at 20 °C are summarized in Table 3-1. Viscosities were measured using a parallel-plate rheometer and verified against reference data from the literature [37], [38]. Interfacial tensions were determined using the pendant drop method, with the core-shell interface consistently measured at approximately 40 mN/m. Food-grade water-based dye was added to the core phase to enhance optical contrast during visualization. The error associated with maximum spreading factor measurements was less than 3.5%.

The experimental setup and compound droplet generation technique, including coaxial needle injection and drop release, are detailed in our previous work (Alkomy et al. [27], see Fig. 2 therein). The equivalent Weber number, accounting for the core-shell configuration, was set by adjusting the release height of the coaxial system and was explored across a range restricted to

intact-encapsulation up to β_{max}, i.e., below the prompt-splashing threshold and without core-substrate contact (around needle-to-surface drop-release heights less than 90-200 mm).

Table 3-1 Physical properties of the core and shell liquids used in the experiments. All values were measured at 20°C.

	Liquids tested	**Abbreviation**	**Density** (g/ml)	**Viscosity** (mPa.s)	**Interfacial tension** (mN/m)
Core	Water	W	1	1.005	72
Core	60%GLY/water	WG60	1.15	16	68.44
Core	70%GLY/water	WG70	1.18	22.5	67.8
Shell	Silicone oil (5 cSt)	S5	0.913	4.565	19.7
Shell	Silicone oil (10 cSt)	S10	0.935	9.35	20.1
Shell	Silicone oil (20 cSt)	S20	0.95	19	20.6
Shell	Silicone oil (50 cSt)	S50	0.96	48	20.8
Shell	Silicone oil (100 cSt)	S100	0.96	96	20.9

Core-shell liquid combinations were varied starting from a reference case of water encapsulated in 5 cSt silicone oil (denoted as W/S5), representing the lowest viscosities for both phases. Subsequently, the water core (W) was tested with all available shell viscosities, while 5 cSt silicone oil (S5) was used as the shell for all water-glycerol core mixtures. Each liquid combination was tested across full range of core size ratios (i.e., α ranged from 0.15 to 0.9), and the equivalent Weber number was varied from 10 to 260 by adjusting the height of the coaxial needle between 2 and 20 cm. The measured β_{max} values will be used to calibrate and assess model predictability and define zones of accuracy within the intact-encapsulation outcomes (e.g., jetting and partial rebound).

3.4 Energy balance

To apply the energy balance (i.e., Equation 3-1) in estimating the maximum spreading factor, the relevant energy components governing the spreading process must be quantified. The analysis is bounded between two states: the initial condition prior to impact (i.e., state 1 in Figure 3-2), associated with initial energy E_1, and state 2 at the moment of maximum spreading (i.e., state 2 in Figure 3-2), associated with energy E_2. The E_1 is composed of kinetic and interfacial components, based on geometrical, material, and kinematic properties of the compound droplet, and can be determined with high confidence. During the spreading phase, this initial energy is gradually transformed into surface energy and dissipated through viscous mechanisms within both the core and shell phases. The evaluation of E_2, composed of interfacial and dissipation components, involves geometrical simplifications and internal flow idealization. The maximum spreading factor, denoted as β_{max}, results from the energy transformation and dissipation during spreading. To bridge the gap between idealized modelling and real behavior, empirical tuning coefficients are introduced within the evaluation of interfacial and dissipation terms to improve agreement with the observed dynamics, as will be described below.

3.4.1 Initial energy before impact (E_1)

The total mass of the compound droplet m_c, accounting for both phases, is given by:

$$m_c = \frac{\pi}{6} d_o^3 [(\rho_i - \rho_o)\alpha + \rho_o] \qquad \textit{Equation 3-5}$$

The kinetic energy before impact is expressed as:

$$K.E._1 = \frac{1}{2} m_c U^2 = \frac{\pi}{12} d_o^3 U^2 [(\rho_i - \rho_o)\alpha + \rho_o] \qquad \textit{Equation 3-6}$$

The interfacial energy in the pre-impact spherical configuration accounts for the outer shell-air interface and the core-shell interface that is a function of the core surface area:

$$S.E._1 = \pi d_o^2 [\sigma_o + \alpha^{2/3} \sigma_{io}] \qquad \textit{Equation 3-7}$$

Here, the term $\alpha^{2/3}$ accounts for the surface area ratio between the core and the overall droplet based on volume fraction. The total initial energy is then defined as; $E_1 = K.E._1 + S.E._1$, and it is used for non-dimensionalizing energy terms during analysis.

3.4.2 Energy at the maximum spreading (E_2)

At the maximum spreading, the compound droplet enters a quasi-static state in which radial expansion temporarily ceases. The droplet is assumed to adopt a simplified axisymmetric geometry consisting of two concentric disks. In this configuration, the shell-air interface (i.e., the top interface) and the core-shell interface (i.e., the internal interface) are stretched, while the base of the shell wets the solid substrate. The lateral surface area of the idealized disk-shaped lamella is neglected, since the lamella is very thin at maximum spreading and this contribution is small relative to the disk faces.

To account for the interaction between the shell and the solid surface, the Young equation is used:

$$\sigma_s - \sigma_{os} = \sigma_o \cos \theta_e \qquad \textit{Equation 3-8}$$

where σ_s is the solid–air surface energy, and σ_{os} is the shell–solid interfacial energy. The total geometrically simplified interfacial energy at maximum spreading is then estimated by:

$$S.E._2 = \frac{\pi}{4} D_o{}^2 [\sigma_o(1 - \cos\theta) + 2\alpha C_h \sigma_{io}] \qquad \textit{Equation 3-9}$$

where (C_h) is a ratio of outer to inner lamella thicknesses that is more than unity, and constrained by the volume conservation of the compound droplet between states 1 and 2.

The total viscous dissipation (W_v) during the spreading phase of the compound droplet is considered as the combined contribution of the core (W_i) and shell (W_o) layers, expressed as $W_v = W_i + W_o$. The general form of the viscous dissipation energy W is given by:

$$W = \int_0^{t_m} \int_\Omega \emptyset \cdot d\Omega \cdot dt \qquad \textit{Equation 3-10}$$

This double integral quantifies the total energy loss due to viscous effects, integrated over the effective droplet volume Ω where dissipation predominantly occurs, and over a characteristic timescale (t_m) up to maximum spreading. The dissipation function ∅ is treated as an effective (volume-averaged) dissipation rate over the dominant dissipation region and over the spreading timescale, to obtain a closed-form estimate; this does not imply that dissipation is physically uniform, which is known to be strong near the wall/contact-line shear region. This implies that velocity gradients and deformation rates remain sufficiently consistent within this effective volume, allowing the integral to be approximated by the product:

$$W \approx \emptyset\, \Omega\, t_m \qquad \textit{Equation 3-11}$$

This approximation avoids the need to resolve complex spatial and temporal evolution of the flow while retaining the primary features governing viscous dissipation during spreading [14], [15], [39]. The dissipation function $\emptyset$ for a Newtonian fluid is defined as [5]:

$$\emptyset = \mu\left(\frac{\partial v_i}{\partial x_j} + \frac{\partial v_j}{\partial x_i}\right)^2 \approx \mu\left(\frac{U}{L}\right)^2 \qquad \textit{Equation 3-12}$$

Here, the $v_{i,j}$ and $x_{i,j}$ denote velocity components and spatial directions, respectively, with i and j corresponding to the radial and vertical directions of the axisymmetric spreading drop. The full tensor expression accounts for deformation contributions from all components and directions of the flow field. However, during droplet spreading on a solid surface, the flow is predominantly radial, and the largest shear develops vertically, within the thin shell-side lamella adjacent to the substrate. Any additional shear at the core-shell interface is accounted for implicitly by scaling into a lumped, later-calibrated dissipation terms (Equation 3-13). Accordingly, the velocity gradient is scaled by $\partial u/\partial y \sim U/L$, where U is the characteristic radial velocity (scaled by the impact velocity), and L is an effective vertical length scale representing the dissipation region.

The timescale t_m used in this viscous dissipation approximation represents the duration of the spreading phase up to maximum deformation. While earlier studies commonly scaled t_m using the initial droplet diameter and impact velocity, i.e., $t_m \sim d/U$,[5], [15] subsequent experimental investigations have shown that fitting the scaling based on the maximum spreading diameter (i.e., D) provides better agreement, particularly when comparing various liquids within similar ranges of impact velocities and viscosities tested here.[11], [14], [39] Therefore, the spreading timescales for the inner and outer liquid layers are scaled using $t_{mi} \sim D_i/U$ and $t_{mo} \sim D_o/U$,

respectively. The effective dissipation volumes for each phase are estimated as: ($\sim \frac{\pi}{4} D_i{}^2 L_i$) for the core and ($\sim \frac{\pi}{4} D_o{}^2 L_{o.eff}$) for the shell, where $L_{o.eff}$ accounts for the region in the shell where dissipation dominates, excluding the core. This consistent scaling of both time and volume ensures that the estimated dissipation energy for each layer reflects the geometry and flow conditions relevant to the spreading dynamics of the compound droplet.

Then, total dissipation within the core and shell layers is further constrained by volume conservation and can be expressed as:

$$W_v \approx \frac{\pi}{8} U D_o{}^2 \left(\alpha C_h \mu_i \frac{D_i}{L_i} + \mu_o \frac{D_o}{L_{o,eff}} \right) \qquad \textit{Equation 3-13}$$

The ratios (D/L) appearing in the dissipation formulation represent the degree of flattening of each phase during impact, i.e., the maximum lateral deformation normalized by the thickness of the effective dissipation layer for each phase. For single-component droplets spreading on smooth solids, this lamella thinning has been empirically correlated with the Reynolds number through power-law relations, which provide a practical closure for the otherwise unknown effective film thickness at maximum spread [16], [40]. Although these correlations were established for single-component droplets, the underlying energetic structure, capillary/interfacial energy changes balanced against viscous dissipation during inertial deformation, remains general. The key extension for a core-shell droplet is therefore not the energy argument itself, but the partitioning of viscous losses between the core and shell and the use of phase-appropriate dissipation volumes and effective thicknesses consistent with the compound-drop geometry.

Accordingly, we relate the flattening ratios for the core and shell to phase Reynolds numbers using power-law closures:

$$\frac{D_i}{L_i} \sim X_n \, Re_i^{\,n}, \qquad \frac{D_o}{L_{o,eff}} \sim X_m \, Re_o^{\,m} \qquad \textit{Equation 3-14}$$

Here, X_n, n, X_m, and m are fitting coefficients to be determined from the experimental dataset, reflecting how inertia-viscosity competition governs the effective thinning in each layer. The Reynolds numbers Re_i and Re_o are defined using pre-impact characteristic lengths (rather than D) so that they remain independent control parameters; D_i and D_o enter separately through the dissipation geometry and timescale at maximum spread.

In the dissipation closure, the Reynolds number appears through the lamella-thinning (i.e., flattening) scalings (Eq. 3-14) and should therefore be defined using the length scale of the dominant shear layer for each phase. A single modified/apparent Reynolds number based on the overall drop diameter would mix wall-bounded shell dissipation with bulk core deformation and can overestimate shell-side inertia especially when the shell volume is small (i.e., large α). Accordingly, the model retains separate phase Reynolds numbers, Re_i and Re_o, defined using the core diameter and an effective shell diameter derived from volume conservation, this provides the intended geometric correction without collapsing phase-separated dissipation pathways into a regime-dependent effective-property Reynolds number.

The Reynolds numbers Re_i and Re_o are defined based on the fluid properties and effective characteristic lengths of the respective phases as follows:

$$Re_i = \frac{\rho_i U d_i}{\mu_i}, \qquad Re_o = \frac{\rho_o U d_{o,eff}}{\mu_o} \qquad \textit{Equation 3-15}$$

In Eq. (3-15), the shell Reynolds number is formed using an effective shell diameter to ensure the Reynolds scaling reflects the liquid that actually feeds the wall-bounded lamella. This choice prevents the core mass from being implicitly included in the shell-controlled lamella dissipation, while the total pre-impact inertia remains accounted for in the global energy balance. Consequently, the Reynolds dependence in the lamella-thinning (flattening) scaling (Eq. 3-14) is phase-consistent and the fitted dissipation coefficients retain a clear physical interpretation.

For self-consistency, the characteristic length scale for the core and shell layers are adjusted using volume conservation, giving $d_i = d_o \alpha^{1/3}$ and $d_{o,eff} = d_o \sqrt[3]{(1-\alpha)}$. This framework enables phase-wise scaling of deformation using $Re_i$and Re_o and, in turn, links each phase to its corresponding viscous dissipation contribution. Here L_i and $L_{o,\text{eff}}$ are effective dissipation length scales (not uniquely measurable geometric thicknesses), particularly for the internal phase where the interface is optically inaccessible during rapid deformation. Therefore, the dissipation model is closed using Reynolds-based lamella-thinning correlations, which link the flattening ratio D/L to pre-impact control parameters in a compact and transferable form.

3.4.3 Empirical model coefficients

Considering Equation 3-1, a closed-form expression for the maximum spreading factor $\beta_{\max}$ can be obtained as below by combining Equation 3-14 and Equation 3-15 into Equation 3-13, which is then substituted into Equation 3-1 together with Equation 3-6, Equation 3-7, and

Equation 3-9. For compound droplets, the viscous-work term W_v in Equation 3-1 is replaced by W_v.

$$\beta_{max} = \sqrt{\frac{(\overline{We} + 12)[\sigma_o + \alpha^{2/3}\sigma_{io}]}{3[\sigma_o(1 - \cos\theta_e) + 2\alpha C_h\sigma_{io}] + \frac{3}{2}U(\alpha C_h\mu_i X_n\, Re_i{}^n + \mu_o X_m\, Re_o{}^m)}} \qquad \textit{Equation 3-16}$$

Five empirical fitting coefficients are therefore introduced: four coefficients (X_n, n, X_m, m) to describe the power-law scaling of the flattening ratio for the viscous dissipation estimations discussed above, while the fifth coefficient (C_h) represents the relative thickness ratio between the shell and core lamellae.

These coefficients were obtained through a constrained nonlinear optimization procedure that simultaneously minimized the sum of squared residuals between the predicted and experimentally measured values of β_{max}, while ensuring consistency with the principle of energy conservation. Specifically, the average normalized energy mismatch was constrained to remain below 0.1% across all cases. Full definitions of the residual and energy metrics, as well as the optimization workflow, are provided in Supplementary Appendix B. The corresponding calibration parity plot is shown in Supplementary Section Appendix B, i.e., Fig. SI 3-2, indicating close agreement between model predictions and the calibration data ($R^2 = 0.91$).

The optimization procedure on calibration data (over 100 data points spanning across the whole range of impact parameters tested) yielded the best-fit values of $(C_h, X_n, n, X_m, m) = (1.96, 0.5, 0.2, 1.17, 0.57)$. The relatively low exponent ($n = 0.2$) associated with the core-

phase Reynolds number indicates a limited contribution of core viscosity to the overall dissipation. This result is consistent with experimental observations, where variations in shell viscosity had a more pronounced influence on the maximum spreading behavior, confirming the dominant role of shell-phase dissipation during impact [27]. The next section presents the performance of this model for unseen data.

3.5 Results and Discussion

The predictive performance of the calibrated energy-based model (i.e., Equation 3-16) for β_{max} is evaluated against over 300 unseen data of compound droplet impact experiments, covering a wide range of Weber numbers, core sizes, and fluid viscosities. Model accuracy is assessed using R^2 and RMSE metrics (for model accuracy metrics definitions, see Appendix B, section 5.6.1), while residual analysis highlights prediction trends across different impact regimes. The influence of key parameters, such as inertia, core size, and shell viscosity, on spreading dynamics is then examined. Finally, energy partitioning is analyzed to reveal the dominant mechanisms controlling compound droplet deformation.

3.5.1 Model validation

On the previously unseen test set ($N = 314$), the model reproduces the measured maximum spreading with $R^2 = 0.910$ and RMSE $= 0.119$ (dimensionless β_{max}). As shown in Figure 3-3, predictions cluster tightly around the 1:1 line with no discernible bias, with a maximum error of ±13%. The normalized energy mismatch between pre- and post-impact states remains negligible on average, consistent with the energy-balance formulation. Definitions of all accuracy and

energy metrics are provided in the Appendix B, section 5.6.1 and section 5.6.2. The complete residual distribution for the test set (histogram with normal-fit overlay) is shown in Fig. SI 3-3.

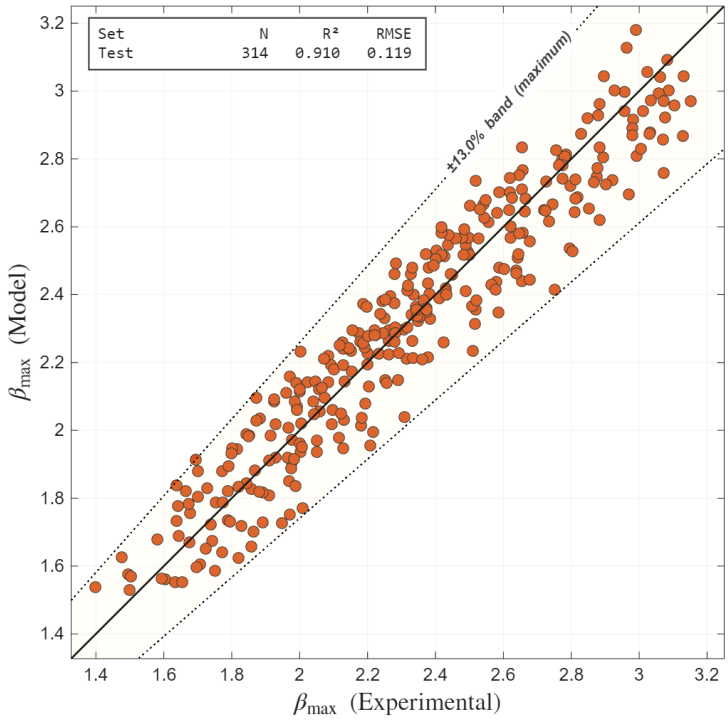

Figure 3-3 Comparison between experimentally measured and model-predicted maximum spreading factors for compound droplets on the unseen test set ($\overline{We}$=10-260, Re_i=38-3637, Re_o =16-720; across all core sizes α). The solid line marks the ideal 1:1 agreement, and the dotted lines indicate the maximum error band (±13%).

Recall that earlier in the Introduction section two modes were indicated for compound droplet spreading; in mode 2 that is the focus of this work and often seen, one can also observe retracting of the core in latter stages of the shell spreading. The retracting can manifest itself as Jetting (core retracts atop the lubricating shell film and ejects a vertical jet) or Partial Rebound (at higher inertia and/or larger cores, the jet carries enough momentum to detach into one or more droplets).

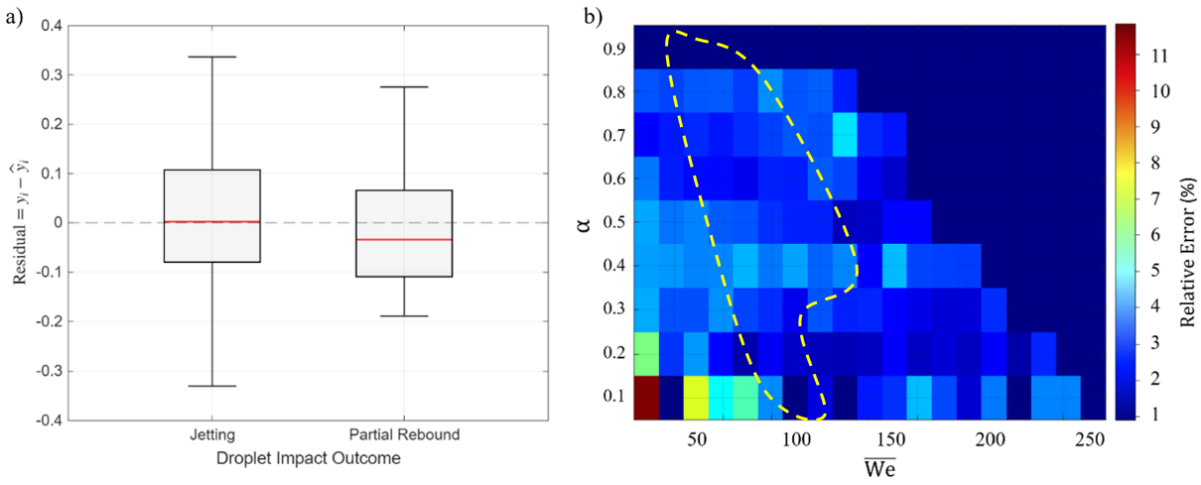

Figure 3-4 Model prediction error across droplet impact outcomes and initial parameters; (a) is a boxplot of residuals grouped by impact outcome, and (b) is a heatmap of relative error over equivalent Weber number and core size, with the yellow contour marking the observed jetting-rebound transition region across liquid combinations.

To evaluate the model's predictive reliability, residuals (measured − predicted β_{max}) were evaluated for the two outcome classes (jetting and partial rebound). As shown in Figure 3-4a, both classes are centered near zero with comparable dispersion; the Partial Rebound distribution exhibits a slightly narrower interquartile range, consistent with more predictable behavior at stronger inertia. To further investigate the residuals in terms of the parameter space of equivalent Weber number and core size is illustrated, the relative error heat map (in Figure 3-4b) is generated. The relative error is calculated per each case as follows:

$$(\text{Relative error})_j = \left|\frac{y_j - \hat{y}_j}{y_j}\right| \qquad \textit{Equation 3-17}$$

Figure 3-4b reveals that the majority of the parametric domain exhibits low prediction errors (blue regions), confirming the model's robustness to identify the class of spreading behavior in mode 2. However, a clear zone of elevated error is observed at very low core fractions ($\alpha \approx 0.1$)

and low Weber numbers, where the relative error could occasionally exceed 10%. This localized spike in error highlights a limitation in the energy-based model. The cause of this discrepancy stems from the modeling assumption used in estimating viscous dissipation in the core phase. In the order-of-magnitude derivation, the core was assumed to deform during spreading due to its own inertia, resisted by its internal viscosity. However, in experiments, compound droplets are generated using coaxial needles, which result in a vertically offset core located near the top of the droplet. As supported by experimental observations (see Figure 3-5**)**, in cases with small cores and viscous oil shells (e.g., water in silicone oil '20 cSt'), the core remains largely undeformed during impact, as the oil layer cushions it from significant motion or shear. Therefore, the model overestimates the core's contribution to dissipation in this regime, leading to higher prediction errors, predominantly in jetting cases, consistent with the broader whiskers of the jetting residuals in Figure 3-4a.

Notably, this high-error region at ($\alpha \approx 0.1$) and low Weber number in Figure 3-4b represents only a small fraction (<1%) of the entire mapped domain, indicating that the limitation is localized and not indicative of a systemic model weakness. Outside this narrow regime, the model maintains high fidelity, even in the transitional zones between jetting and rebound outcomes, outlined by the dashed yellow contour in Figure 3-4b.

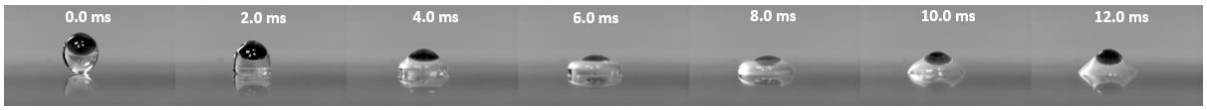

Figure 3-5 Time sequence of a W/S20 compound droplet with core size ratio α≈0.1 impacting at $\overline{We} \approx 17$*, showing minimal core deformation throughout the spreading process.*

3.5.2 Spreading dependency on impact parameters

After calibration and validation as explained above, the developed model (Equation 3-16) is used to generate spreading outcomes over a wide parameter space. The idea is to provide a physics-based analysis to study the effect of governing parameters to assess the influence of inertia, core size/interfacial energy, and viscous dissipation on the droplet impact dynamics and the β_{max}.

Figure 3-6 presents β_{max} as a function of the core volume ratio α, arranged into panels by shell viscosity from low to high (top to bottom panels). Within each panel, marker color and size encode the equivalent Weber number $\overline{We}$. As expected from inertial-capillary scaling, spreading consistently increases with Weber number, reflecting the greater radial deformation enabled by higher initial inertial energy. Across the full range of impact conditions, this trend remains consistent, confirming the model's ability to replicate the scaling between $\overline{We}$ and droplet spreading.

Core size exerts a clear and systematic influence on spreading. At fixed shell viscosity and comparable equivalent Weber number (points of similar size and color), β_{max} declines as the core volume fraction, α, increases. The decay is strongest in the least viscous shells (i.e., S5 - S20, Figure 3-6a, b and c), where small cores ($\alpha \approx 0.1$) form the upper envelope of β_{max}, while large cores ($\alpha \approx 0.9$) populate the lower range. Importantly, once the core becomes large ($\alpha \geq 0.7$), the ordering by $\overline{We}$ increasingly governs the spreading: although absolute values of β_{max} are reduced, increments in $\overline{We}$ still produce clear gains in spreading and data points separate

primarily by $\overline{We}$ rather than by α. The drop across each panel is about 20 to 30% in the lowest-viscosity cases and contracts with increasing shell viscosity to only a few percent in the most viscous set (i.e., S50 and S100, Figure 3-6d and e). This behavior can be understood from Equation 3-16: enlarging the core raises the interfacial work associated with the core–shell area (i.e., Equation 3-9) and confines the shell to a thinner, more restricted lamella, so a smaller fraction of the initial kinetic energy converts into radial deformation before capillarity and viscous losses arrest the spread. As viscosity increases, dissipation within the shell becomes the primary limitation, which suppresses the sensitivity to α and leaves inertia, expressed through $\overline{We}$, as the dominant control on the variation of β_{max}.

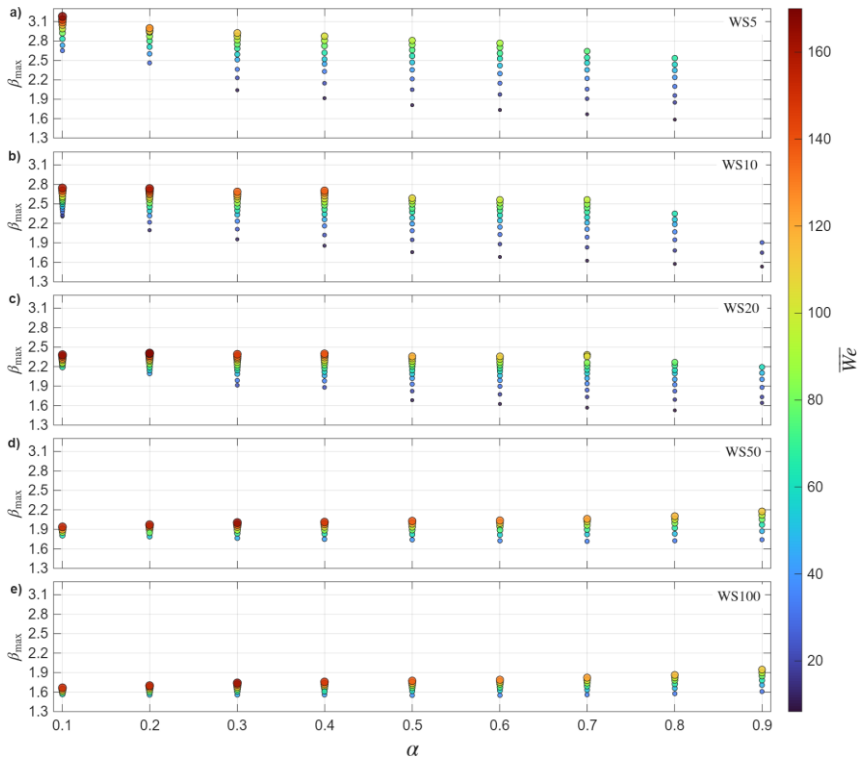

Figure 3-6 Model predictions (Equation 3-16) of maximum spreading, βmax, versus core volume ratio, α, for five shell viscosities (S5-S100, corresponding to a-b panels). Markers color and size reflect the Weber number $\overline{We}$.

Figure 3-7 quantifies the influence of wettability on maximum spreading. Wettability is varied through the shell–solid equilibrium contact angle θ over 5–150°, with cases pooled across the validated ranges of $\overline{\mathrm{We}}$ and α. At each θ, the box-and-whisker distributions aggregate variability arising from $\overline{\mathrm{We}}$ and α, while the overlaid medians trace the central trend. The normalized response $\beta_{\max}(\theta)/\beta_{\max}(5°)$ decreases monotonically with θ for all viscosity sets, indicating that increasing hydrophobicity reduces spreading (note that depending on the shell liquid and substrate not all contact angle values can be practical; this is meant to show the theoretical influence for θ). The rate of this decline depends on shell viscosity: the slope is steeper for lower-viscosity shells and becomes progressively shallower as viscosity increases. The spread of the distributions also grows with θ, most prominently at low viscosity, consistent with the increasing contribution of the contact-angle work term and its coupling with inertia and core size. In magnitude, the median reduction in wettability (i.e., shell-solid contact angle) from $5°$ to $150°$ is up to about 10% for the lowest-viscosity shell (S5) and only a few percent, roughly 3%, for the highest-viscosity shell (S100), giving a diminishing role to the wettability.

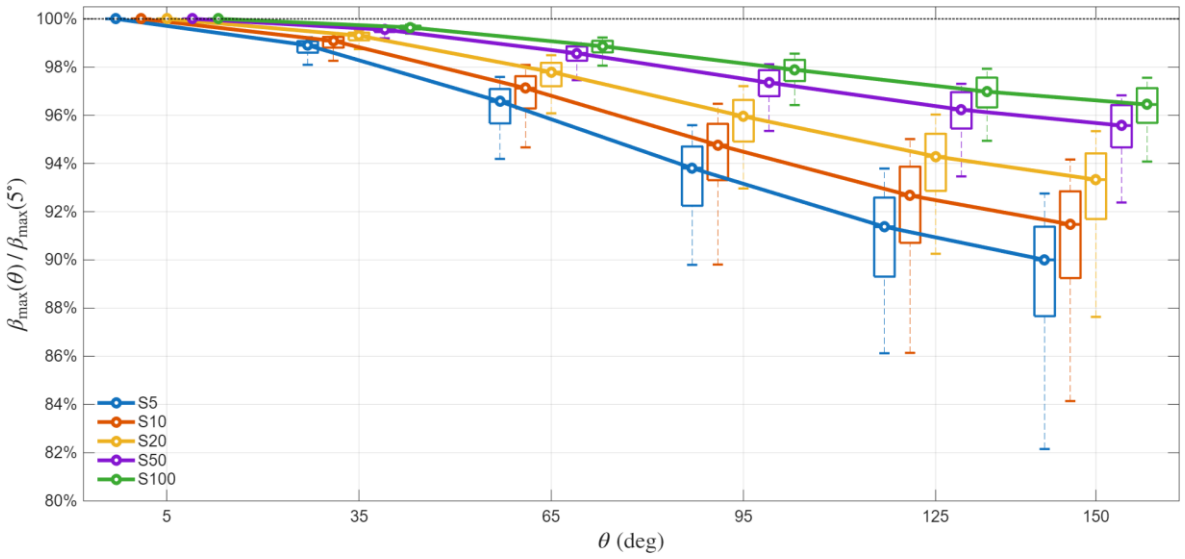

Figure 3-7 Normalized spreading βmax (θ)/βmax (5°) versus contact angle θ for viscosity sets S5–S100; lines with circular markers denote medians, and box-and-whisker symbols show distributions at each θ; legend colors identify S5–S100. A higher normalized value indicates weaker sensitivity of β_{max} to wettability (smaller reduction relative to the 5° baseline), not larger absolute spreading.

The above plots generated using the developed model, i.e., Equation 3-16, underscore that high impact inertia promotes greater spreading, but the effect is attenuated by either a large core, or greater surface hydrophobicity, or highly viscous shell. A large core limits shell deformation (a feature unique to compound drop impact, distinct from single-component drop impact where only kinetics and fluid property play a role). High hydrophobicity (larger shell-solid equilibrium contact angle, θ) similar to simple drop impact can reduce spreading due to capillary mechanizes in action. Finally, a highly viscous shell, dissipates energy before significant spreading can occur. These insights are consistent with experimental findings and affirm the physical fidelity of the model across a broad range of compound droplet configurations not examined to date.

3.5.3 Energy analysis for spreading factor

The energy-based modeling framework not only enables accurate prediction of the maximum spreading factor, but also provides detailed insight into how the initial energy E_1 is distributed among the governing mechanisms during droplet impact. All energy quantities reported here are model-derived and computed from the governing expressions: initial kinetic energy $K.E._1$ (Equation 3-6), initial surface energy $S.E._1$ (Equation 3-7), and surface energy at β_{max}, $S.E._2$ (Equation 3-9) and the total viscous work W_c (Equation 3-13). Viscous work is partitioned into core and shell contributions as W_i and W_o, corresponding to the first and second terms of (Equation 3-13), respectively. Segmenting the final energy state (E_2) into interfacial energy and viscous dissipation within the core and shell layers allows for a mechanistic understanding of how each component contributes to the final outcome under different impact conditions.

Figure 3-8 illustrates the model-derived distribution of the initial energy E_1 and its partitions at maximum spreading E_2 across a range of equivalent Weber numbers for six representative cases. Each panel contrasts the energy redistribution for small ($\alpha = 0.2$) and large ($\alpha = 0.8$) cores, while varying the core and shell viscosities. Together, the panels show how various types of energy transform the initial available energy, promoting greater deformation, depending on the internal structure and rheological properties of the droplet.

The effect of core size is immediately evident in comparing left and right columns for each row. Larger cores result in increased interfacial energy share due to the greater inner surface area of the core-shell interface. This additional energy cost suppresses the spreading, particularly at low Weber numbers where interfacial energy accounts for a large fraction of the total (where

raising α from 0.2 to 0.8 increases $\mathrm{S.E._2/E_1}$ by $\sim 10\% - 25\%$. As inertia grows, however, this interfacial term becomes progressively less dominant. At higher $\overline{We}$, viscous dissipation, particularly within the shell (i.e., $\mathrm{W_o/E_1}$), becomes the primary sink for energy, reducing the influence of interfacial geometry (α-effect contracts to $< 5\% - 10\%$). This transition is central to identifying whether a particular impact lies within a capillary- or viscous-dominated regime.

Across all configurations, dissipation within the shell layer consistently emerges as the most significant channel for energy loss. This holds even for cases with large or highly viscous cores, indicating that the shell, being the outermost and directly interacting with the substrate, plays the dominant role in resisting deformation. Core dissipation is largely negligible across most conditions, but it becomes non-trivial when both the core viscosity and volume are high. This is seen most clearly in the upper-right panel, where large, viscous cores begin to show black bars representing core dissipation that are comparable in size to shell dissipation, though still secondary (i.e., peaking at $\mathrm{W_i/E_1} \approx 15$ % at highest $\overline{We}$ panel).

In the reference case of moderate viscosities (water cores in 5 cSt silicone oil), the energy landscape (see Figure 3-8**)** is more balanced: the interfacial contribution gradually declines with increasing We, while shell dissipation grows, smoothly reflecting the shift from capillary-limited to viscous-limited spreading. On the other hand, when the shell layer is significantly more viscous, as in the 20 cSt silicone oil cases, this dominance becomes pronounced regardless of the core size. The spreading is effectively arrested by the shell's resistance to flow, and even at high Weber numbers, the increase in deformation is limited. Here, the energy budget is almost entirely

dominated by W_o, confirming that when the shell viscosity exceeds the core's by a large margin, it governs the spreading dynamics almost independently of the inner configuration.

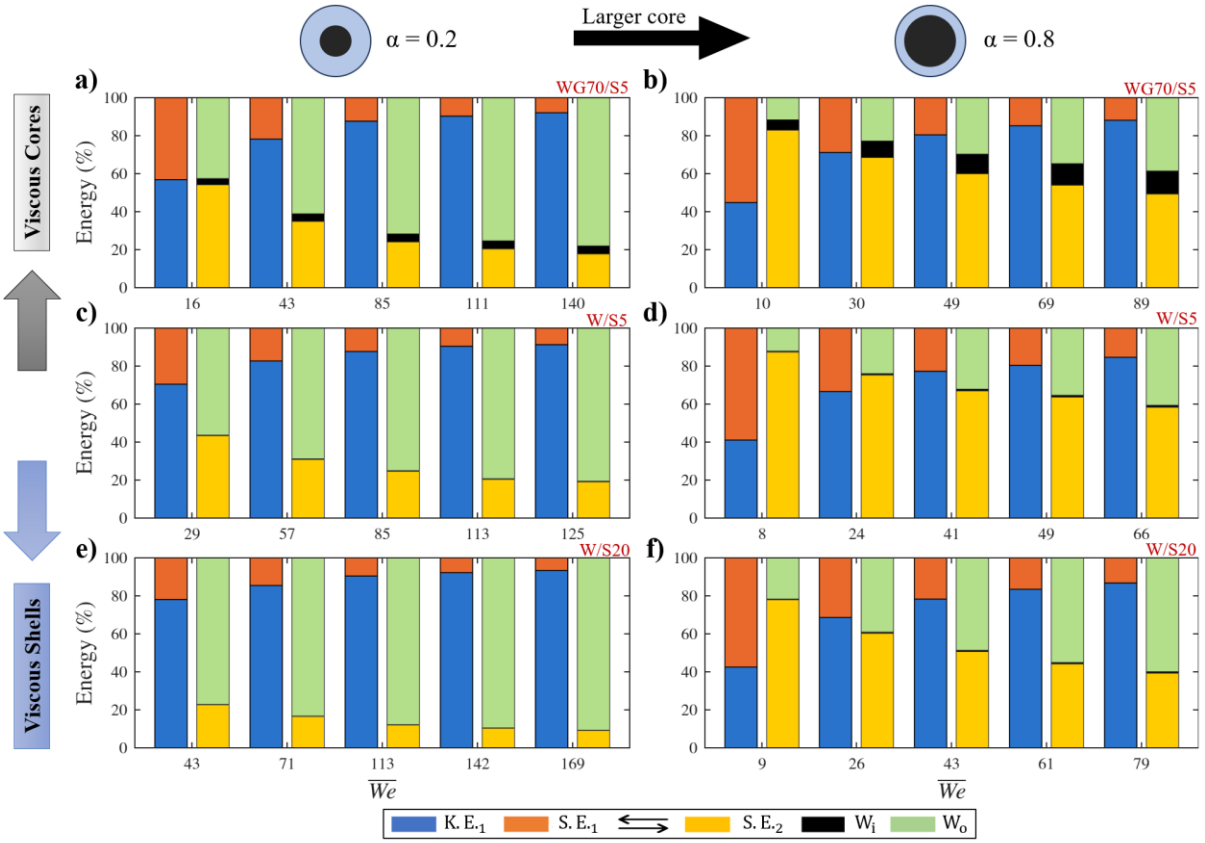

Figure 3-8 Energy budget distribution for compound droplet impacts across varying Weber numbers. Each column shows the percentage of initial kinetic and interfacial energy ($K.E._1$ and $S.E._1$) and its redistribution into final interfacial energy ($S.E._2$) and viscous dissipation within the core (W_i) and shell (W_o). Panels (a) and (b): water–glycerol core (70% glycerol, percentage in volume) in 5 cSt. Panels (c) and (d): water core in 5 cSt oil shell. Panels (e) and (f): water core in 20 cSt oil shell. All cases span increasing Weber numbers along the horizontal axis. Small cores are (α = 0.2), while large cores are (α = 0.8) for all cases.

Considering the above discussion, the model allows the identification of thresholds where viscous dissipation overtakes capillary resistance and where the influence of geometry, primarily through α, translates into measurable changes in energy distribution. In turn, this provides a foundation for the regime map illustrated in Figure 3-9 defining capillary, viscous, and

transitional zones as functions of core size and Weber number. Each data point corresponds to a specific impact case, color-coded based on the dominant energy mode at maximum spreading. A case is considered surface-dominated (yellow) when the final interfacial energy $S.E._2$ exceeds the total viscous dissipation W_c by more than 5%, indicating that capillary forces are more effective in resisting deformation than viscous forces. Conversely, a case is classified as viscous-dominated (green) when W_c exceeds $S.E._2$ by the same threshold, signifying that energy is primarily dissipated through internal friction in the shell and, to a lesser extent, the core. The transitional zone (red x) is defined for cases where $S.E._2$ and W_c differ by less than 5%, implying a balance between capillary and viscous mechanisms in controlling the spreading dynamics.

Unlike classical regime charts for single-component impacts that are parameterized by We and Re, this map explicitly incorporates the core-size ratio α and separates dissipation in the shell from that in the core. It therefore generalizes capillary-viscous demarcations to compound droplets and exposes how geometry and shell rheology shift the boundary. As α increases, the surface-dominated region contracts significantly, as more interfacial area must be stretched to accommodate the growing core, requiring more energy that cannot be maintained at low Weber numbers. This results in a strong dependence of the surface-to-viscous transition on geometry. Simultaneously, the viscous-dominated regime expands upward and toward the right of the map, capturing how increased inertial input (via Weber number) and higher confinement (via larger α) amplify the role of dissipation, especially in the shell.

Notably, the transitional regime is most prominent at moderate Weber numbers and mid-range core sizes, where the balance between interfacial and viscous energy is most sensitive. These conditions often yield the most variable spreading outcomes and offer a fertile region for tuning impact behavior through controlled changes in droplet composition or velocity. A single universal critical threshold $\overline{We}(\alpha)$ is not expected for core-shell droplets because the transition depends on viscosity ratios and phase Reynolds numbers in addition to α and $\overline{We}$. For any fixed liquid pair, however, an effective $\overline{We}(\alpha)$ can be extracted directly from the model using the condition $S.E._2 \approx W_c$ (the same criterion used to generate Fig. 9).

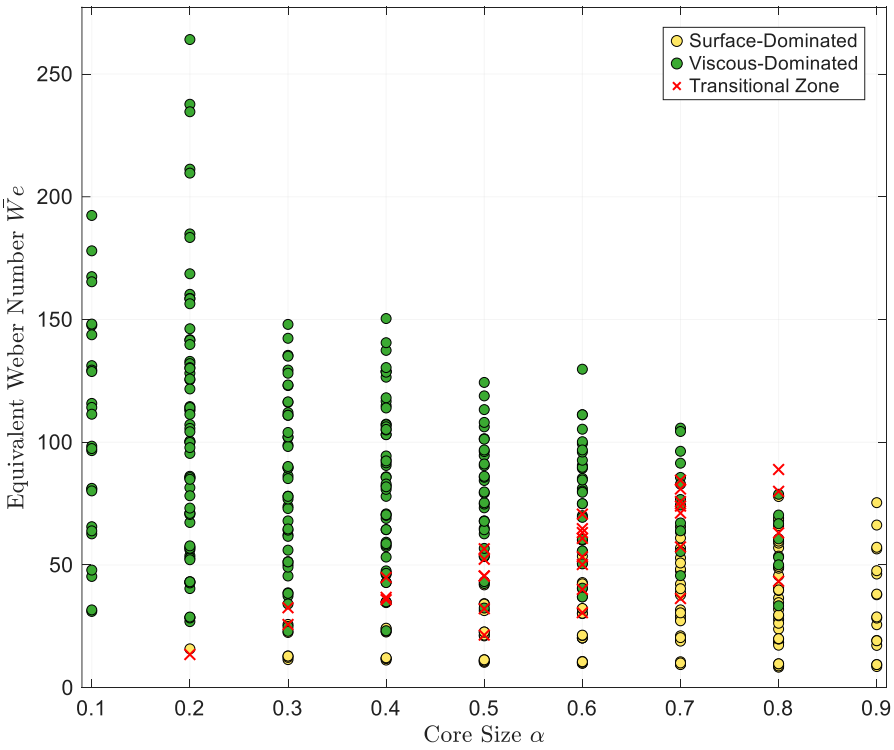

Figure 3-9 Regime classification map showing surface-dominated (yellow), viscous-dominated (green), and transitional (red x) impact cases based on the relative contribution of final interfacial energy and total viscous dissipation. Points are model-predicted and plotted as a function of core size α and equivalent Weber number $\overline{We}$. Classification is based on a 5% threshold in the relative difference between $S.E._2$ and W_v.

The dashed line indicates the upper practical threshold of the model's validity. Beyond this limit, either prompt splashing or core-substrate contact may occur, phenomena that are excluded from the current modeling assumptions but critically define the safe operational window for controllable spreading.

Altogether, this classification scheme contextualizes the results of the energy model within a predictive framework, guiding both experimental design and theoretical interpretation. It reveals how droplet impact behavior emerges from the interplay of inertial, capillary, and viscous forces, and offers a map to navigate the transitions between regimes in multiphase droplet systems.

3.6 Conclusion – Key highlights

- Developed and validated an energy-based model for spreading of core–shell droplets that predicts the maximum spreading factor with good accuracy on more than 300 unseen impacts ($R^2 \approx 0.91$, RMSE ≈ 0.12 for dimensionless $\beta_{\max}$).
- Showed that $\beta_{\max}$ increases with impact inertia and decreases with larger core volume fraction and higher shell viscosity, while core viscosity alone has only a minor influence; deformation over most conditions is governed by the combination of core size and shell dissipation.
- Demonstrated through energy budgeting that viscous dissipation in the shell is the dominant sink of initial droplet energy, with core-layer dissipation and interfacial energy varying systematically with inertia and geometry and explaining why large cores and viscous shells suppress spreading even at high Weber numbers.

- Used the model's energy partition to construct a physics-based regime map that classifies impacts as surface-dominated, viscous-dominated, or transitional, extending classical single-component charts by explicitly incorporating core fraction $\alpha$and separating shell and core dissipation, and providing direct guidance on how α and μ_o shift operating conditions between these regimes.

3.7 References

[1] A. M. Worthington, "XXVIII. On the forms assumed by drops of liquids falling vertically on a horizontal plate," *Proceedings of the royal society of London*, vol. 25, no. 171–178, pp. 261–272, 1877.

[2] C. Josserand and S. T. Thoroddsen, "Drop impact on a solid surface," *Annu Rev Fluid Mech*, vol. 48, pp. 365–391, 2016, doi: 10.1146/annurev-fluid-122414-034401.

[3] R. Rioboo, C. Tropea, and M. Marengo, "Outcomes from a drop impact on solid surfaces," *At. Sprays*, vol. 11, no. 2, 2001.

[4] A. L. Yarin, "Drop impact dynamics: splashing, spreading, receding, bouncing…," *Annu. Rev. Fluid Mech.*, vol. 38, no. 1, pp. 159–192, 2006.

[5] S. Chandra and C. T. Avedisian, "On the collision of a droplet with a solid surface," *Proc R Soc Lond A Math Phys Sci*, vol. 432, no. 1884, pp. 13–41, 1991.

[6] G. Liang and I. Mudawar, "Review of spray cooling–Part 1: Single-phase and nucleate boiling regimes, and critical heat flux," *Int J Heat Mass Transf*, vol. 115, pp. 1174–1205, 2017.

[7] S. V Murphy and A. Atala, "3D bioprinting of tissues and organs," *Nat Biotechnol*, vol. 32, no. 8, pp. 773–785, 2014, doi: 10.1038/nbt.2958.

[8] M. J. Docherty, P. Naderi, G. Grau, K. Sefiane, and A. Amirfazli, "Inkjet printing on hydrophobic surface: Practical implementation of stacked coin strategy," *Adv Eng Mater*, vol. 26, no. 11, p. 2400237, 2024.

[9] G. Liang, Y. Chen, L. Chen, and S. Shen, "Maximum spreading for liquid drop impacting on solid surface," *Ind Eng Chem Res*, vol. 58, no. 23, pp. 10053–10063, 2019.

[10] J. Du, X. Wang, Y. Li, Q. Min, and X. Wu, "Analytical consideration for the maximum spreading factor of liquid droplet impact on a smooth solid surface," *Langmuir*, vol. 37, no. 24, pp. 7582–7590, 2021.

[11] H.-M. Huang and X.-P. Chen, "Energetic analysis of drop's maximum spreading on solid surface with low impact speed," *Phys. Fluids*, vol. 30, no. 2, 2018.

[12] S. Lin, B. Zhao, S. Zou, J. Guo, Z. Wei, and L. Chen, "Impact of viscous droplets on different wettable surfaces: Impact phenomena, the maximum spreading factor, spreading time and post-impact oscillation," *J Colloid Interface Sci*, vol. 516, pp. 86–97, 2018.

[13] C. Ukiwe and D. Y. Kwok, "On the maximum spreading diameter of impacting droplets on well-prepared solid surfaces," *Langmuir*, vol. 21, no. 2, pp. 666–673, 2005.

[14] J. B. Lee, D. Derome, R. Guyer, and J. Carmeliet, “Modeling the maximum spreading of liquid droplets impacting wetting and nonwetting surfaces,” *Langmuir*, vol. 32, no. 5, pp. 1299–1308, 2016, doi: 10.1021/acs.langmuir.5b04557.

[15] M. Pasandideh-Fard, Y. M. Qiao, S. Chandra, and J. Mostaghimi, “Capillary effects during droplet impact on a solid surface,” *Phys. Fluids*, vol. 8, no. 3, pp. 650–659, 1996.

[16] I. V Roisman, “Inertia dominated drop collisions. II. An analytical solution of the Navier–Stokes equations for a spreading viscous film,” *Phys. Fluids*, vol. 21, no. 5, 2009.

[17] A. L. N. Moreira, A. S. Moita, and M. R. Panao, “Advances and challenges in explaining fuel spray impingement: How much of single droplet impact research is useful?,” *Prog Energy Combust Sci*, vol. 36, no. 5, pp. 554–580, 2010, doi: 10.1016/j.pecs.2010.01.002.

[18] B. Derby, “Inkjet printing of functional and structural materials: fluid property requirements, feature stability, and resolution,” *Annu Rev Mater Res*, vol. 40, pp. 395–414, 2010.

[19] R. E. Johnson and S. S. Sadhal, “Fluid mechanics of compound multiphase drops and bubbles,” *Annu Rev Fluid Mech*, vol. 17, no. 1, pp. 289–320, 1985, doi: 10.1146/annurev.fl.17.010185.001445.

[20] P. Attané, F. Girard, and V. Morin, “An energy balance approach of the dynamics of drop impact on a solid surface,” *Phys. Fluids*, vol. 19, no. 1, 2007.

[21] H. Jones, “Cooling, freezing and substrate impact of droplets formed by rotary atomization,” *J Phys D Appl Phys*, vol. 4, no. 11, p. 1657, 1971.

[22] J. Madejski, “Solidification of droplets on a cold surface,” *Int J Heat Mass Transf*, vol. 19, no. 9, pp. 1009–1013, 1976.

[23] R. McPherson, “On the formation of thermally sprayed alumina coatings,” *J Mater Sci*, vol. 15, pp. 3141–3149, 1980.

[24] T. Bennett and D. Poulikakos, “Splat-quench solidification: estimating the maximum spreading of a droplet impacting a solid surface,” *J Mater Sci*, vol. 28, pp. 963–970, 1993.

[25] E. W. Collings, A. J. Markworth, J. K. McCoy, and J. H. Saunders, “Splat-quench solidification of freely falling liquid-metal drops by impact on a planar substrate,” *J Mater Sci*, vol. 25, no. 8, pp. 3677–3682, 1990.

[26] C. Clanet, C. Béguin, D. Richard, and D. Quéré, “Maximal deformation of an impacting drop,” *J Fluid Mech*, vol. 517, pp. 199–208, 2004.

[27] I. Alkomy, M. Marengo, and A. Amirfazli, “Impact of a core–shell compound droplet on a solid surface,” *Exp Fluids*, vol. 66, no. 5, p. 97, 2025.

[28] N. Blanken, M. S. Saleem, M.-J. Thoraval, and C. Antonini, “Impact of compound drops: a perspective,” *Curr Opin Colloid Interface Sci*, vol. 51, 2020, doi: 10.1016/j.cocis.2020.09.002.

[29] H.-R. Liu, C.-Y. Zhang, P. Gao, X.-Y. Lu, and H. Ding, “On the maximal spreading of impacting compound drops,” *J Fluid Mech*, vol. 854, p. R6, 2018.

[30] Y. Wei and M.-J. Thoraval, “Maximum spreading of an impacting air-in-liquid compound drop,” *Phys. Fluids*, vol. 33, no. 6, p. 061703, 2021.

[31] N. Blanken, M. S. Saleem, C. Antonini, and M.-J. Thoraval, “Rebound of self-lubricating compound drops,” *Sci Adv*, vol. 6, no. 11, p. eaay3499, 2020, doi: 10.1126/sciadv.aay3499.

[32] Y. Du, L. Dai, L. Qian, F. Zhou, and Y. Ma, “Impact of a compound droplet on a solid surface: The effect of the shell on the core,” *Exp Therm Fluid Sci*, vol. 160, p. 111330, 2025.

[33] D. Liu and T. Tran, “Emergence of two lamellas during impact of compound droplets,” *Appl Phys Lett*, vol. 112, no. 20, p. 203702, 2018, doi: /10.1063/1.5026821.

[34] D. Liu and T. Tran, “The ejecting lamella of impacting compound droplets,” *Appl Phys Lett*, vol. 115, no. 7, p. 073702, 2019, doi: 10.1063/1.5097370.

[35] A. Kumar and D. K. Mandal, “Impact Dynamics of a Compound Drop on a Plane Solid: Effect of the Core Drop Viscosity,” in *Conf Fluid Mech Fluid Power*, Springer, 2021, pp. 391–396. doi: 10.1007/978-981-19-7055-9_66.

[36] A. Kumar and D. K. Mandal, “Impact of compound drops on a plane solid: Role of the core diameter,” *At. Sprays*, vol. 32, no. 2, pp. 1–18, 2022, doi: 10.1615/AtomizSpr.2021038825.

[37] K. Takamura, H. Fischer, and N. R. Morrow, “Physical properties of aqueous glycerol solutions,” *J Pet Sci Eng*, vol. 98, pp. 50–60, 2012, doi: 10.1016/j.petrol.2012.09.003.

[38] M. L. Sheely, “Glycerol viscosity tables,” *Ind Eng Chem*, vol. 24, no. 9, pp. 1060–1064, 1932, doi: 10.1021/ie50273a022.

[39] A. Amirfazli, M. D. Bustamante, Y. Hu, and L. Ó Náraigh, “Bounds on the spreading radius in droplet impact: the inviscid case,” *Proceedings of the Royal Society A*, vol. 480, no. 2294, p. 20230760, 2024.

[40] R. K. Singh, L. K. Mahato, and D. K. Mandal, “Airflow-assisted impact of drops of various viscosities: the role of viscous dissipation, normal imposed pressure, and shear flow of air,” *Langmuir*, vol. 37, no. 31, pp. 9504–9517, 2021.

Chapter 4 Machine learning approach[3]

4.1 Introduction

Upon impact on a solid surface, a droplet can exhibit several distinct outcomes: stable deposition, splashing with peripheral ejection of secondary droplets, complete or partial rebound, or intricate combinations thereof [1], [2], [3], [4], [5], [6]. The precise outcome in each scenario is intrinsically governed by the intricate confluence of inertial forces, viscous dissipation, capillary forces, and prevailing ambient conditions. Consequently, accurate prediction of the outcome and quantitative assessment of the largest attainable coverage are fundamental to technologies that require precise liquid placement and controlled wetting. For instance, printing and additive manufacturing require predictable footprints to preserve line-edge fidelity and layer continuity [7], [8], [9]. Spray coating, cooling, and cleaning depend on rapid yet regulated coverage without unintended atomization [10], [11], [12], [13]. Fuel injection and agricultural spraying seek a controllable balance between penetration and dispersion while limiting waste and aerosol exposure [14], [15]. Given these critical industrial requirements, predictive formulation in this domain concentrates on two primary objectives: (i) impact regime classification, which categorizes the observed outcome phenomenon (e.g., deposition, splash, rebound, bouncing-splash transitions), and (ii) maximum spreading factor (β_{max}), which quantifies the largest coverage as the ratio of the droplet's maximum lateral extent to its initial diameter.

[3] *This chapter forms the basis of a manuscript being prepared for submission to Physics of Fluids on machine-learning-based prediction of core-shell droplet impact outcome and maximum spreading.*

The machine-learning models introduced here are not intended to replace physics-based modeling. Instead, they complement the energy-balance framework by learning the nonlinear couplings and interaction effects that become difficult to represent in compact mechanistic closures, especially near regime boundaries where small parameter changes can switch outcomes. Importantly, all models are trained and interpreted using the same physics-organized predictors used throughout the thesis, so that improved predictive performance is accompanied by physically meaningful trends rather than purely numerical fitting.

The dynamics of droplet impact are governed by an extensive array of controlling parameters, which are grouped into three categories that reflect the constituents of the droplet-impact system: droplet intrinsic properties (e.g., density ρ, viscosity μ, surface tension σ, and initial diameter d), target solid surface characteristics (e.g., roughness, temperature, and static and dynamic wettability via contact angles that govern contact-line resistance and lamella arrest), and ambient conditions (e.g., gas density, pressure, and temperature) [2], [6], [16]. To distill the underlying mechanics and enable comparison across systems, these parameters are conventionally cast into nondimensional force ratios. For instance, the Weber number ($We = \frac{\rho U^2 d}{\sigma}$) and the Reynolds number ($Re = \frac{\rho U d}{\mu}$), defined with the impact velocity U, quantify inertia relative to capillarity and viscosity, respectively. Together, We and Re provide coordinates for impact phase diagrams and for correlations of the maximum spreading factor (β_{max}), and they delineate transitions among deposition, partial or full rebound, and splash [17], [18], [19], [20].

Compound droplets, defined as core-shell configurations in which an inner liquid core (subscript i) is encapsulated by an immiscible outer shell (subscript o), introduce an additional degree of tunability and complexity beyond single-liquid impacts [21]. The resultant multi-component droplet is fundamentally governed by an expanded set of controlling parameters, including the core-to-total volume fraction (α), the internal core-shell interfacial tension (σ_{io}), and the independently adjustable phase properties (ρ_i, μ_i and ρ_o, μ_o) [22], [23]. To effectively represent the inertia-capillarity balance in this multi-component setting, an equivalent Weber number $\overline{We}$ (Equation 4-1 has been introduced augmenting the contribution of the inner interfacial energy reservoir [24], [25]. This expanded system mandates the use of phase-specific Reynolds numbers, Re_i and Re_o, which are formed to attain the inertia-dissipation within the core and shell liquids using characteristic diameters determined by volume conservation: the core diameter ($\mathrm{d}_i = d_o\alpha^{1/3}$) and an effective shell diameter ($\mathrm{d}_{o.eff} = d_o\sqrt[3]{1-\alpha}$).

$$\overline{We} = \frac{[\rho_i\alpha + (1-\alpha)\rho_o]U^2 d_o}{\sigma_o + \sigma_{io}\alpha^{\frac{2}{3}}}, \qquad For\ 0 \le \alpha < 1 \qquad \textit{Equation 4-1}$$

Core-shell droplets add an internal interface that stores surface energy and redistributes inertia between the core and shell, shifting outcome boundaries and spreading relative to single-liquid drops [21], [24], [26], [27]. At low $\overline{\mathrm{We}}$, the core retracts over an intact lubricating shell film and forms a vertical central jet (i.e., jetting mode, J); increasing $\overline{\mathrm{We}}$ or core size α destabilizes this vertical liquid column and produces core-rich satellites followed by lift-off (i.e., partial rebound mode, PR). When the shell film thins to rupture, the core contacts and wets the substrate and

recoil is arrested (i.e., spreading-contact mode, SC). Each primary mode may acquire a splashing counterpart (i.e., J+S, PR+S, and SC+S) when the spreading rim destabilizes at higher inertia, ejecting peripheral secondary droplets (i.e., prompt splashing, +S) [22], [24]. Classical methods (i.e., experimental, numerical, and analytical) show that self-lubricating rebound hinges on the oil film's integrity; rising $\overline{\mathrm{We}}$ and α narrow the jetting outcome window and favor PR; rupture at large α (i.e., insufficient shell thickness) leads to SC; and prompt splash is governed largely by $\overline{\mathrm{We}}$, shell viscosity, and α, with a negligible core-viscosity effect on splash onset [23], [24], [25], [26]. Beyond delineating outcome regime boundaries, $\beta_{\max}$ grows with $\overline{\mathrm{We}}$ but is curtailed by shell-side viscous losses, that small cores ($\alpha \lesssim 0.5$) weakly affect $\beta_{\max}$, and that large or more viscous cores reduce spreading by raising interfacial resistance and/or overall viscous dissipation [24], [25], [28], [29], [30], [31], [32], [33]. These points are consolidated below in two sensitivity tables: Table 4-1, reports outcome likelihood versus $\overline{\mathrm{We}}$, α, Re_i, Re_o; and Table 4-2, reports $\beta_{\max}$ sensitivity for encapsulated-spreading cases, i.e., J and PR. Entries use a compact legend in which arrows indicate promotion (↑) or suppression (↓), double arrows mark strong effects (↑↑, ↓↓), the symbol (→) denotes weak or negligible dependence, (NM) denotes a non-monotonic trend, and (T) flags a threshold/onset. The tables integrate experimental, numerical, and energy-balance evidence; taken together they identify the dominant controls and justify focusing on $\overline{\mathrm{We}}$, α, Re_i, and Re_o as the minimal, physically organized predictor set.

Table 4-1 Sensitivity of compound-drop impact outcomes to $\overline{We}$, α, Re_i, and Re_o. Entries encode the direction and strength of the tendency in outcome likelihood as each predictor varies.

Outcome class	$\overline{\mathbf{We}}$	$\boldsymbol{\alpha}$	$\boldsymbol{Re_i}$	$\boldsymbol{Re_o}$	Mechanism
Jetting (J)	↓	↓	↓↓	↓	Low inertia and an intact shell sustain a stable recoil column; larger cores thin the film; a more viscous core stabilizes the recoil column; a more viscous shell damps lamella flow and helps preserve the film [21], [22], [24], [26].
Partial rebound (PR)	↑	↑	↑	↑	Increased inertia strengthens recoil and column instability; larger α raises stored interfacial energy; reduced viscous damping at higher Re_i and Re_o favors pinch-off into core-rich satellites before lift-off [22], [24], [26].
Spreading-contact (SC)	↑	↑↑ (T)	→	↑	Spreading thins the shell to a rupture thickness set mainly by core fraction, inertia, and shell viscosity; after core-substrate contact on a wetting solid, recoil is suppressed [22], [24], [32], [33].
J + splash (J+S)	↑↑	↑	↓	↑↑	Encapsulation persists but the spreading rim becomes unstable at high inertia; low shell viscosity promotes rim corrugation and prompt ejection while the core remains enclosed [24], [26], [34].
PR + splash (PR+S)	↑↑	↑	↑	↑↑	In the highest-inertia window the recoil column pinches off as the rim simultaneously sheds droplets; larger cores increase interfacial loading, and weak shell damping intensifies ejecta [24].
SC + splash (SC+S)	↑↑	↑↑ (T)	→	↑↑	After film rupture and core-substrate contact, very high inertia with weak shell damping destabilizes the rim and produces prompt splash near the rupture threshold in core size [24].

Table 4-2 Sensitivity of the maximum spreading factor β_{max} for encapsulated-spreading impacts (i.e., cases where cores remain encapsulated up to β_{max}, such as jetting and partial rebound) to $\overline{We}$, α, Re_i, and Re_o.

	$\overline{\mathbf{We}}$	$\boldsymbol{\alpha}$	$\boldsymbol{Re_i}$	$\boldsymbol{Re_o}$	**Mechanism**
$\boldsymbol{\beta_{max}}$	↑↑	$NM \rightarrow then \downarrow$	$NM \rightarrow to \downarrow (weak)$	↑↑	β_{max} grows with equivalent Weber through inertial-capillary balance but is limited by viscous losses concentrated in the shell; small cores have little influence, whereas large or viscous cores confine the shell lamella and reduce spreading; shell viscosity is the dominant viscous control, with core viscosity secondary at fixed core fraction [24], [27], [28], [29], [30], [31], [32], [35].

Building on the classical physical insights summarized in Table 4-1 and Table 4-2, the next objective is enhancing accurate prediction rather than description. Experiments and simulations clarify mechanisms and validate regimes, but they are costly to sweep across the parameter space and do not yield fast, generalizable predictors for new fluid pairs, core fractions, or impact conditions [24], [25], [36]. Analytical and semi-empirical correlations are rapid and physically grounded, yet they rely on case-specific closures and tuned dissipation coefficients; accuracy deteriorates outside the calibration domain and near regime boundaries [37], [38], [39]. None of these approaches scales to fuse heterogeneous datasets or to represent the strong nonlinear and nonmonotonic interactions among the four nondimensional controls highlighted by the previous sensitivity tables. This motivates a data-driven formulation that learns the complex, nonlinear mapping from the established four-variable feature space to both core-shell drop impact outcome and $\beta_{\max}$, while remaining physics-aware through trend constraints, interpretable feature

attributions, and rigorous validation. Because data-driven studies for core-shell liquids are essentially absent and curated datasets remain scarce, the literature review below examines machine-learning work for single-liquid droplets, first on outcome classification and then on $\beta_{\max}$ regression, to establish model families, metrics, and validation practices that will be adapted to the multi-component drop impacts.

4.1.1 Machine learning for impact regime classification (single-liquid droplets)

Impact regime classification is a supervised labeling task over a finite single-liquid drop impact outcome set (e.g., deposition, partial/complete rebound, splash, and mixed or thermal variants) with two persistent issues: class data imbalance and label noise near decision boundaries. Feature sets draw on non-dimensional groups that encode the governing balances. These include We, Re, and the Ohnesorge number $Oh = \mu/\sqrt{\rho\sigma d}$ (i.e., viscous to inertial–capillary scale). Wettability is represented by a static or advancing contact angle. Temperature variants must be explicit: substrate undercooling ΔT for supercooled targets, or surface temperature T_s for heated targets. Roughness r_a is included when surface morphology varies. Image inputs (i.e., sequences of high-speed camera frames or processed binary silhouettes) are appropriate when the class boundary is morphological and cannot be inferred reliably from scalars alone (i.e., We, Re, Oh, and other surface descriptors), for example, for detecting fingering onset, rim corrugation, or icing textures. Methodologically, class-weighted losses or training-only resampling mitigate imbalance, stratified splits reduce sampling bias, and reporting should include per-class precision, recall, and F_1 together with probability calibration, not only overall accuracy (definitions in Appendix C, section 5.7.1).

On tabular inputs, variance-reduction ensembles have proven reliable baselines. In a five-class taxonomy for droplet impacts on hydrophobic and superhydrophobic silicone rubber, Random Forests and compact artificial neural networks (ANN) achieved mid-80% test accuracy under a simple random train/test hold-out split [40]. The same study showed that naïve oversampling can inflate headline accuracy toward ~98% due to leakage of duplicated minority-class samples into both training and test sets; any resampling must be confined strictly to the training partition within each fold. In practice this means applying SMOTE (i.e., Synthetic Minority Over-sampling Technique, which generates new minority points along line segments between nearest neighbors) only inside the training split after each fold is formed. Incorporating thermal effects expands the outcome space and clarifies feature hierarchies: in a six-class setting with temperature as an explicit input, models trained with training-only SMOTE reached weighted $F_1 \approx 0.89$ and feature attributions consistently ranked Weber and Reynolds numbers above temperature and contact angle unless those variables were deliberately spanned [41]. Where an explicit, portable boundary is preferred, splash/no-splash can be cast as a margin problem: a linear SVM with uncertainty-weighted samples produced an interpretable threshold that outperformed several analytical criteria on the same corpus, with about 83% accuracy under eight-fold cross-validation while no separate external test set reported [42]. In heated, nano-textured settings where temperature and morphology interact, class-weighted shallow ANNs using tabular inputs (T_s, nano-packing or pillar fraction φ, roughness r_a, and We) achieved about 95% test accuracy under an 85/15 split with 5-fold cross-validation for tuning, outperforming tree and SVM baselines in stability [43].

When scalar features saturate, image-based inputs offer a powerful alternative by revealing morphological cues associated with instability onset. On supercooled silicon, Yang (2022) employed a compact pipeline, using K-means clustering to prefilter and balance a small image dataset, followed by a VGG-style convolutional neural network (CNN) with stacked 3×3 filters, to distinguish spreading from icing morphologies. This approach achieved ~90% held-out accuracy under a stratified 70/15/15 train/validation/test split [44]. A subsequent study in the same thermal regime (Yang, 2023) applied a similar CNN architecture to classify spreading versus fingering, again reaching ~90% accuracy [45]. In both cases, the advantage of vision-based features is fundamentally physical: visual signatures such as rim corrugation, finger nucleation, and icing textures encode class-relevant information that scalar descriptors (e.g., We, Re, Oh) cannot reliably capture.

Taken together, these results support a pragmatic recipe for outcome classification. Start with non-dimensional tabular features aligned with the governing balances and select learners that accommodate nonlinearity and class imbalance without overfitting on small-medium datasets (e.g., variance-reduction ensembles such as Random Forests, or cost-sensitive shallow neural networks). Use linear margins when an explicit threshold is required. Introduce image-based models only when the boundary is morphological and adequate imaging is available. Generalization claims should be supported by calibrated probabilities and validation protocols that go beyond a single random split, since reported accuracy typically contracts under stricter, group-aware or repeated k-fold splits. Emphasizing physics-aligned features, careful imbalance

handling, probability calibration, and rigorous validation provides a stable foundation for extending outcome classification to multi-component droplets.

4.1.2 Machine learning for maximum spreading regression (single-liquid droplets)

Machine-learning regression for single-liquid droplet impacts can be organized by target: the trajectory $\beta(t)$ or the endpoint $\beta_{\max}$. For $\beta(t)$, experimental records are sequential and typically irregularly sampled, whereas classical reconstructions rely on fixed energy-balance/similarity time laws and, in practice, uniformized time grids [46], [47]. That mismatch degrades early-time accuracy for classical methods (steep inertial growth followed by viscous relaxation). A Nonlinear Auto-Regressive network with eXogenous inputs (NARX-ANN) treats $\beta(t)$ explicitly as a time-series map, using past β values and controlling inputs $(We, Oh, \tan\theta)$ as regressors while taking the actual sampling interval Δt as an exogenous input, where Oh is the Ohnesorge number (i.e., viscous to inertial–capillary ratio) and θ is the equilibrium contact angle (i.e., wettability proxy). Because it trains on the native, non-uniform timestamps (i.e., no pre-interpolation), the network aligns the model with the way the data were acquired, which improves fidelity at early times. On a 51-experiment corpus, this configuration achieved $R^2 \approx 0.993$ ($MSE \approx 3.26 \times 10^{-4}$) and outperformed standard energy-balance correlations evaluated on the same sequences [48]. The remainder of this section focuses on $\beta_{\max}$, the endpoint target of the present study.

For tabular regression of $\beta_{\max}$, two design choices govern both performance and portability: how the features encode the physics and how heterogeneous the dataset is. In single-lab datasets with controlled surfaces and narrow parameter ranges, dimensional predictors

$(\rho, \sigma, \mu, d, U, \theta_{adv})$ coupled with variance-reduction ensembles (e.g., Random Forests) yield fair in-split accuracy (e.g., $R^2 \approx 0.88$ for water/saline drops on hydrophobic/superhydrophobic silicone rubber surfaces) [49]. However, this approach inflates the apparent importance of scale variables, most notably d and U, because scale is encoded directly, this limits mechanistic interpretability and transfer beyond the lab's specific ranges. Using non-dimensional groups sharpens attribution and improves portability. On compiled, multi-source corpora spanning different surfaces and laboratories, gradient-boosted regression trees (i.e., GBRT) trained on non-dimensional inputs (We, Re, θ) outperform linear, single-tree, and bagged-tree baselines (e.g., $R^2 \approx 0.963$) [50]. GBRT builds a stage-wise additive model by fitting shallow trees to the current residuals and shrinking their contributions, which captures regime-specific structure while controlling variance. When surface morphology varies across sources, it must be encoded explicitly: adding a roughness descriptor (r_a) alongside (We, Re, θ) often yields near-perfect internal fits; however, cross-lab heterogeneity in surface preparation, wettability measurement, and imaging/segmentation can still drive large drops on blind external tests (e.g., $R^2 \approx 0.78$) [51]. Thus, credible generalization depends on feature completeness and boundary-aware validation (e.g., leave-one-lab or leave-one-surface out), not on headline in-fold scores. Across studies, variable-importance and partial-dependence analyses consistently rank We and Re as dominant drivers; θ contributes measurably only when wettability is deliberately spanned, particularly at lower We [49], [50], [51], [52].

When substrate temperature is a control variable, it must be included explicitly, undercooling ΔT for supercooled surfaces or surface temperature T_s for heated ones, because temperature alters

viscosity, phase change and contact-line dissipation, thereby reorganizing lamella dynamics. For water on supercooled silicon, Yang (2022) trained a compact back-propagation neural network on non-dimensional inputs $(Re, We, Oh, \Delta T)$ to predict both $\beta_{\max}$ and τ_{max}, where $\tau_{max} = t_{max}U/\mathrm{d}$ is the non-dimensional time to maximum spread. With a 70/15/15 train/validation/test split, the study reports a test correlation $R = 0.963$ (i.e., errors ≈ 4.6% for $\beta_{\max}$, and ≈ 2.1% for τ_{max}), showing that a low-capacity neural regressor is adequate for a single liquid/surface system when temperature is encoded [44]. A subsequent supercooled study (Yang, 2023) again used a shallow neural network but augmented the feature set to $(Re, We, Oh, Ca, \tilde{T})$, where $Ca = \mu U/\sigma$ (i.e., capillary number) captures viscous-shear loading and $\tilde{T}$ is a dimensionless temperature (i.e., normalized thermal forcing). Accuracy was reported as sub-percent relative errors on the held-out set; the gain comes from feature expressiveness (separating Ca from Oh), not from increased model capacity, and remains specific to the controlled supercooled regime [45]. In the heated counterpart, Au-Yeung & Tsai (2023) regressed $\beta_{\max}$ on T_s, nano-packing/geometry (e.g., pillar fraction ϕ), surface roughness r, and impact inertia via We. Using 5-fold cross-validation with an 85/15 train/test split, kernel SVR provided the most stable generalization (i.e., test $R^2 \approx 0.97$) compared with neural and tree-based baselines, and yielded interpretable trends: a high-inertia plateau in $\beta_{\max}$ (~3.8), diminishing temperature influence at large We, and spreading suppression by nano-pillars with a leftward shift of the plateau onset [43]. In summary, temperature-controlled datasets favor shallow neural networks for well-curated supercooled systems and cross-validated SVR for heated nano-textures with mixed thermal/morphology

descriptors; in both cases, $\Delta T/T_s$ and morphology must appear as first-class features, and validation design (explicit splits, k-fold CV) is critical for credible performance.

To further improve stability and physical consistency on mixed datasets and to connect predictions to conserved budgets, two complementary directions have emerged. First, physics-aware loss shaping: in a 785-experiment, 15-source compilation restricted to $(\mathrm{We}, \mathrm{Re})$ after sensitivity screening excluded θ, augmenting a feed-forward network with a low-weight physics term that enforces monotonic growth of $\beta_{\max}$ with We and penalizes departures from a stable empirical relation lowered the average relative error from 16.56% to $\approx 13.6\%$ under a single 80/20 train/test split [53]. This modification targets the characteristic failure modes of heterogeneous compilations, variance inflation and non-physical extrapolation, while preserving model flexibility. Because single-split estimates on mixed sources are often optimistic, k-fold cross-validation is required to quantify split-to-split variability and to tune hyperparameters. Second, time-resolved energetic surrogates: stacked Long Short-Term Memory networks trained on sequences of kinetic, surface, and dissipated energies from high-fidelity runs reproduce held-out energy trajectories with test $R^2 > 0.99$. Predicting energy histories encodes conservation and dissipation pathways directly in the target, and the resulting physics-structured signals can regularize or augment $\beta_{\max}$ regressors, for example by enforcing energy-consistent trends or by supplying auxiliary features correlated with spreading. The same sequence models also support a two-stage inversion that recovers $(\mathrm{Re}, \mathrm{We})$ from the predicted energy series [54].

In summary, β_{max} regression for single-liquid impacts is most transferable when non-dimensional groups (We, Re) anchor the feature set and θ is treated as a secondary modifier, most relevant at low Weor when wettability is deliberately varied. Credible reporting should prioritize generalization rather than in-split fit, using boundary-aware train/test splits when heterogeneity is present, k-fold cross-validation for model selection and variance estimation, and regularization or early stopping to limit overfitting.

Collectively, the single-liquid studies establish a rigorous template for feature selection, learner design, and validation strategy. The key gap is extension to core-shell droplets, where the internal interface introduces a new set of control parameters, namely the equivalent Weber number $\overline{We}$, core fraction α, and phase-specific Reynolds numbers Re_i and Re_o, together with non-monotonic regime boundaries and increased heterogeneity. The methodology that follows operationalizes this transition by systematically benchmarking a compact library of linear models, decision trees, k-nearest-neighbor classifiers, support vector machines, ensembles of trees, Gaussian-process regressors, and feed-forward neural networks implemented through capacity-controlled presets; these families are used for both regime classification and β_{max} regression. Stability is assessed under boundary-aware train/test splits and repeated k-fold cross-validation, and calibrated class.

4.2 Machine learning method

This section formalizes the learning protocol that follows from the physics summarized in the Introduction. The dataset is assembled under controlled core-shell impact conditions, inputs are prepared to reflect the governing balances with all preprocessing parameters learned on training

folds only, and data handling uses stratified train and unseen test partitions with inner cross-validation, on the training data, to yield unbiased, variance aware estimates. The model library spans multiple families and uses capacity-controlled MATLAB presets that cover efficient ranges of hyperparameters such as depth, width, margin complexity, and neighborhood size, so we probe expressiveness without ad hoc search. Evaluation and selection rely on accuracy-oriented metrics and the stability of results across the split and fold conditions, ensuring conclusions are robust and traceable.

4.2.1 Data source, features, and preparation

The data corpus for all machine-learning models was assembled from an internally consistent, in-house experimental campaign on core-shell droplet impacts on smooth glass substrates [24]. Seven liquid pairings were prepared by combining water or water–glycerol cores with silicone-oil shells spanning 5 to 100 cSt, providing a broad and controlled property space. From this single-lab source, two supervised tasks were defined: a multi-class classification of the observed impact outcomes and a regression of the maximum spreading factor. Both tasks use the same physics-organized set of four nondimensional predictors introduced earlier: the equivalent Weber number, the core volume fraction, and the Reynolds numbers of the core and shell. Because these predictors occupy very different numeric scales in practice, features were standardized for scale-sensitive algorithms using z-score normalization to zero mean and unit variance. The standardization parameters were estimated only on the training set and then applied unchanged to all evaluation data, including the final test set, which preserves reproducibility, prevents information leakage, and keeps the pipeline aligned with the governing physics.

4.2.1.1 Outcome classification dataset

The classification set comprises $N_{class} = 550$ labeled impacts distributed across six outcomes. The distribution is strongly skewed, with Jetting the dominant class and Spreading + Splash extremely rare. Figure 4-1 summarizes the prevalence of each outcome for the full corpus. To avoid overfitting through synthetic resampling, imbalance is handled during training with cost-sensitive learning [55]. Each class is assigned a misclassification weight that is inversely proportional to its prevalence in the training data and then normalized so that the average weight across classes equals one. Rare splash categories therefore carry larger penalties than common categories, which improves attention to minority outcomes without distorting the underlying sample geometry. These class weights are computed from the training partition only and held fixed when models are evaluated.

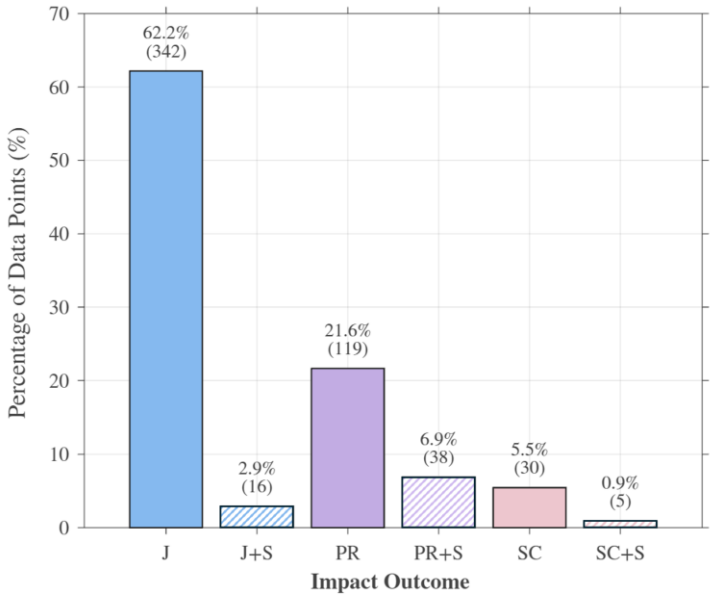

Figure 4-1 Class imbalance in the classification corpus ($N_{class} = 550$). Bars show outcome prevalence as percentages with counts in parentheses; hatched bars denote splash counterparts.

4.2.1.2 Maximum spreading factor (β_{max}) regression dataset

The regression dataset, comprising $N_{reg} = 421$ impacts, is a curated subset strictly limited to encapsulated-spreading trajectories. This inclusion criterion selects only events where the core remains fully lubricated by an intact shell, without contacting the substrate up to the point of maximum spread (β_{max}). Consequently, all impacts involving prompt splash, rim atomization, or premature shell rupture are excluded. This curated subset retains the full diversity of the original corpus, spanning all seven liquid combinations and the complete operating range. This ensures the dataset populates the entire physical state-space, covering the capillary-dominated, transitional, and viscous-dominated regimes, which were demarcated by prior energy-balance analysis. This provides a robust foundation for the continuous prediction of the maximum spreading factor, β_{max}.

4.2.2 Train-test splitting and cross-validation

Reliable assessment of generalization requires that predictive models be confronted with impact events that are statistically representative of, yet strictly unseen with respect to, the data used for training. In the present corpus, impacts are heterogeneous across outcome classes, liquid combinations, and the controlling nondimensional predictors, so naive random partitioning would risk leaking strongly correlated observations into both training and test sets and would distort rare regimes. A stratified, structure-aware splitting strategy is therefore adopted to preserve the experimental organization and the coverage of the physical space while still exposing the models to genuinely unseen conditions.

To quantify sensitivity to the amount of training information, three global train-test fractions are considered: 70/30, 75/25, and 80/20, with the larger portion reserved for training in each case. For each split, the same procedure is applied to both the classification and regression tasks. The resulting combinations are summarized schematically in Figure 4-2. Within each training subset, performance and hyperparameters are estimated by k-fold cross validation, with k set successively to 5, 7, and 10. This nested design emphasizes that all preprocessing, model fitting, and tuning steps are confined to the training folds, while the held-out test subset remains untouched until the final evaluation. Comparing results across the three values of k provides an internal measure of variance and tests the sensitivity of the models to the choice of cross validation granularity, so that reported metrics reflect both central performance and stability.

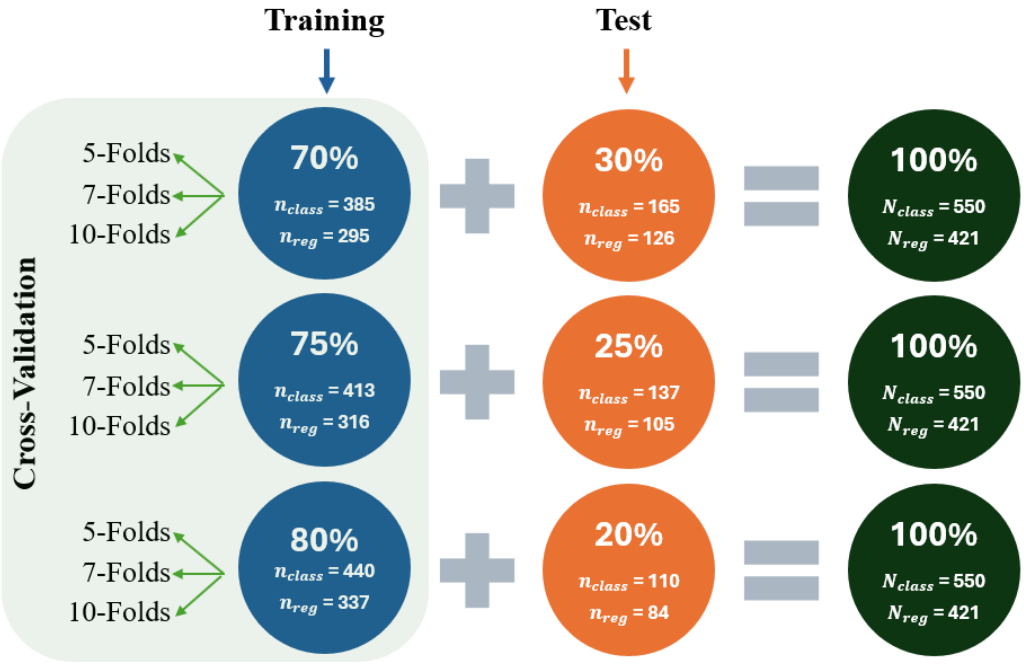

Figure 4-2 Schematic of the train–test and cross-validation settings used for the classification and regression datasets, with three global splits (70/30, 75/25, 80/20) and 5-, 7-, and 10-fold cross-validation on the training subsets.

The quality of any split must be judged not only by sample counts but also by how well the partitions reproduce the joint distribution of the governing predictors. To provide a baseline for this assessment, Figure 4-3 displays the full four-dimensional controlling feature space through a matrix of pairwise scatter plots and marginal histograms for $\overline{\mathrm{We}}$, α, Re_i, and Re_o. Symbols distinguish the non-splashing outcomes (i.e., J, PR, and SC) by marker shape and fill color, while red-outlined symbols mark their splashing counterparts. The diagonals of this array reveal broad, multi-regime coverage in each predictor, while the off-diagonal panels highlight structured relationships within and across classes, such as the concentration of jetting events at low $\overline{\mathrm{We}}$ and moderate Reynolds numbers and the clustering of splashing counterparts at higher inertia. Subsequent diagnostics for the training and test subsets are interpreted relative to this reference distribution (see Appendix C Figures S1-S3).

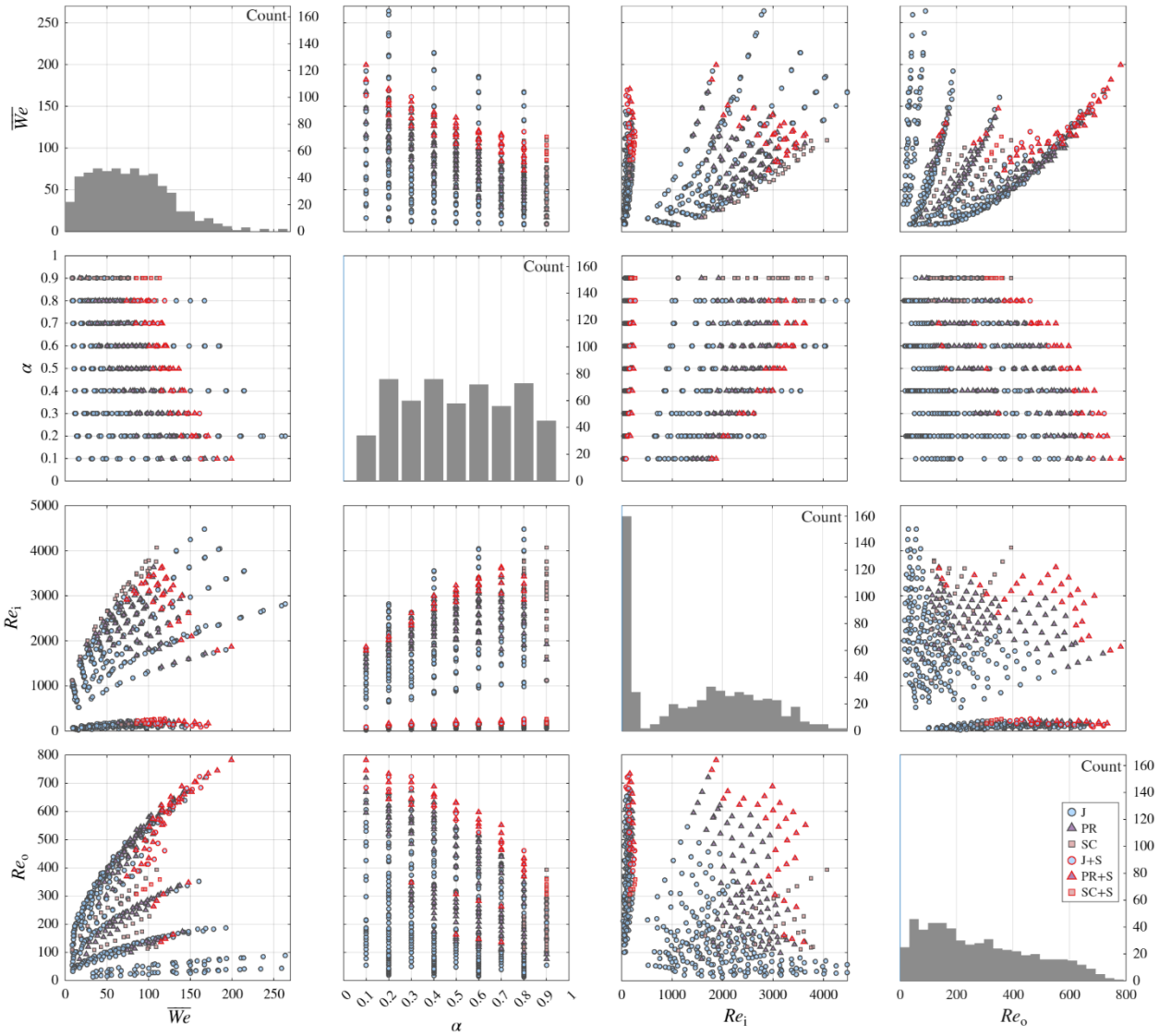

Figure 4-3 Pairwise scatter–histogram matrix of the nondimensional predictors $\overline{We}$, α, Re_i, and Re_o for the classification corpus; marker shape and fill denote non-splashing outcomes (J, PR, SC), and red-outlined markers indicate their splashing counterparts (J+S, PR+S, SC+S).

4.2.2.1 Classification data splitting

The classification task comprises six imbalanced outcome labels, seven liquid combinations that constitute distinct property groupings, and broad ranges of the four controlling predictors. The split must therefore preserve class proportions, ensure that every liquid combination appears in both partitions, and maintain coverage of the governing feature space. Preserving class balance keeps test priors aligned with the population and prevents majority-driven inflation while retaining support for rare splash modes. Mirroring liquid combinations across partitions mitigates block effects arising from fluid pairing. Matching the joint distribution of the controlling features limits covariate shift and avoids truncation of tail regimes, supporting stable probability calibration and transferable hyperparameters.

To enforce these constraints, each impact is assigned to a discrete group formed by the Cartesian product of four attributes: liquid combination, discrete core fraction α, outcome label, and a three-tier magnitude code (low, medium, high) summarizing typical ranges of $\overline{\mathrm{We}}$, Re_i, and Re_o within that liquid pair. Within every group, approximately the target share for training (70, 75, or 80 percent, as per the global setting) is allocated and the remainder is assigned to test, with at least one observation kept on each side whenever a group contains multiple samples. A small, within-combination rebalancing step then aligns the achieved totals with the intended train and test sizes without emptying any populated group.

Figure 4-4 provides the first diagnostic at the label level. For each outcome, the stacked bars show the fractions routed to training (blue) and test (orange) under the three global split settings. The bars remain close to the nominal targets and, crucially, even the rare splash classes retain test examples, which guards against optimistic headline scores driven by unseen minority modes.

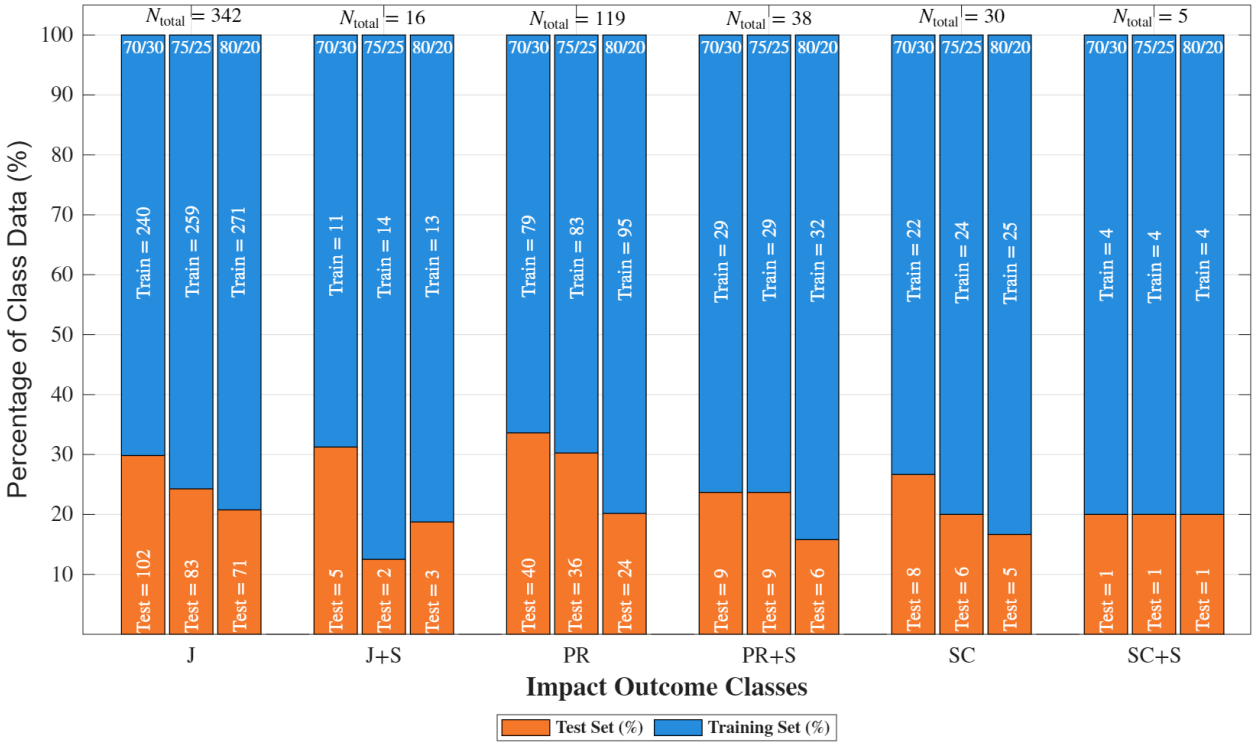

Figure 4-4 Class-wise train and test proportions under the three global splits.

The second diagnostic verifies balance across liquid combinations. Figure 4-5 displays the outcome composition within each fluid pair using stacked bars, while the overlaid curves trace the achieved training fraction for the 70/30, 75/25, and 80/20 settings. All seven combinations

contribute to both partitions and the realized training shares track the intended values despite different class mixtures across liquids. This protects against covariate shift tied to fluid pairing.

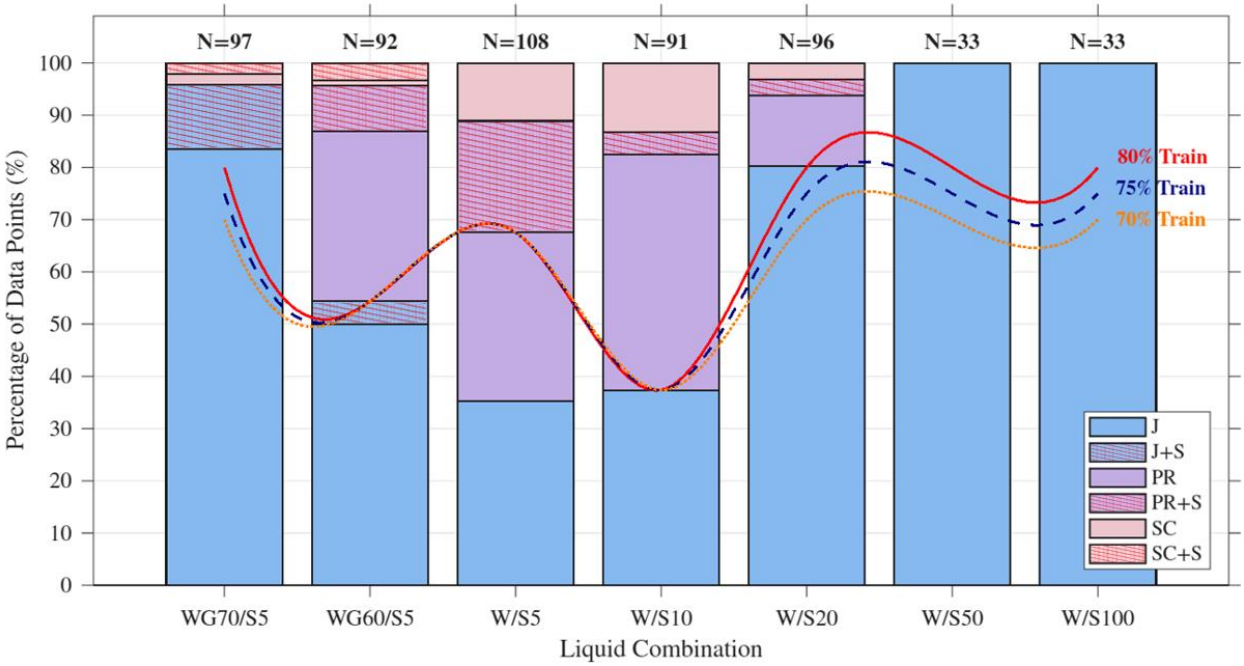

Figure 4-5 Outcome composition by liquid combination (stacked by outcome class), with overlaid curves indicating the achieved training fraction for each global split (70/30, 75/25, 80/20).

Feature-space fidelity is assessed on a global standardized scale. Observations from all three split ratios and from both partitions are pooled to compute a single mean μ_{global} and standard deviation σ_{global} for each predictor $X \in \{\overline{\text{We}}, \alpha, Re_i, Re_o\}$, and values are transformed to $z = (X - \mu_{\text{global}})/\sigma_{\text{global}}$. Figure 4-6 juxtaposes the training and test z-distributions using mirrored violins with embedded boxplots across the 70/30, 75/25, and 80/20 settings. The close overlap of the violins, together with near-coincident medians and comparable interquartile ranges around $z \approx 0$, indicates alignment in location, spread, and tails. In combination with Figure 4-4 and Figure 4-5, this confirms statistically comparable yet strictly disjoint partitions suitable for

credible generalization estimates in the classification task. Per-split versions using the same μ_{global} and σ_{global}, along with additional feature distribution diagnostics, are provided in Appendix C Figure S4-S5.

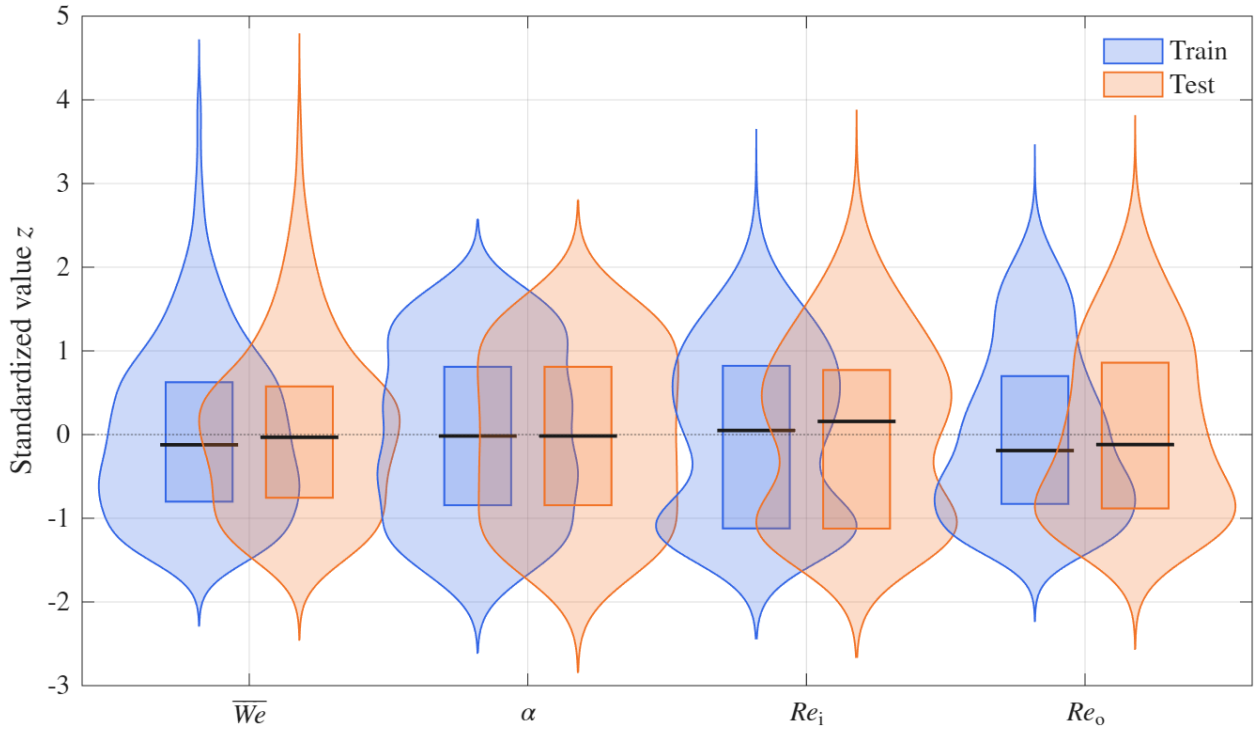

Figure 4-6 Train versus test distributions of standardized predictors for all splitting settings, violins and boxplots indicate matched location, spread, and tails.

4.2.2.2 Regression data splitting

The regression subset targets $\beta_{\max}$ for encapsulated-spreading events (jetting and partial-rebound). Here the priority is breadth of physical coverage rather than label balance: partitions must span capillary-controlled, transitional, and viscous-damped spreading while retaining every liquid pair on both sides. To achieve this, impacts are stratified by the Cartesian product of liquid

combination, discrete core-fraction levels, and a three-tier intensity bin (low, medium, high) that summarizes the local inertial-viscous loading for that liquid pair. Within each stratum, the target share for training (70, 75, or 80 percent) is assigned and the remainder held out for testing, keeping at least one observation on each side when multiple samples exist. This construction preserves regime coverage and prevents empty pockets in the held-out set.

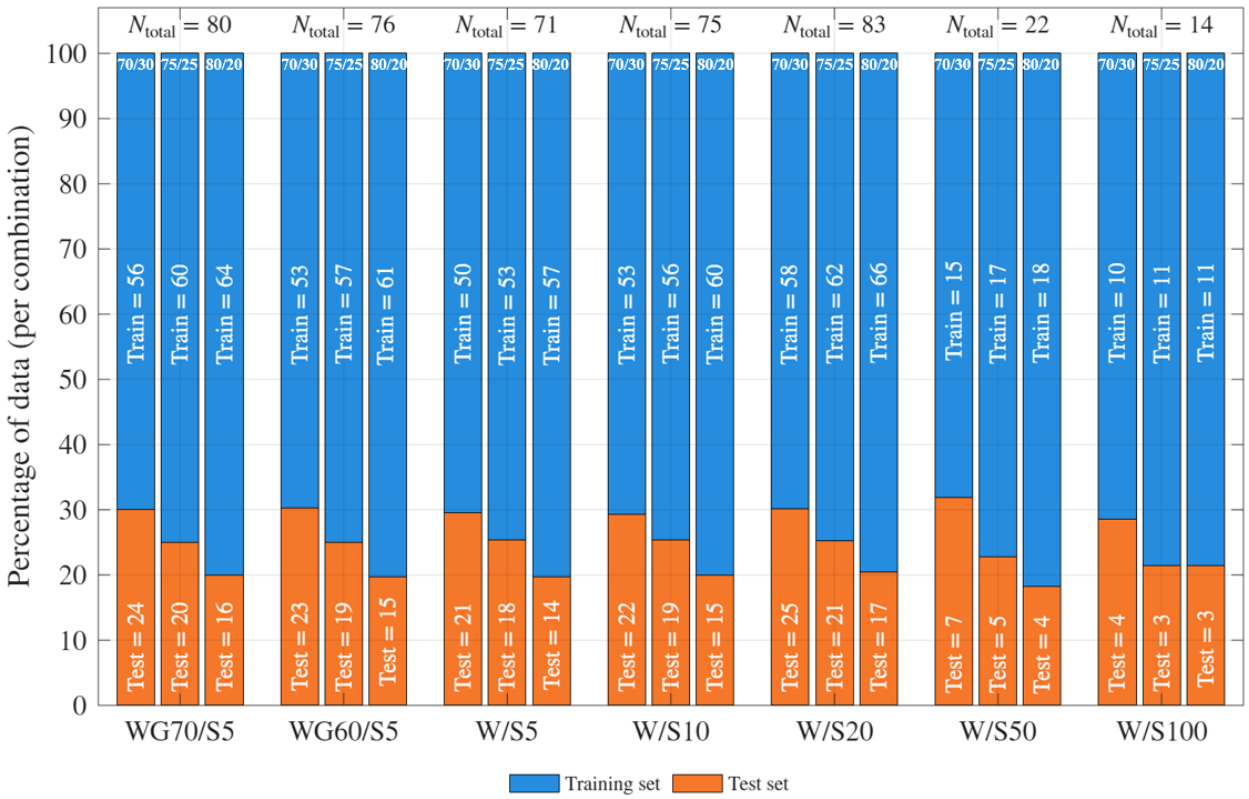

Figure 4-7 Stratified train–test allocation for the regression subset across liquid combinations under the three global settings; stacked bars encode training and test fractions per combination.

Figure 4-7 confirms liquid-pair representation: every combination appears in both partitions, and the realized training proportions closely follow the nominal 70/30, 75/25, and 80/20 settings.

Feature-space alignment is assessed on the global z-scale; Figure 4-8 overlays pooled train and test densities with mirrored violins and embedded boxplots. The strong overlap, nearly coincident medians, and comparable interquartile ranges about $z \approx 0$ indicate matched location, spread, and tails. Per-split violin panels for 70/30, 75/25, and 80/20 are provided in Appendix C Figure S6 and show the same agreement. Collectively, these diagnostics demonstrate that the regression splits preserve regime coverage and yield statistically comparable yet strictly disjoint partitions, supporting unbiased training, tuning, and generalization testing.

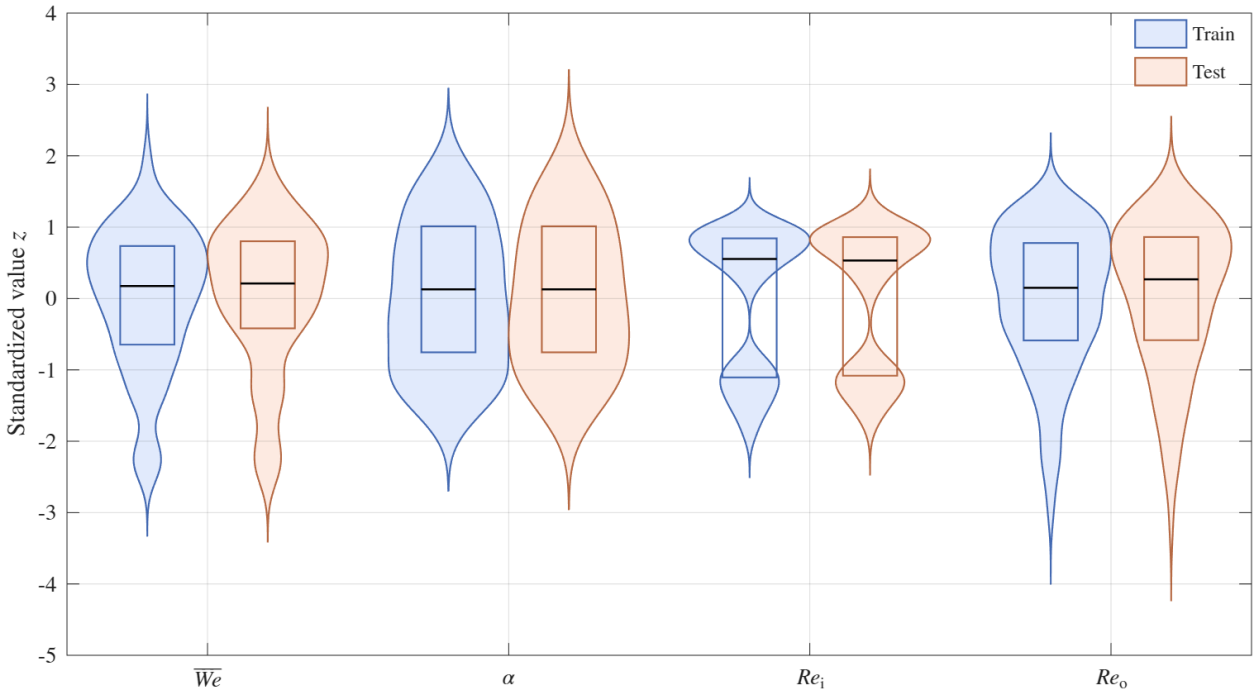

Figure 4-8 Global-standardized distributions of predictors for the regression train and test partitions; violins with embedded boxplots, pooled across all split ratios.

4.2.3 Model families and capacity-controlled hyperparametric presets

The model library is organized to compare families on equal footing, progressing from high-capacity nonlinear learners and proceeds toward simpler, more interpretable baselines. This

ordering reflects the problem physics: outcome boundaries and $\beta_{\max}$ trends are nonlinear and sometimes non-monotone, while interpretability and stability remain essential. Presets from MATLAB's Classification and Regression Learner apps define fixed capacity rungs within each family, so performance differences reflect inductive bias and model complexity rather than ad hoc hyperparameter search. All models share the same preprocessing and stratified splits, with inner cross-validation restricted to the training folds and parameters estimated only within those folds. Family applicability is task-aligned: Gaussian-process models are used for regression only, KNN presets are used for classification only, and all other families serve both tasks.

Neural networks provide the top tier of expressiveness among parametric models. Feed-forward ReLU architectures are included along a controlled capacity ladder: single-hidden-layer narrow, medium, and wide variants map smooth but nonlinear response surfaces; bi-layered and tri-layered presets introduce shallow hierarchy for interactions that require depth. This ladder probes how much architectural width and depth are actually needed by the physics-organized features without drifting into bespoke tuning. Gaussian-process regression complements neural networks by supplying a nonparametric Bayesian view with calibrated predictive variances. Four kernels span smoothness assumptions and multi-scale effects: squared-exponential for very smooth mappings, Matérn 5/2 for controlled roughness that often fits laboratory tabular data well, rational-quadratic for mixtures of length scales typical of regime transitions, and exponential for comparatively less smooth responses. Together these presets cover gradual to moderately abrupt changes in $\beta_{\max}$.

Ensembles of decision trees offer a robust middle ground for tabular data. Bagging aggregates deep, high-variance trees to reduce variance through averaging, which is valuable when the data mix regimes and local trends. Boosting adds small trees stage-wise to correct residuals, sharpening boundaries where single trees underfit. Support-vector machines contribute margin-based models with controlled geometry. Linear, quadratic, and cubic kernels provide global margins of increasing curvature; Gaussian kernels at fine, medium, and coarse scales vary the locality of the decision surface, from highly localized to broadly smooth. These presets expose how much locality is required by the governing features. Standalone trees and nearest-neighbor baselines complete the coverage. Fine, medium, and coarse trees control split granularity via leaf size, trading fit to local structure against stability. The KNN presets vary the neighborhood size and distance metric, including Euclidean, cosine, and a higher-order Minkowski variant, with a weighted option that emphasizes near points; these give nonparametric references for class boundaries defined by local density rather than global margins. Finally, linear discriminant analysis and ordinary least squares anchor the library with fully interpretable linear baselines for classification and regression, respectively.

Table 4-3 consolidates the preset library by family, preset name, task use, key hyperparameters, and a one-line rationale: depth and nominal width for neural networks; kernel class and the standard fine, medium, and coarse Gaussian scales for SVM; leaf size for trees; neighborhood size and metric for KNN; kernel class for GPR. The collection spans geometry from global linear to highly localized boundaries and smoothness from very smooth to moderately rough, under fixed, reproducible capacities. Within this regime only fold-internal

quantities are learned: linear models estimate coefficients on the training folds; single trees learn split thresholds at the preset leaf size, bagging averages deep bootstrap trees, and boosting adds shallow trees stage-wise; SVMs fit maximum-margin models with kernel and locality fixed by the preset; KNN stores standardized features and votes within the preset neighborhood; GPR maximizes marginal likelihood under the chosen kernel to infer characteristic scales and noise, yielding a mean and uncertainty; neural networks learn weights and biases by gradient methods with early stopping inside cross-validation while depth and width remain fixed. Class weights address imbalance during classification, and all preprocessing statistics are computed on training folds only.

Table 4-3 Model families and capacity-controlled presets with defining hyperparameters and brief rationale.

Model family	**Preset**	**Applied for**	**Defining hyperparameters**	**Rationale**
Neural Network (NN)	Narrow Neural Network	Both	1 hidden layer, 10 neurons, ReLU activations	Lightweight baseline for tabular data; low variance.
	Medium Neural Network	Both	1 hidden layer, 25 neurons, ReLU	Balanced single-layer expressiveness.
	Wide Neural Network	Both	1 hidden layer, 100 neurons, ReLU	High-capacity shallow net to capture strong nonlinearity.
	Bilayered Neural Network	Both	2 hidden layers, [10, 10] neurons, ReLU	Adds hierarchical structure with modest depth.
	Trilayered Neural Network	Both	3 hidden layers, [10, 10, 10] neurons, ReLU	Deepest preset; models coupled interactions while keeping size modest.
Ensemble	Bagged Trees	Both	Bootstrap aggregation of deep decision trees	Variance reduction by averaging; robust across mixed regimes.
	Boosted Trees	Both	Adaptive boosting of shallow trees	Bias reduction with stage-wise learning; strong on hard boundaries.

Gaussian Process Regression (GPR)	Matern 5/2 GPR	Regression	Matérn ν=5/2 kernel, constant basis; kernel scale estimated	Smooth but flexible prior; strong empirical fit for $\beta_{\max}$
	Rational Quadratic GPR	Regression	Rational-quadratic kernel, constant basis; kernel scale estimated	Multi-scale variability via mixture of length scales.
	Squared Exponential GPR	Regression	Squared-exponential (Gaussian radial basis) kernel, constant basis; kernel scale estimated	Very smooth prior when $\beta_{\max}$ varies gradually.
	Exponential GPR	Regression	Exponential kernel, constant basis; kernel scale estimated	Allows rougher functions and mild kinks.
Support Vector Machine (SVM)	Linear SVM	Both	Linear kernel	Fast, interpretable margin; baseline for near-linear trends.
	Quadratic SVM	Both	Polynomial kernel, degree 2	Captures simple global curvature.
	Cubic SVM	Both	Polynomial kernel, degree 3	Adds higher-order structure without locality.
	Fine Gaussian SVM	Both	Gaussian radial-basis kernel, kernel scale 0.5	Very local decision regions; sharp boundaries.
	Medium Gaussian SVM	Both	Gaussian radial-basis kernel, kernel scale 2	Balanced locality vs smoothness; reliable general-purpose choice.
	Coarse Gaussian SVM	Both	Gaussian radial-basis kernel, kernel scale 8	Smooth boundaries; lower variance on small datasets.
K-Nearest Neighbors (KNN)	Fine KNN	Classification	k=1, Euclidean distance, equal weights	Maximally local; highest variance.
	Medium KNN	Classification	k=10, Euclidean distance, equal weights	Balanced smoothing; standard baseline.
	Coarse KNN	Classification	k=100, Euclidean distance, equal weights	Strong smoothing; resists overfit but may underfit sharp transitions.
	Cosine KNN	Classification	k=10, cosine distance, equal weights	Direction-based similarity; works well with standardized features.
	Cubic KNN	Classification	k=10, Minkowski distance with order 3, equal weights	Alternative norm geometry for boundary shape.
	Weighted KNN	Classification	k=10, Euclidean distance, distance-squared weights	Emphasizes nearby neighbors; sharper locality.
Tree	Fine Tree	Both	Small leaf size (deep tree)	Detailed partitions; higher variance.

	Medium Tree	Both	Moderate leaf size	Bias–variance balance; interpretable splits.
	Coarse Tree	Both	Large leaf size (shallow tree)	Stable, simple structure; high-bias baseline.
Linear	Linear Discriminant	Classification	Shared-covariance linear discriminant	Simple, interpretable baseline for class margins.
	Linear Regression	Regression	Classical least squares	Fast $\beta_{\max}$ trend baseline.

4.2.4 Model selection criteria

Model choice is anchored in the strictly unseen test-set accuracy, stability across partitioning, calibration, and consistency with known physical trends. For classification, accuracy is reported as Micro-F1 on the unseen test data. Micro-F1 pools true and false counts over all classes before combining precision and recall, so it reflects the actual operating priors of the corpus and remains numerically stable under imbalance. In single-label multiclass settings it coincides with accuracy, keeping interpretation straightforward, while still penalizing any loss of recall on rare splash outcomes. This is appropriate here because test priors are preserved by design and class-weighted training already counteracts rarity during fitting. For regression, the headline metric is RMSE on the unseen test set. RMSE aligns with the squared-loss objectives used by the regressors, emphasizes large deviations, and is therefore suited to $\beta_{\max}$ where occasional big errors near regime boundaries are more consequential than many small ones. RMSE is reported in the same magnitude as $\beta_{\max}$, which keeps comparisons physically meaningful.

Families and presets are compared by their mean test Micro-F1 or RMSE and by dispersion across split and fold settings; preference goes to models that pair strong central performance with low variability. If scores are effectively tied, priority is given to better-calibrated classifiers and

to regressors whose predictive uncertainty coheres with residual structure, as in well-behaved GPR. Final selections report best-in-family and best-overall presets that are accurate on unseen data, stable to splitting and folding, and consistent with expected trends such as increasing $\beta_{\max}$ with inertia at fixed viscous loading and core fraction.

4.3 Results and Discussion

All results are out-of-sample under the stratified splitting protocol. Evaluation proceeds along three complementary lenses: first, family-level stability across the various splitting and folding settings; second, preset-level comparisons within each family to identify capacity-appropriate configurations; and third, physics-grounded interpretability for the top-performing model, using feature-importance rankings and dependency profiles to verify that learned trends respect the governing balances rather than dataset artifacts. Together, these lenses separate raw accuracy from robustness and physical credibility.

4.3.1 Classification results

4.3.1.1 Performance of model families and presets across split-fold settings

At the family level, the heat map in Figure 4-9 and the preset dispersion in Figure 4-10 (per-split-fold boxplots aggregated over the nine settings) reveal a stable hierarchy that is consistent across all splitting and folding settings. Learners whose hypothesis spaces admit smooth, coupled nonlinear decision surfaces, i.e., a good match to the way outcome boundaries bend with $\overline{\mathrm{We}}$, α, Re_i, and Re_o, consistently lead the table, whereas models that enforce rigid geometry (global linear margins, axis-aligned partitions, or purely local voting) trail. Neural Networks therefore occupy the top band across all settings, with Micro-F1 peaking near 94.5% at the 80/20 split with

5-fold cross-validation. A single hidden layer already captures the broad manifolds that separate jetting, partial rebound, and spreading contact while accommodating kinks near film-rupture and

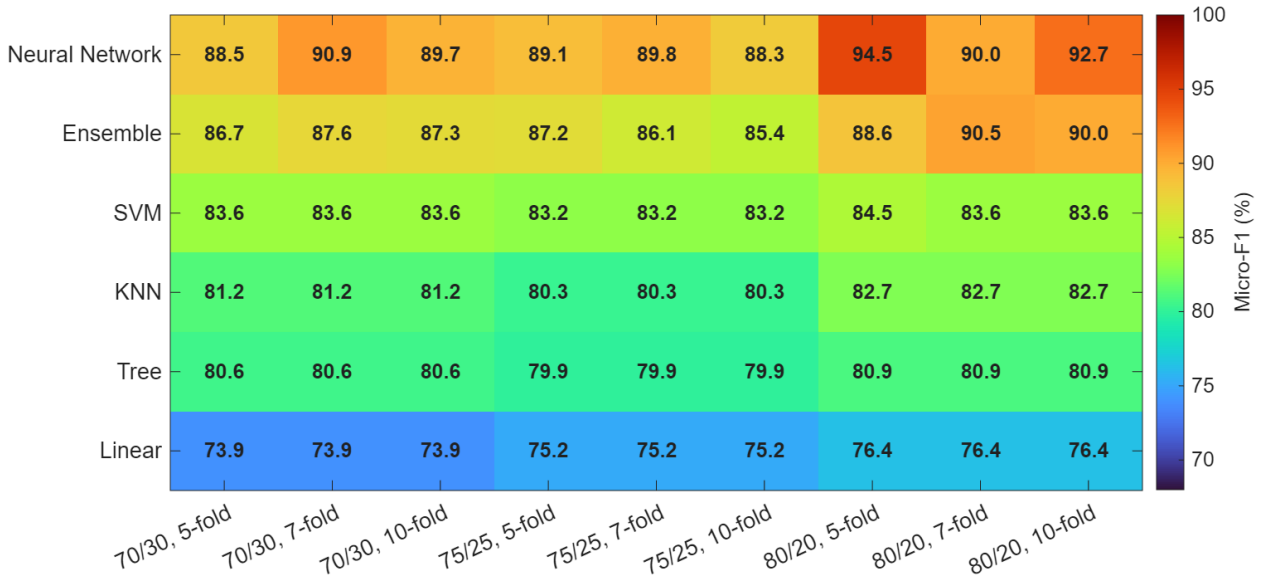

Figure 4-9 Family-level heat map of test Micro-F1 scores (%) across the nine split–fold settings. Rows are model families and columns are split–fold combinations.

rim-instability thresholds; early stopping and class-weighted losses keep variance low despite imbalance. Tree ensembles follow closely: boosting reduces bias at sharp onsets such as prompt splash, while bagging stabilizes performance when regimes mix, yielding high-80s to low-90s Micro-F1 scores with tight spreads. Support-vector machines sit a tier lower, typically mid-80s Micro-F1 scores, reflecting sensitivity to kernel scale since fixed locality can either under-resolve or over-localize regime bends depending on the split. KNN and single trees cluster around 80-83% Micro-F1 scores, limited by locality or axis-aligned cuts when multiple nondimensional groups move together. The linear baseline anchors the floor near 74-76% Micro-F1 scores, confirming that a single global margin is insufficient for this physics and providing a useful difficulty reference for the corpus.

At the preset-level, Figure 4-10 summarizes dispersion for each preset across the nine settings formed by the three split ratios and threefold counts. Within Neural Networks, the single-hidden-layer medium preset provides the highest central Micro-F1 scores with the narrowest interquartile ranges, indicating sufficient capacity to capture the smooth, coupled nonlinear boundaries without inviting variance. The wide single-layer preset matches peak scores sporadically but shows larger spread, consistent with overfitting pressure from minority splash modes. Adding depth to two or three layers yields small gains in particular settings but increases variability, which aligns with the limited sample size within some strata. In the ensemble family, boosted trees slightly edge bagging when sharp onsets are present, while bagging exhibits the smallest dispersion when regimes mix. For SVMs, the medium Gaussian kernel offers the most stable trade-off between locality and smoothness; fine and coarse scales alternately under- or over-localize depending on the split, which raises variability. Stand-alone trees show the expected progression from fine to coarse leaves, with stability improving as leaf size grows at the expense of bias. KNN presets cluster below SVMs and ensembles, with the weighted variant outperforming its equal-weight neighbors, which is consistent with the advantage of emphasizing nearby points in standardized space.

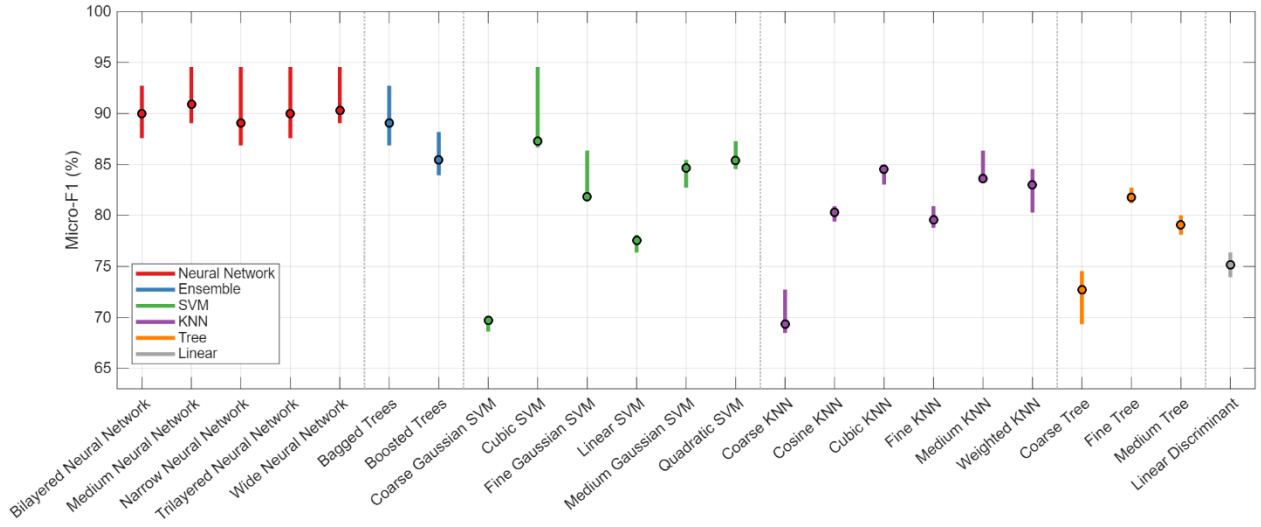

Figure 4-10 Preset-level performance dispersion aggregated over all nine split–fold settings. Points show the mean test Micro-F1 score per preset and vertical bars indicate the range across settings.

Sensitivity to the split and fold settings is modest for the top families and more pronounced for lower-capacity baselines. As the training share increases from 70 to 80 percent, the median Micro-F1 scores rise slightly and the interquartile ranges contract, most clearly for Neural Networks and ensembles in Appendix C Figure S7 (i.e., per-split-fold boxplots aggregated over the nine settings). Varying k-folds between 5, 7, and 10 mainly reduces dispersion without altering the family ordering. The preset-level heat map in Appendix C Figure S8 shows the same behavior within families: the stronger presets maintain their rank across all nine settings, whereas models with rigid geometry or purely local voting exhibit larger split-to-split spread. Overall, capacity-appropriate models are stable to partition choices, while locality-driven and axis-aligned models are more sensitive.

4.3.1.2 Top performing model preset and physical interpretability

The Medium Neural Network is the most accurate and stable preset across the nine split–fold settings. In the all-preset heat map (see Appendix C Figure S8) it maintains Micro-F1 scores around 89-91 percent for the 70/30 and 75/25 splits and rises to 94.5 percent at 80/20 with 5-, 7-, or 10-fold cross-validation, indicating that a single hidden layer with moderate width is sufficient to capture the coupled nonlinear boundaries induced by $\overline{\mathrm{We}}$, α, Re_i, and Re_o.

This strong NN performance, despite the moderate dataset size, is consistent with both the structure of the present problem and prior droplet-impact literature. First, the learning task is compact and physics-organized, since the models use only four non-dimensional predictors, namely equivalent Weber number, core volume fraction, and the Reynolds numbers of the core and shell. Second, the dataset originates from a single internally consistent experimental campaign, which reduces heterogeneity relative to pooled multi-source datasets. Third, the neural-network presets considered here were shallow and capacity-controlled, rather than highly over-parameterized deep architectures. In fact, the results show that the medium single-hidden-layer network achieved the best balance of accuracy and stability, whereas wider and deeper variants exhibited greater variability, indicating that only moderate nonlinear capacity was needed to capture the governing regime boundaries and spreading trends. This behavior is also consistent with previous droplet-impact studies on single-liquid systems, where compact or shallow neural networks trained on small-to-medium datasets were sufficient to delineate transitions between impact outcomes and to predict maximum spreading, provided that the inputs were physically meaningful and the validation protocol was rigorous [40]-[45], [48]. These

studies suggest that, for droplet-impact problems, strong neural-network performance depends less on very large sample size than on the use of compact physics-based features, internally consistent data, and appropriate regularization. In the present work, standardization, stratified train-test splitting, repeated cross-validation, early stopping, and class-weighted learning further limited overfitting and improved generalization. Therefore, the NN performed well not because large data requirements are unimportant in general, but because this particular problem was well suited to a shallow network operating on a compact and physically structured feature space.

The confusion matrices in Figure 4-11a (cross-validated validation folds) and Figure 4-11b (held-out test set) show high true-positive rates (TPR) on the dominant non-splashing regimes and credible signal on rare splash counterparts. On the test set the true-positive rates are 93.0 percent for Jetting, 77.9 percent for Partial Rebound, 80.0 percent for Spreading-Contact, 61.5 percent for J+S, 65.6 percent for PR+S, and 75.0 percent for SC+S. Errors concentrate along adjacent physical transitions rather than across distant regimes, for example PR sometimes

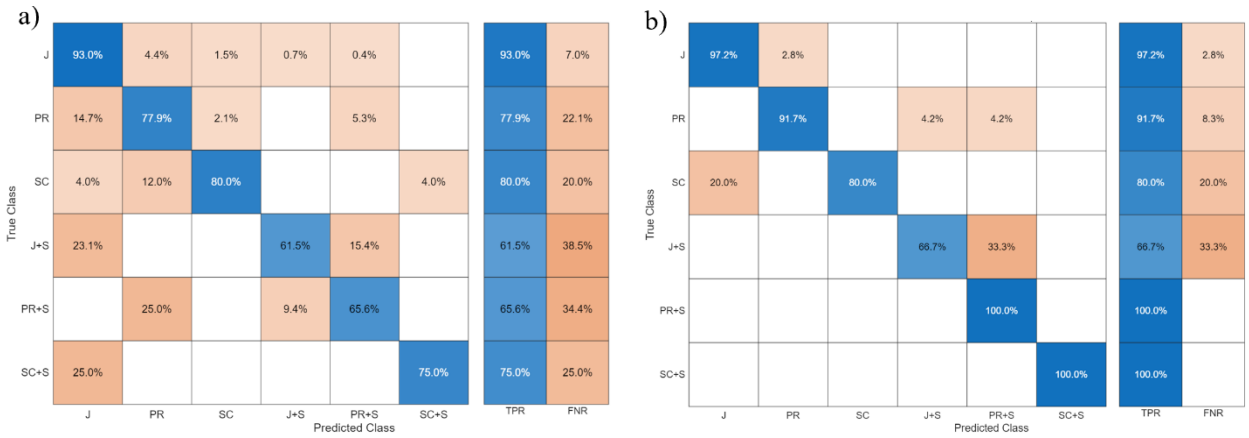

Figure 4-11 Confusion matrices for the Medium Neural Network at the best-performing setting (i.e., 80/20 with 5-folds): (a) cross-validated folds and (b) held-out test set. Rows are true classes and columns are predicted classes. Side panels report class-wise true positive rates and false negative rates.

settling to J or PR+S and J+S occasionally merging with J, which matches the proximity of lift-off and rim-instability thresholds in the governing space.

To verify that the model's predictions reflect the governing balances rather than sampling artifacts, feature attribution was obtained via Shapley values to quantify feature influence by class (Figure 4-12). For each prediction, Shapley values measure how much a feature shifts the class score away from a baseline while accounting for interactions; taking the mean absolute value over all examples in a class yields an average magnitude of influence. The resulting rankings reproduce the sensitivities in Table 4-1. For J, Re_o dominates followed by $\overline{\mathrm{We}}$ and α, consistent with jetting being favored by low inertia and strong shell-side damping. For PR, $\overline{\mathrm{We}}$ contributes the most with influence from α and Re_i, matching inertia-driven

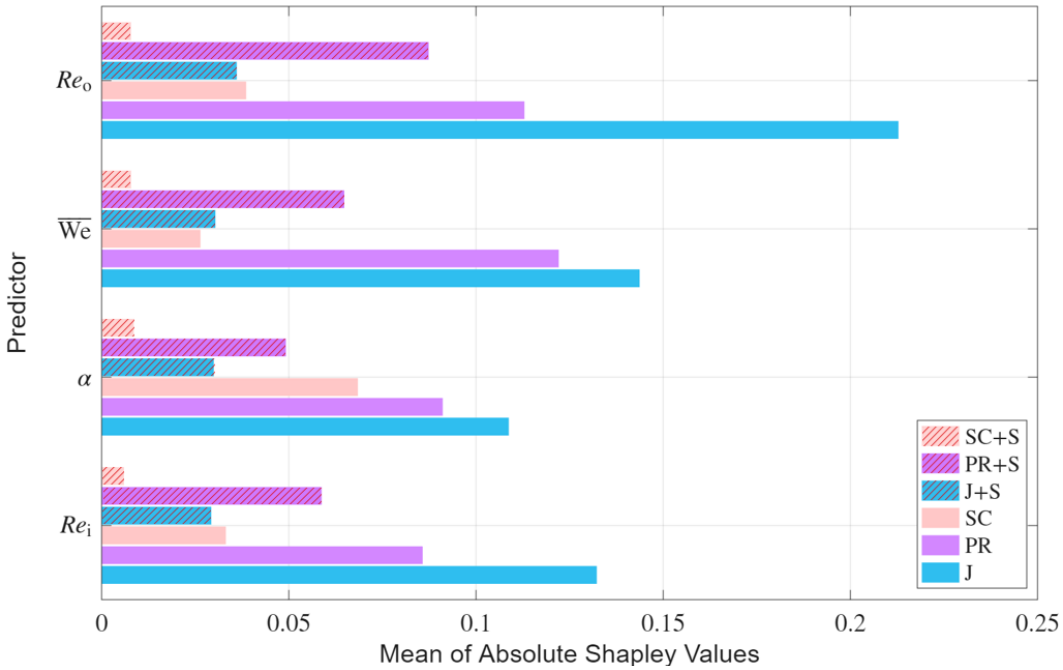

Figure 4-12. Mean absolute Shapley values for the top performing preset (i.e., Medium Neural Network) by class and predictor. Solid fill denotes non-splashing classes (J, PR, SC) and hatched bars denote splashing counterparts (J+S, PR+S, SC+S). Larger bars indicate stronger influence.

recoil moderated by core volume (enhancing the surface-energy reservoir at the inner-outer interface) and core viscosity (lower viscosity promoting breakup of the vertical jet). For SC, α and Re_o exceed Re_i, which accords with spreading being controlled mainly by core fraction and shell dissipation after contact. The splashing counterparts shift weight toward $\overline{\mathrm{We}}$ and Re_o, indicating that higher inertia and weaker shell damping promote rim corrugation and prompt ejection. The alignment between these attributions and the mechanism tables supports the physical credibility of the Medium NN.

Univariate dependency profiles (Figure 4-13) provide a complementary, physics-oriented check on what the Medium NN has learned. Each curve traces the class score as a single predictor varies while the remaining predictors are fixed at their median values, isolating first-order trends without confounding interactions. The resulting shapes align with the regime mechanics summarized earlier in Table 4-1. Along $\overline{\mathrm{We}}$, the jetting score decays from low-inertia conditions and reaches a minimum in the transitional window where the recoil column destabilizes; partial rebound rises through this window and then cedes to its splashing counterpart as rim corrugation becomes energetically favorable at higher inertia. Increasing α strengthens spreading-contact and eventually suppresses partial rebound, reflecting shell thinning and the approach to a rupture thickness set by core fraction; jetting declines monotonically with α, while SC+S appears only at the largest cores where rupture coincides with strong rim forcing. Growth in Re_i modestly elevates partial rebound relative to jetting by reducing core-side viscous damping of the recoil column, consistent with easier pinch-off into core-rich satellites. In contrast, growth in Re_o strongly suppresses jetting and elevates both PR and PR+S because higher shell Reynolds

number corresponds to lower shell viscosity and weaker lamella damping, conditions that favor column break-up and rim instability. Taken together, these dependencies mirror the Shapley rankings and the mechanism tables: film integrity and shell-side dissipation govern jetting; inertia and core fraction drive recoil and its splashing transition; and shell viscosity sets the stability of the spreading rim.

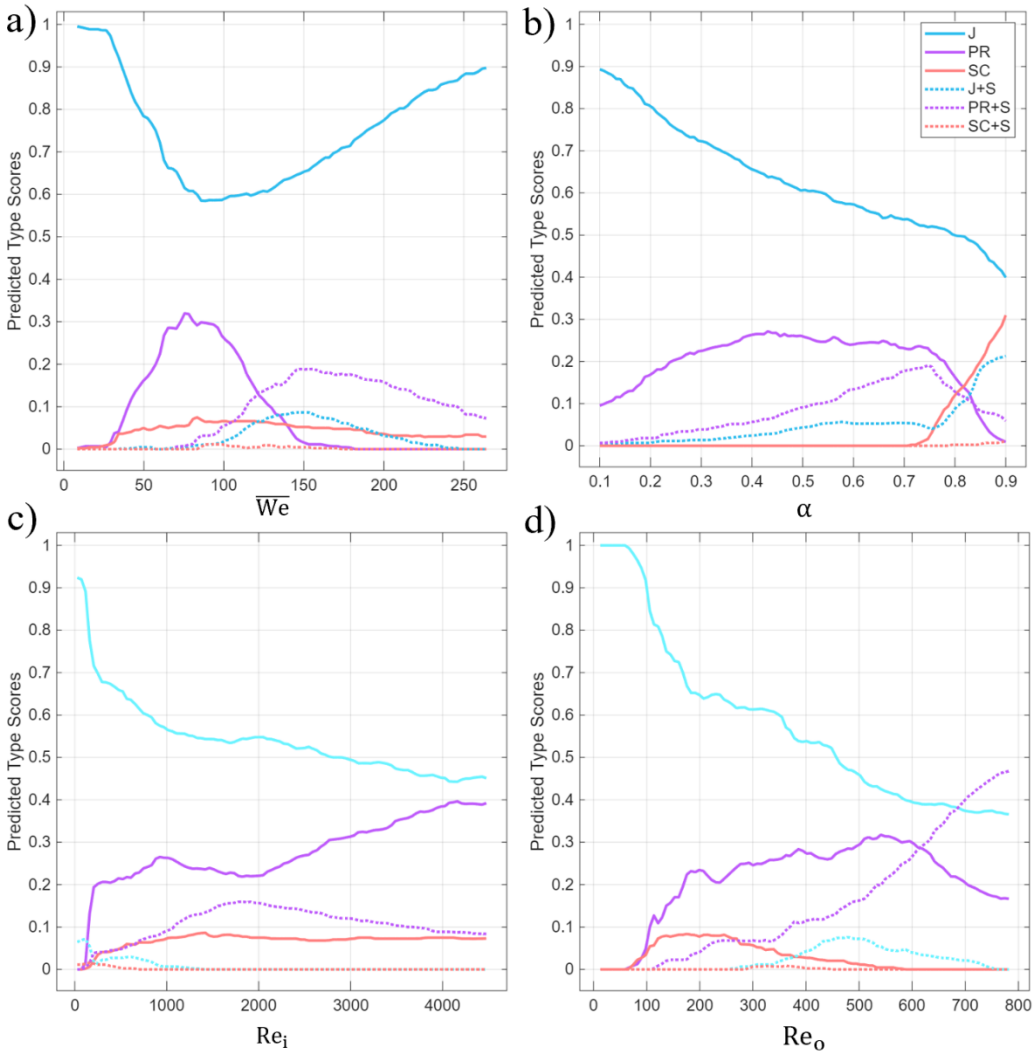

Figure 4-13 Class-score dependency profiles for the top preset (i.e., Medium Neural Network) versus (a)$\overline{We}$, (b) α, (c) Re_i, and (d) Re_o. Curves show predicted class scores with the other predictors fixed at their medians. Solid lines denote non-splashing classes and dashed lines denote splashing counterparts.

For a direct qualitative comparison with the experimentally observed regime topology, Figure S11 in Appendix C presents a neural-network-predicted impact regime map for the W/S5 liquid pair in the same $\overline{We} - \alpha$ plane as the experimental map in Figure 2-7, generated using the top-performing classification preset. The predicted map reproduces the main organization of the outcome space, with only minor differences near transition boundaries, consistent with the neighboring-class confusion discussed above.

4.3.2 Regression results

4.3.2.1 Performance of model families and presets across split–fold settings

At the family level, the heat map in Figure 4-14 shows a clear and stable ordering that persists across the nine split–fold settings. Gaussian-process regression (GPR) yields the lowest errors, with test RMSE clustering near 0.050 to 0.055. Single-hidden-layer neural networks follow with RMSE near 0.058 to 0.063. Support-vector regressors occupy a middle tier around 0.088 to 0.094. Tree models and ensembles are higher, typically 0.095 to 0.107, and linear regression grounds the baseline near 0.12 to 0.14. This hierarchy is consistent with the physics of $\beta_{\max}$: the response varies smoothly with $\overline{\mathrm{We}}$ and exhibits broad, gently non-monotone trends in α and $Re_o$with weak sensitivity to Re_i. Kernels that represent multi-scale smoothness and moderate curvature therefore match the problem well, which favors GPR. Neural networks with controlled capacity approximate the same structure but require slightly more data to stabilize. Fixed-scale SVM kernels and piecewise models are disadvantaged when the characteristic length scales change across the operating window.

Sensitivity to the split ratio is small, whereas increasing the number of the cross-validation folds from 5 to 10 tightens dispersion and yields modest but systematic RMSE reductions across families. The same pattern is visible per preset in Appendix C Figure S9: RMSE heat maps decrease slightly and R^2 heat maps increase slightly as k-folds grows, with ordering unchanged. These effects indicate that the main gains come from variance reduction through deeper cross-validation rather than from marginal increases in the training fraction.

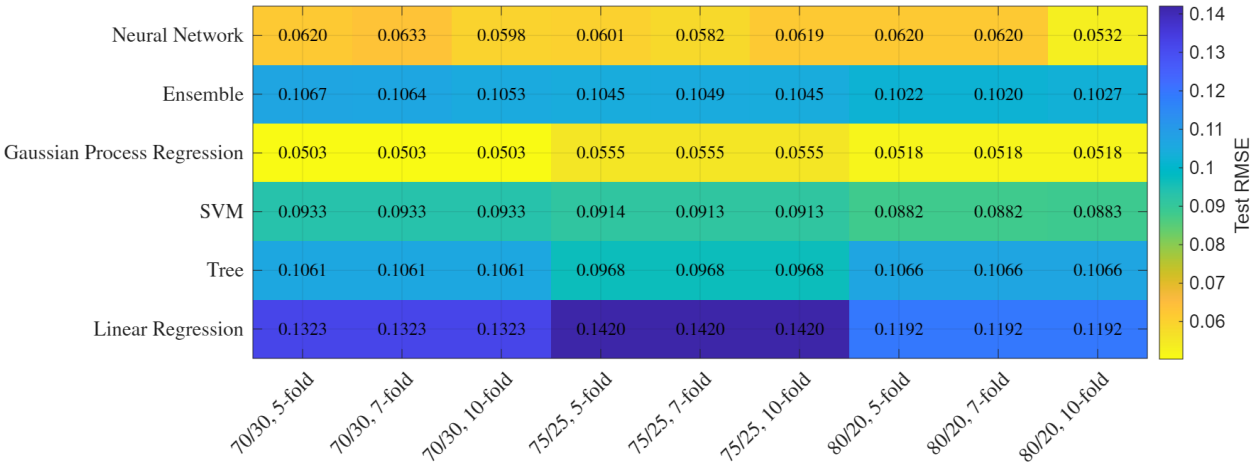

Figure 4-14 Family-level heat map of test RMSE across the nine split–fold settings. Rows are model families and columns are split–fold combinations. Lower values indicate better accuracy.

Preset-level aggregation in Figure 4-15 confirms the family picture. Within GPR, the Matérn 5/2 kernel is the most accurate with narrow ranges across settings; the rational-quadratic and squared-exponential kernels follow closely. Among neural networks, the medium single-hidden-layer preset is the best calibrated, with the wide and trilayer variants occasionally matching its mean but with larger spread. Bagged trees outperform boosted trees in this corpus, consistent with variance reduction being more valuable than stage-wise bias correction for the smooth $\beta_{\max}$

surface. Within SVMs, cubic and medium Gaussian kernels form the leading cluster. The stability of these ranks across the nine settings matches the expectation for a response dominated by smooth inertial–capillary balance with viscosity-limited saturation.

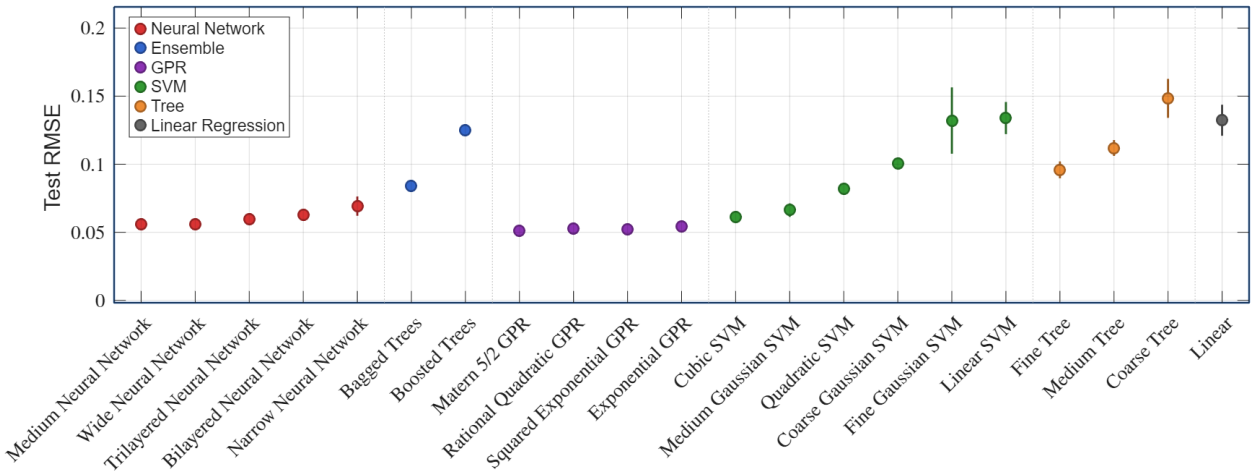

Figure 4-15 Preset-level performance aggregated over all nine split–fold settings. Points show the mean test RMSE per preset and vertical bars indicate the range across settings.

4.3.2.2 Top performing model preset and physical interpretability

The Matérn 5/2 GPR preset emerges as the top preset. Parity plots in Figure 4-16 show tight alignment to the identity line on both training and held-out test sets, with R^2 near 98% at all split-fold configurations reported in Appendix C Figures S9-S10, and no visible heteroscedastic fan-out. Residuals are centered with narrow spread, indicating unbiased fit and good generalization.

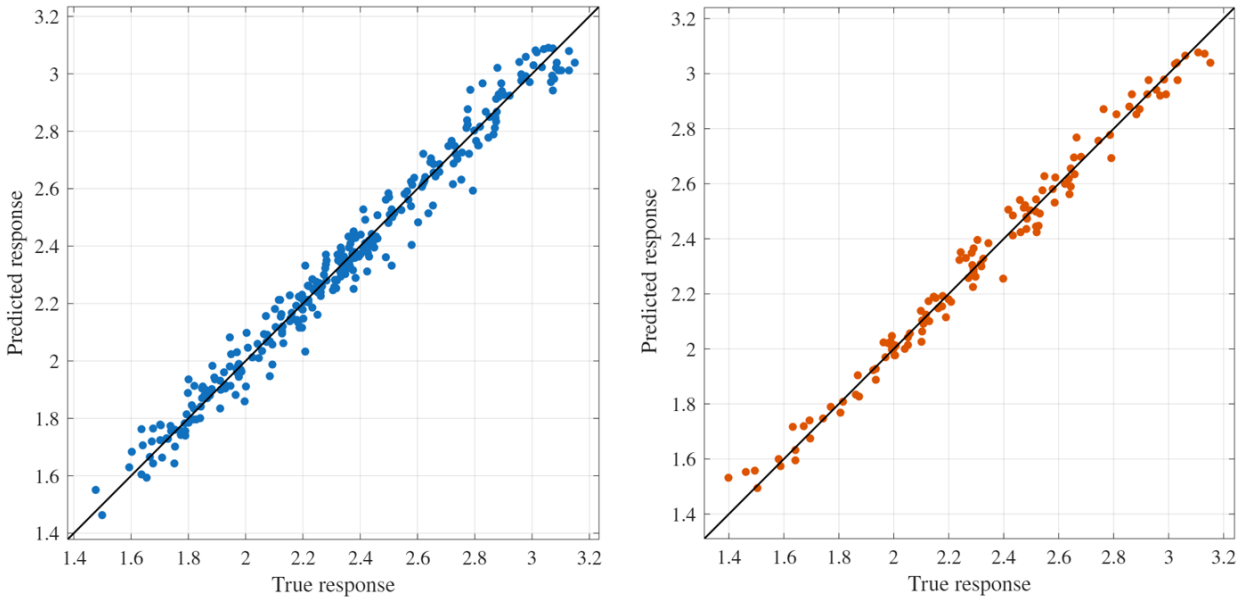

Figure 4-16 Parity plots for the top preset (Matérn 5/2GPR): left, training folds; right, held-out test set. Each marker is one impact and the solid line is the identity.

Shapley attribution in Figure 4-17 quantifies feature influence at the prediction level and then aggregates it across the dataset. For each impact, a Shapley value measures how much a predictor shifts the predicted $\beta_{\max}$ away from a baseline while accounting for interactions; the sign indicates increase or decrease and the magnitude reflects strength. The beeswarm shows $\overline{\mathrm{We}}$ as the largest positive driver over much of its range, consistent with inertial-capillary growth of the lamella. Re_o contributes positively at low to moderate values and weakly negative at the highest values, which aligns with shell viscosity controlling dissipation early in the spread and a reduction at very high Re_o when lamella thinning and rim drainage limit further growth. α exhibits mixed contributions with a broad band around zero, reflecting a shallow optimum: small cores have little effect, mid-range cores enhance spread by adding interfacial-energy storage and

inertia, and very large cores begin to confine the shell film. Re_i shows the weakest effect and is slightly negative at high values, consistent with core-side viscous losses being secondary at fixed α and with increased core mobility not feeding additional energy into the shell after contact. These attributions are consistent with the sensitivities summarized in Table 4-2.

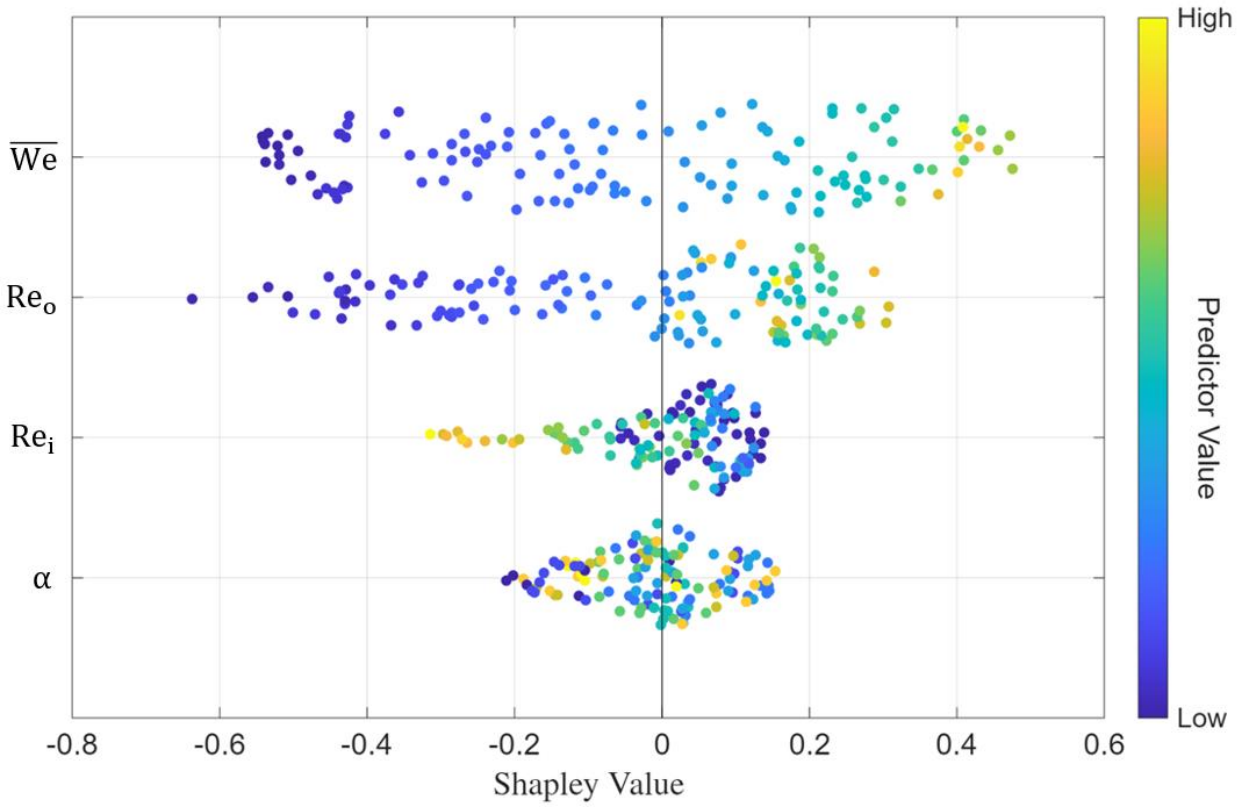

Figure 4-17 Shapley beeswarm for the top preset. Each point is a prediction; horizontal position is the Shapley value for the labeled predictor; color encodes the predictor's value from low to high. Positive values increase predicted β_{max}.

One-predictor dependency profiles in Figure 4-18 provide a complementary, physically oriented check. With the remaining predictors fixed at their medians, $\beta_{\max}$ increases steeply with $\overline{\mathrm{We}}$ and then approaches a gentle plateau with a slight rollover at the very highest inertia. This shape matches inertial growth bounded by capillarity and shell-side dissipation. The curve versus αshows a broad maximum at intermediate core fractions, reflecting the balance between added inertia and interfacial-energy storage at mid $\alpha$and film confinement at large α. The dependence on Re_i is weak and trends downward beyond $O(10^3)$, consistent with core viscosity being a secondary control at fixed α. The curve versus Re_o is hump-shaped: reduced shell viscosity initially increases $\beta_{\max}$, followed by a mild decline at high Re_o where the lamella is thin and rim growth and drainage limit lateral coverage. Taken together, the dependencies and the Shapley signatures agree with Table 4-2 and indicate that the Matérn $5/2$ GPR is learning the governing balances rather than incidental correlations.

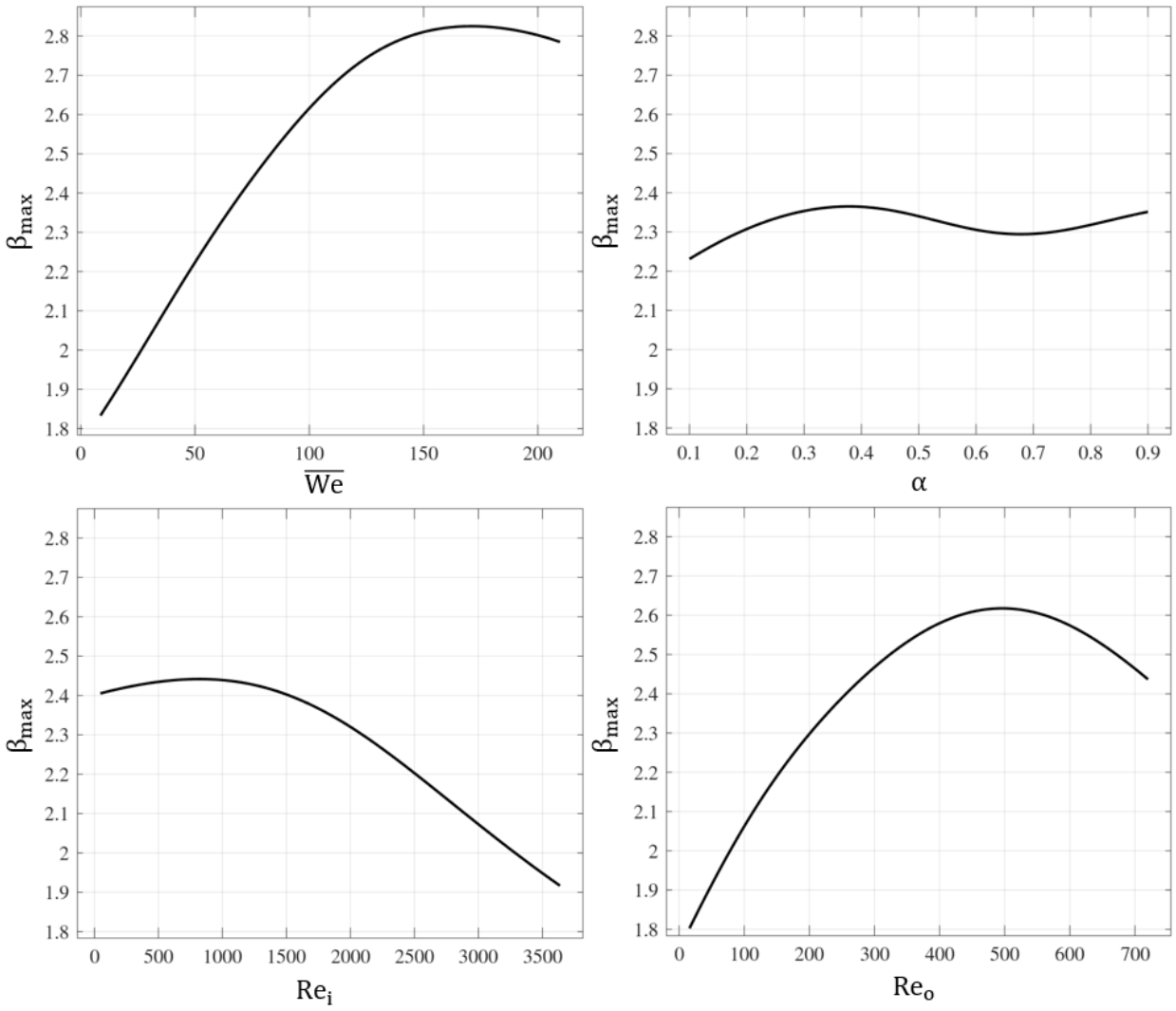

Figure 4-18 One-predictor dependency profiles for the top preset showing β_{max} versus $\overline{We}$, α, Re_i, and Re_o with the remaining predictors fixed at their medians.

Beyond predictive accuracy, the machine-learning analysis provides additional physical insight by quantifying the hierarchy of controls and clarifying where model complexity is most needed. Across both classification and regression, the SHAP attributions and dependency profiles consistently identify the equivalent Weber number, $\overline{\mathrm{We}}$, and the core volume fraction, α, as the

dominant predictors, showing that impact inertia and internal geometry set the first-order response of the system. The shell Reynolds number, Re_o, emerges as the next most important control, which is physically consistent with the shell being the phase that forms the lamella, interacts directly with the wall, and governs rim stability and viscous damping during spreading and recoil. In contrast, the core Reynolds number, Re_i, generally has the weakest influence, indicating that core-side viscous effects are secondary over much of the explored domain and become important mainly in recoil-sensitive cases or when the core is both large and highly viscous. This ranking is physically useful because it suggests that reduced-order mechanistic models for regime prediction or maximum spreading may treat $\overline{\mathrm{We}}$, α, and Re_oas leading-order variables, while Re_i can often be retained as a refinement term rather than a primary control parameter. The class-wise dependency trends provide further insight into the phenomenon: jetting is favored by low inertia and strong shell-side damping, partial rebound grows in the intermediate window where recoil becomes strong enough for lift-off, and splashing classes are promoted by higher inertia together with weaker shell damping that encourages rim instability. For maximum spreading, the same interpretability tools show a steep increase with $\overline{\mathrm{We}}$, a broad optimum with α, a secondary shell-viscosity effect through Re_o, and only weak sensitivity to Re_i. In this sense, the ML framework does more than reproduce the data: it identifies which mechanisms dominate each response, shows that most regime transitions are local in parameter space, and indicates where future physics-based models may be simplified without losing the leading-order structure of the problem.

4.4 Conclusions – Key highlights

- Developed a physics-organized machine-learning framework for core–shell droplet impact, using a compact set of multicomponent non-dimensional predictors (equivalent Weber number, core volume fraction, shell and core Reynolds numbers) to model both impact outcome (classification) and maximum spreading factor β_{max}(regression).

- Achieved high and robust classification performance across stratified train–test splits and k-fold cross-validation, with most misclassifications confined to physical boundaries between neighboring regimes (for example, jetting versus partial rebound and non-splashing versus splashing variants).

- Identified Gaussian process regression with a Matérn-type kernel as the most accurate and stable regression model for β_{max}, delivering tight parity with experiments, high R^2, and low error norms on held-out test data without visible heteroscedastic fan-out.

- Used interpretability tools to show that equivalent Weber number and core volume fraction are the dominant predictors for both outcome and β_{max}, with shell Reynolds number acting as a secondary control and core Reynolds number playing a minor role, in agreement with experimental trends and the energy-balance model.

- Demonstrated that, once trained on the experimental dataset, the machine-learning models provide fast, accurate, and physically consistent predictions across the explored parameter space, complementing the energy-balance model and enabling data-driven exploration and design of core–shell droplet impact conditions.

4.5 References

[1] B.-J. Wei *et al.*, "Droplet impact outcomes: Effect of wettability and Weber number," *Physics of Fluids*, vol. 36, no. 7, 2024.

[2] C. Josserand and S. T. Thoroddsen, "Drop impact on a solid surface," *Annu Rev Fluid Mech*, vol. 48, pp. 365–391, 2016, doi: 10.1146/annurev-fluid-122414-034401.

[3] G. Riboux and J. M. Gordillo, "Experiments of drops impacting a smooth solid surface: a model of the critical impact speed for drop splashing," *Phys Rev Lett*, vol. 113, no. 2, p. 024507, 2014, doi: 10.1103/PhysRevLett.113.024507.

[4] A. L. Yarin, "Drop impact dynamics: splashing, spreading, receding, bouncing…," *Annu. Rev. Fluid Mech.*, vol. 38, no. 1, pp. 159–192, 2006.

[5] R. Rioboo, C. Tropea, and M. Marengo, "Outcomes from a drop impact on solid surfaces," *At. Sprays*, vol. 11, no. 2, 2001.

[6] A. Mohammad Karim, "Physics of droplet impact on various substrates and its current advancements in interfacial science: A review," *J Appl Phys*, vol. 133, no. 3, 2023.

[7] M. J. Docherty, P. Naderi, G. Grau, K. Sefiane, and A. Amirfazli, "Inkjet printing on hydrophobic surface: Practical implementation of stacked coin strategy," *Adv Eng Mater*, vol. 26, no. 11, p. 2400237, 2024.

[8] D. Lohse, "Fundamental fluid dynamics challenges in inkjet printing," *Annu Rev Fluid Mech*, vol. 54, pp. 349–382, 2022.

[9] S. V Murphy and A. Atala, "3D bioprinting of tissues and organs," *Nat Biotechnol*, vol. 32, no. 8, pp. 773–785, 2014, doi: 10.1038/nbt.2958.

[10] G. Liang and I. Mudawar, "Review of spray cooling–Part 1: Single-phase and nucleate boiling regimes, and critical heat flux," *Int J Heat Mass Transf*, vol. 115, pp. 1174–1205, 2017.

[11] W.-L. Cheng, W.-W. Zhang, H. Chen, and L. Hu, "Spray cooling and flash evaporation cooling: The current development and application," *Renewable and Sustainable Energy Reviews*, vol. 55, pp. 614–628, 2016.

[12] W. M. Grissom and F. A. Wierum, "Liquid spray cooling of a heated surface," *Int J Heat Mass Transf*, vol. 24, no. 2, pp. 261–271, 1981.

[13] T. Li, M. Li, and H. Li, "Impact-induced removal of a deposited droplet: Implications for self-cleaning properties," *J Phys Chem Lett*, vol. 11, no. 15, pp. 6396–6403, 2020.

[14] A. L. N. Moreira, A. S. Moita, and M. R. Panao, "Advances and challenges in explaining fuel spray impingement: How much of single droplet impact research is useful?," *Prog Energy Combust Sci*, vol. 36, no. 5, pp. 554–580, 2010.

[15] B. Wang *et al.*, "Sustained agricultural spraying: from leaf wettability to dynamic droplet impact behavior," *Global Challenges*, vol. 7, no. 9, p. 2300007, 2023.

[16] S. Moghtadernejad, C. Lee, and M. Jadidi, "An introduction of droplet impact dynamics to engineering students," *Fluids*, vol. 5, no. 3, p. 107, 2020.

[17] A. Amirfazli, M. D. Bustamante, Y. Hu, and L. Ó Náraigh, “Bounds on the spreading radius in droplet impact: the inviscid case,” *Proceedings of the Royal Society A*, vol. 480, no. 2294, p. 20230760, 2024.

[18] L. Xu, W. W. Zhang, and S. R. Nagel, “Drop splashing on a dry smooth surface,” *Phys Rev Lett*, vol. 94, no. 18, p. 184505, 2005.

[19] L. Xu, L. Barcos, and S. R. Nagel, “Splashing of liquids: Interplay of surface roughness with surrounding gas,” *Physical Review E—Statistical, Nonlinear, and Soft Matter Physics*, vol. 76, no. 6, p. 066311, 2007.

[20] C. Tang *et al.*, “Dynamics of droplet impact on solid surface with different roughness,” *International Journal of Multiphase Flow*, vol. 96, pp. 56–69, 2017.

[21] N. Blanken, M. S. Saleem, M.-J. Thoraval, and C. Antonini, “Impact of compound drops: a perspective,” *Curr Opin Colloid Interface Sci*, vol. 51, 2020, doi: 10.1016/j.cocis.2020.09.002.

[22] N. Blanken, M. S. Saleem, C. Antonini, and M.-J. Thoraval, “Rebound of self-lubricating compound drops,” *Sci Adv*, vol. 6, no. 11, p. eaay3499, 2020, doi: 10.1126/sciadv.aay3499.

[23] Z. Zhang, C.-Y. Zhang, H.-R. Liu, and H. Ding, “Impact dynamics of compound drops of fluids with density contrast,” *J Fluid Mech*, vol. 964, p. A34, 2023.

[24] I. Alkomy, M. Marengo, and A. Amirfazli, “Impact of a core–shell compound droplet on a solid surface,” *Exp Fluids*, vol. 66, no. 5, p. 97, 2025.

[25] Y. Du, L. Dai, L. Qian, F. Zhou, and Y. Ma, “Impact of a compound droplet on a solid surface: The effect of the shell on the core,” *Exp Therm Fluid Sci*, vol. 160, p. 111330, 2025.

[26] R. H. Chen, M. J. Kuo, S. L. Chiu, J. Y. Pu, and T. H. Lin, “Impact of a compound drop on a dry surface,” *J Mech Sci Technol*, vol. 21, pp. 1886–1891, 2007, doi: 10.1007/BF03177445.

[27] S. Tasoglu, G. Kaynak, A. Szeri, … U. D.-P. of, and undefined 2010, “Impact of a compound droplet on a flat surface: A model for single cell epitaxy,” *pubs.aip.org*, Accessed: Oct. 30, 2023. [Online]. Available: https://pubs.aip.org/aip/pof/article/22/8/082103/256539

[28] S. Tasoglu, G. Kaynak, A. J. Szeri, U. Demirci, and M. Muradoglu, “Impact of a compound droplet on a flat surface: A model for single cell epitaxy,” *Phys. Fluids*, vol. 22, no. 8, 2010.

[29] H.-R. Liu, C.-Y. Zhang, P. Gao, X.-Y. Lu, and H. Ding, “On the maximal spreading of impacting compound drops,” *J Fluid Mech*, vol. 854, p. R6, 2018.

[30] A. Kumar and D. K. Mandal, “Impact Dynamics of a Compound Drop on a Plane Solid: Effect of the Core Drop Viscosity,” in *Conf Fluid Mech Fluid Power*, Springer, 2021, pp. 391–396. doi: 10.1007/978-981-19-7055-9_66.

[31] A. Kumar and D. K. Mandal, “Impact of compound drops on a plane solid: Role of the core diameter,” *At. Sprays*, vol. 32, no. 2, pp. 1–18, 2022, doi: 10.1615/AtomizSpr.2021038825.

[32] D. Liu and T. Tran, “Emergence of two lamellas during impact of compound droplets,” *Appl Phys Lett*, vol. 112, no. 20, p. 203702, 2018, doi: /10.1063/1.5026821.

[33] D. Liu and T. Tran, “The ejecting lamella of impacting compound droplets,” *Appl Phys Lett*, vol. 115, no. 7, p. 073702, 2019, doi: 10.1063/1.5097370.

[34] R.-H. Chen, S.-L. Chiu, and T.-H. Lin, “Resident time of a compound drop impinging on a hot surface,” *Appl Therm Eng*, vol. 27, no. 11–12, pp. 2079–2085, 2007, doi: 10.1016/j.applthermaleng.2006.11.014.

[35] L. D. L. Q. F. Z. Y. M. Yuying Du, “Impact of a Compound Droplet on a Solid Surface: The Effect of the Shell on the Core,” Jun. 2024. Accessed: Jun. 29, 2024. [Online]. Available: https://papers.ssrn.com/sol3/papers.cfm?abstract_id=4876400

[36] Y. Wei and M.-J. Thoraval, “Maximum spreading of an impacting air-in-liquid compound drop,” *Phys. Fluids*, vol. 33, no. 6, p. 061703, 2021.

[37] T. Bennett and D. Poulikakos, “Splat-quench solidification: estimating the maximum spreading of a droplet impacting a solid surface,” *J Mater Sci*, vol. 28, pp. 963–970, 1993.

[38] S. Chandra and C. T. Avedisian, “On the collision of a droplet with a solid surface,” *Proc R Soc Lond A Math Phys Sci*, vol. 432, no. 1884, pp. 13–41, 1991.

[39] J. B. Lee, D. Derome, R. Guyer, and J. Carmeliet, “Modeling the maximum spreading of liquid droplets impacting wetting and nonwetting surfaces,” *Langmuir*, vol. 32, no. 5, pp. 1299–1308, 2016, doi: 10.1021/acs.langmuir.5b04557.

[40] A. A. Yancheshme, S. Hassantabar, K. Maghsoudi, S. Keshavarzi, R. Jafari, and G. Momen, “Integration of experimental analysis and machine learning to predict drop behavior on superhydrophobic surfaces,” *Chemical Engineering Journal*, vol. 417, p. 127898, 2021.

[41] S. Keshavarzi, J. Sourati, G. Momen, and R. Jafari, “Temperature-dependent droplet impact dynamics of a water droplet on hydrophobic and superhydrophobic surfaces: An experimental and predictive machine learning–based study,” *Int J Heat Mass Transf*, vol. 195, p. 123190, 2022.

[42] M. Pierzyna, D. A. Burzynski, S. E. Bansmer, and R. Semaan, “Data-driven splashing threshold model for drop impact on dry smooth surfaces,” *Physics of Fluids*, vol. 33, no. 12, 2021.

[43] L. Au-Yeung and P. A. Tsai, “Predicting impact outcomes and maximum spreading of drop impact on heated nanostructures using machine learning,” *Langmuir*, vol. 39, no. 50, pp. 18327–18341, 2023.

[44] S. Yang, Y. Hou, Y. Shang, and X. Zhong, “BPNN and CNN-based AI modeling of spreading and icing pattern of a water droplet impact on a supercooled surface,” *AIP Adv*, vol. 12, no. 4, 2022.

[45] S. Yang, Z. Zhang, X. Liu, T. Lai, and Y. Hou, “Spreading dynamics of a droplet impacts on a supercooled substrate: Physical models and neural networks,” *Colloids Surf A Physicochem Eng Asp*, vol. 677, p. 132381, 2023.

[46] H.-Y. Kim and J.-H. Chun, “The recoiling of liquid droplets upon collision with solid surfaces,” *Physics of fluids*, vol. 13, no. 3, pp. 643–659, 2001.

[47] P. Attané, F. Girard, and V. Morin, “An energy balance approach of the dynamics of drop impact on a solid surface,” *Phys. Fluids*, vol. 19, no. 1, 2007.

[48] E. Heidari, A. Daeichian, M. A. Sobati, and S. Movahedirad, “Prediction of the droplet spreading dynamics on a solid substrate at irregular sampling intervals: Nonlinear Auto-Regressive eXogenous Artificial Neural Network approach (NARX-ANN),” *Chemical Engineering Research and Design*, vol. 156, pp. 263–272, 2020.

[49] A. A. Yancheshme, S. Enayati, Y. Kashcooli, R. Jafari, H. Ezzaidi, and G. Momen, “Dynamic behavior of impinging drops on water repellent surfaces: Machine learning-

assisted approach to predict maximum spreading," *Exp Therm Fluid Sci*, vol. 139, p. 110743, 2022.

[50] M. Tembely, D. C. Vadillo, A. Dolatabadi, and A. Soucemarianadin, "A machine learning approach for predicting the maximum spreading factor of droplets upon impact on surfaces with various wettabilities," *Processes*, vol. 10, no. 6, p. 1141, 2022.

[51] R. Choudhury *et al.*, "Uncovering the effect of physical conditions and surface roughness on the maximum spreading factor of impinging droplets using a supervised artificial neural network model," *Ind Eng Chem Res*, vol. 62, no. 49, pp. 21208–21221, 2023.

[52] I. Yoon, J. Chergui, D. Juric, and S. Shin, "Maximum spreading of droplet-particle collision covering a low Weber number regime and data-driven prediction model," *Physics of Fluids*, vol. 34, no. 10, 2022.

[53] W. Yu *et al.*, "A comparison of models for predicting the maximum spreading factor in droplet impingement," *Physics of Fluids*, vol. 36, no. 7, 2024.

[54] D. A. de Aguiar, H. L. França, and C. M. Oishi, "Predicting energy budgets in droplet dynamics: A recurrent neural network approach," *Int J Numer Methods Fluids*, 2024.

[55] H. He and E. A. Garcia, "Learning from imbalanced data," *IEEE Trans Knowl Data Eng*, vol. 21, no. 9, pp. 1263–1284, 2009.

Chapter 5 Conclusions and future work

The work presented in this thesis has examined the normal impact of core–shell compound droplets on smooth solid surfaces, with a particular emphasis on understanding and predicting impact outcome and the maximum spreading factor β_{max}. The central premise has been that internal structure in multicomponent droplets is not merely a complication but a controllable degree of freedom that can be exploited to manipulate impact behavior, provided that appropriate non-dimensional descriptors and modeling frameworks are available. To address this, the thesis combined a systematic experimental campaign, a physics-based energy-balance model that explicitly accounts for the compound nature of the droplets, and a machine-learning framework built on the same multicomponent non-dimensional space.

5.1 Integrated summary and contributions

The experimental component established a single-laboratory dataset of core–shell droplet impacts on a smooth glass surface over a broad range of impact conditions. Core–shell droplets were generated using water and water–glycerol cores encapsulated in silicone oil shells of various viscosities, and were allowed to impact a horizontal glass substrate under well controlled conditions. High-speed imaging was used to track the evolution of each event, from initial approach through spreading, possible jetting, receding, rebound, and any subsequent splashing.

A physically motivated outcome taxonomy was adopted, organized around three primary non-splashing morphologies and their splashing counterparts. The non-splashing outcomes were jetting, partial rebound, and spreading-contact. In jetting, the droplet formed a radially spreading

lamella accompanied by an axial jet, dominated by core liquid, which could pinch off into core-rich satellite droplets. Partial rebound involved the central portion of the compound droplet lifting from the surface while a residual shell film remained attached to the substrate. Spreading-contact described events in which the shell ruptured or thinned sufficiently to allow the core to contact the substrate, after which recoil was arrested. At higher impact intensities, prompt splashing variants of these morphologies were observed, where the lamella rim emitted secondary droplets directly from the contact.

To organize these behaviors, the thesis employed a multicomponent non-dimensional framework. An equivalent Weber number was defined to compare total droplet inertia with a composite capillary scale that includes both the outer shell–gas interface and the internal core–shell interface. The core volume fraction controlled the relative sizes of core and shell and therefore the shell thickness and internal interfacial area. Phase-specific Reynolds numbers for core and shell quantified inertia relative to viscosity in each phase separately. Within this space, the experiments produced regime maps that clearly showed equivalent Weber number and core volume fraction as the primary controls on outcome, with shell Reynolds number playing a secondary role and core Reynolds number exerting comparatively modest influence on regime boundaries.

Several robust trends emerged. At low equivalent Weber numbers, spreading-contact and non-splashing jetting dominated. Increasing the equivalent Weber number promoted more energetic jetting, partial rebound, and eventually splashing. Small core fractions, corresponding to thick shells, produced behavior close to that of single-liquid droplets with an additional internal energy

reservoir. Large core fractions, corresponding to thin shells and large internal interface area, promoted strong axial jets and partial rebound, and increased the susceptibility to shell rupture and spreading-contact at comparable impact conditions. Shell viscosity consistently reduced β_{max}, attenuated jet strength, and widened the parameter regions in which spreading-contact and non-rebounding outcomes appeared. In contrast, substantial changes in core viscosity modified the internal jet structure and the fine details of rebound, but had limited impact on regime boundaries and on measured β_{max}. These observations emphasize the dominant role of the shell, which forms the lamella, interacts directly with the substrate, and experiences the largest shear stresses.

The first major contribution of the thesis is therefore a curated experimental dataset and regime map for core–shell droplet impact, expressed in a compact multicomponent non-dimensional space. Unlike many existing studies that treat only narrow parameter windows or provide qualitative descriptions, this dataset identifies outcome classes and β_{max} in a systematic way across a wide span of equivalent Weber numbers, core fractions, and shell viscosities, while controlling core viscosity and substrate properties. It provides a quantitative reference against which models and data-driven predictors can be calibrated and tested.

Building on this dataset, the thesis developed a compound-droplet energy-balance model for the maximum spreading factor. Classical models for single-liquid droplets treat the liquid as homogeneous and balance initial kinetic energy against increased surface energy and viscous dissipation at maximum spreading, typically represented through the Weber and Reynolds numbers. In the present work, this structure was extended to core–shell droplets by introducing

an equivalent Weber number and separate Reynolds numbers for shell and core, thereby preserving the logic of non-dimensional analysis while respecting the distinct roles of the two liquid phases.

Within this framework, viscous dissipation in the shell and in the core was described by separate scaling expressions, with fitted coefficients and exponents, and geometric relations were used to relate footprint radius, lamella thickness, and droplet height at maximum spreading. The resulting model yields β_{max}as the solution of an energy balance in which the initial kinetic and surface energies are redistributed into increased external and internal interfacial energies and viscous losses in shell and core.

After calibration on part of the experimental dataset, the model was able to predict β_{max} across the remaining data with good accuracy, capturing both the dependence on equivalent Weber number and the decrease of β_{max} with increasing shell viscosity and core fraction. The few outliers were predominantly located near outcome transitions, where small variations in shell rupture or jet formation can alter the effective energy pathways. Beyond prediction, the model enabled a detailed decomposition of the energy budget at maximum spreading. It was shown that external surface energy and shell dissipation dominate in most regimes, that core dissipation becomes significant for large, viscous cores, and that deformation of the core–shell interface stores a measurable fraction of the initial energy, especially at intermediate core fractions.

The second major contribution of the thesis is thus a physically transparent energy-balance model for β_{max} in core–shell droplets, which extends single-liquid formulations by including an

internal interface and phase-specific dissipation. The model provides both a predictive tool and a diagnostic instrument that connects observed β_{max} values to underlying energy mechanisms.

The third pillar of the work consisted of a machine-learning framework that uses the same multicomponent non-dimensional predictors to infer impact outcome and β_{max} from the experimental data. Each impact event was encoded by the equivalent Weber number, core volume fraction, shell Reynolds number, core Reynolds number, and related non-dimensional groups, and labeled by the corresponding outcome class and measured β_{max}. Supervised learning models were trained for both classification and regression tasks, using stratified splits and k-fold cross-validation that preserved the physical structure of the dataset.

For the classification task, the models achieved high accuracy in reproducing the outcome regime map, with misclassifications mainly near physical boundaries between modes such as jetting and partial rebound, or non-splashing and splashing variants. Feature-importance analyses consistently identified equivalent Weber number and core fraction as the dominant predictors, followed by shell Reynolds number, in agreement with the experimental interpretations and the energy-balance perspective. For the regression task, Gaussian process regression with a suitable kernel provided accurate predictions of β_{max} on held-out test data, with high coefficients of determination and low error norms. The learned dependence of β_{max} on equivalent Weber number, core fraction, and shell Reynolds number mirrored both the energy-balance model and the experimental trends.

The third major contribution of the thesis is therefore a physics-organized machine-learning framework for core–shell droplet impact, which uses multicomponent non-dimensional features to predict both regime and β_{max} with high accuracy, and whose interpretability analyses recover and clarify the main physical dependencies identified by the experiments and energy-balance model.

Taken together, these three pillars form a unified, cross-consistent framework for core–shell droplet impact. The experiments provide the empirical foundation, the energy-balance model encodes mechanistic understanding in a compact analytical form, and the machine-learning models deliver flexible, data-driven predictors that are anchored in the same non-dimensional state space and remain interpretable in physical terms. Within the scope of normal impact on smooth glass surfaces for the liquid systems considered, this framework offers a comprehensive description of how internal structure and impact conditions jointly control outcome and maximum spreading.

From a comparative standpoint, the physics-based and machine-learning approaches developed in this thesis serve different but complementary purposes for core-shell droplet impact. The physics-based energy-balance model is primarily a mechanistic and interpretable tool for explaining and estimating the maximum spreading factor. By resolving the overall balance among initial kinetic energy, external and internal interfacial energies, and viscous dissipation in the core and shell, it identifies the dominant mechanisms governing spreading and clarifies why equivalent Weber number, core fraction, and especially shell-side dissipation control the response. This makes the model particularly valuable for physical understanding, compact

scaling, and first-order design, since it shows which parameters must be adjusted to increase spreading, suppress recoil, or shift the response between capillary-dominated and viscous-dominated behavior. Such insight is useful in applications such as coating, printing, and spray cooling, where interpretable operating rules are needed in addition to prediction. In contrast, the machine-learning framework is primarily a predictive and pattern-discovery tool. Using the same physically motivated non-dimensional inputs, it learns the nonlinear mapping from droplet properties and impact conditions to both impact outcome and maximum spreading, and is therefore especially effective for rapid prediction, regime classification, and identification of transition boundaries within the explored parameter space. This is particularly important for practical operating-window selection, where small parameter changes may shift the response from spreading-contact to partial rebound or splashing. Beyond improved predictive performance, the ML analysis also provides additional insight by ranking predictor importance and revealing nonlinear sensitivities, thereby identifying which variables dominate each outcome and which play a secondary role. In this way, the physics-based model provides explanation and simplified design guidance, whereas ML provides predictive screening and multidimensional sensitivity mapping; together, they support both scientific understanding and engineering application of core-shell droplet impact.

5.2 Limitations and scope of validity

The conclusions drawn in this thesis are subject to limitations that delineate the domain in which the proposed framework is most reliable. The experiments considered Newtonian water and water-glycerol cores encapsulated by silicone-oil shells impacting a smooth, rigid glass

surface in quiescent air at atmospheric pressure. Other substrate attributes, such as controlled micro- or nano-texture, engineered roughness, compliance, or active thermal control, were not explored, and ambient pressure and gas composition were held fixed. As a result, the reported regime maps, calibrated energy-balance parameters, and trained machine-learning models are most directly applicable to impacts that are similar in rheology, interfacial chemistry, and surface state to those studied here, and they should be interpreted as a repeatable baseline rather than as universal boundaries.

The use of a hydrophilic glass substrate also defines a clear wettability reference point. At the same time, the core–shell configuration introduces a lubricating outer shell layer that typically wets many solids readily, which reduces the direct sensitivity of spreading to the underlying substrate compared with single-liquid impacts. This mitigated wettability dependence is reflected in the physics-based model, where contact-angle effects are included explicitly, and where the predicted influence of wettability variations on β_{max} is modest within the ranges examined. Model-based exploration using synthetic variations in contact angle indicates that, within the lubricated regime accessed by the present conditions, changes in wettability lead to comparatively small shifts in β_{max} relative to the dominant roles of inertia, phase viscosities, and core fraction as represented through the chosen non-dimensional groups. Nonetheless, this conclusion is conditional. For surfaces or conditions that promote shell drainage, early rupture, or intermittent core exposure, the substrate can regain a stronger influence and the wettability sensitivity may increase.

In practical terms, the strongest validity is expected for impacts that remain in the same mechanistic class captured in the dataset and modeling assumptions. This includes cases in which the outer phase continues to act as the lamella-forming phase up to maximum spreading and the event remains close to axisymmetric, so that outcome and β_{max} can be organized primarily by the multicomponent non-dimensional state variables employed in the thesis. Within this class, extension to other smooth, rigid, non-porous solids is reasonable when the contact-angle dependence remains comparable to that represented in the model. Outside this class, especially when surface texture, compliance, thermal gradients, or gas-mediated effects alter contact-line dynamics, when shell rupture becomes pervasive before maximum spreading, or when violent breakup dominates, both regime boundaries and β_{max} trends can shift and should be revalidated.

The behavior of very thin shells that undergo early rupture, of strongly splashing at very high equivalent Weber numbers, and of cases with pronounced three-dimensional asymmetries was not characterized in detail. The energy-balance model is formulated for impacts in which the shell continues to act as the lamella-forming phase up to maximum spreading, and the dataset used for regression models is correspondingly dominated by intact or mildly ruptured shells. For impacts that involve extensive shell breakup or strong gas–liquid-solid interactions beyond those observed here, additional physics would need to be incorporated.

The experimental measurements focus on global quantities such as final outcome, β_{max}, and qualitative jet characteristics, rather than full internal velocity fields or local film-thickness distributions. The energy-balance model therefore rests on global scaling assumptions for viscous dissipation and interfacial deformation rather than on detailed flow measurements. Machine-

learning models are built on scalar non-dimensional features derived from these global descriptors and do not yet exploit the full spatiotemporal richness of high-speed imagery.

Finally, the machine-learning results are based on a finite dataset within a bounded, physics-organized non-dimensional parameter space. Because the models use $\overline{We}$, α, Re_o, and Re_i, rather than raw dimensional variables, they retain transferability beyond the exact tested conditions, provided that new cases remain within the same underlying impact-physics class represented in the training data. However, this does not imply unrestricted extrapolation. For maximum-spreading prediction, reliability is expected only while the impact remains within the shell-dominated spreading regime captured during training; cases involving splashing, early shell rupture, or core-substrate contact lie outside the intended predictive scope. Likewise, although impact-outcome classification may remain useful somewhat beyond the exact training points, major changes in substrate roughness, thermal conditions, compliance, wettability, or liquid rheology introduce additional physics not represented during training and therefore require caution and further validation. Uncertainty quantification and targeted exploration of such regions were not primary objectives in this first implementation.

of poorly sampled regions were not primary objectives in this first implementation.

Within these bounds, the combined experimental, analytical, and data-driven framework developed in the thesis provides a robust and internally consistent description of core-shell droplet impact. Outside them, it offers a starting point and a set of concepts that can be refined and extended in future work, including controlled variation of surface wettability and texture,

broadened liquid chemistries, and complementary numerical interrogation where local flow-field resolution is required.

5.3 Future directions

The results obtained here suggest several avenues for further research, both in extending the physical parameter space and in deepening the modeling and data-driven components. To maintain focus, the discussion below highlights a small number of central directions that most directly broaden validity and mechanistic resolution, followed by additional extensions that can be pursued as a secondary set of studies.

A first direction is the extension to other substrates and ambient conditions. Investigating the impact of core-shell droplets on surfaces with controlled wettability, engineered roughness, or compliant coatings would reveal how internal droplet structure interacts with substrate design features and would establish the conditions under which the substrate regains strong influence despite the presence of a lubricating outer layer. Measurements on heated or cooled substrates would connect compound droplet impact with phase-change processes, such as evaporation, boiling, or solidification, and would test the influence of internal interfaces on thermally driven flows and Marangoni stresses. Systematic variation of ambient pressure and gas composition could clarify how gas-mediated splashing mechanisms, established for single-liquid droplets, are modified by the presence of a core–shell structure.

A second direction concerns improving mechanistic observability through enhanced experimental diagnostics that resolve internal and interfacial dynamics more directly. Combining

side and bottom views with appropriate optical methods could enable reconstruction of lamella thickness and core position as functions of time, and could distinguish between outcomes that appear similar in silhouette but differ in shell integrity or core exposure. Measurements of internal velocity fields through particle image velocimetry or related techniques would allow direct assessment of core and shell recirculation patterns and shear rates, providing stricter tests of dissipation scaling in the energy-balance model and higher-information training data for numerical simulations and data-driven models. Tracking the pre-impact position of the core under gravity as a function of core fraction and density ratio would clarify how gravitational stratification affects shell thickness at the impact point and, consequently, outcome statistics and dispersion near regime boundaries.

A third direction is to strengthen the predictive framework by tighter coupling between mechanistic and data-driven components. On the modeling side, the present energy-balance formulation can be refined and generalized by incorporating explicit criteria for shell rupture and splashing, informed by lamella thickness thresholds, rim instability conditions, or stress-based failure criteria, thereby extending the range of impact outcomes directly addressed by the model. A more detailed treatment of wetting dynamics, including advancing and receding contact angles and hysteresis, would facilitate application to chemically or topographically structured surfaces. On the data-driven side, hybrid or physics-informed strategies in which the energy-balance model provides baseline predictions and machine learning accounts for residual dependencies can leverage the strengths of both viewpoints while reducing data requirements. Active learning can

further guide new experiments toward regions of high model uncertainty, enabling more efficient closure of gaps in parameter space and improved stability near transition zones.

Additional directions that naturally follow from the present work include broadening the class of liquids to include non-Newtonian cores or shells, as encountered in polymer solutions, suspensions, and biofluids, which would require incorporation of appropriate rheological models and the introduction of additional non-dimensional groups such as Weissenberg or Bingham numbers. Image-based learning using high-speed sequences, either through engineered descriptors or convolutional architectures, can be used to exploit spatiotemporal information beyond scalar non-dimensional inputs. Complementary numerical investigations can interrogate internal velocity and pressure fields and multi-interface deformation within selected regimes identified by the experiments and regime maps, providing mechanism-level validation of closures and rupture criteria. Further extensions include systematic uncertainty quantification, probabilistic outcome prediction near regime boundaries, and inverse design formulations that target prescribed outcomes or β_{max} values.

Finally, the framework developed here can be applied and adapted to concrete technological contexts. In inkjet and additive manufacturing, the combination of non-dimensional analysis, energy-balance modeling, and machine-learning surrogates could be used to define operating windows that deliver desired impact outcomes and footprints for given core–shell formulations and substrate types. In spray cooling and quenching, the ability to predict and control β_{max} and rebound probability for core–shell droplets could inform the design of sprays that maximize useful wetted area and contact time while minimizing splashing losses. In encapsulation and

controlled-release systems, the insights into how core fraction and shell viscosity influence shell rupture, jetting, and partial rebound could be used to tailor impact-triggered release strategies or to protect sensitive cores from accidental exposure upon impact.

In summary, this thesis has shown that core-shell droplets offer a rich, tunable platform for controlling droplet impact behavior and that a combination of targeted experiments, multicomponent energy-balance modeling, and physics-organized machine-learning can capture this behavior in a compact and interpretable way. The tools and ideas developed here provide a foundation on which more complex multicomponent, non-Newtonian, and thermally coupled systems can be explored, and they point toward a broader integration of structured droplet impact physics into the design of practical processes and devices.

APPENDICES

Appendix A: Chapter 2 supplementary information

Fig. SI 2-2 presents the free-fall trajectories of compound droplets with different core size ratios (α=0.2,0.5 and 0.7), comparing experimental observations with predictions assuming either zero initial velocity (yellow markers) or an estimated initial velocity from the empirical correlation by Kurniawan et al. (2022) (blue markers). The experimental trajectories align closely with the zero initial velocity assumption across all cases, whereas incorporating an initial velocity systematically overpredicts the droplet positions. This consistency across varying core sizes further supports the validity of neglecting initial velocity at pinch-off, reinforcing that detachment under the given experimental conditions is predominantly governed by surface tension rather than inertia.

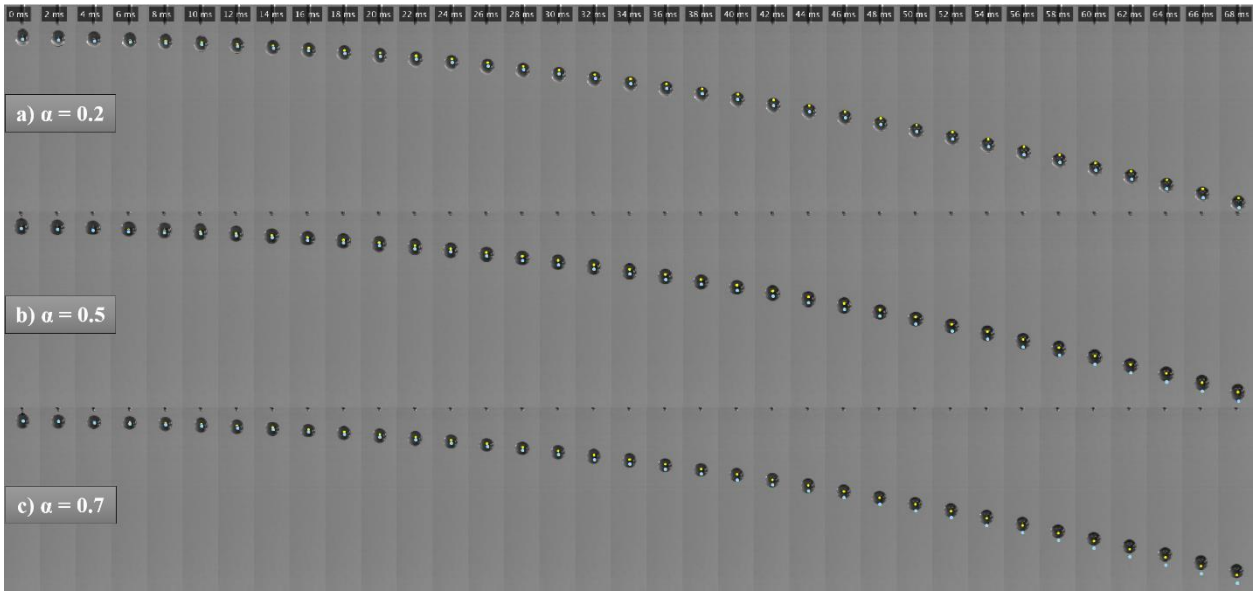

Fig. SI 2-2 Free-fall trajectories of compound droplets with core size ratios (a) α=0.2, (b) α=0.5, and (c) α=0.7. Droplet positions assuming no initial velocity are marked in yellow, while those incorporating an estimated initial velocity at pinch-off are marked in blue

At high Weber numbers, prompt splashing is observed, where the turbulent lamella flow at the contact line ejects secondary droplets. **Fig. SI 2-3** shows this behavior for a compound droplet with a dyed water core and an S5 silicone oil shell (core size 0.8). The splashing originates exclusively from the shell layer, with secondary droplets composed entirely of silicone oil. The dyed water core remains intact, retracting on the surface without fragmenting. These results demonstrate that prompt splashing is specific to the shell layer in compound droplet impacts.

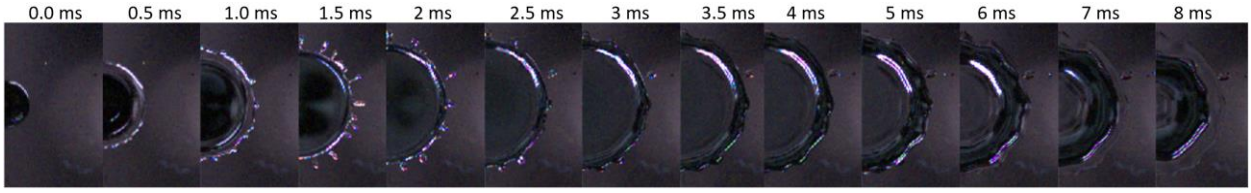

Fig. SI 2-3 Spreading and prompt splashing of a water-in-oil (S5) droplet with a core size of 0.8 on a glass surface at a Weber number of 91

Fig. SI 2-4 shows the impact of different liquid combinations of compound droplets with the same core size (α=0.5). The drops spread on the surface to their maximum extent, after which the cores recede, creating a central jet. As the shell viscosity increases, there is a greater total dissipation of initial energy during both the spreading and receding phases, especially at the rim of the lamella, where it consists mainly of the shell liquid. Limiting the contact line movement forces the core to spread less on the surface, less energy being stored at the interfaces, which dampens the central jet.

Increasing the core viscosity leads to a more dissipated energy at the bulk body of the spreading compound droplet. The receding phase follows the spreading, and the central jet is

formed and consists mainly of the core material. The viscous cores damp the undulations of the liquid column perimeter preventing the breakup of the jet.

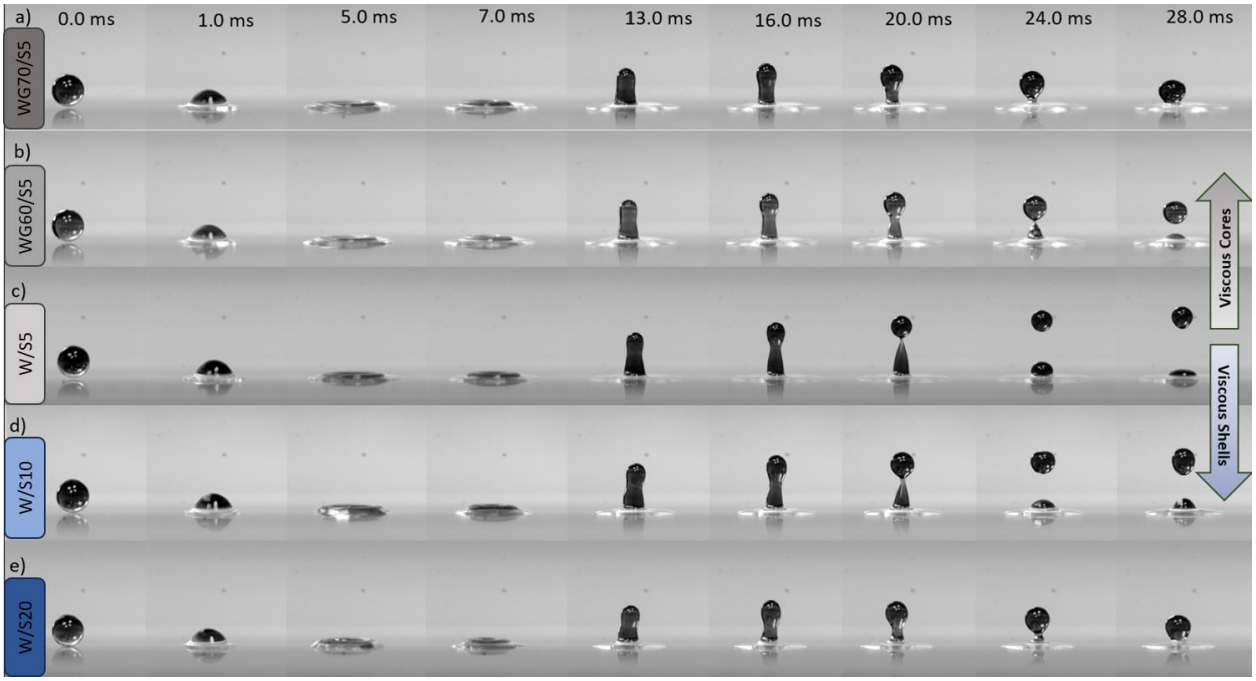

Fig. SI 2-4 Impact of (a) [WG70/S5], (b) [WG60/S5], (c) [W/S5], (d) [W/S10], and [W/S20] liquid combinations) compound drops with a core size of α=0.5 at average Weber number of 83.8 on glass substrates. Increasing core or viscosity shows less jetting and damped rebound.

The core viscosity has an insignificant effect on the maximum spreading for different core sizes (**Fig. SI 2-5**). The influence of core viscosity is apparent only on magnifying the effect of the core size on the maximum spreading as explained before in **Fig. SI 2-4.**

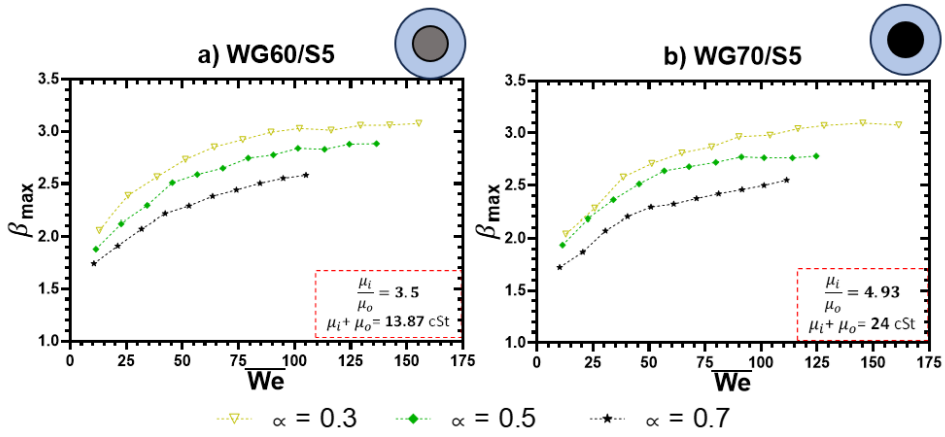

Fig. SI 2-5 Maximum spreading factor as a function of core size for different liquid combinations. The viscosity ratio of the core to the shell is increasing from (a-e)

Snapshots (**Fig. SI 2-6 a-c**) illustrate, using the bottom view of the impact, the evolution of the maximal spreading the drop exhibits after impact for an increasing Weber number. Water cores encapsulated inside silicon oil (S5) shells are presented below for core size (α=0.6). Increasing the equivalent Weber number corresponds to higher spreading factors.

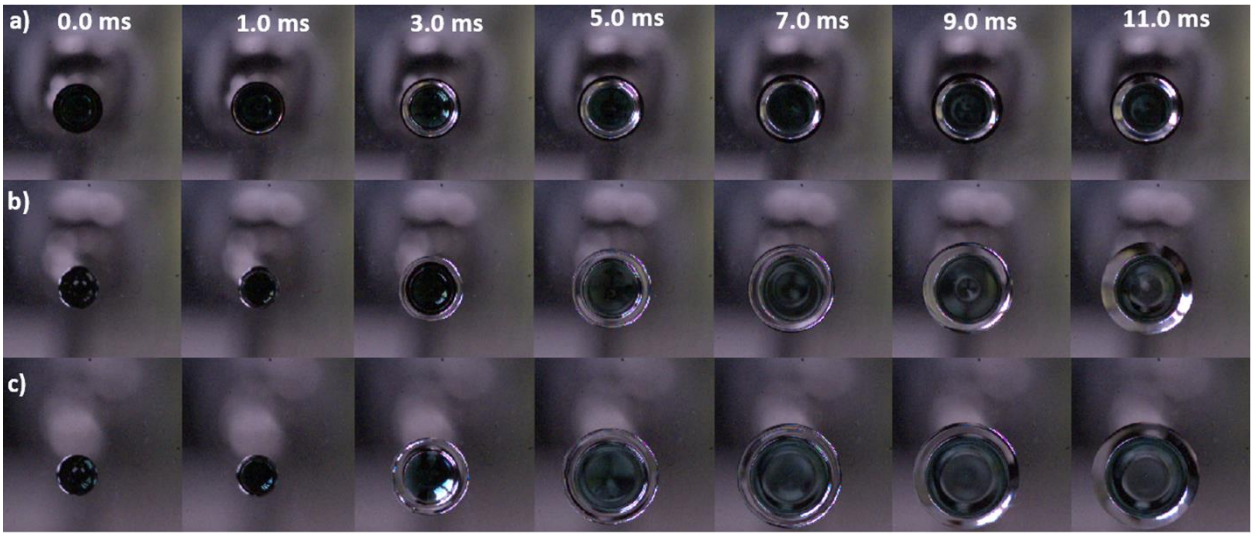

Fig. SI 2-6 W/S5 compound drops of core size α=0.6 impacting glass surfaces with various Weber numbers for a-d corresponds to 10, 30.2, and 60.8

Fig. SI 2-7 below illustrates the effect of shell viscosity (μ_o=5,10 and 20 cSt) on the rupture dynamics of spreading compound droplets. At the lowest viscosity (5 cSt), the shell ruptures asymmetrically, including at the rim of the spreading contact line, leading to irregular spreading. At higher viscosities (10 cSt, and 20 cSt), rupture occurs primarily at the bottom of the spreading compound droplet, with both cases exhibiting similar rupture behavior and minimal rim thinning, indicating greater rim stability during rupture upon impact.

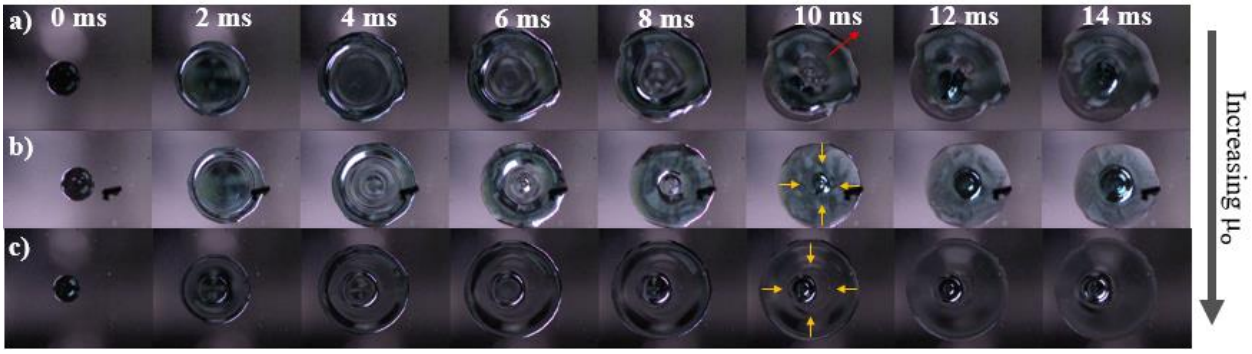

Fig. SI 2-7 Time sequence of spreading compound droplets for increasing shell viscosity: (a) 5 cSt, (b) 10 cSt, and (c) 20 cSt silicone oil

Appendix B: Chapter 3 supplementary information

- **Model Calibration and Optimization Workflow**

To support the accuracy and physical consistency of the model (i.e., Equation 16), this section outlines the mathematical definitions of the statistical metrics, and the energy error used during the coefficient optimization process. These formulations, along with the optimization workflow, ensure that the model is both predictive and energetically balanced.

The summation of the squared residuals (SSR) is defined by:

$$\mathrm{SSR} = \sum_{j=1}^{N} (\mathrm{Residulas})^2 = \sum_{j=1}^{N} \left(y_j - \hat{y}_j\right)^2 \qquad \textit{Equation SI3-1}$$

Here, y_j represents the experimentally measured maximum spreading factor for the j^{th} data point (error is less than 3.5%), while $\hat{y}_j$ is the corresponding model prediction obtained from Equation 16 using a given set of fitting coefficients. The total number of the calibration experimental observations (N) was over 107 data points. To ensure energy conservation during optimization, the total energy mismatch is evaluated through a normalized error metric that captures the deviation between the initial and final energy states. Energy error metric is normalized and constrained by a value less than 0.1% and is defined by:

$$Energy\ Error = \frac{1}{N} \sum_{j=1}^{N} \left| \frac{E_{2,j} - E_{1,j}}{E_{1,j}} \right| \qquad \textit{Equation SI3-2}$$

Fig. SI 3-1 summarizes the optimization workflow, including model construction, parameter fitting, residual minimization, and energy conservation enforcement, providing a visual summary of the methodology used to generate optimized parameters. On the calibration dataset, $N = 107$, the model achieved $RMSE = 0.127$ and $R^2 = 0.907$, and the normalized energy mismatch was essentially zero (less than 0.1%); see FIG. S2 for the corresponding calibration data parity plot.

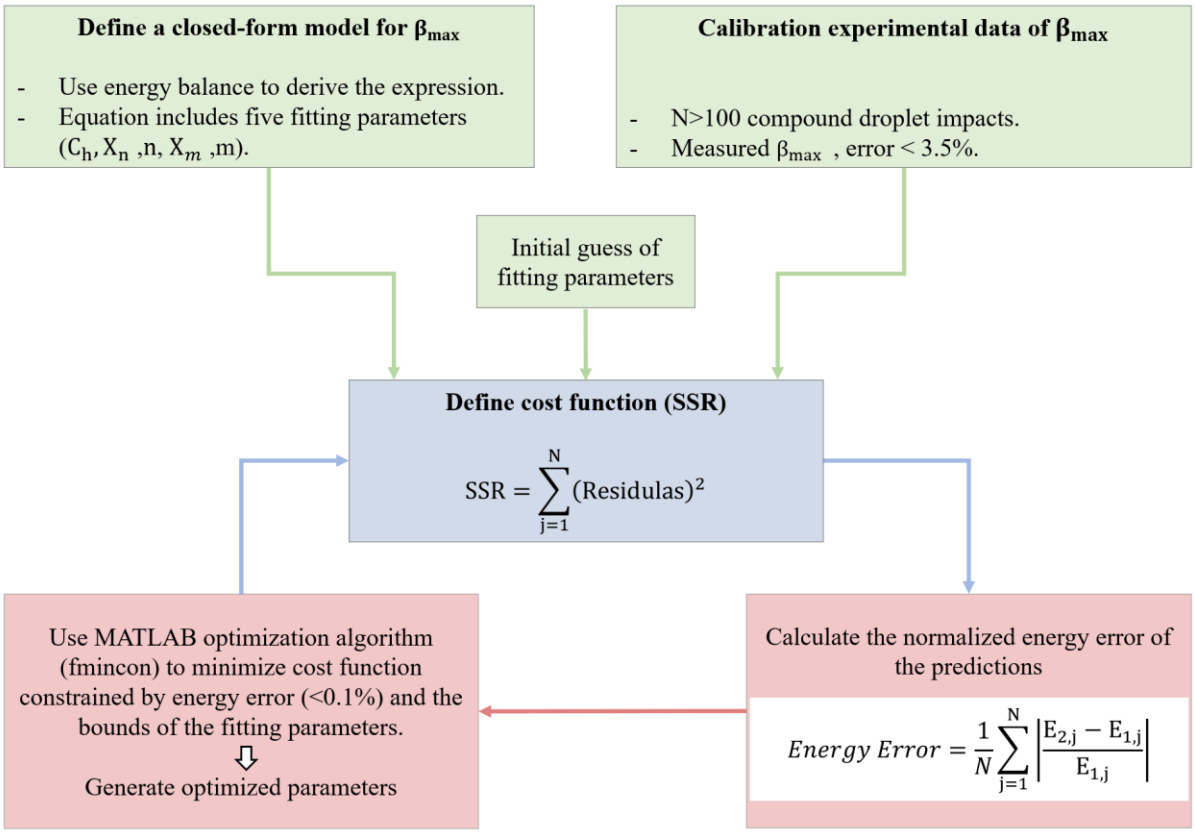

Fig. SI 3-1 Flowchart illustrates the optimization workflow for fitting empirical coefficients in the maximum spreading model. The process integrates experimental data, a closed-form energy-based equation, and constrained nonlinear optimization to minimize prediction error while enforcing energy conservation.

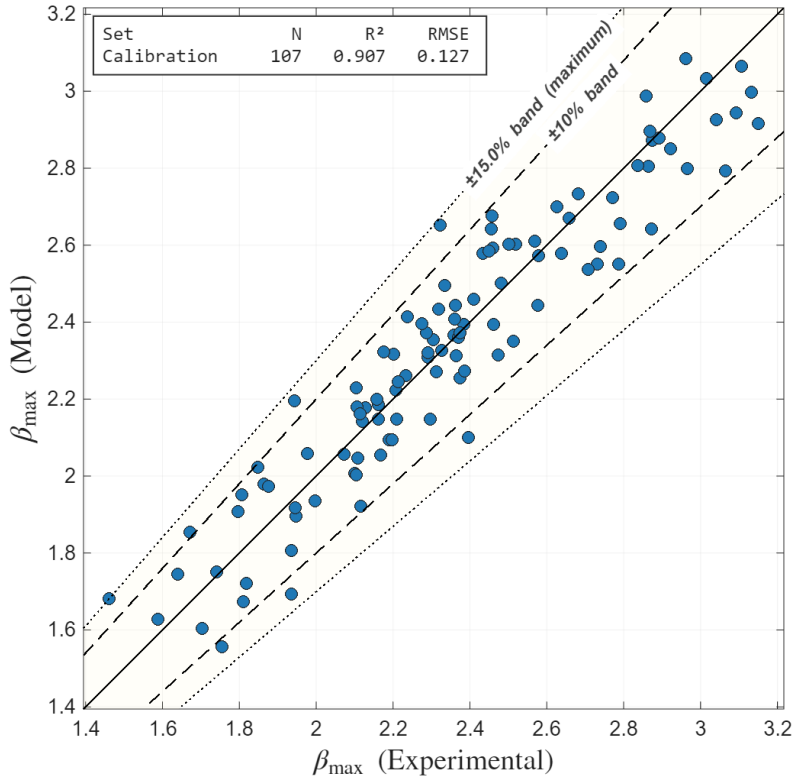

Fig. SI 3-2 Parity plot for the calibration set: model prediction versus experimental β_{max}. The solid line denotes the ideal 1:1 agreement. Dashed lines show the ±10% error band; dotted lines show the ±15% error band.

- **Accuracy Metrics for Model Validation**

The total sum of squares (SST), which represents the total variance in the experimental test data relative to the sample mean ($\bar{y}$), is:

$$\mathrm{SST} = \sum_{\mathrm{j=1}}^{\mathrm{N}} \left(\mathrm{y_j} - \bar{\mathrm{y}}\right)^2 \qquad \textit{Equation SI3-3}$$

For the held-out test set ($\mathrm{N} = 314$), the mean is $\bar{y} = 2.323$, and $\mathrm{SST} = 49.713$. The coefficient of determination is:

$$R^2 = 1 - \frac{SSR}{SST}$$ *Equation SI3-4*

The resulting value of $R^2 = 0.910$ indicates that the model explains 91% of the variance in the experimental data, demonstrating a high degree of predictive accuracy and consistency. The root-mean-square error (RMSE), representing the typical prediction error magnitude, is:

$$RMSE = \sqrt{\frac{SSR}{N}}$$ *Equation SI3-5*

- **Residual Histogram**

Residuals, defined as the difference between experimental values and model predictions ($y_j - \hat{y}_j$), summarize the distribution and consistency of prediction errors. **Fig. SI 3-3** shows a histogram of residuals with a fitted normal curve to assess symmetry and bias. The distribution is centered near zero and appears symmetric, indicating no systematic over- or under-prediction on the unseen test set. The mean residual is 0.005, which reflects a negligible positive bias, and the standard deviation is 0.121. Thus, about two-thirds of predictions fall within ±0.12 of the measured β_{max}, and roughly 95% within ±0.24. These values are consistent with the test-set RMSE of 0.119, confirming that errors are well contained, approximately Gaussian, and statistically well controlled across the tested conditions.

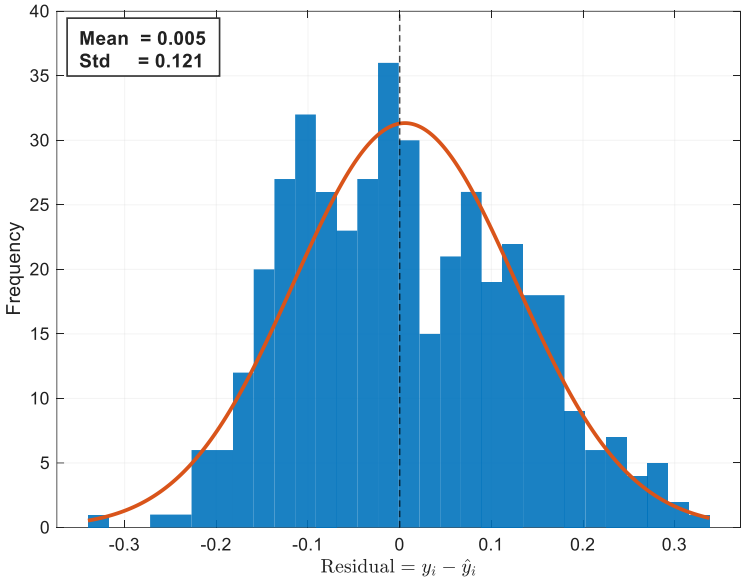

Fig. SI 3-3 Histogram of residuals ($y_j - \hat{y}_j$) with fitted normal distribution. The residuals are symmetrically distributed around zero, with a mean of 0.005 and a standard deviation of 0.121, indicating minimal bias and well-contained prediction error on unseen data.

Appendix C: Chapter 4 supplementary information

- **Accuracy metrics**

All metrics are evaluated on the independent test set. For classification, we count, for each outcome class, true positives (impacts correctly assigned to that class), false positives (impacts predicted as that class but actually belonging to another class), and false negatives (impacts that belong to that class but are predicted otherwise). Precision for a class is the fraction of its predicted labels that are correct, and recall is the fraction of its actual occurrences that are recovered. The F1 score combines both as a single number that is high only when precision and recall are simultaneously high. We report precision, recall, and F1 for each outcome, then summarize performance with the micro F1 score, which is obtained by pooling true positives, false positives, and false negatives over all classes before computing F1. In a single label problem

this micro-F1 is numerically equal to overall accuracy, but it is preferable to report it in F1 form because it is defined consistently with precision and recall and keeps the same interpretation if class probabilities or multilabel settings are considered. For completeness we also report the macro-F1 score, which is the simple average of the class F1 values and therefore gives equal weight to rare and frequent outcomes. For regression of the maximum spreading factor, we use the coefficient of determination R^2 and the root mean squared error (RMSE). R^2 measures the fraction of the variance in the observed spreading that is captured by the model predictions, with values closer to one indicating a better fit, while RMSE gives the typical magnitude of the prediction error in the same units as the target quantity.

- **Stratified splitting**

To complement the global feature map in Figure 3 of the main text, Figures S1–S3 reproduce the same pairwise matrix of the four controlling predictors, $\overline{\mathrm{We}}$, α, Re_i, and Re_o, separately for each stratified train/test split (70/30, 75/25, and 80/20). For every split, diagonal panels show marginal histograms of each predictor, while off-diagonal panels show the corresponding pairwise scatter plots. Training samples are plotted in blue and test samples in orange, so that both the marginal coverage and the joint structure of the control space can be inspected visually for each partition.

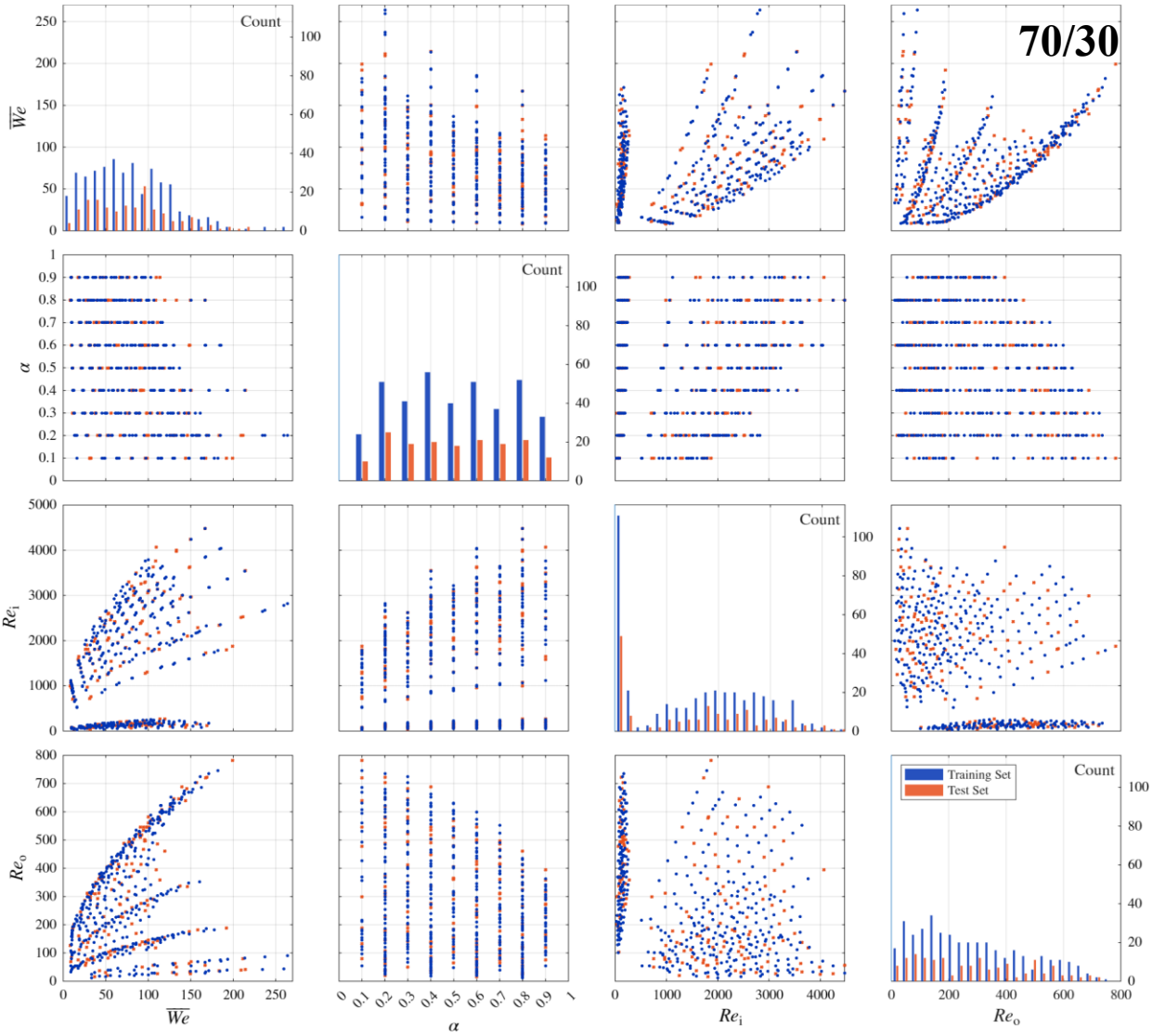

Figure S1. Stratified 70/30 train/test split visualized in the four-dimensional control space $(\overline{We}, \alpha, Re_i, Re_o)$. *Diagonal panels: marginal histograms of each predictor. Off-diagonal panels: pairwise scatter plots. Blue: training samples; orange: test samples.*

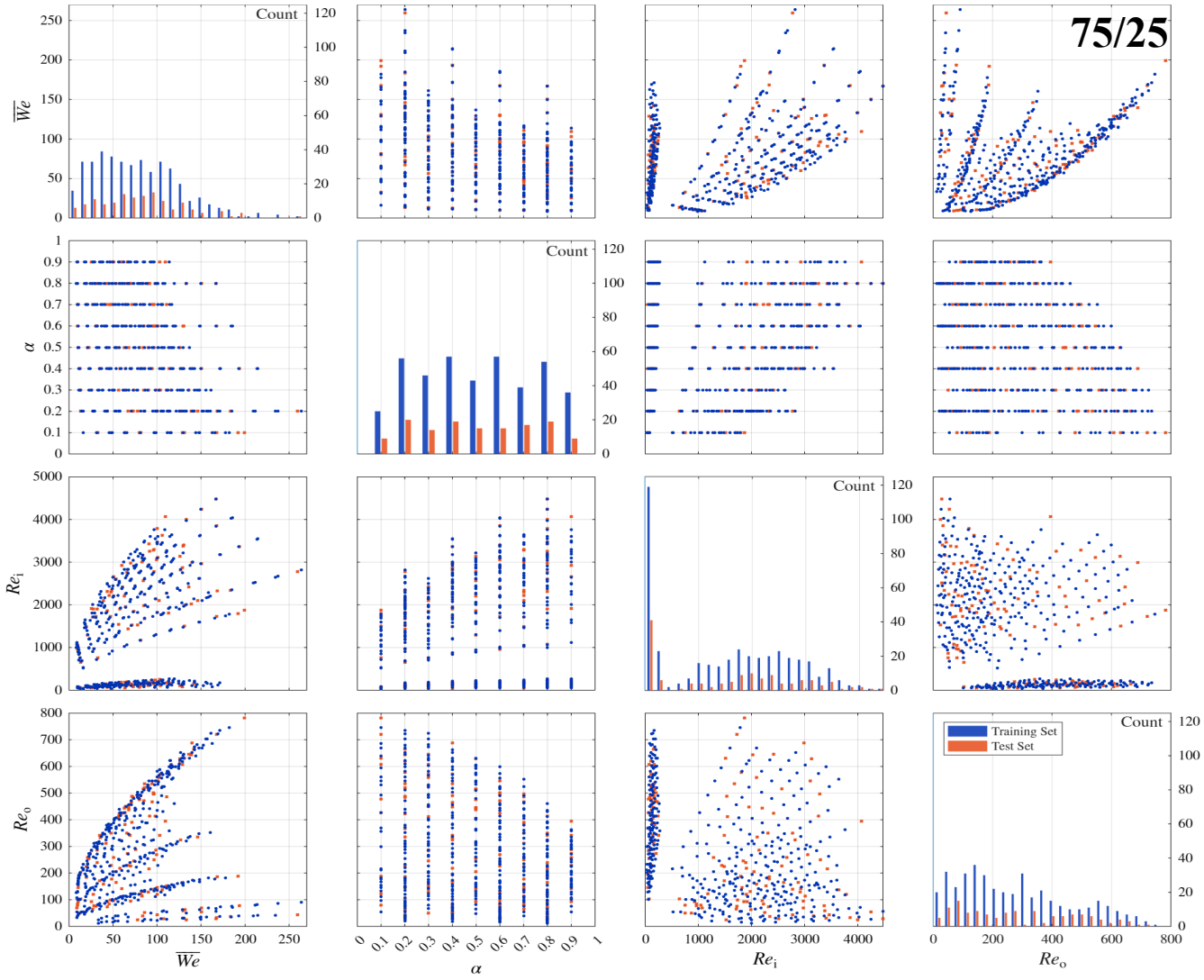

Figure S2. Stratified 75/25 train/test split visualized in the four-dimensional control space $(\overline{We}, \alpha, Re_i, Re_o)$. Diagonal panels: marginal histograms of each predictor. Off-diagonal panels: pairwise scatter plots. Blue: training samples; orange: test samples

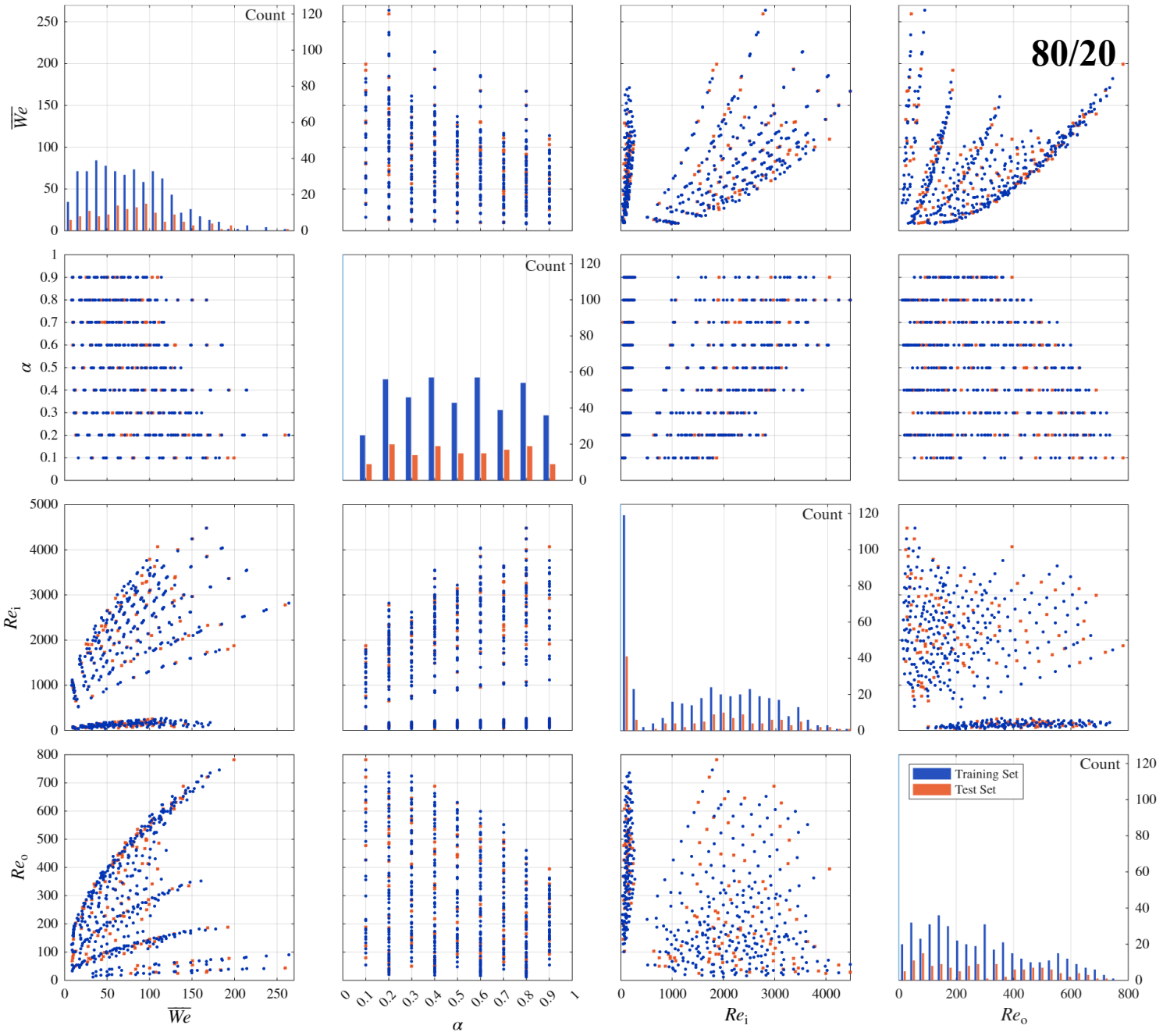

Figure S3. Stratified 80/20 train/test split visualized in the four-dimensional control space $(\overline{We}, \alpha, Re_i, Re_o)$. Diagonal panels: marginal histograms of each predictor. Off-diagonal panels: pairwise scatter plots. Blue: training samples; orange: test samples

To expand the feature space diagnostics shown in Figure 6 of the main text, Supplementary Figures S4 and S5 provide per-split views of the four controlling predictors for each stratified partition. All impacts from the three split ratios and from both partitions are first pooled to compute a single global mean and standard deviation for each predictor ($\overline{\mathrm{We}}, \alpha, Re_i, Re_o$); individual values are then expressed as standardized scores $z$on this common scale. Figure S4 displays, for each split, mirrored violin plots with embedded boxplots that compare the training and test z-distributions. Figure S5 reports the same information in physical units through separate boxplots of each predictor versus split ratio, again with training samples in blue and test samples in orange.

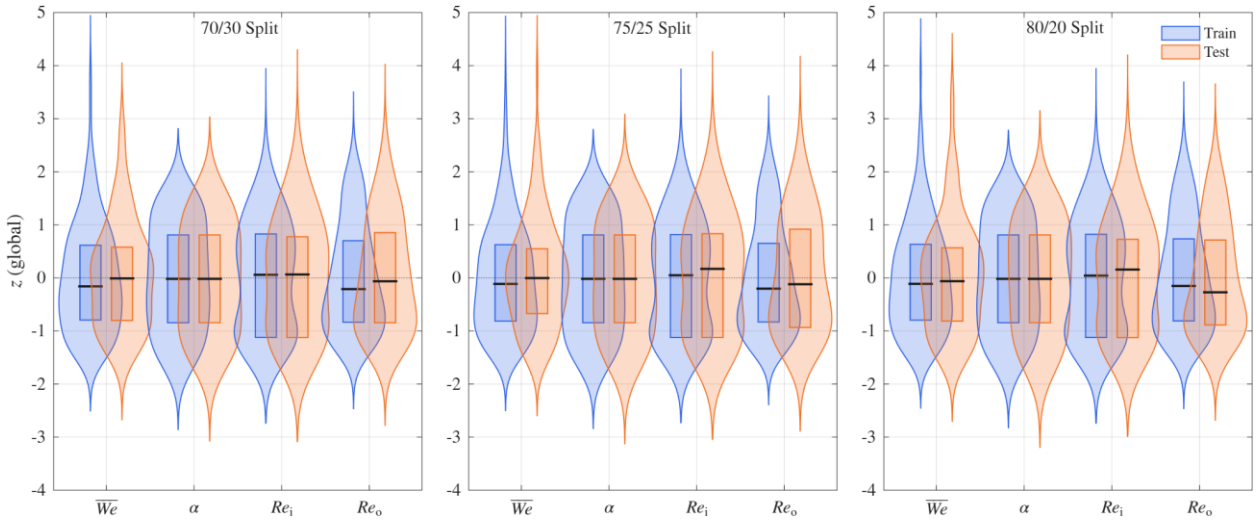

Figure S4. Standardized feature distributions for the 70/30, 75/25, and 80/20 stratified splits. For each split and each predictor ($\overline{We}, \alpha, Re_i, Re_o$), training (blue) and test (orange) samples are shown as mirrored violin plots with internal boxplots on the global standardized scale z.

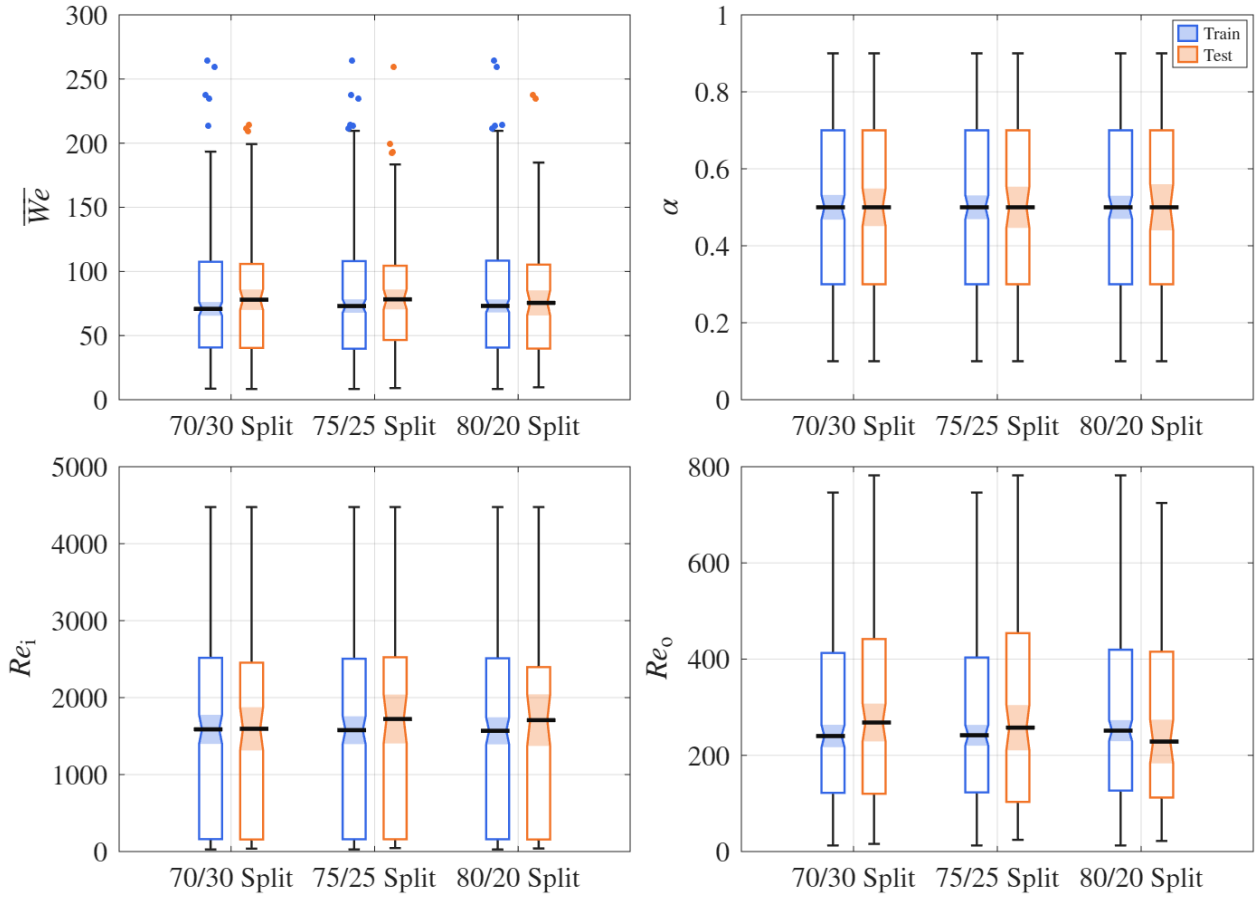

Figure S5. Boxplots of the four controlling predictors ($\overline{We}$, α, Re_i, Re_o) for the 70/30, 75/25, and 80/20 stratified splits. For each predictor, training (blue) and test (orange) samples are shown side by side for the three split ratios; boxes indicate medians and interquartile ranges, whiskers mark the central spread, and points denote outliers.

For the regression task, the z-standardized feature diagnostics used in Figure 8 of the main text are decomposed by split ratio in Supplementary Figure S6. As before, a single global mean and standard deviation are computed for each predictor ($\overline{\mathrm{We}}, \alpha, Re_i, Re_o$) by pooling all impacts across the three split ratios and both partitions, and individual values are mapped to the corresponding standardized score z. Supplementary Figure S6 then shows, for each of the 70/30, 75/25, and 80/20 splits, mirrored violin plots with embedded boxplots that compare the training and test z-distributions of all four predictors.

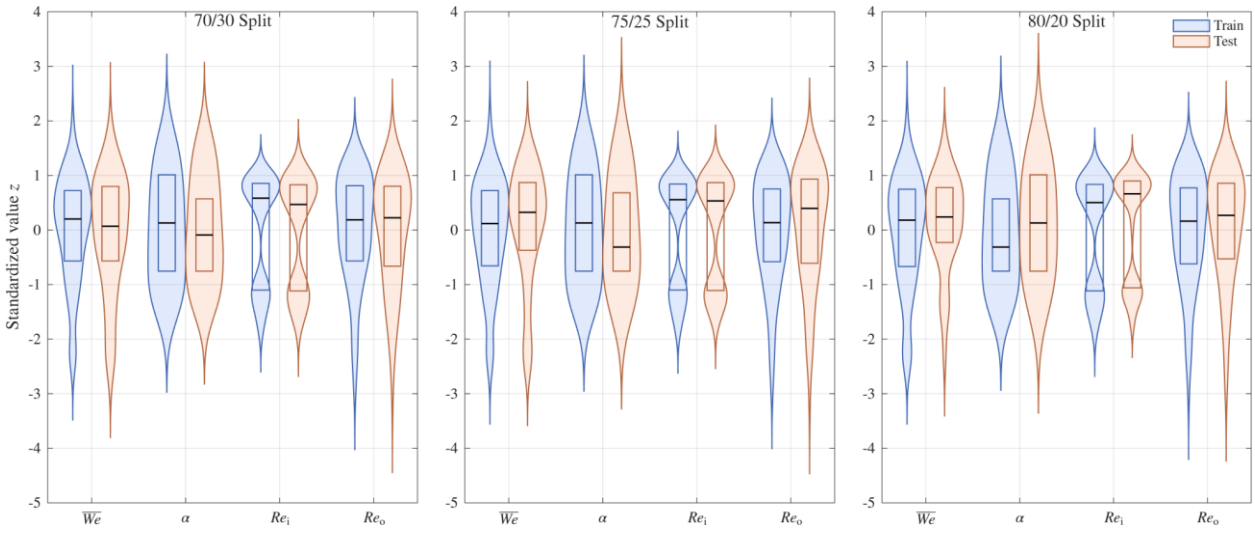

Figure S6. Standardized feature distributions for the regression dataset under the 70/30, 75/25, and 80/20 stratified splits. For each split and each predictor ($\overline{We}, \alpha, Re_i, Re_o$), training (blue) and test (orange) samples are shown as mirrored violin plots with internal boxplots on the global standardized scale z.

- **Model families and presets accuracy**

Supplementary Figures S7 and S8 expand the classification results by examining how test Micro-F1 varies with the choice of split ratio and number of folds. For each of the nine partition settings (70/30, 75/25, 80/20 combined with 5, 7, and 10 folds), the family level distributions in

Figure S7 summarize the spread of test Micro-F1 across all presets within a family, while the preset level heat map in Figure S8 reports the corresponding Micro-F1 values model by model. Together, these plots document the sensitivity of both families and individual presets to partitioning choices, and complement the main text discussion of stability versus capacity and locality.

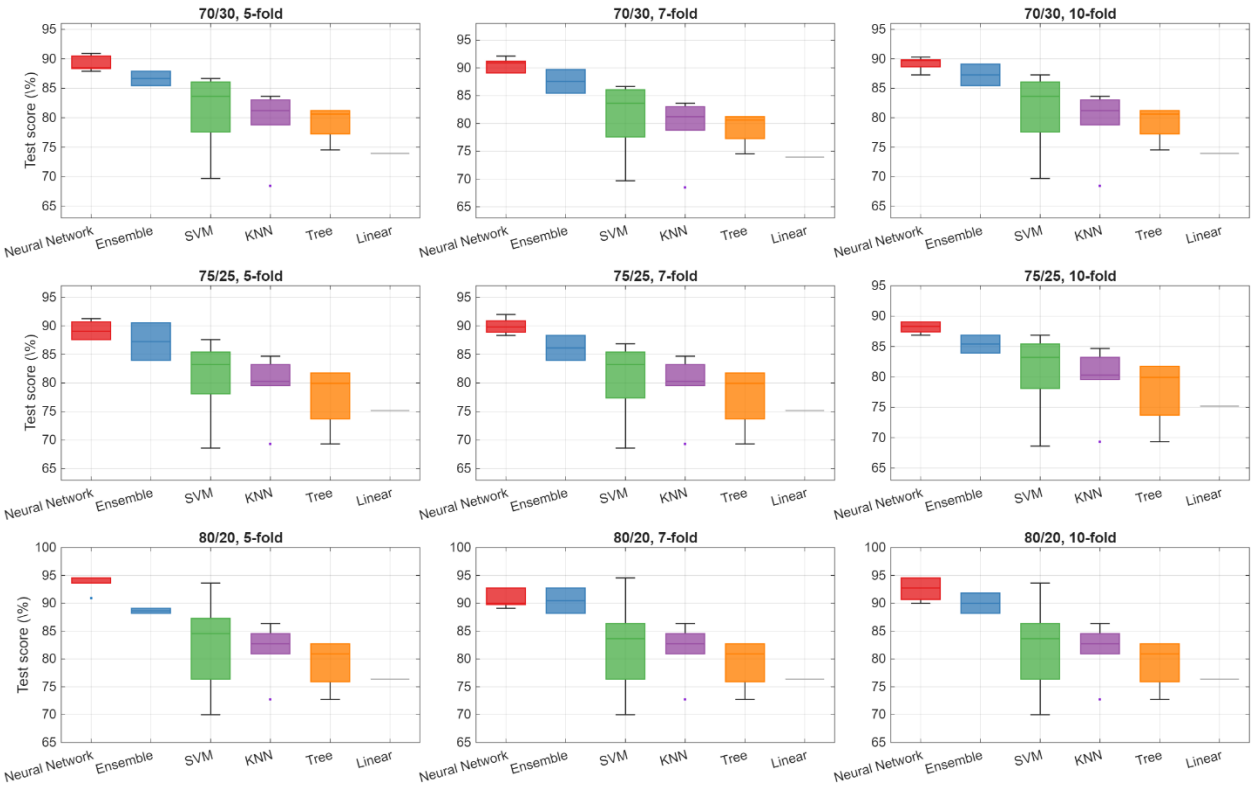

Figure S7. Test Micro-F1 distributions for the six classifier families (Neural Network, Ensemble, SVM, KNN, Tree, Linear) across all nine split and fold combinations. Each panel corresponds to one stratified split ratio and one k-fold value, and shows boxplots of test Micro-F1 for all presets within each family.

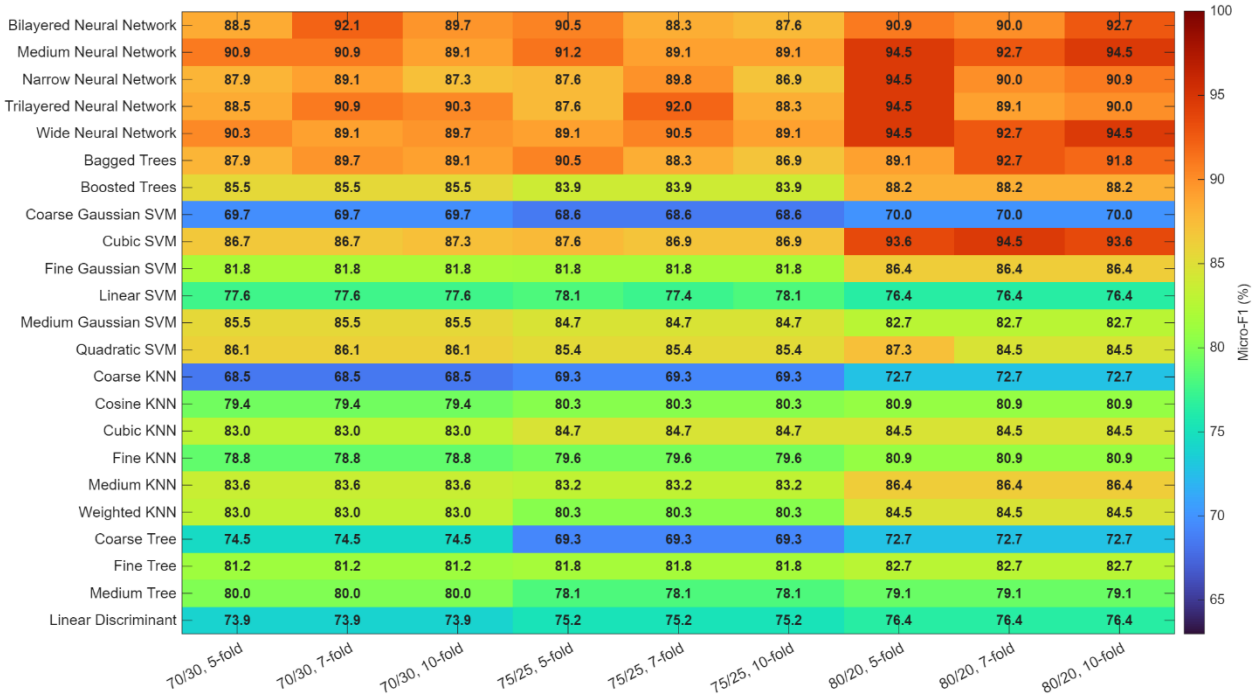

Figure S8. Heat map of test Micro-F1 for all classification presets over the nine split and fold combinations. Rows correspond to individual presets ordered by family; columns correspond to the three split ratios combined with 5, 7, and 10 folds.

Supplementary Figures S9 and S10 provide preset-level summaries of the regression performance across all partition configurations. Each row corresponds to one regression preset from the Neural Network, ensemble tree, Gaussian-process, SVM, tree, and linear families. Columns index the nine combinations of split ratio and cross-validation depth (70/30, 75/25, 80/20, each with 5, 7, and 10 folds). Figure S9 encodes the test RMSE for every preset–configuration pair, while Figure S10 reports the corresponding test R^2values in percent. The numerical scores are printed in each cell for direct comparison and to facilitate reading trends along individual rows (preset sensitivity) and down columns (family structure). Together, these

heat maps complement the main-text summaries of split and fold sensitivity and highlight the behavior of individual presets, including the Matérn 5/2 GPR model.

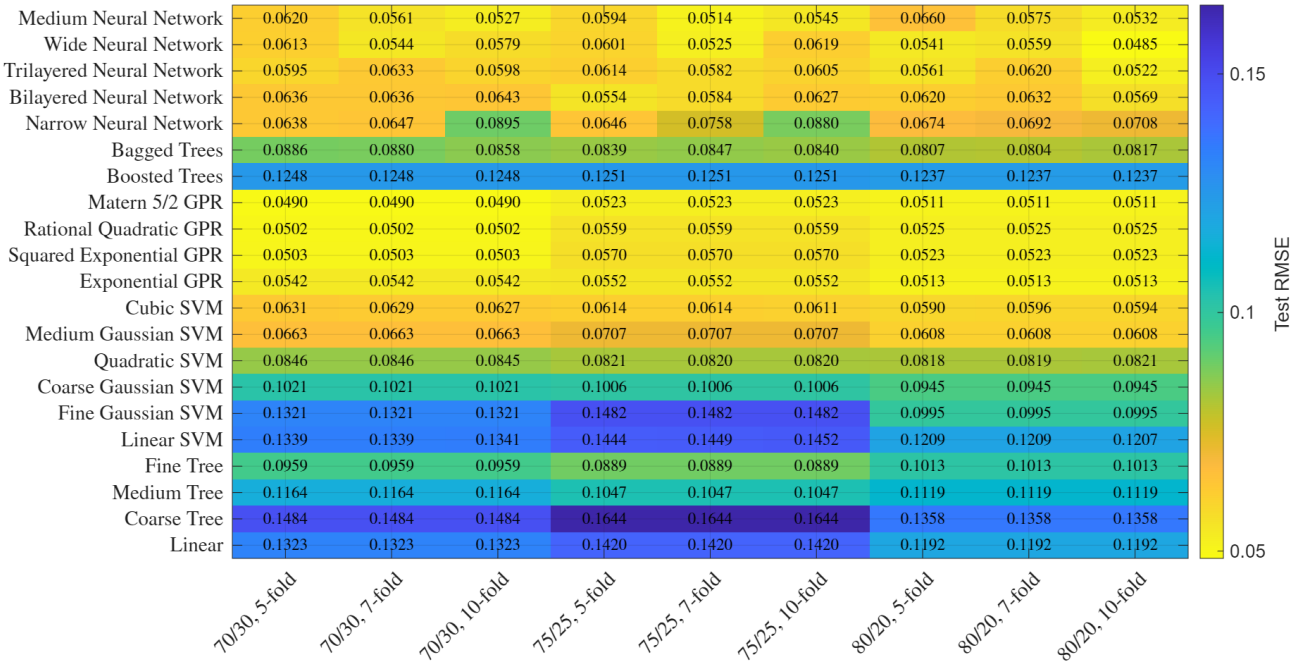

Figure S9. Test RMSE heat map for all regression presets across the nine split and fold combinations. Rows list individual presets grouped by family; columns correspond to 70/30, 75/25, and 80/20 splits with 5, 7, and 10 folds. Color and overlaid numbers indicate the test RMSE for each preset-configuration pair.

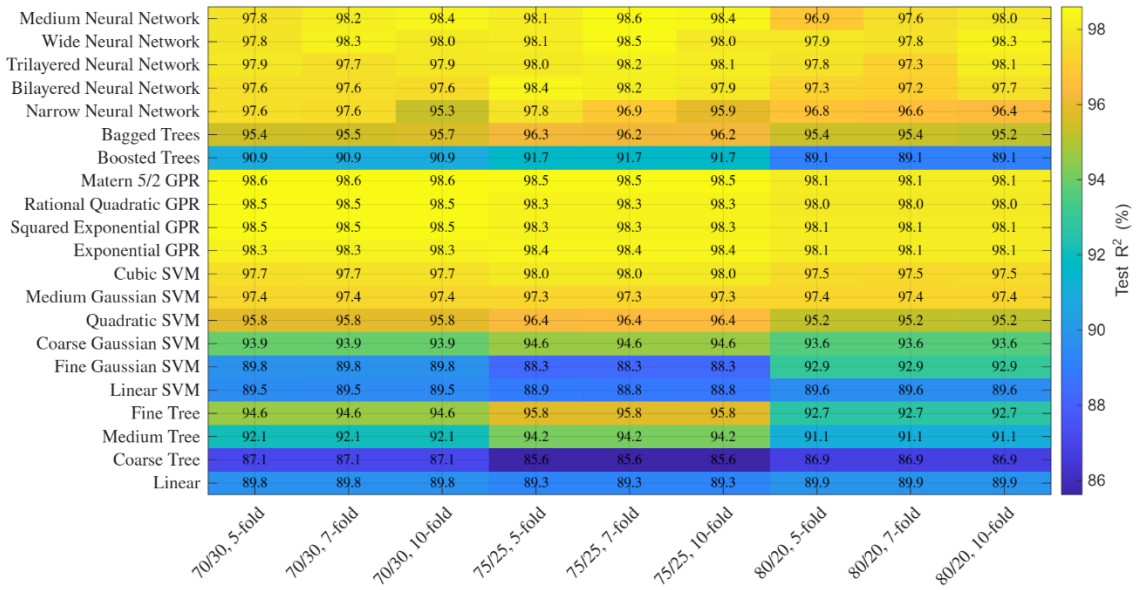

Figure S10. Test R^2 heat map for all regression presets across the nine split and fold combinations. Layout matches Figure S9, with rows as presets and columns as split-fold settings; color and overlaid numbers indicate the test R^2(%) for each preset-configuration pair.

- **Neural-network-predicted regime map in the $\overline{We}$–α plane**

For qualitative comparison with the experimental regime maps presented in Chapter 2, a neural-network-predicted impact regime map was constructed for the W/S5 liquid combination in the same $\overline{We}$–α plane. The map was generated using the top-performing classification preset, namely the Medium Neural Network, and the predicted class at each experimental condition was plotted using the same outcome taxonomy adopted for the experiments. Figure S11 below compares the resulting NN-predicted regime distribution with the corresponding experimental map (Figure 2-7). The NN reproduces the main structure of the regime space, including the low-$\overline{We}$ jetting region, the broad partial-rebound band at intermediate $\overline{We}$, the spreading-contact

region near $\alpha \to 1$, and the onset of splashing at higher $\overline{We}$. Minor differences are confined mainly to transition locations, which is consistent with the class-confusion behavior discussed in Section 4.3.1. Overall, this comparison supports the interpretation that the classifier has learned the physically organized regime topology in the chosen non-dimensional space, rather than only isolated pointwise labels. The experimental regime maps and the role of the Medium Neural Network as the most accurate and stable classification preset are already documented in the thesis.

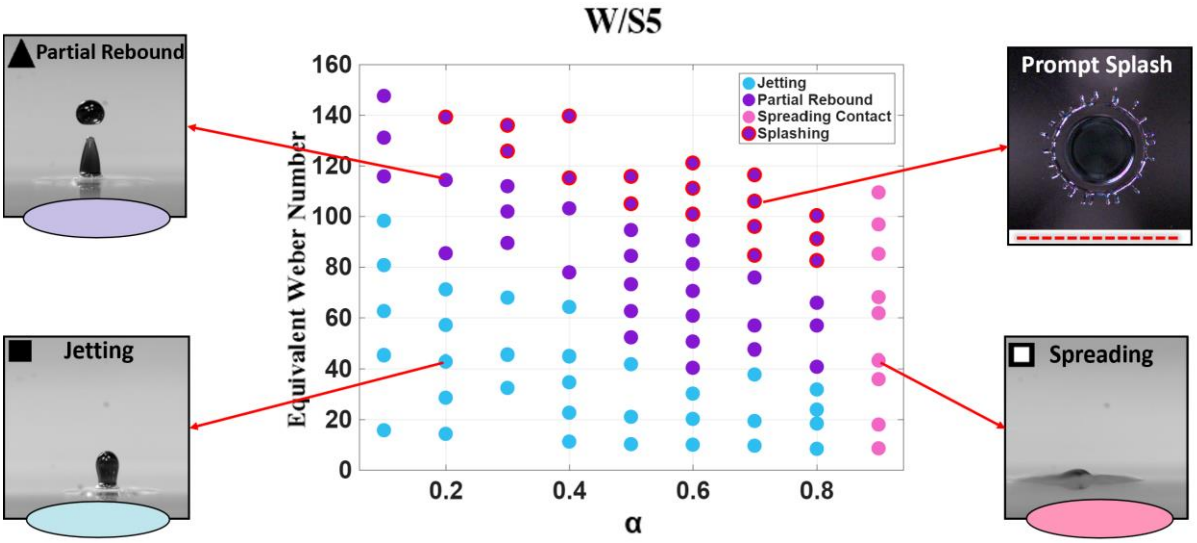

Figure S11. Neural-network-predicted impact regime map for the W/S5 liquid combination in the $\overline{We}$–α plane, generated using the top-performing Medium Neural Network classifier. The predicted outcome regions are shown using the same taxonomy as the experimental regime maps in Chapter 2.